

UNIVERSITÉ DU QUÉBEC À RIMOUSKI

**Conception et analyse des dispositifs multibandes et
d'amplificateur de puissance pour les applications de
communication sans fil**

Mémoire présenté

dans le cadre du programme de maîtrise en ingénierie
en vue de l'obtention du grade de maîtrise ès sciences appliquées

PAR

© **Zhebin WANG**

Mars 2013

UNIVERSITÉ DU QUÉBEC À RIMOUSKI
Service de la bibliothèque

Avertissement

La diffusion de ce mémoire ou de cette thèse se fait dans le respect des droits de son auteur, qui a signé le formulaire « *Autorisation de reproduire et de diffuser un rapport, un mémoire ou une thèse* ». En signant ce formulaire, l'auteur concède à l'Université du Québec à Rimouski une licence non exclusive d'utilisation et de publication de la totalité ou d'une partie importante de son travail de recherche pour des fins pédagogiques et non commerciales. Plus précisément, l'auteur autorise l'Université du Québec à Rimouski à reproduire, diffuser, prêter, distribuer ou vendre des copies de son travail de recherche à des fins non commerciales sur quelque support que ce soit, y compris l'Internet. Cette licence et cette autorisation n'entraînent pas une renonciation de la part de l'auteur à ses droits moraux ni à ses droits de propriété intellectuelle. Sauf entente contraire, l'auteur conserve la liberté de diffuser et de commercialiser ou non ce travail dont il possède un exemplaire.

Composition du jury:

Jean-Sébastien Deschênes, président du jury, Université du Québec à Rimouski

Chan-Wang Park, directeur de recherche, Université du Québec à Rimouski

Serioja Tatu, examinateur externe, Institut National de La Recherche Scientifique

Dépôt initial le 08 janvier 2013

Dépôt final le 27 mars 2013

REMERCIEMENTS

Je tiens à remercier chaleureusement mon directeur de recherche, monsieur Chan-Wang Park, professeur au département de mathématiques, informatique et génie à l'UQAR, pour sa délicatesse, son ouverture d'esprit, sa patience, sa souplesse, sa droiture et son grand professionnalisme.

Également, je remercie monsieur Mohammed Bahoura, monsieur Adrian Ilinca, et monsieur Abderrazak El Ouafi, professeurs au département de mathématiques, informatique et génie à l'UQAR, pour leur aide enthousiaste et leur patience tout au long de mes études en maîtrise. Par la même occasion, je tiens à remercier monsieur Claude Bouchard et monsieur Karel Uhler, personnels de soutien au département de mathématiques, informatique et génie à l'UQAR, pour leur grand soutien dans l'expérience dont j'ai bénéficié. Je tiens également à remercier monsieur Jean-Sébastien Deschênes, professeur au département de mathématiques, informatique et génie à l'UQAR, et monsieur Serioja Tatu, professeur au Centre Énergie Matériaux Télécommunications à l'université INRS, pour avoir accepté d'être membres de mon jury.

J'en profite également pour dire un merci particulier à madame France Canuel, secrétaire au département de mathématiques, informatique et génie à l'UQAR pour son accueil, son écoute et tous les bons conseils qu'elle m'a fournis tout au long de mon cursus de maîtrise.

Un grand merci à monsieur Sulav Adhikari (candidat en doctorat au Centre de Recherche Poly-Grames, École Polytechnique Montréal), monsieur Dousset David (Associé de recherche au Centre de Recherche Poly-Grames, École Polytechnique Montréal), et monsieur Jules Gauthier (Superviseur technique au Centre de Recherche Poly-Grames, École Polytechnique Montréal) pour avoir participé à cette étude en mettant à

ma disposition leurs connaissances de mesure et d'évaluation afin de m'aider à avancer dans mon projet de recherche.

Enfin, je tiens à remercier ma femme Yaoyao Xie d'avoir accepté de me partager avec mon aventure en maîtrise. Je tiens à remercier mon père monsieur Hao Wang et ma mère madame Shuhua Dai pour leur soutien à mes études et à ma vie. J'aimerais remercier toute ma famille, mes enseignants, mes professeurs, mes camarades de classe et mes amis. Je souhaite à tous de connaître le bonheur et la richesse de partager leur vie avec de si belles personnes. Je vous aime!

RÉSUMÉ

Dans les systèmes modernes de communication sans fil, il existe plusieurs standards de communication, comme WCDMA (Wideband Code Division Multiple Access), WLANs (Wireless Local Area Networks), GSM (Global Systems for Mobile Communications), WiMAX (Worldwide Interoperability for Microwave Access), et LTE (Long Term Evolution). L'interopérabilité et la coexistence entre les multistandards deviennent les principaux points communs entre les applications multibandes. En outre, pour les standards de téléphonie mobile de quatrième génération (4G) à large bande passante comme LTE *Advanced* pouvant fonctionner jusqu'à 100 MHz, il est nécessaire d'augmenter le débit de données et la vitesse de communication mobile. Pour satisfaire aux applications multibandes dans ce mémoire, j'ai analysé, conçu, et fabriqué un diviseur de Wilkinson multibande, une jonction *rat-race* multibande, et un amplificateur de puissance multibande. Pour satisfaire aux exigences larges bandes de 4G, en particulier pour améliorer le PAE (power added efficiency), un PA à large bande et à haut PAE utilisant le MRS (microstrip radial stub) pour supprimer les harmoniques est présenté.

Dans le chapitre 1, une ligne de transmission quarte d'onde multibande en forme de Pi avec des résonateurs est présentée et analysée à l'aide de la matrice ABCD. Un diviseur de Wilkinson bibande, un diviseur de Wilkinson tribande, et une jonction *rat-race* tribande sont analysés, conçus, et fabriqués pour démontrer la méthode de conception multibande proposée. La compacité est réalisée en mettant les lignes des circuits ouverts des deux circuits adjacents multibandes en forme de Pi à l'intérieur des composants multibandes proposés. En comparant la simulation et la mesure, les résultats de la simulation sont en bon accord avec les résultats de mesure.

Dans le chapitre 2, les méthodes de conception multibande des amplificateurs de puissance bibande et tribande sont présentées. Pour réaliser un amplificateur de puissance bibande fonctionnel, les résonateurs avec les lignes circuits ouverts sont analysés et appliqués à la fois dans les réseaux d'adaptation (MNs) d'entrée et de sortie. Deux amplificateurs de puissance bibandes sont conçus, fabriqués, et mesurés. Le réseau d'adaptation tribande est réalisé en utilisant un groupe de résonateurs qui se compose de deux résonateurs pour sélectionner la fréquence. La méthode de conception du réseau d'adaptation tribande est analysée et améliorée. Un amplificateur de puissance tribande est conçu, fabriqué, et mesuré pour démontrer la méthode de conception tribande proposée. Les résultats mesurés montrent qu'à différentes fréquences, les amplificateurs de puissance bibande et tribande ont d'excellentes performances.

Dans le chapitre 3, un PA à large bande à haut PAE est présenté en utilisant le MRS dans le réseau d'adaptation. Avec la caractéristique de suppression à large bande du MRS,

le MRS est utilisé pour supprimer les harmoniques du PA et satisfaire l'exigence de la 4G à large bande. Le MRS est comparé à la ligne quarte d'onde circuit ouvert par simulation et mesure. Avec le résultat de la mesure du PA fabriqué en utilisant le MRS, au moins 50 % de PAE et 37 dBm de puissance de sortie sont obtenus sur une largeur de bande de 12 % à partir de 2 GHz à 2,26 GHz. Le PAE maximal peut atteindre 80,52 % avec 40,53 dBm de puissance de sortie à 2,14 GHz. La méthode de conception proposée à large bande peut être utilisée pour le LTE *Advanced*.

La méthode et la procédure de conception multibande proposées du diviseur de Wilkinson, de la jonction *rat-race*, du PA, et la méthode de conception de PA à large bande dans ce mémoire peuvent être largement appliquées dans les applications des systèmes de communication modernes et futures.

Mots-clés: Harmonic suppression, microstrip radial stub, multiband, power added efficiency, power amplifier, rat-race coupler, resonator, wide bandwidth, Wilkinson power divider.

ABSTRACT

In the modern wireless communication systems, there are many communication standards exist, such as WCDMA (Wideband Code Division Multiple Access), WLANs (Wireless Local Area Networks), GSM (Global Systems for Mobile Communications), WiMAX (Worldwide Interoperability for Microwave Access), and LTE (Long Term Evolution). Interoperability and co-existence between multi-standards become the main issue of multiband applications. In addition, for the 4G mobile telecommunications network systems, wide bandwidth is required to increase the data rate and speed of mobile communication, such as LTE Advanced is up to 100 MHz. In this thesis, to meet the multiband applications of the present, I analyzed, designed, and fabricated multiband Wilkinson power divider, multiband rat-race coupler, and multiband power amplifier (PA). To satisfy wideband requirement for 4G, especially to enhance PAE (power added efficiency) of PA in wide bandwidth, a wideband PA with high PAE using MRS (microstrip radial stub) to suppress harmonic components is presented.

In chapter 1, a multiband quarter wavelength Pi-shaped transmission line with resonators is introduced and analyzed by using ABCD matrix. A dual-band Wilkinson power divider, a tri-band Wilkinson power divider, and a tri-band rat-race coupler are analyzed, designed, and fabricated to demonstrate the proposed multiband design method using the proposed multiband Pi-shaped structure. Compactness is realized by sharing the open-circuited stubs of the two adjacent multiband Pi-shaped circuits and putting all stubs inside the proposed multiband components themselves. Comparing the simulation and measurement, the simulated results are in good agreement with the measured results.

In chapter 2, the multiband design methods of dual-band PAs and tri-band PA are presented. To realize dual-band operation of PA, resonator with open-circuited stub is analyzed and applied in both input and output matching networks. Two dual-band PAs are designed, fabricated, and measured. Tri-band matching network is realized by employing resonator group which consists of two resonators as frequency selection element. Tri-band matching network design method is analyzed and advanced. One tri-band PA is designed, fabricated, and measured to demonstrate the proposed tri-band design method. Measured results show that at different frequencies, the proposed dual-band and tri-band PAs have excellent performance.

In chapter 3, one wideband high PAE PA is presented using MRS in matching network. With the wide bandwidth suppression characteristic of MRS, MRS is used to suppress harmonic components for PA to satisfy wideband requirement of 4G. MRS is compared with normal quarter wavelength open-circuited stub by both simulation and

measurement. With measured result of the fabricated PA using MRS, at least 50% PAE and 37 dBm output power over a 12% bandwidth from 2 GHz to 2.26 GHz is achieved. The maximum PAE can reach to 80.52% with 40.53 dBm output power at 2.14 GHz. The proposed wideband design method can be used for LTE Advanced.

The proposed multiband design method and procedure of Wilkinson power divider, rat-race coupler, and PA, and the wideband design method of PA presented in this thesis can be widely applied in applications of modern and future communication systems.

Keywords: Harmonic suppression, microstrip radial stub, multiband, power added efficiency, power amplifier, rat-race coupler, resonator, wide bandwidth, Wilkinson power divider.

TABLE DES MATIÈRES

REMERCIEMENTS.....	VII
RÉSUMÉ	IX
ABSTRACT.....	XI
TABLE DES MATIÈRES.....	XIII
LISTE DES TABLEAUX.....	XVII
LISTE DES FIGURES.....	XIX
LISTE DES ABRÉVIATIONS, DES SIGLES ET DES ACRONYMES ...	XXXIII
INTRODUCTION GÉNÉRALE	1
I MOTIVATION ET OBJECTIFS	1
II PROBLÉMATIQUE.....	4
III MÉTHODOLOGIE.....	11
IV CONTRIBUTIONS	14
CHAPITRE 1 STRUCTURE MULTIBANDE EN FORME DE PI UTILISANT DES RESONATEURS POUR LE DIVISEUR DE WILKINSON MULTIBANDE ET LA JONCTION <i>RAT-RACE</i> MULTIBANDE.....	19
1.1 RÉSUMÉ.....	19
1.2 MULTIBAND PI-SHAPED STRUCTURE WITH RESONATORS FOR MULTIBAND WILKINSON POWER DIVIDER AND MULTIBAND RAT-RACE COUPLER	20
1.2.1 ABSTRACT	20
1.2.2 INTRODUCTION.....	21
1.2.3 CONVENTIONAL WILKINSON POWER DIVIDER AND RAT-RACE COUPLER..	22
1.2.4 PROBLEM, OBJECTIVE, AND METHODOLOGY	25

1.2.5 ANALYSIS AND DESIGN OF NEW MULTIBAND PI-SHAPED STRUCTURE WITH RESONATORS.....	26
1.2.6 NEW DUAL-BAND WILKINSON POWER DIVIDER.....	64
1.2.7 NEW TRI-BAND WILKINSON POWER DIVIDER AND NEW TRI-BAND RACE COUPLER.....	78
1.2.8 CONCLUSION.....	98
 CHAPITRE 2 AMPLIFICATEUR DE PUISSANCE MULTIBANDE UTILISANT DES RESONATEURS DANS LES RESEAUX D'ADAPTATION.....	 101
2.1 RÉSUMÉ	101
2.2 MULTIBAND POWER AMPLIFIER USING RESONATORS IN MATCHING NETWORKS	103
2.2.1 ABSTRACT.....	103
2.2.2 INTRODUCTION	104
2.2.3 CONVENTIONAL POWER AMPLIFIER.....	105
2.2.4 PROBLEM, OBJECTIVE, AND METHODOLOGY	113
2.2.5 ANALYSIS AND DESIGN OF NEW MULTIBAND MATCHING NETWORK WITH RESONATORS.....	114
2.2.6 NEW CONCURRENT DUAL-BAND POWER AMPLIFIER.....	120
2.2.7 NEW CONCURRENT TRI-BAND POWER AMPLIFIER.....	146
2.2.8 CONCLUSION.....	162
 CHAPITRE 3 NOUVEL AMPLIFICATEUR DE PUISSANCE A LARGE BANDE EN UTILISANT LES STUBS RADIAUX MICRORUBANS POUR SUPPRIMER LES HARMONIQUES.....	 165
3.1 RÉSUMÉ	165
3.2 NOVEL WIDEBAND GAN HEMT POWER AMPLIFIER USING MICROSTRIP RADIAL STUB TO SUPPRESS HARMONICS.....	166
3.2.1 ABSTRACT.....	166
3.2.2 INTRODUCTION	166

3.2.3 PROBLEM, OBJECTIVE, AND METHODOLOGY	167
3.2.4 NEW ANALYSIS METHOD OF MICROSTRIP RADIAL STUB	168
3.2.5 DESIGN OF THE PROPOSED NEW WIDEBAND PA	175
3.2.6 FABRICATION AND MEASUREMENT	184
3.2.7 CONCLUSION	189
CONCLUSION GÉNÉRALE	191
RÉFÉRENCES BIBLIOGRAPHIQUES	195

LISTE DES TABLEAUX

Tableau 1: Measured results of the proposed dual-band Wilkinson power divider.....	76
Tableau 2: Comparison of the dual-band Wilkinson power divider and other references. .	77
Tableau 3: Measured results of the proposed tri-band Wilkinson power divider	90
Tableau 4: Comparison of the tri-band Wilkinson power divider and another reference ...	90
Tableau 5: Measured results of the proposed tri-band rat-race coupler	96
Tableau 6: Comparison of the tri-band rat-race coupler and another reference	97
Tableau 7: Measured results of the proposed tri-band power amplifier.....	160

LISTE DES FIGURES

Figure 1: (a) Amplificateur équilibré multibande, (b) Amplificateur Doherty multibande ...	3
Figure 2: (a) Diviseur de Wilkinson conventionnel, (b) Jonction <i>rat-race</i> conventionnelle .	4
Figure 3: Outil LineCalc dans ADS	5
Figure 4: (a) ADS simulation de ligne microruban avec une longueur électrique 90° et une impédance caractéristique 70,7 Ohm. (b) résultat simulé de la figure 4 (a)	6
Figure 5: Résultats simulés de <i>load pull</i> de CGH40010, (a) 1 GHz, (b) 1.5 GHz, (c) 2.5 GHz, ligne continue: PAE, ligne pointe: puissance de sortie	8
Figure 6: Réseau d'adaptation de type L.....	9
Figure 7: Amplificateur de puissance multibande utilisant des commutateurs	9
Figure 8: Harmoniques de la technologie LTE <i>Advanced</i> à 2.14 GHz.....	10
Figure 9: Réseau de deux ports en forme de Pi constitué par deux admittances shunts (Y_1 et Y_2), et une admittance série Y_3	11
Figure 10: La compacité améliorée du diviseur de Wilkinson bibande	12
Figure 11: Topologies des réseaux d'adaptation multibandes, (a): réseau d'adaptation bibande, (b): réseau d'adaptation tribande	13
Figure 12: Topologie de la composante proposée de suppression d'harmonique à large bande, MRS (microstrip radial stub)	14
Figure 13: Conventional Pi-shaped two-port network consisting of two shunt admittances (Y_1 and Y_2), and one series admittance Y_3	20

Figure 14: Conventional Wilkinson power divider	23
Figure 15: Conventional rat-race coupler	24
Figure 16: Ideal models in ADS, (a): capacitor model, (b): inductor model.....	27
Figure 17: Simulated results of the ideal models, (a): ideal 0.1 pF capacitor model, (b): ideal 1.8 nH inductor model.....	29
Figure 18: Models of Modelithics, (a): capacitor model, (b): inductor model	30
Figure 19: Simulated results of Modelithics models, (a): ATC 600S 0.1 pF capacitor model, (b): Coilcraft 0603HP 1.8 nH inductor model.....	31
Figure 20: Comparison between ideal models (solid line) and measured models from Modelithics (dot line), (a): capacitor models, (b): inductor models.....	32
Figure 21: Simulated models, (a): Ideal model provided by ADS, (b): ATC model provided by Modelithics, (c): MURATA model provided by Modelithics.....	33
Figure 22: Simulated results of capacitor models, solid line: ideal model provided by ADS, dot line: ATC model provided by Modelithics, and dash line: MURATA model provided by Modelithics	34
Figure 23: Parallel resonant circuit structure	35
Figure 24: Ideal 1.5 GHz resonator design schematic diagram in ADS.....	36
Figure 25: Simulated results of the ideal 1.5 GHz resonator design in ADS, solid line: insertion loss, and dot line: return loss.....	37
Figure 26: 1.5 GHz resonator circuit designed by using models from Modelithics compared with the ideal resonator circuit shown in Fig. 24	38

Figure 27: Simulated result of the 1.5 GHz resonator circuit designed by using models from Modelithics with the same value as the ideal 1.5 GHz resonator design, solid line: insertion loss, and dot line: return loss	38
Figure 28: Tuning tool in ADS used to adjust the variable capacitance and inductance of capacitor and inductor models, respectively	39
Figure 29: Simulated result of 1.5 GHz resonator by using the models of Modelithics with 1 pF capacitor and 9.37 nH inductor, solid line: insertion loss, and dot line: return loss	40
Figure 30: Resonator designed for (a): 2.5 GHz and (b): 1.5 GHz by using existent component values from manufacturers.....	41
Figure 31: Simulated results of resonators designed for (a): 2.5 GHz and (b): 1.5 GHz by using existent component values from manufactures, solid line: insertion loss, and dot line: return loss	42
Figure 32: 2.5 GHz resonator by using microstrip line instead of inductor	43
Figure 33: Simulated result of 2.5 GHz resonator by using microstrip line type inductor instead of chip inductor, solid line: insertion loss, and dot line: return loss	44
Figure 34: Schematic diagram of 2.5 GHz resonator using momentum model	45
Figure 35: Simulated result of momentum model 2.5 GHz resonator, solid line: insertion loss, dot line: return loss	45
Figure 36: Conventional Pi-shaped structure consists of one series microstrip line and two open-circuited stubs.....	46
Figure 37: Two-port network consisting of one transmission line	47
Figure 38: Two-port network consisting of one shunt admittance	48

Figure 39: Open-circuited transmission line	49
Figure 40: Principle of dual-band quarter wavelength transmission line, (a): at frequency f_1 , and (b): at frequency f_2	51
Figure 41: Tri-band Pi-shaped structure with resonators	54
Figure 42: Principle of the proposed tri-band Pi-shaped structure with resonators	55
Figure 43: Multiband Pi-shaped structure with resonators.....	60
Figure 44: Principle of multiband Pi-shaped structure.....	61
Figure 45: Proposed topology of dual-band Wilkinson power divider	65
Figure 46: The designed schematic diagram of dual-band Pi-shaped structure	66
Figure 47: 3.6 GHz resonator circuit in ADS using models of Modelithics	67
Figure 48: Simulated result of 3.6 GHz resonator circuit in ADS, solid line: insertion loss, and dot line: return loss	67
Figure 49: Equivalent circuit of Pi-shaped circuit at 2.5 GHz, (a): Pi-shaped circuit, (b): equivalent quarter wavelength microstrip line	68
Figure 50: Tuning the length of l_1 in Fig. 46	69
Figure 51: Simulated result of tuning the length of l_1 shown in Fig. 46.....	69
Figure 52: S_{11} simulated result of the dual-band Pi-shaped structure in Fig. 46 with characteristic impedance 70.7 Ohm.....	70
Figure 53: Simulated results of dual-band Pi-shaped structure in Fig. 46, solid line: insertion loss, and dot line: return loss.....	71
Figure 54: ADS Momentum simulation circuit of the proposed dual-band Wilkinson power divider	72

Figure 55: Fabricated circuit of the proposed dual-band Wilkinson power divider	73
Figure 56: Simulated (cross) and measured (round and triangle) results of insertion loss of the proposed dual-band Wilkinson power divider	74
Figure 57: Simulated (cross) and measured (round) results of output port isolation of the proposed dual-band Wilkinson power divider	74
Figure 58: Simulated (cross) and measured (round) results of input return loss of the proposed dual-band Wilkinson power divider	75
Figure 59: Simulated (cross) and measured (round and triangle) results of output return loss of the proposed dual-band Wilkinson power divider	75
Figure 60: Measured phases of two output ports of the proposed dual-band Wilkinson power divider, round: Port 2, cross: Port3	76
Figure 61: Proposed topology of tri-band Wilkinson power divider	79
Figure 62: Proposed topology of tri-band rat-race coupler	79
Figure 63: Designed schematic diagram of the proposed tri-band Pi-shaped structure.....	81
Figure 64: Phase simulated result of the proposed tri-band Pi-shaped structure.....	82
Figure 65: S_{11} simulated result of the tri-band Pi-shaped structure shown in Fig. 63 with reference impedance 70.7 Ohm in the center of Smith chart.....	83
Figure 66: Simulated results of the proposed tri-band Pi-shaped structure, solid line: insertion loss, and dot line: return loss	84
Figure 67: ADS Momentum simulation schematic diagram of the proposed tri-band Wilkinson power divider.....	85
Figure 68: Fabricated circuit of the proposed tri-band Wilkinson power divider	86

Figure 69: Simulated (cross) and measured (round and triangle) results of insertion loss of the proposed tri-band Wilkinson power divider.....	87
Figure 70: Simulated (cross) and measured (round) results of output port isolation of the proposed tri-band Wilkinson power divider.....	88
Figure 71: Simulated (cross) and measured (round) results of input return loss of the proposed tri-band Wilkinson power divider.....	88
Figure 72: Simulated (cross) and measured (round and triangle) results of output return loss of the proposed tri-band Wilkinson power divider.....	89
Figure 73: Measured phases of two output ports of the proposed tri-band Wilkinson power divider, round: <i>Port 2</i> , cross: <i>Port 3</i>	89
Figure 74: ADS momentum simulation circuit of the proposed tri-band rat-race coupler...	91
Figure 75: Fabricated circuit of the proposed tri-band rat-race coupler.....	92
Figure 76: Simulated and measured results of insertion loss of S_{23} and S_{43} of the proposed tri-band rat-race coupler.....	93
Figure 77: Simulated and measured results of $\angle S_{23}-\angle S_{43}$ of the proposed tri-band rat-race coupler.....	93
Figure 78: Simulated and measured results of insertion loss of S_{21} and S_{41} of the proposed tri-band rat-race coupler.....	94
Figure 79: Simulated and measured results of $\angle S_{21}-\angle S_{41}$ of the proposed tri-band rat-race coupler.....	94
Figure 80: Simulated and measured results of return loss of <i>Port 1</i> and <i>Port 4</i> of the proposed tri-band rat-race coupler.....	95

Figure 81: Simulated and measured results of return loss of <i>Port 2</i> and <i>Port 3</i> of the proposed tri-band rat-race coupler.....	95
Figure 82: Simulated and measured results of isolation of S_{31} and S_{42} of the proposed tri-band rat-race coupler	96
Figure 83: Conventional lumped-element bias circuit	106
Figure 84: Source pull simulation schematic diagram of output power and PAE	107
Figure 85: Load pull simulation schematic diagram of output power and PAE.....	108
Figure 86: Simulated results of source pull simulation at (a): 1 GHz, (b): 1.5GHz, and (c): 2.5 GHz, solid line: PAE, and dot line: output power	109
Figure 87: Simulated results of load pull simulation at (a): 1 GHz, (b): 1.5GHz, and (c): 2.5 GHz, solid line: PAE, and dot line: output power.....	110
Figure 88: Stability simulation schematic diagram.....	111
Figure 89: Source and load stability circles of CGH40010F_r6 model, (a): 1 GHz, (b): 1.5 GHz, (c): 2.5 GHz, solid line: source stability circle, and dot line: load stability circle	112
Figure 90: Conventional L-type matching network.....	113
Figure 91: Parallel resonators, (a): the resonant circuit to block signal at frequency f_1 , and (b): the resonant circuit to block signal at frequency f_2	115
Figure 92: Block diagram of the proposed dual-band power amplifier	115
Figure 93: Principle and topologies of dual-band matching networks, (a): input matching network, and (b): output matching network.....	116
Figure 94: Parallel resonator circuits for (a): frequencies f_1 , (b): frequency f_2 , (c): frequency f_3 , and (d): resonator group	117

Figure 95: Principle and topologies of tri-band matching networks, (a): input matching network, and (b): output matching network	118
Figure 96: Desired source and load impedance points of CGH40010 at 2.5 GHz, 1.5 GHz, and 1 GHz	119
Figure 97: Resonators designed for the proposed dual-band power amplifier, (a): 2.5 GHz and (b): 1.5 GHz	121
Figure 98: Simulated results of the resonators designed for the proposed dual-band power amplifier, (a): 2.5 GHz and (b): 1.5 GHz, solid line: insertion loss, and dot line: return loss	122
Figure 99: The design schematic diagrams of resonant circuit with open-circuited stub, (a): 2.5 GHz and (b): 1.5 GHz	123
Figure 100: Simulated results of the resonant circuit with open-circuited stub shown in Fig. 99, (a): 2.5 GHz resonator and (b): 1.5 GHz resonator	124
Figure 101: The design schematic diagram of the source matching network of the proposed dual-band power amplifier	126
Figure 102: The design schematic diagram of the load matching network of the proposed dual-band power amplifier	127
Figure 103: Layout of the proposed dual-band class AB power amplifier.....	128
Figure 104: Simulated impedance results of the proposed dual-band matching networks, (a): input matching network, and (b): output matching network with 0.01 GHz step.	129
Figure 105: The test setup diagram of the proposed dual-band power amplifier	130
Figure 106: Fabricated dual-band class AB power amplifier using resonators constructed by chip capacitor and chip inductor.....	131

Figure 107: Measured (round point) and simulated (triangular point) results of PAE versus output power of the proposed dual-band power amplifier, (a): 2.4 GHz, and (b): 1.5 GHz.....	132
Figure 108: Measured output power versus frequency of the proposed dual-band power amplifier	133
Figure 109: Measured AM-AM curves at 2.4 GHz (round point) and 1.5 GHz (triangular point) of the proposed dual-band power amplifier	133
Figure 110: Measured PAE versus frequency of the proposed dual-band power amplifier	134
Figure 111: Resonator consists of capacitor and microstrip line, (a) 2.5 GHz resonator, (b) 1.5 GHz resonator.....	135
Figure 112: Simulated results of resonator that consists of capacitor and microstrip line, (a) 2.5 GHz, (b) 1.5 GHz.....	136
Figure 113: ADS momentum design schematic diagram of the proposed dual-band source matching network using resonators with microstrip line type inductor	138
Figure 114: ADS momentum design schematic diagram of the proposed dual-band load matching network using resonators with microstrip line type inductor	139
Figure 115: Simulated results of the proposed dual-band matching networks using resonators with microstrip line type inductor, (a) source, and (b) load, with 0.01 GHz step.....	140
Figure 116: The adjusted dual-band load matching network by adding another dual-band matching network after the structure shown in Fig. 114	141
Figure 117: Simulated results of the adjusted dual-band load matching network with frequency step 0.01 GHz.....	142

Figure 118: Total layout of the proposed dual-band power amplifier using resonators with microstrip line.....	143
Figure 119: Fabricated circuit of the proposed dual-band power amplifier using resonators with microstrip line.....	143
Figure 120: Measured AM-AM curves at 2.5 GHz (round point) and 1.5 GHz (triangular point) of the proposed dual-band power amplifier shown in Fig. 119	144
Figure 121: Measured gain curves at 2.5 GHz (round point) and 1.5 GHz (triangular point) of the proposed dual-band power amplifier shown in Fig. 119.....	144
Figure 122: Measured PAE curves at 2.5 GHz (round point) and 1.5 GHz (triangular point) of the proposed dual-band power amplifier shown in Fig. 119.....	145
Figure 123: Resonator groups designed to pass the signal at (a): 2.5 GHz, (b): 1.5 GHz, and (c): 1 GHz.....	147
Figure 124: ADS simulated results of the resonator groups designed to pass the signal at (a): 2.5 GHz, (b): 1.5 GHz, and (c): 1 GHz	148
Figure 125: The desired load impedance point of CGH40010 for 1 GHz.....	149
Figure 126: The simplest L-type matching network for 1 GHz.....	149
Figure 127: ADS design schematic diagram of the matching network for 1 GHz	150
Figure 128: Simulated result of the 1 GHz matching network shown in Fig. 127 with frequency step 0.01 GHz.....	151
Figure 129: ADS design schematic diagram of the proposed tri-band load matching network for 1 GHz, 1.5 GHz, and 2.5 GHz.....	152
Figure 130: Simulated result of the proposed tri-band load matching network shown in Fig. 129, frequency step: 0.01 GHz.....	153

Figure 131: ADS momentum design schematic diagram of the advanced tri-band load matching network	154
Figure 132: Equivalent matching circuit of the proposed advanced tri-band load matching network shown in Fig. 131 at 1 GHz.....	155
Figure 133: Simulated result of the proposed advanced tri-band load matching network..	155
Figure 134: ADS momentum design schematic diagram of the proposed tri-band source matching network	156
Figure 135: Simulated result of the proposed tri-band source matching network.....	157
Figure 136: The layout of the proposed tri-band power amplifier	157
Figure 137: The fabricated proposed concurrent tri-band power amplifier	158
Figure 138: Measured results of the resonators designed for 1 GHz, 1.5 GHz, and 2.5 GHz	159
Figure 139: Measured results of AM-AM of the proposed tri-band power amplifier at 1 GHz, 1.5 GHz, and 2.5 GHz	160
Figure 140: Measured results of gain of the proposed tri-band power amplifier at 1 GHz, 1.5 GHz, and 2.5 GHz.....	161
Figure 141: Measured results of PAE of the proposed tri-band power amplifier at 1 GHz, 1.5 GHz, and 2.5 GHz.....	161
Figure 142: Microstrip radial stub (MRS), θ : the angle subtended by MRS, W : the bottom length of MRS, L : the length of MRS.....	169
Figure 143: MRSs with sweeping θ from 50° to 150°	169
Figure 144: Simulated results of MRSs with sweeping θ from 50° to 150°	170

Figure 145: MRSs with sweeping W from 47 mil to 97 mil.....	171
Figure 146: Simulated results of MRSs with sweeping W from 47 mil to 97 mil	172
Figure 147: ADS momentum design schematic diagrams of the MRSs and normal rectangular quarter-wave stubs for 2.14 GHz, 4.28 GHz, and 6.42 GHz	173
Figure 148: Simulated comparisons of the MRSs (solid line) and normal rectangular quarter-wave stubs (dot) designed for (a): 2.14 GHz, (b): 4.28 GHz, and (c): 6.42 GHz	174
Figure 149: Desired input and output impedance points of CGH40010	176
Figure 150: Simulated result of load pull simulation at 2.14 GHz	176
Figure 151: Topologies of the proposed MRS matching network, (a): output and (b): input	177
Figure 152: Momentum simulation circuit of the proposed MRS output matching network	178
Figure 153: Momentum simulation circuit of the proposed MRS input matching network	179
Figure 154: The simulated result of the proposed MRS output matching network	180
Figure 155: The simulated result of the proposed MRS input matching network.....	181
Figure 156: Simulated results of the proposed matching networks with MRSs, (a): output, (b): input, solid line: insertion loss, and dot line: return loss	182
Figure 157: Layout of the proposed PA using MRS to suppress harmonic components...	183
Figure 158: Fabricated MRSs and normal quarter-wave rectangular stubs, (a): 2.14 GHz, (b): 4.28 GHz, and (c): 6.42 GHz.....	184

Figure 159: Measured results of the fabricated MRS and normal quarter-wave rectangular stub for 2.14 GHz	185
Figure 160: Measured results of the fabricated MRS and normal quarter-wave rectangular stub for 4.28 GHz	185
Figure 161: Measured results of the fabricated MRS and normal quarter-wave rectangular stub for 6.42 GHz	186
Figure 162: The fabricated proposed PA with MRS	187
Figure 163: Measured AM-AM of the proposed PA with MRS	187
Figure 164: Measured PAE and gain versus output power of the proposed PA with MRS	188
Figure 165: Measured PAE and output power obtained from 1.92 GHz to 2.27 GHz of the proposed PA with MRS	188

LISTE DES ABRÉVIATIONS, DES SIGLES ET DES ACRONYMES

3G	Third Generation
	Troisième génération
4G	Fourth Generation
	Quatrième génération
ADS	Advanced Design System
	Système de conception avancée
ATC	American Technical Ceramics
	Céramique technique américaine
CAD	Computer Aided Design
	Conception assistée par ordinateur
CRLH	Composite Right/Left-Handed
	Composite à droite / à gauche
D	Dimensional
	Dimensionnel
DC	Direct Current
	Courant continu

EM	Electromagnetic
	Électromagnétique
GaN	Gallium Nitride
	Nitruure de gallium
GSM	Global Systems for Mobile Communications
	Système mondial de communications mobiles
HEMT	High Electron Mobility Transistor
	Transistor à électron à haute mobilité
HMSIW	Half-Mode Substrate Integrated Waveguide
	Guide d'onde de substrat intégré demi-mode
HSB	Harmonic Suppressing Bandwidth
	La largeur de bande de la suppression d'harmonique
LTE	Long Term Evolution
	Évolution à long terme
MIMO	Multiple-Input multiple-Output
	Multi-Entrées multi-sorties
MN	Matching Network
	Réseau d'adaptation
PA	Power Amplifier
	Amplificateur de puissance

PAE	Power Added Efficiency Rendement de puissance ajoutée
RF	Radio Frequency Fréquence radio
SIW	Substrate Integrated Waveguide Guide d'onde de substrat intégré
TL	Transmission Line Ligne de transmission
VNA	Vector Network Analyzer Analyseur de réseau vectoriel
VSWR	Voltage Standing Wave Ratio Rapport d'ondes stationnaires de tension
WCDMA	Wideband Code Division Multiple Access Accès multiple par répartition en code à large bande
WE	Waveform Engineering Ingénierie de forme d'onde
WiMAX	Worldwide Interoperability for Microwave Access L'interopérabilité mondiale pour l'accès micro-onde
WLANs	Wireless Local Area Networks Réseaux locaux sans fil

INTRODUCTION GÉNÉRALE

I. MOTIVATION ET OBJECTIFS

Avec le développement rapide des systèmes modernes de communication sans fil, il y a plusieurs types de standards de communication utilisés pour les différentes applications de communication, comme WCDMA (wideband code division multiple access) à 2,14 GHz (Lee *et al.*, 2009; Steinbeiser *et al.*, 2007; Jeong *et al.*, 2009), WLANs (wireless local area networks) à 2.4 GHz et 5.2 GHz (Wu *et al.*, 2009 a; Chiou *et al.*, 2009), et GSM (the global systems for mobile communication systems) à 0.9 GHz et 1.8GHz (Wu *et al.*, 2009 a; Chiou *et al.*, 2009; Chou *et al.*, 2010). Dans la quatrième génération (4G), les standards LTE (long term evolution) et WiMAX (worldwide interoperability for microwave access) ont été largement appliqués pour augmenter le débit de données et la vitesse de communication mobile (Kang *et al.*, 2010; Kang *et al.*, 2011). L'interopérabilité et la coexistence entre les standards deviennent le principal enjeu des systèmes de communication modernes. Des composants et dispositifs avec performances multibandes sont requis pour satisfaire les applications multibandes. En outre, afin de fournir des services de débit de données, des signaux à bande passante plus large sont utilisés dans 4G (Kim *et al.*, 2010), tels que WiMAX, LTE, et LTE *Advanced*, ce dernier ayant une bande passante jusqu'à 100 MHz (Wu *et al.*, 2010; Wright *et al.*, 2009). Des composants et dispositifs ayant une large bande passante sont également nécessaires pour répondre aux exigences des nouvelles normes de communication.

Mon objectif est de concevoir et de fabriquer un diviseur de Wilkinson multibande, une jonction *rat-race* multibande, et un amplificateur de puissance multibande pour satisfaire les exigences multistandards pour les applications multibandes. En outre, pour les nouvelles normes de communication, tel que WiMAX, LTE, et LTE *Advanced*, je vais

concevoir et fabriquer un amplificateur de puissance à large bande à haut PAE (power added efficiency) par l'amélioration de la bande passante et la suppression des harmoniques.

Les objectifs précis sont résumés comme suit:

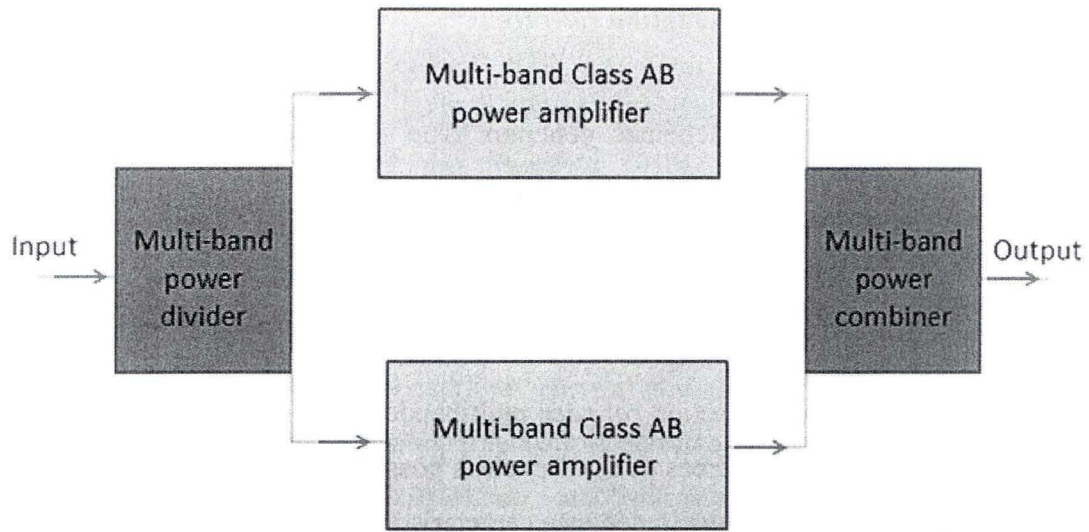
1 : Concevoir un diviseur de Wilkinson, une jonction *rat-race*, et un amplificateur de puissance avec une performance multibande simultanée, où deux ou trois fréquences distinctes sont traitées simultanément. La performance multibande simultanée est obtenue sans commutateur et sans circuit de commande électronique.

2 : Réduire la taille de chaque circuit multibande. Faire des structures de circuits compacts, pour économiser l'espace de la carte de fabrication. Minimiser le nombre de composants utilisés, surtout pour les composants actifs comme le transistor.

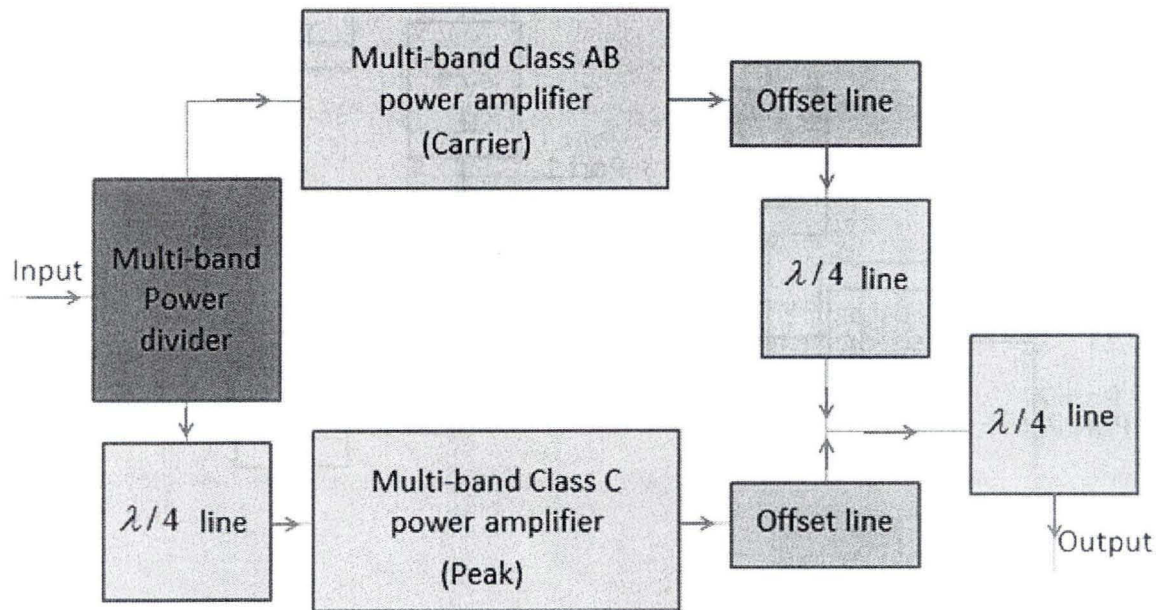
3 : Réduire la complexité de la procédure de conception. Simplifier la méthode de conception pour chaque circuit multibande.

4 : Obtenir une performance à haut PAE pour l'amplificateur de puissance pour les applications à large bande. Pour l'amplificateur de puissance à haut PAE, comme classe F et classe F inverse, les harmoniques doivent être bien supprimées dans une plus grande bande passante. Je vais trouver une méthode pour concevoir le circuit de suppression des harmoniques à large bande pour réaliser l'amplificateur de puissance à haut PAE à large bande.

5 : Pour d'autres fins d'application multibandes, on peut utiliser le diviseur de Wilkinson multibande, la jonction *rat-race* multibande, et l'amplificateur de puissance multibande proposé dans d'autres circuits multibandes avec une structure plus complexe. L'amplificateur équilibré multibande et l'amplificateur Doherty multibande sont des exemples de structure plus complexes. Ils sont respectivement représentés dans les figures 1 (a) et (b).



(a)



(b)

Figure 1: (a) Amplificateur équilibré multibande, (b) Amplificateur Doherty multibande

II. PROBLÉMATIQUE

(a) Diviseur de Wilkinson et jonction *rat-race*

La figure 2 montre les schémas généraux d'un diviseur de Wilkinson et d'une jonction *rat-race* (Aflaki *et al.*, 2010). L'élément principal de ces deux dispositifs est la ligne quarte d'onde dont l'impédance caractéristique est de 70,7 Ohm. Le diviseur de Wilkinson classique est constitué de deux lignes quartes d'onde et la jonction *rat-race* classique est constituée de six lignes quartes d'onde. Pour concevoir un diviseur de Wilkinson multibande et une jonction *rat-race* multibande, il faut s'assurer que pour chaque fréquence, l'élément principal de ces deux dispositifs possède une longueur qui équivaut au quart de la longueur d'onde et une impédance caractéristique 70,7 Ohm.

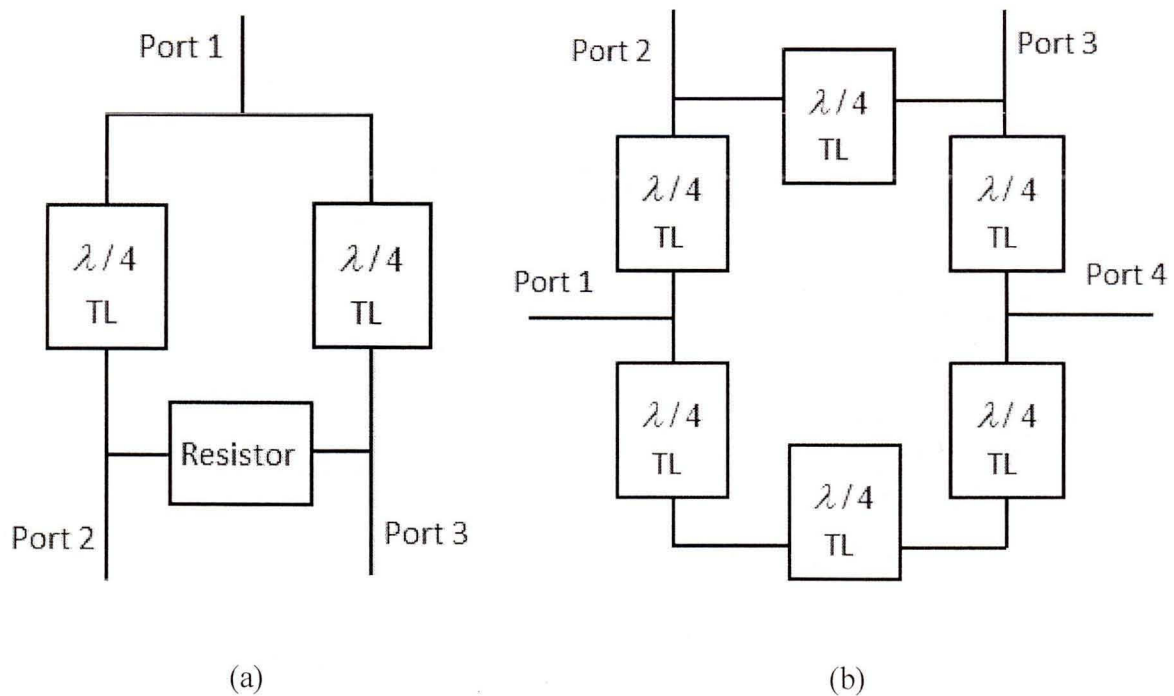


Figure 2: (a) Diviseur de Wilkinson conventionnel, (b) Jonction *rat-race* conventionnelle

La ligne microruban conventionnelle à quart d'onde ne peut pas avoir la bonne longueur électrique pour les différentes fréquences simultanément. La longueur physique de la ligne microruban est donc fixée pour avoir la bonne longueur électrique à la fréquence 2.5 GHz. En utilisant l'outil LineCalc en ADS (Advanced Design System), la longueur et la largeur de la ligne microruban sont calculées. La ligne possède une longueur électrique 90° et une impédance caractéristique 70,7 Ohm à 2,5 GHz comme la montre sur la figure 3. C'est le substrat TLX-8 qui est utilisé. Ses paramètres électriques, soit la fréquence centrale, la longueur électrique efficace, et l'impédance caractéristique, sont spécifiés dans le logiciel. Cela permet d'obtenir la largeur de la ligne microruban ($W = 47,2$ mil) et la longueur de la ligne ($L = 829,1$ mil).

Er: Dielectric constant;
 H: Dielectric thickness;
 T: Copper thickness

Component
Type: **MLIN** ID: **MLIN: MLIN_DEFAULT**

Substrate Parameters
ID: **MSUB_DEFAULT**

Er	2.550	N/A
Mur	1.000	N/A
H	31.000	mil
Hu	3.9e+34	cm
T	35.000	um
Cond	4.1e7	N/A

Component Parameters
Freq: **2.500** GHz

Wall1: mil
Wall2: mil

Values are consistent

Physical

W: **47.209843** mil
L: **829.137795** mil

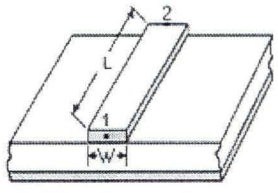
Synthesize Analyze

Electrical

Z0: **70.700** Ohm
E_Eff: **90.000** deg

Width of microstrip line

Length of microstrip line



Calculated Results

K_Eff = 2.026
A_DB = 0.029
SkinDepth = 0.061

Center frequency

Characteristic impedance of microstrip line

Effective electrical length

Figure 3: Outil LineCalc dans ADS

La figure 4 montre le diagramme schématique du logiciel ADS et le résultat simulé de la phase d'une ligne microruban ayant une longueur électrique de 90° et une impédance caractéristique de 70,7 Ohm. D'après la figure 4 (b), on remarque que, la ligne microruban quart d'onde conventionnelle possède une longueur électrique de 90° à 2,5 GHz, tandis qu'à 1,5 GHz et 1 GHz, la longueur électrique est respectivement de $53,96^\circ$ et $35,97^\circ$. La ligne microruban quart d'onde traditionnelle ne peut donc pas être utilisée comme ligne de transmission quart d'onde multibande.

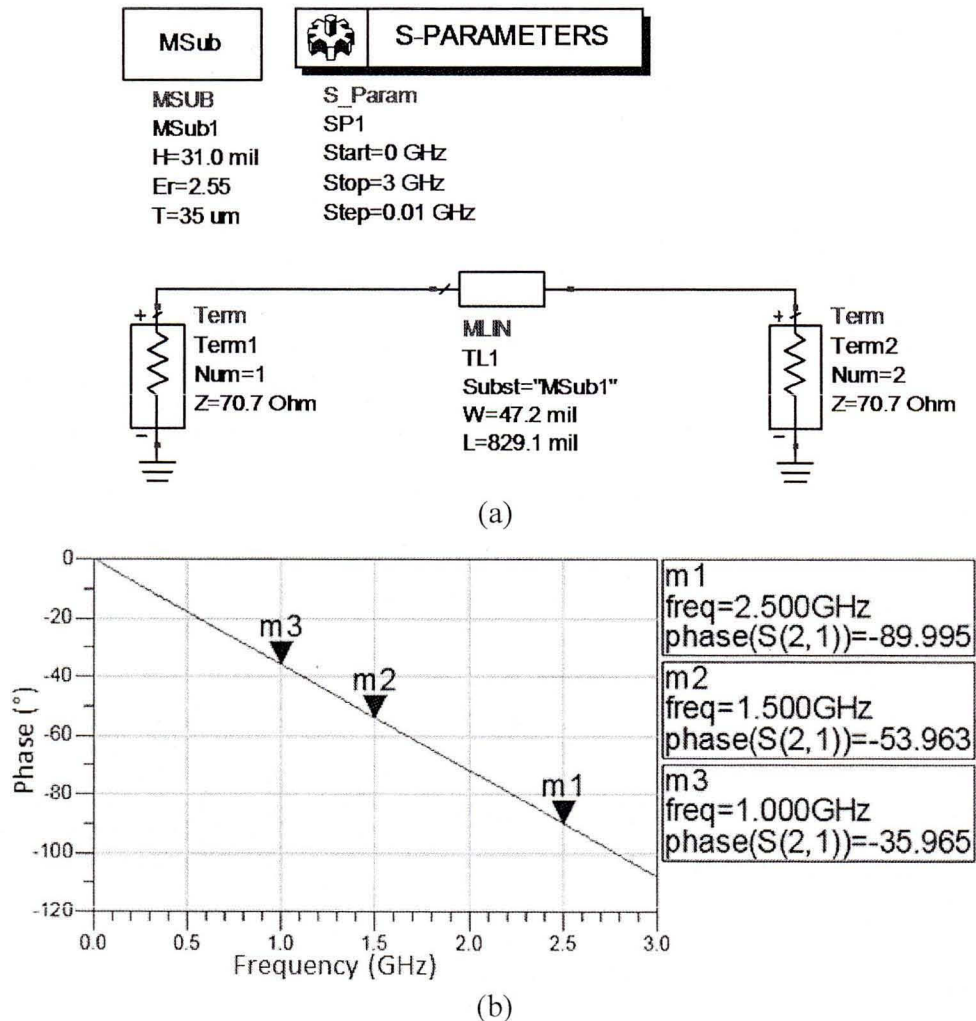


Figure 4: (a) ADS simulation de ligne microruban avec une longueur électrique 90° et une impédance caractéristique 70,7 Ohm. (b) résultat simulé de la figure 4 (a)

Le fonctionnement multibande du diviseur de Wilkinson classique et de la jonction *rat-race* classique est limité par la ligne microruban quarte d'onde classique (Lin *et al.*, 2004; Park, 2009 b; Chin *et al.*, 2010; Kong *et al.*, 2006). Pour concevoir et fabriquer un diviseur de Wilkinson multibande et une jonction *rat-race* multibande, la ligne de transmission quarte d'onde doit être explorée et conçue.

(b) Amplificateur de puissance

Un amplificateur de puissance avec la même condition de polarisation a différents points d'impédance du réseau d'adaptation correspondant aux différentes fréquences pour le PAE maximal ou la puissance de sortie maximale. Par exemple, la figure 5 représente le résultat de la simulation de *load pull* pour le PAE et la puissance de sortie à fréquences différentes (1 GHz, 1,5 GHz, et 2,5 GHz) en utilisant le modèle de transistor de CGH40010 CREE. De même, aux différentes fréquences, avec la même condition de polarisation, les contours de stabilité sur l'abaque de Smith seront aussi différents.

Le réseau d'adaptation conventionnel de type L de l'amplificateur de puissance est montré dans la figure 6. Ce réseau d'adaptation est conçu pour obtenir le PAE maximal ou la puissance de sortie maximale. Parce que la longueur physique de la ligne microruban du réseau d'adaptation de type L conventionnel est fixée à une fréquence spécifique, tel que discuté précédemment, la longueur électrique de la ligne microruban ne peut pas être modifiée à d'autres fréquences pour un usage multibande. En d'autres termes, l'adaptation d'impédance en utilisant un réseau d'adaptation conventionnel de type L pour deux ou trois fréquences distinctes n'est pas indépendante.

Dans les travaux précédents, pour réaliser une opération multibande, un commutateur a été exploré pour la conception d'amplificateur de puissance multibande (Eo *et al.*, 2004; Adar *et al.*, 1998). La figure 7 montre le schéma général de l'amplificateur de puissance multibande en utilisant des commutateurs. Le basculement entre les différents réseaux d'adaptation et l'ajustement des composants ajustables sont incapables d'offrir un fonctionnement simultané en cas de changement de fréquence (Negra *et al.*, 2008). En

outre, un amplificateur de puissance multibande utilisant des commutateurs a généralement une structure parallèle. Il contient plusieurs amplificateurs de puissance ou réseaux d'adaptation parallèles pour différentes fréquences. L'espace de fabrication totale est grand et le coût des composants ou des transistors est élevé.

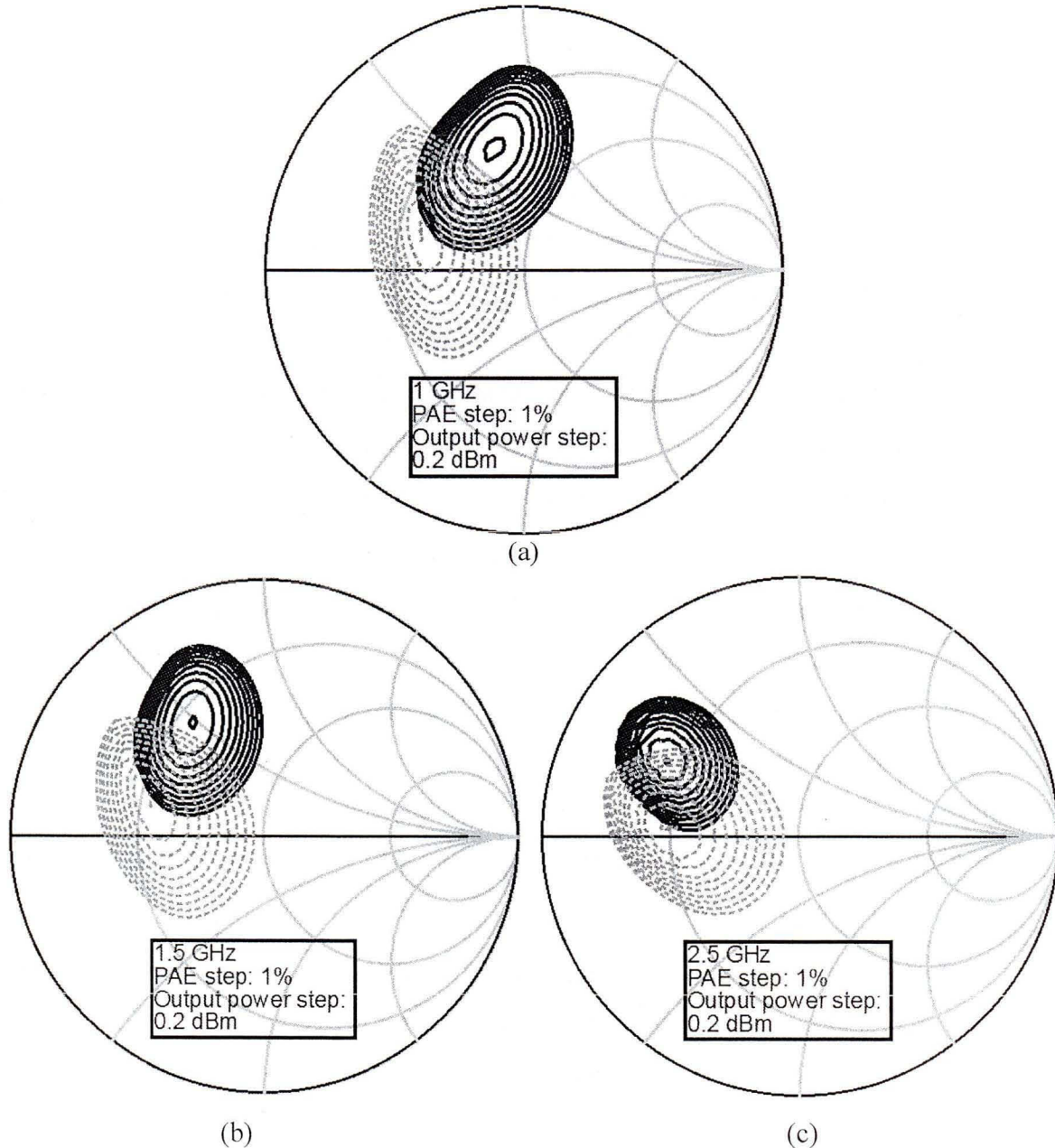


Figure 5: Résultats simulés de *load pull* de CGH40010, (a) 1 GHz, (b) 1.5 GHz, (c) 2.5 GHz, ligne continue: PAE, ligne pointée: puissance de sortie

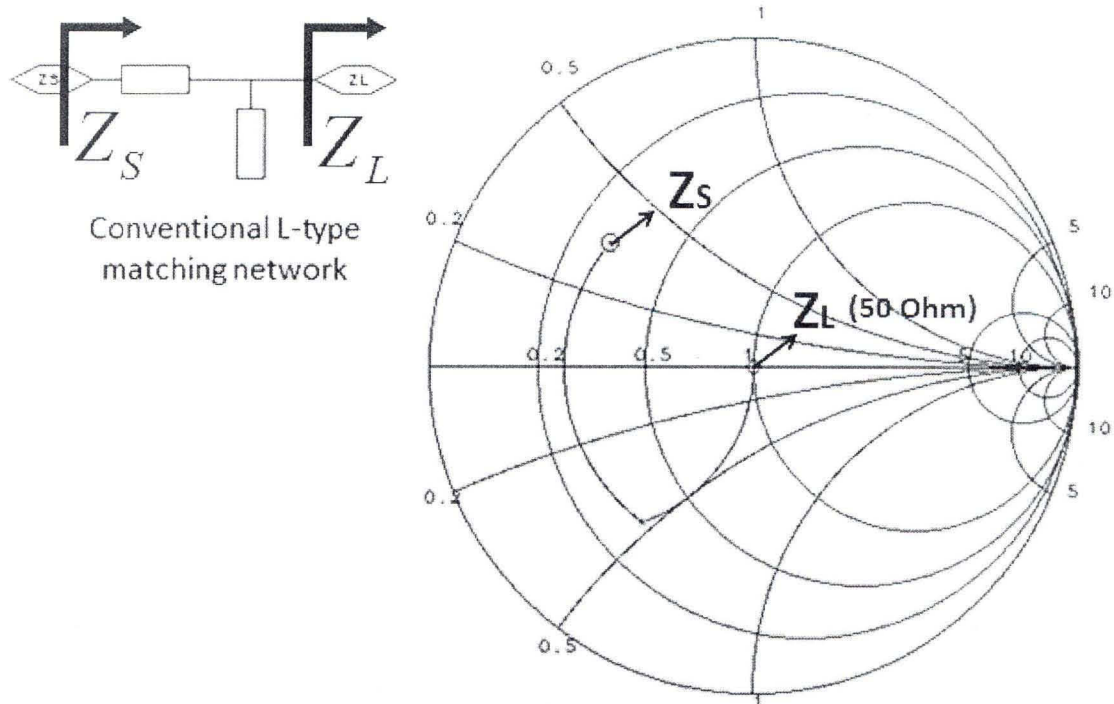


Figure 6: Réseau d'adaptation de type L

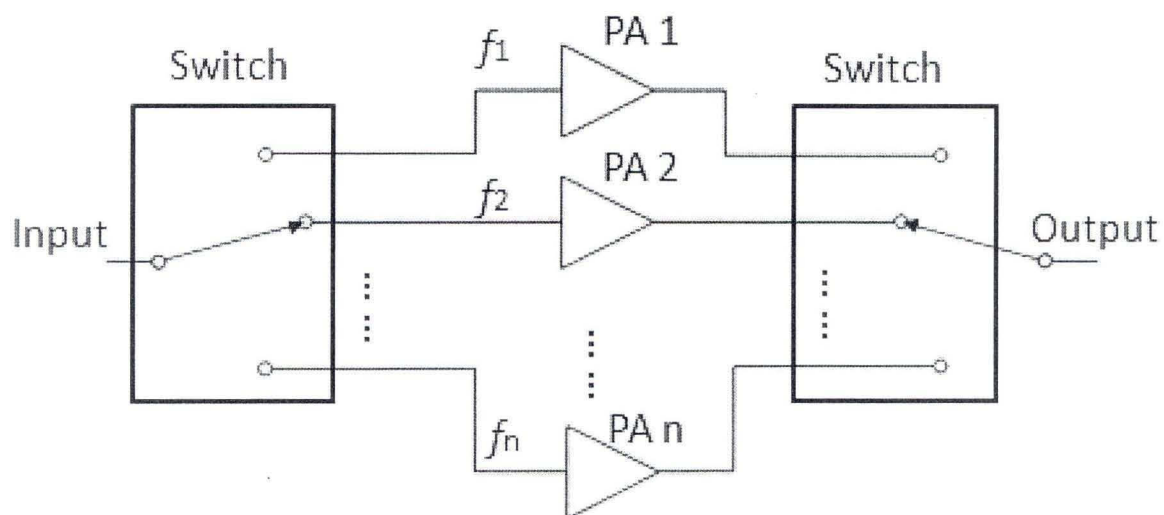


Figure 7: Amplificateur de puissance multibande utilisant des commutateurs

Pour réduire la taille des circuits parallèles d'amplificateurs de puissance et pour économiser le coût des composants, particulièrement pour le composant actif, nous devons concevoir un circuit polyvalent de réseau d'adaptation pour réaliser l'opération multibande simultanée.

(c) Suppression d'harmonique

Comme mentionné précédemment, 4G, WiMAX, LTE et *LTE Advanced* avec large bande passante sont appliqués pour satisfaire à l'exigence de haut débit de données. Les composants et dispositifs avec une performance large bande sont très nécessaires. Pour l'amplificateur de puissance, la technologie de WE (*Waveform Engineering*) est largement utilisée pour la réalisation du haut PAE. Les modes de biharmonique et polyharmonique sont appliqués dans le WE, comme la classe F et classe F inverse où le circuit de suppression d'harmoniques est nécessaire. La bande passante de la deuxième et troisième harmonique est respectivement 2 et 3 fois plus grande que la bande passante de la fréquence fondamentale. Pour la technologie *LTE Advanced* à 2,14 GHz par exemple, la bande passante de la fréquence fondamentale est 100 MHz, la bande passante de la deuxième et troisième harmonique est respectivement 200 MHz et 300 MHz, comme représenté sur la figure 8.

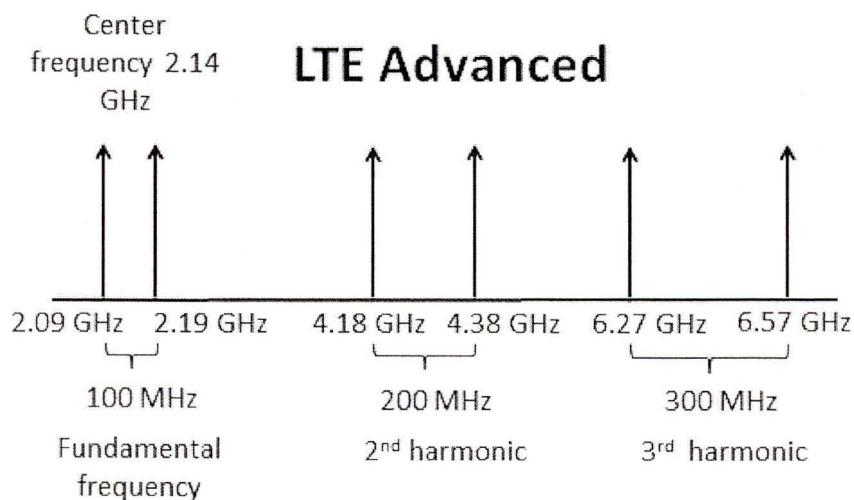


Figure 8: Harmoniques de la technologie *LTE Advanced* à 2.14 GHz

Pour concevoir un amplificateur de puissance de classe F ou de classe F inverse, un tronçon de ligne à quart d'onde est utilisé pour supprimer les harmoniques. Mais il a la caractéristique à bande étroite (Wu *et al.*, 2010), de sorte qu'il est difficile de concevoir un amplificateur de puissance large bande à haut PAE en utilisant la méthode classique. Pour réaliser l'amplificateur de puissance large bande à haut PAE, l'enjeu principal est de concevoir le circuit pour satisfaire l'exigence de suppression d'harmoniques à large bande passante.

III. MÉTHODOLOGIE

Dans le chapitre 1, je vais vous présenter une ligne quarte d'onde multibande nouvelle en forme de Pi en utilisant les résonateurs pour réaliser le diviseur de Wilkinson multibande et la jonction *rat-race* multibande. En employant les résonateurs dans la structure conventionnelle en forme de Pi comme le montré dans la figure 9 (Pozar, 2005: 185; Edwards, 1992: 11), la ligne quarte d'onde multibande peut être réalisée. On peut réduire la taille des dispositifs multibandes proposés en partageant les tronçons circuits ouverts des deux lignes adjacentes à quart d'onde et en orientant tous les tronçons circuits ouverts vers l'intérieur du circuit. Par exemple, l'amélioration de la compacité du diviseur de Wilkinson bibande est montrée dans la figure 10. La compacité est ainsi augmentée.

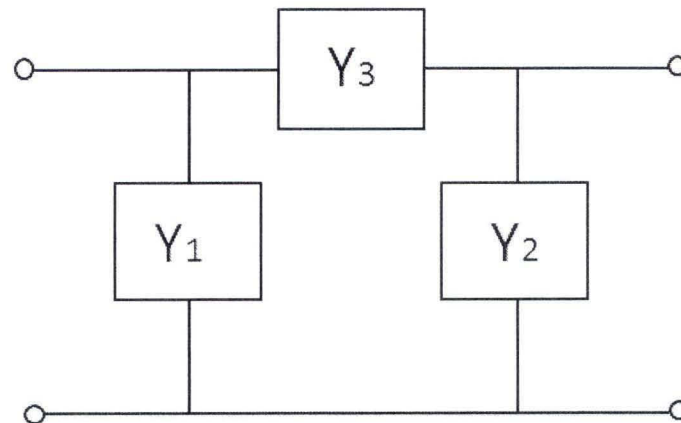


Figure 9: Réseau de deux ports en forme de Pi constitué par deux admittances shunts (Y_1 et Y_2), et une admittance série Y_3

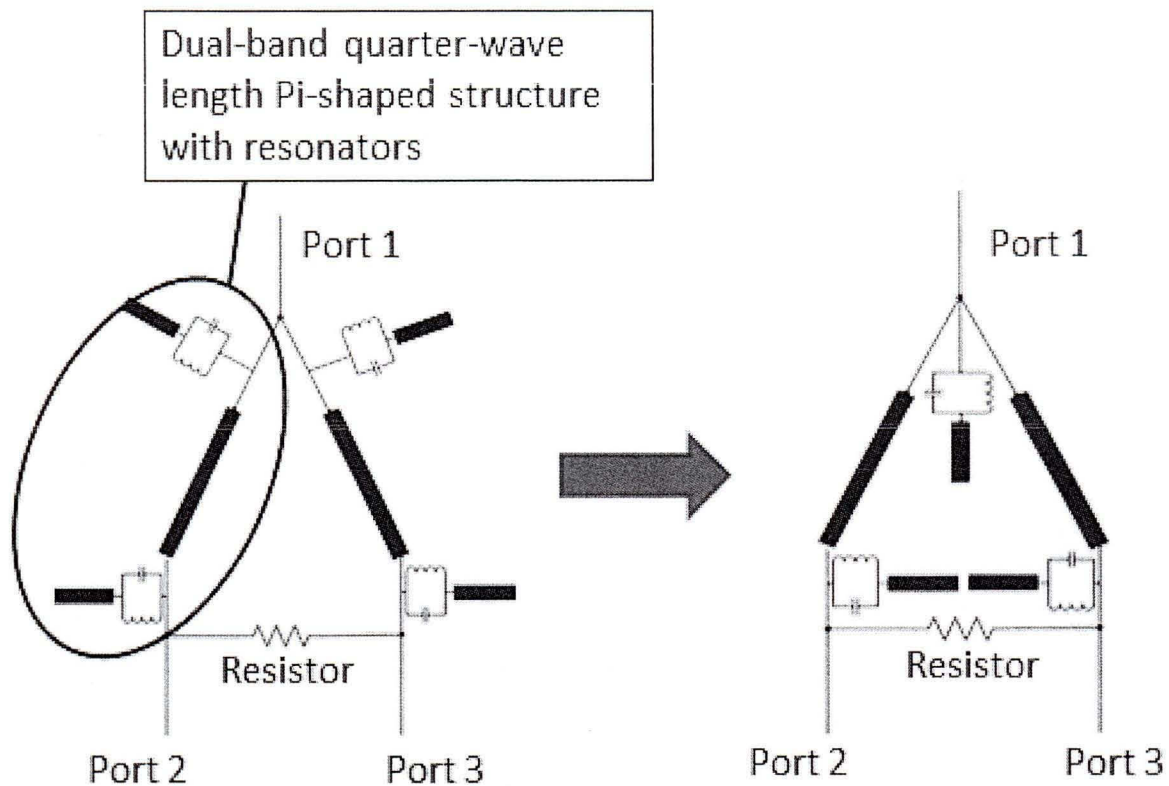


Figure 10: La compacité améliorée du diviseur de Wilkinson bibande

Dans le chapitre 2, une nouvelle méthode utilisant des résonateurs à la fois dans les réseaux d'adaptation (MNs) d'entrée et de sortie est présentée pour la conception d'amplificateur de puissance multibande. Pour l'amplificateur de puissance bibande, à la fois dans les réseaux d'adaptation d'entrée et de sortie, nous ajoutons des résonateurs bobine-condensateur (LC) parallèles entre les lignes microruban séries et les stubs circuit ouvert pour réaliser l'opération bibande. La topologie de l'amplificateur de puissance bibande proposée est montrée dans la figure 11 (a). Avec la structure bibande proposée, on peut utiliser la structure conventionnelle de type L pour concevoir le réseau d'adaptation pour chaque fréquence de fonctionnement. La procédure de conception est donc simplifiée. En outre, en utilisant un seul transistor sans aucun élément électronique ajustable et sans commutateur, l'opération multibande simultanée est réalisée, la dimension et le coût, particulièrement le coût du composant actif, sont économisés.

Pour l'amplificateur de puissance tribande, deux résonateurs en série comme un élément de sélection de fréquences sont utilisés pour chaque fréquence de fonctionnement. En appliquant cet élément de sélection de fréquences à la fois dans les réseaux d'adaptation d'entrée et de sortie avec la ligne microruban, le réseau d'adaptation tribande est réalisé. La topologie du réseau d'adaptation tribande proposée est montrée dans la figure 11 (b). Avec l'élément de sélection de fréquence proposé, nous pouvons utiliser la structure conventionnelle de type L pour concevoir le réseau d'adaptation tribande. Dans le processus de conception de l'amplificateur de puissance tribande, nous avons également proposé un nouveau réseau d'adaptation de sortie simplifié en utilisant le circuit de polarisation pour adapter l'impédance de la fréquence de fonctionnement la plus basse afin de réduire le nombre de groupes de résonateurs.

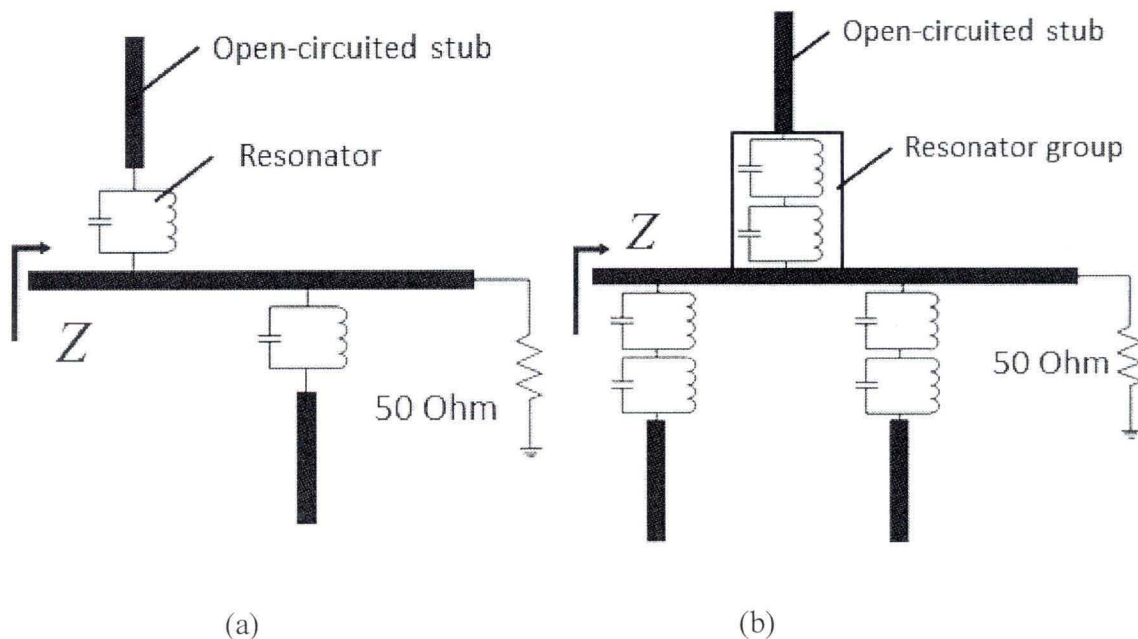


Figure 11: Topologies des réseaux d'adaptation multibandes, (a): réseau d'adaptation bibande, (b): réseau d'adaptation tribande

Dans le chapitre 3, je vais vous présenter un nouvel amplificateur de puissance de technologie GaN HEMT à large bande en utilisant les MRSs (microstrip radial stub) à la fois dans les réseaux d'adaptation d'entrée et de sortie pour supprimer les harmoniques pour l'application de *LTE Advanced*. La topologie du MRS est montrée dans la figure 12. L'impact de suppression d'harmonique de l'angle du MRS (θ) et la longueur en bas du MRS (w) seront analysés dans le chapitre 3. La caractéristique large bande de suppression des harmoniques du MRS sera comparée au stub normal à quart d'onde de 50 Ohm aussi. En utilisant le MRS dans les réseaux d'adaptation d'entrée et de sortie, l'amplificateur de puissance à large bande à haute PAE est obtenu.

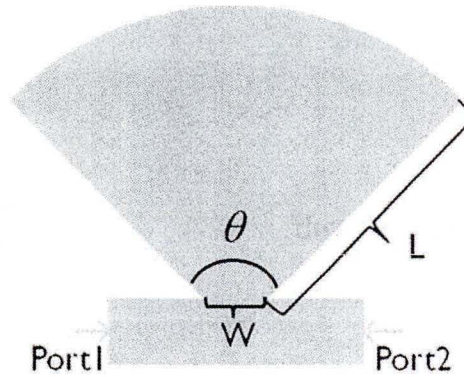


Figure 12: Topologie de la composante proposée de suppression d'harmonique à large bande, MRS (microstrip radial stub)

IV. CONTRIBUTIONS

Dans ce mémoire, pour satisfaire aux exigences multibandes dans les systèmes de communication d'aujourd'hui, un diviseur de Wilkinson bibande, un diviseur de Wilkinson tribande, et une jonction *rat-race* tribande ont été conçus, fabriqués et testés dans le chapitre 1. Dans le chapitre 2, deux amplificateurs de puissance bibandes et un amplificateur de puissance tribande sont présentés. Enfin, dans le chapitre 3, un

amplificateur de puissance large bande à haute PAE est analysé et fabriqué pour répondre à l'exigence de large bande passante des systèmes de 4G.

Les contributions du mémoire sont résumées comme suit:

1: Les performances multibandes simultanées du diviseur de Wilkinson, de la jonction *rat-race*, et de l'amplificateur de puissance sont réalisées. En comparant avec les circuits multibandes utilisant des commutateurs ou composants électroniques ajustables, nous n'avons pas besoin de basculer les commutateurs entre les différents circuits ou d'ajuster les composants électroniques ajustables lors du changement de la fréquence. Les circuits bibandes ou tribandes proposés peuvent simultanément travailler à deux ou trois fréquences distinctes.

2 : Les méthodes au sujet de maintenir la compacité des circuits multibandes proposés sont présentées. La taille des dispositifs passifs multibandes proposés, comme le diviseur de Wilkinson bibande, le diviseur de Wilkinson tribande, et la jonction *rat-race* tribande, est réduite en partageant le stub circuit ouvert avec les résonateurs des deux structures multibandes adjacentes en forme de Pi et mettant tous les stubs circuit ouvert avec les résonateurs à l'intérieur des composants multibandes proposés eux-mêmes. En comparant avec la structure multibande utilisant des commutateurs dans les amplificateurs de puissance parallèles, la taille de l'amplificateur de puissance multibande proposée est réduite en utilisant un seul transistor et un seul réseau d'adaptation multibande d'entrée et de sortie.

3: Le coût des circuits multibandes est économisé, particulièrement le coût des transistors. Comme mentionnés précédemment, nous utilisons simplement un transistor avec un seul réseau d'adaptation multibande d'entrée et de sortie pour réaliser les amplificateurs de puissance multibandes proposés. En outre, en utilisant le circuit de polarisation comme le réseau d'adaptation pour la fréquence de fonctionnement la plus basse dans l'amplificateur de puissance tribande proposé, deux groupes de résonateurs sont économisés.

4: Les procédures de conception des circuits multibandes proposées sont simplifiées. Pour le diviseur de Wilkinson bibande, le diviseur de Wilkinson tribande, et la jonction *rat-race* tribande, une matrice ABCD est appliquée pour simplifier la conception. Pour les amplificateurs de puissance multibandes, le réseau d'adaptation plus simple de type L est appliqué dans la conception du réseau d'adaptation multibande.

5: La méthode de conception multibande proposée peut être appliquée dans d'autres applications multibandes et d'autres circuits multibandes plus complexes, comme l'amplificateur équilibré multibande et l'amplificateur de puissance Doherty multibande.

6: Pour satisfaire à l'exigence large bande passante dans les systèmes de 4G, nous présentons la méthode pour concevoir le circuit large bande de suppression des harmoniques en utilisant MRS à la fois dans des réseaux d'adaptation d'entrée et de sortie. Un amplificateur puissance à large bande à haut PAE est réalisé.

Dans ma période de maîtrise, j'ai participé à la compétition de "2012 IEEE MTT-S International Microwave Symposium Student High Efficiency Power Amplifier Design Competition" tenu par 2012 IEEE MTT-S International Microwave Symposium à Montréal et j'ai obtenu la deuxième place:

- [1] **Zhebin Wang** and Chan-Wang Park, "2012 IEEE MTT-S International Microwave Symposium Student High Efficiency Power Amplifier Design Competition," **win the second place**, IEEE MTT-S International Microwave Symposium, Montreal, Quebec, Canada, 17-22 June 2012.

J'ai publié plusieurs articles sur les méthodes de conception multibande et large bande du diviseur de Wilkinson, de la jonction *rat-race*, et de l'amplificateur de puissance sur micro-ondes de 2010 à 2012. Toutes mes publications dans les conférences scientifiques sont énumérées ci-dessous:

- [1] **Zhebin Wang** and Chan-Wang Park, "Multiband Pi-shaped Structure with Resonators for Tri-band Wilkinson Power Divider and Tri-band Rat-Race Coupler," IEEE MTT-S International Microwave Symposium Digest, pp. 1-3, Montréal, Canada, 17-22 June 2012.
- [2] **Zhebin Wang** and Chan-Wang Park, "Novel Wideband GaN HEMT Power Amplifier Using Microstrip Radial Stub to Suppress Harmonics," IEEE MTT-S International Microwave Symposium Digest, pp. 1-3, Montréal, Canada, 17-22 June 2012.
- [3] **Zhebin Wang**, Sulav Adhikari, David Dousset, Chan-Wang Park, and Ke Wu, "Substrate Integrated Waveguide (SIW) Power Amplifier Using CBCPW-to-SIW Transition for Matching Network," IEEE MTT-S International Microwave Symposium Digest, pp. 1-3, Montréal, Canada, 17-22 June 2012.
- [4] **Zhebin Wang** and Chan-Wang Park, "Novel Substrate Integrated Waveguide (SIW)-Based Power Amplifier Using SIW-Based Filter to Suppress Up to the Fourth Harmonic," 2012 Asia-Pacific Microwave Conference (APMC), pp. 1-3, Kaohsiung, Taiwan, 4-7 December 2012.
- [5] **Zhebin Wang** and Chan-Wang Park, "Concurrent Tri-Band GaN HEMT Power Amplifier Using Resonators in Both Input and Output Matching Networks," The 13th Annual IEEE Wireless and Microwave Technology (WAMI) Conference, pp. 1-4, Cocoa Beach, FL., U.S.A., 15-17 April 2012.
- [6] **Zhebin Wang** and Chan-Wang Park, "Dual-band GaN HEMT Power Amplifier Using Resonators in Matching Networks," The 12th Annual IEEE Wireless and Microwave Technology (WAMI) Conference, pp. 1-4, Clearwater, FL., U.S.A., 18-19 April 2011.
- [7] **Zhebin Wang**, Jae Sik Jang, and Chan-Wang Park, "Compact Dual-Band Wilkinson Power Divider Using Lumped Component Resonators and Open-Circuited Stubs," The 12th Annual IEEE Wireless and Microwave Technology (WAMI) Conference,

pp. 1-4, Clearwater, FL., U.S.A., 18-19 April 2011.

- [8] **Zhebin Wang**, Jae-Sik Jang, and Chan-Wang Park, "Tri-band Wilkinson Power Divider Using Resonators," 2011 IEEE Radio and Wireless Symposium, pp. 287-290, Phoenix, AZ., U.S.A., 16-19 January 2011.
- [9] **Zhebin Wang**, Shengjie Gao, and Chan-Wang Park, "A Simple Method for Tunable Load Impedance Matching Network of Power Amplifier," 2010 IEEE International Conference on Microwave and Millimeter Wave Technology, pp. 484-487, Chengdu, China, 8-11 May 2010.

CHAPITRE 1

STRUCTURE MULTIBANDE EN FORME DE PI UTILISANT DES RÉSONATEURS POUR LE DIVISEUR DE WILKINSON MULTIBANDE ET LA JONCTION *RAT-RACE* MULTIBANDE

1.1 RÉSUMÉ

Ce chapitre présente une nouvelle structure multibande en forme de Pi avec une longueur électrique quarte d'onde utilisant des résonateurs. En employant les résonateurs dans la structure conventionnelle en forme de Pi comme indiqué dans la figure 13 (Pozar, 2005: 185; Edwards, 1992: 11), la ligne de transmission multibande avec une longueur électrique quart d'onde est obtenue. Afin de démontrer la structure multibande proposée en forme de Pi, nous avons conçu et fabriqué un diviseur de Wilkinson bibande, un diviseur de Wilkinson tribande, et une jonction *rat-race* tribande. Nous pouvons réduire la taille des dispositifs multibandes proposés en partageant les deux stubs circuits ouverts avec résonateurs des deux structures multibandes adjacents en forme de Pi et mettant tous les stubs circuits ouverts à l'intérieur des dispositifs multibandes eux-mêmes. La compacité des dispositifs multibandes proposés est bien maintenue. Les résultats mesurés montrent d'excellentes performances des dispositifs multibandes et sont en bon accord avec les résultats simulés.

1.2 MULTIBAND PI-SHAPED STRUCTURE WITH RESONATORS FOR MULTIBAND WILKINSON POWER DIVIDER AND MULTIBAND RAT-RACE COUPLER

1.2.1 Abstract

This chapter presents a novel multiband quarter wavelength Pi-shaped structure with resonators. By employing resonators in conventional Pi-shaped structure as shown in Fig. 13 (Pozar, 2005: 185; Edwards, 1992: 11), multiband quarter wavelength transmission line is achieved. In order to demonstrate our proposed multiband quarter wavelength Pi-shaped structure, we designed and fabricated a dual-band Wilkinson power divider, a tri-band Wilkinson power divider, and a tri-band rat-race coupler. We can reduce the size of the proposed multiband components by sharing the open-circuited stub with resonators of two adjacent multiband Pi-shaped structures and making all open-circuited stubs with resonators inside the demonstrated multiband components themselves. Compactness of the proposed multiband components is kept well. Measured results show excellent performances of the demonstrated multiband components and are in good agreement with simulated results.

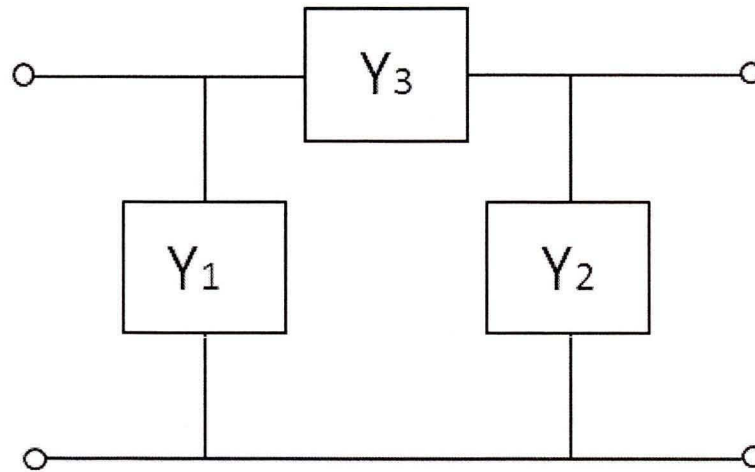


Figure 13: Conventional Pi-shaped two-port network consisting of two shunt admittances (Y_1 and Y_2), and one series admittance Y_3

1.2.2 Introduction

Interoperability and co-existence between multi-standards is the main issue in modern communication systems, such as wireless local area networks (WLANs) at 2.4 GHz and 5.2 GHz (Wu *et al.*, 2009 a; Chiou *et al.*, 2009) and the global systems for mobile communication systems (GSM) at 0.9 GHz and 1.8GHz (Wu *et al.*, 2009 a; Chiou *et al.*, 2009; Chou *et al.*, 2010). To satisfy this harsh requirement, multiband radio systems are required and used for different frequencies associated with different standards.

New types of multiband components such as power divider, rat-race coupler, and power amplifier (PA) are investigated and developed to meet the trend of multiband radio system. In past years, many researches for multiband applications have been presented. For multiband Wilkinson power divider, coupled line (Park, 2009 a; Park, 2009 b) has been applied effectively in dual-band Wilkinson power divider; T-type transmission line with short-circuited stub (Lee *et al.*, 2008) and that with open-circuited stub (Park *et al.*, 2008) are introduced for dual-band Wilkinson power divider, T-type transmission line with open-circuited stub is also applied in a unequal dual-band Wilkinson power divider design (Wu *et al.*, 2009 b); two-section (Srisathit *et al.*, 2003; Cheng *et al.*, 2007) and three-section (Chongcheawchamnan *et al.*, 2006) transmission-line transformer have been developed and employed for dual-band and tri-band Wilkinson power divider, respectively; A varactor tuned dual-band Wilkinson power divider is achieved by adding varactor diodes as tunable elements (Draskovic *et al.*, 2009). For multiband rat-race coupler, composite right/left-handed transmission line (CRLH TL) is advanced and applied in dual-band rat-race coupler (Lin *et al.*, 2004; Chi *et al.*, 2008), the CRLH behavior of half-mode substrate integrated waveguide (HMSIW) is obtained and employed in dual-band rat-race design (Dong *et al.*, 2010); Stepped-impedance microstrip line is analyzed and used for dual-band rat-race coupler (Hsu *et al.*, 2007; Chin *et al.*, 2010); The C-section together with two transmission line sections is proposed and synthesized for dual-band operation of rat-race coupler (Chiou *et al.*, 2009; Wu *et al.*, 2009 a). Size reduction is also an important issue for distributed circuits operating at relatively low frequencies (Hsu *et al.*, 2007), in previous works,

compactness is considered in design procedure (Alkanhal, 2008; Chou *et al.*, 2010; Hsu *et al.*, 2007; Chi *et al.*, 2008; Siso *et al.*, 2009).

Our objective is to design multiband components such as multiband Wilkinson power divider and multiband rat-race coupler by using the proposed multiband quarter wavelength Pi-shaped structure with resonators and to reduce the size of the proposed multiband components, make circuit's structure compact for dual or tri-band applications.

1.2.3 Conventional Wilkinson power divider and rat-race coupler

a) Conventional Wilkinson power divider

The Wilkinson power divider is one of the most commonly used components in wireless communication system for power division and/or combination (Mohra, 2008). In the design of microwave and millimeter-wave circuits, such as the feeding network for an antenna array (Cheng *et al.*, 2007), vector modulator (Lee *et al.*, 2008), balanced mixers, and push-pull amplifiers (Mohra, 2008), Wilkinson power divider plays an important role.

In 1960, Wilkinson described an N-way hybrid power combiner which can be realized with transmission lines such as coaxial, microstrip and strip lines (Wilkinson, 1960; Alkanhal, 2008). When the termination is 50 Ohm, conventional Wilkinson power divider is simply consisting with two quarter wavelength transmission lines with fixed characteristic impedance 70.7 Ohm for each branch, a lumped 100 Ohm resistor is connected between two output ports for a better isolation as shown in Fig. 14 (Wilkinson, 1960; Pozar, 2005: 318; Gonzalez, 1997: 332; Bahl, 2003: 372).

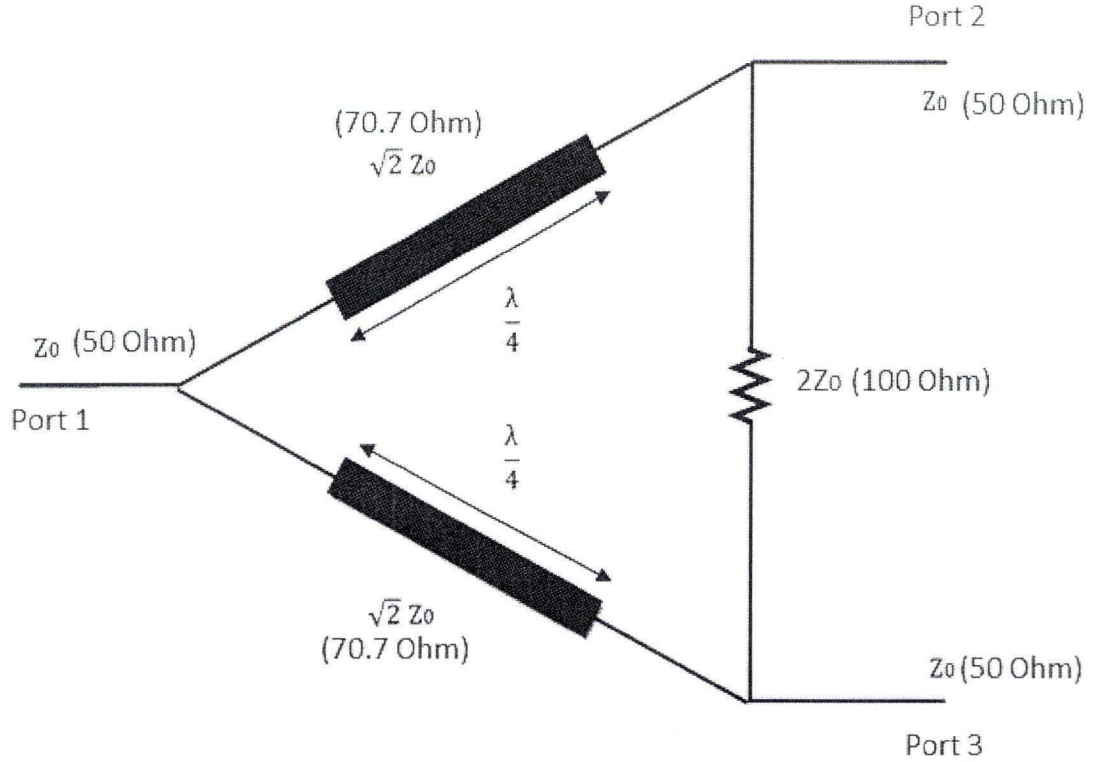


Figure 14: Conventional Wilkinson power divider

Conventional Wilkinson power divider can divide RF, microwave, and millimeter-wave power equally from input port (*Port 1*) to output ports (*Port 2* and *Port 3*) with low insertion loss and high isolation between two output ports. The ideal phase difference between two output ports (*Port 2* and *Port 3*) is 0° .

b) Conventional rat-race coupler

Rat-race coupler is one of the most popular passive circuits for microwave and millimeter-wave applications (Kong *et al.*, 2006). It is widely used for dividing an input signal into two signals having 0° and 180° phase difference (Lin *et al.*, 2004). For example, in class-D switching-mode PAs, rat-race coupler is able to equally split and combine RF signals with 180° phase shift (Aflaki *et al.*, 2010); in the front-end of a multiple-input multiple-output (MIMO) system, when be used as a transmitter, the rat-race serves to excite

two orthogonal radiation modes and when be used as a receiver, the rat-race acts as a mode decoupling network (Chi *et al.*, 2008).

The conventional rat-race coupler has 4 ports with the circumference of $3\lambda/2$ wavelength as shown in Fig. 15. It contains six identical parts, each of the identical parts is quarter wavelength transmission line with impedance of $\sqrt{2} Z_0$, λ and Z_0 representing the wave length and the characteristic impedance, respectively. Each port is known has the impedance of Z_0 . If $Z_0 = 50$ Ohm, the characteristic impedance of each quarter wavelength transmission line is 70.7 Ohm (Pozar, 2005: 352; Bahl, 2003: 362).

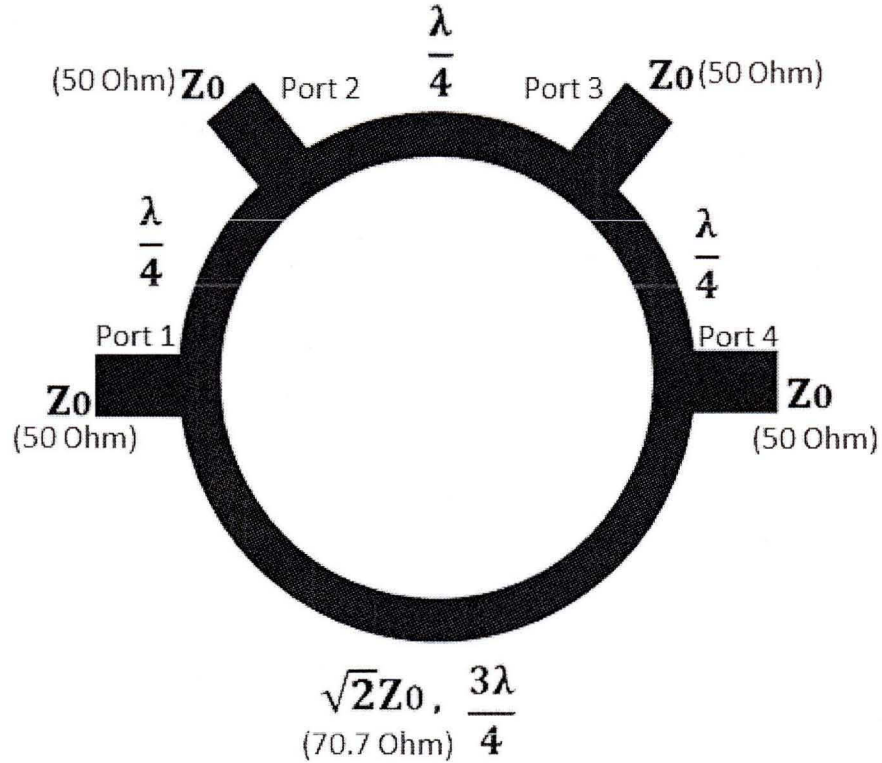


Figure 15: Conventional rat-race coupler

If we connect the 50 Ohm load at *Port 1* as the isolation port, make *Port 3* as the power input port, *Port 2* and *Port 4* as the power output ports, we call *Port 2* and *Port 4* as in phase output ports. Ideally, the insertion loss of *Port 2* and *Port 4* is around 3 dB. Phase difference between in phase output ports is around 0°. Be different, if we choose *Port 3* as the isolation port, *Port 1* as the input port, we call *Port 2* and *Port 4* as out of phase output ports. Phase difference between out of phase output ports is around 180°. Insertion loss of both out of phase output ports is around 3 dB.

1.2.4 Problem, objective, and methodology

For conventional Wilkinson power divider and rat-race coupler, their structures are limited in operation around a single frequency band due to quarter wavelength transmission line (Lin *et al.*, 2004; Park, 2009 b; Chin *et al.*, 2010; Kong *et al.*, 2006). Conventional Wilkinson power divider contains two quarter wavelength transmission lines and conventional rat-race coupler consists of six quarter wavelength transmission lines. Equation (1.1) (Gonzalez, 1997: 10), equation (1.2) (Pozar, 2005: 15), and equation (1.3) (Pozar, 2005: 16) show us, when frequency changes, the value of wavelength will change correspondingly. Therefore, with a single line structure, the conventional quarter wavelength transmission line is impossible to operate with quarter wavelength performance at multiple frequency bands which have obviously wave length difference.

$$\omega = 2\pi f \quad (1.1)$$

$$v_p = \frac{\omega}{k} = \frac{1}{\sqrt{\mu\epsilon}} \quad (1.2)$$

$$\lambda = \frac{2\pi}{k} = \frac{2\pi v_p}{\omega} = \frac{v_p}{f} \quad (1.3)$$

where f is the frequency, v_p is the phase velocity, λ is the wavelength, k is propagation constant of the medium (Pozar, 2005: 15), ϵ is the complex permittivity of the medium (Pozar, 2005: 10), μ is the permeability of the medium (Pozar, 2005: 11), and π is circumference ratio.

My objective is to realize multiband performance of Wilkinson power divider and rat-race coupler for multiband requirements. To do that, I employed one specific multiband component which is multiband quarter wavelength Pi-shaped circuit with resonators that can control the performance of signal at different frequency bands. By employing this kind of signal controlling element in Wilkinson power divider and rat-race coupler, multiband performances are achieved. Furthermore, by optimizing the proposed components, the whole size of them will be kept compact.

1.2.5 Analysis and design of new multiband Pi-shaped structure with resonators

In this section, the principles and novel structures of the proposed multiband Pi-shaped quarter wavelength transmission lines are presented. Models of capacitor and inductor, and resonators are analyzed to be used in the new concept of the proposed multiband quarter wavelength Pi-shaped structures. ABCD matrix is also employed to simplify the calculation for the new proposed multiband Pi-shaped structures.

a) Models of capacitor and inductor

All of the simulations in this chapter are executed in software ADS (Advanced Design System) from Agilent Technologies. In ADS, the ideal models of capacitor and inductor are provided as shown in Fig. 16.

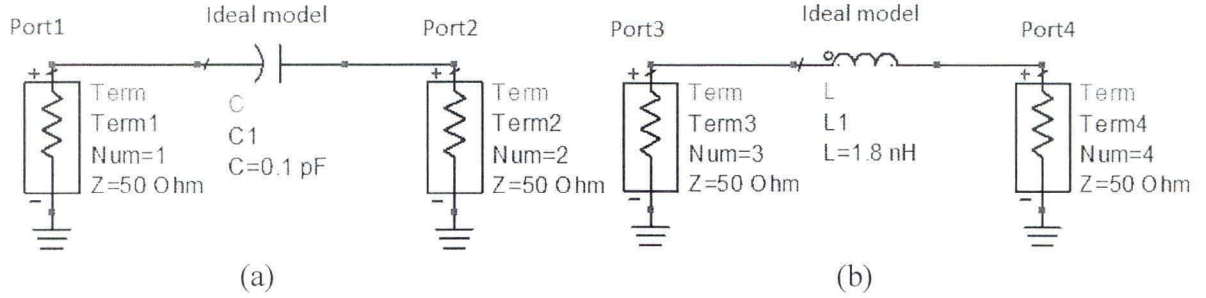


Figure 16: Ideal models in ADS, (a): capacitor model, (b): inductor model

The relationship between impedance and admittance is expressed by equation (1.4) (Besser *et al.*, 2003: 22). To calculate the impedance of capacitor, we use equation (1.5) (Bahl, 2003: 166). Equation (1.6) transformed from equation (1.5) is used in ADS simulation to calculate capacitance value of capacitor model.

$$Z = \frac{1}{Y} \quad (1.4)$$

where Z is impedance and Y is admittance.

$$Z_C = -\frac{j}{\omega C_e} \Rightarrow Y_C = j\omega C_e \quad (1.5)$$

where Z_C is the impedance of capacitor, C_e is the effective capacitance.

In ADS simulation, we can express C_e using equation (1.6):

$$C_e = \frac{\text{imag}(Y(1,1))}{2 * \pi * \text{freq}} \quad (1.6)$$

where C_e is the effective capacitance, $Y(l, l)$ is the admittance of *Port 1* in ADS shown in Fig. 16, $\text{imag}(Y(l, l))$ is the imaginary part of $Y(l, l)$, PI is circumference ratio, and freq is frequency.

The same, to calculate the impedance of inductor, we use equation (1.7) (Bahl, 2003: 21). Equation (1.8) transformed from equation (1.7) is used in ADS simulation to calculate inductance value of inductor model.

$$Z_i = j\omega L_e \Rightarrow \frac{1}{Y_i} = j\omega L_e \quad (1.7)$$

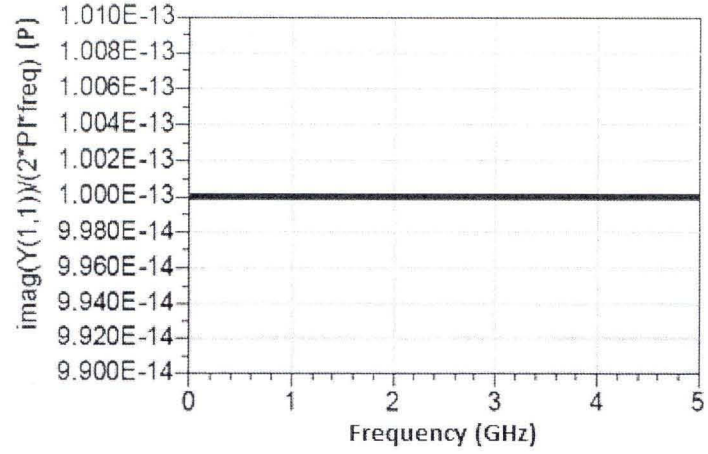
where Z_i is the impedance of inductor, L_e is the effective inductance.

In ADS simulation, we can express L_e using equation (1.8):

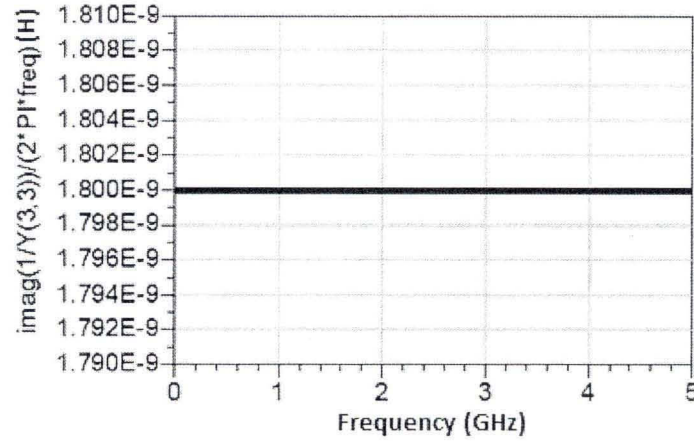
$$L_e = \frac{\text{imag}(1/Y(3,3))}{2 * PI * \text{freq}} \quad (1.8)$$

where L_e is the effective inductance, $Y(3,3)$ is the admittance of *Port 3* in ADS shown in Fig. 16, $\text{imag}(1/Y(3,3))$ is the imaginary part of $(1/Y(3,3))$.

The simulated results using equation (1.6) and equation (1.8) for the ideal 0.1 pF capacitor model and the ideal 1.8 nH inductor model from 0 GHz to 5 GHz are shown in Fig. 17.



(a)



(b)

Figure 17: Simulated results of the ideal models, (a): ideal 0.1 pF capacitor model, (b): ideal 1.8 nH inductor model

By our research, ideal capacitor or inductor model just explains the most ideal case. Big difference exists between ideal model and real lumped component. We can't consider ideal model as the same as real component. In ADS simulation, for real circuit design, we employed measured models provided by Modelithics whose performances are considered more approaching to real components. For different types of capacitor or inductor, there are corresponding different models in Modelithics. In Modelithics models, we can choose manufacture, size, and component value to simulate. The capacitor and inductor models of

Modelithics are shown in Fig. 18. To demonstrate the model of Modelithics, the chosen capacitor model of Modelithics is modeled for ATC (American Technical Ceramics) 600S 0.1 pF capacitor and the chosen inductor model of Modelithics is modeled for Coilcraft 0603HP 1.8 nH inductor.

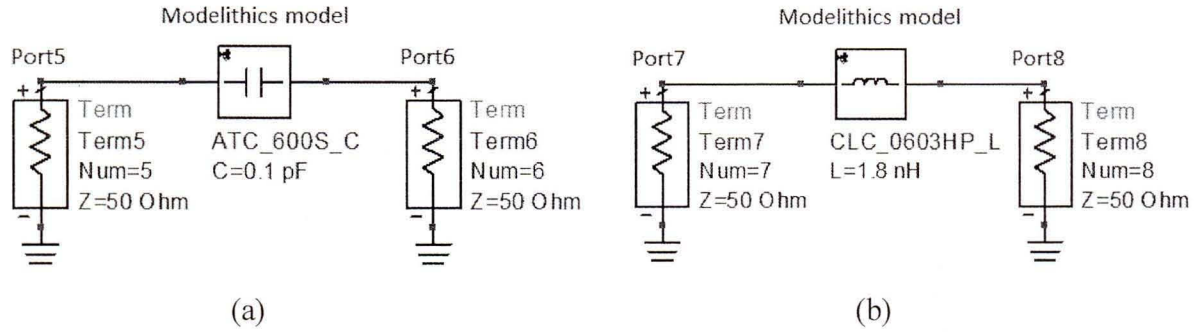
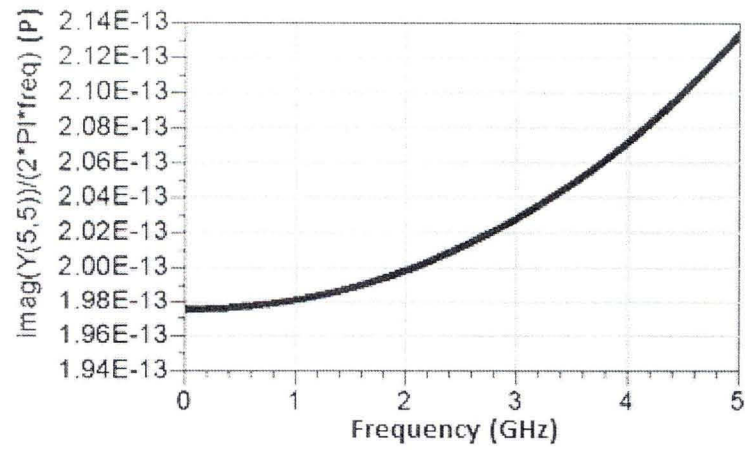
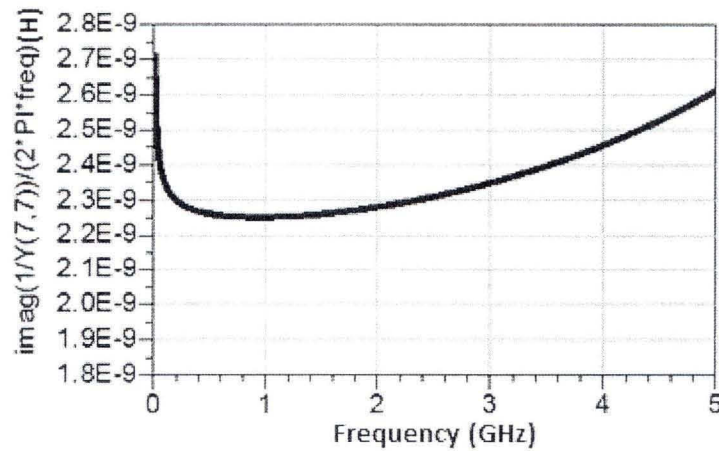


Figure 18: Models of Modelithics, (a): capacitor model, (b): inductor model

The simulated results of these two chosen component models from Modelithics are shown in Fig. 19 from 0 GHz to 5 GHz. Not like ideal capacitor and inductor models shown in Fig. 16, the values of capacitance and inductance of the models of capacitor and inductor from Modelithics are changed with the change of frequency.



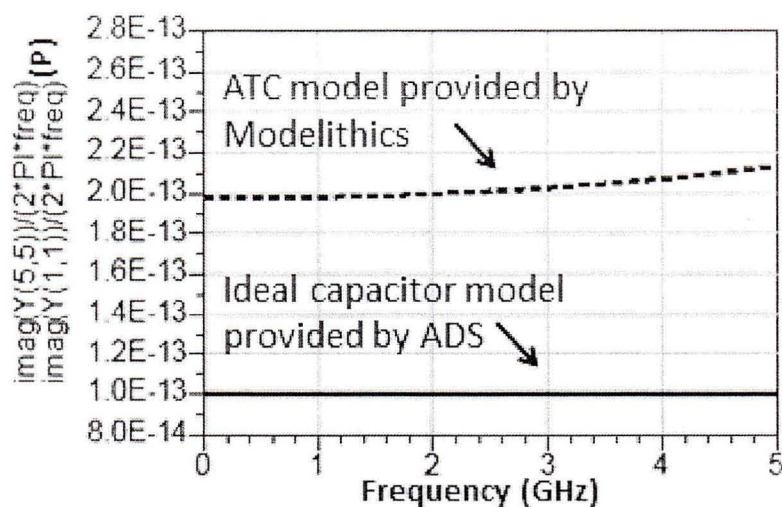
(a)



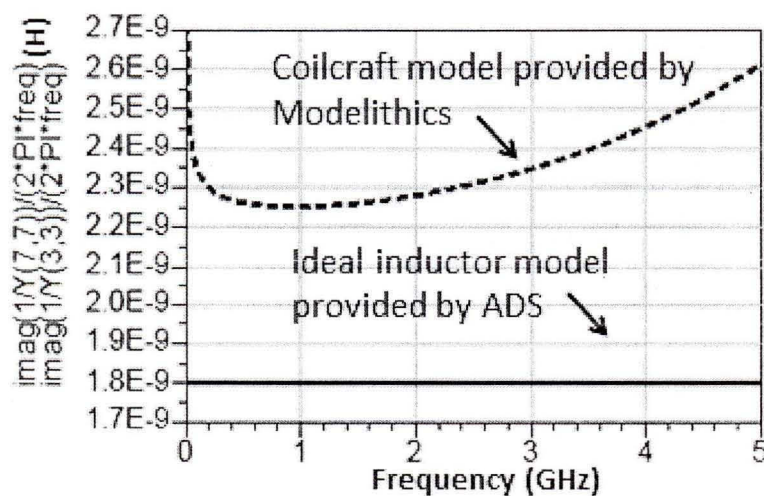
(b)

Figure 19: Simulated results of Modelithics models, (a): ATC 600S 0.1 pF capacitor model, (b): Coilcraft 0603HP 1.8 nH inductor model

The comparison results between ideal model and Modelithics model are shown in Fig. 20. From these comparison results, we notice that, with the change of frequency, the capacitance of measured capacitor model and the inductance of measured inductor model will change. According to the simulated results of the measured models from Modelithics, there is deviation from the marked ideal values on the measured model itself.



(a)



(b)

Figure 20: Comparison between ideal models (solid line) and measured models from Modelithics (dot line), (a): capacitor models, (b): inductor models

For chip capacitors, it has an associated parasitic series inductance. Chip capacitors are available with tolerance of $\pm 5\%$, $\pm 10\%$, and $\pm 20\%$ (Bahl, 2003:166). For chip inductors, it has associated parasitic capacitance (due to interturn and ground plane effects) in parallel with its inductance (Bahl, 2003:20).

For evaluation purpose, we choose two models of capacitor made by Modelithics for two different manufacturers, such as ATC and MURATA. As shown in Fig. 21, with the same capacitance 10 pF, the models act differently as Fig. 22 shows us. We notice that, at 1.2 GHz, the value of ideal 10 pF model provided by ADS maintains 10 pF no matter how the frequency changes. However, the capacitances of the model of ATC and MURATA made by Modelithics are quite different versus frequency.

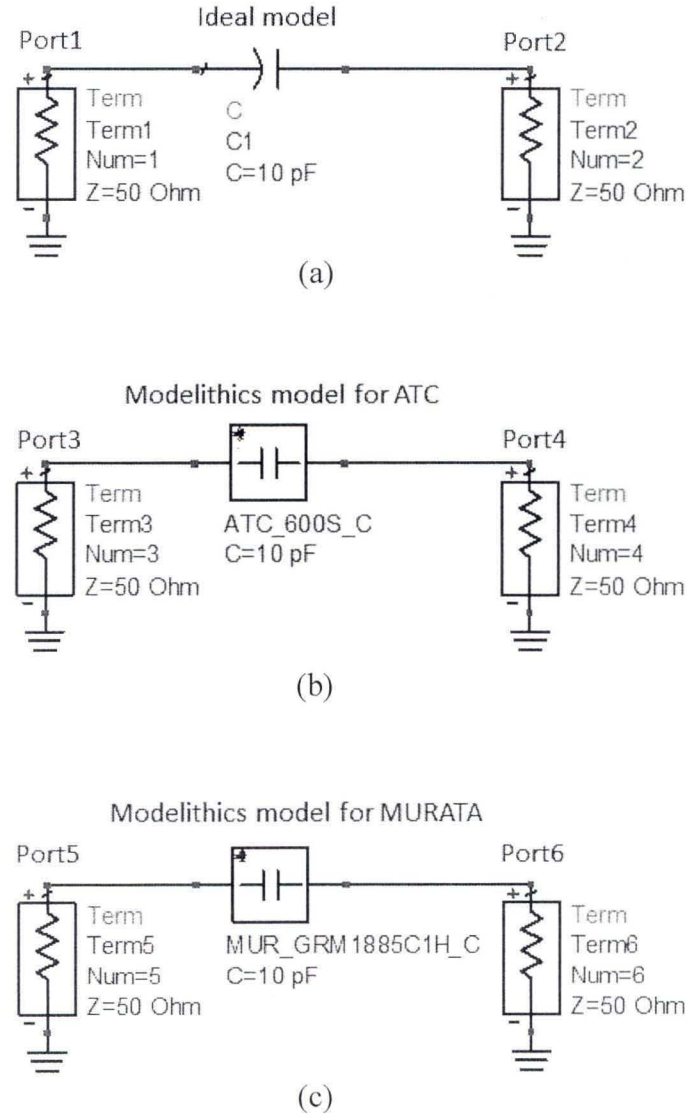


Figure 21: Simulated models, (a): Ideal model provided by ADS, (b): ATC model provided by Modelithics, (c): MURATA model provided by Modelithics

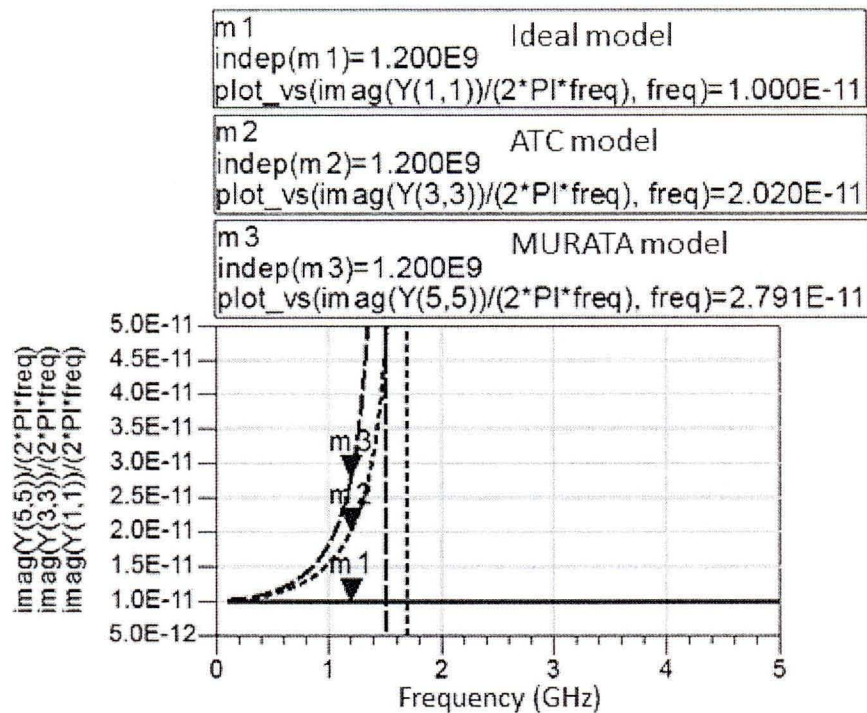


Figure 22: Simulated results of capacitor models, solid line: ideal model provided by ADS, dot line: ATC model provided by Modelithics, and dash line: MURATA model provided by Modelithics

Because the models provided by Modelithics are based on measured results of the real components fabricated by different manufacturers, and the ideal model provided by ADS just gives an ideal capacitance value or inductance value while not including parasitic inductance in capacitor or parasitic capacitance in inductor, throughout all of my simulations, I used Modelithics models to avoid the deviation between simulation and measurement.

b) Resonator

A resonant circuit or LC circuit consists of one capacitor and one inductor. We employed parallel LC circuit in all of my dual-band or tri-band designs. At resonant frequency, the impedance of parallel resonant circuit becomes higher and signal generated at this frequency is blocked by resonant effect. The resonant frequency can be easily calculated with equation (1.9) (Pozar, 2005: 272).

$$f_R = \frac{1}{2\pi\sqrt{LC}} \quad (1.9)$$

where f_R is resonant frequency, C is capacitance of capacitor, and L is inductance of inductor.

The structure of the parallel resonant circuit consists of one capacitor C and one inductor L is shown in Fig. 23 below. *Port 1* is the input port and *Port 2* is the output port. At the resonant frequency f_R , signal is blocked by resonant effect with the chosen capacitor C and inductor L . Instead of using chip inductor in parallel resonant circuit, we can also use microstrip line type inductor to provide inductance.

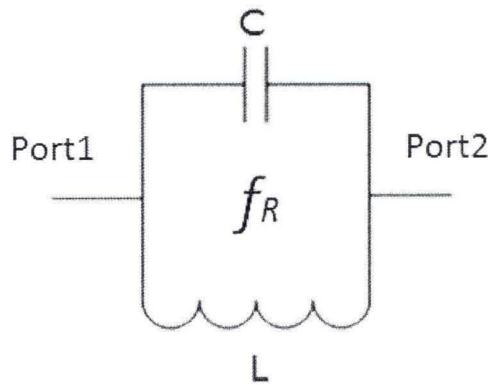


Figure 23: Parallel resonant circuit structure

b.1) Parallel resonator constructed by capacitor and inductor

As an example, for ideal case, if we want to design a resonator with resonant frequency 1.5 GHz and choose the capacitance of capacitor as 1 pF, the inductance of the idea inductor calculated by equation (1.9) is 11.25 nH. The constructed structure of the ideal parallel resonator circuit for 1.5 GHz is shown in Fig. 24.

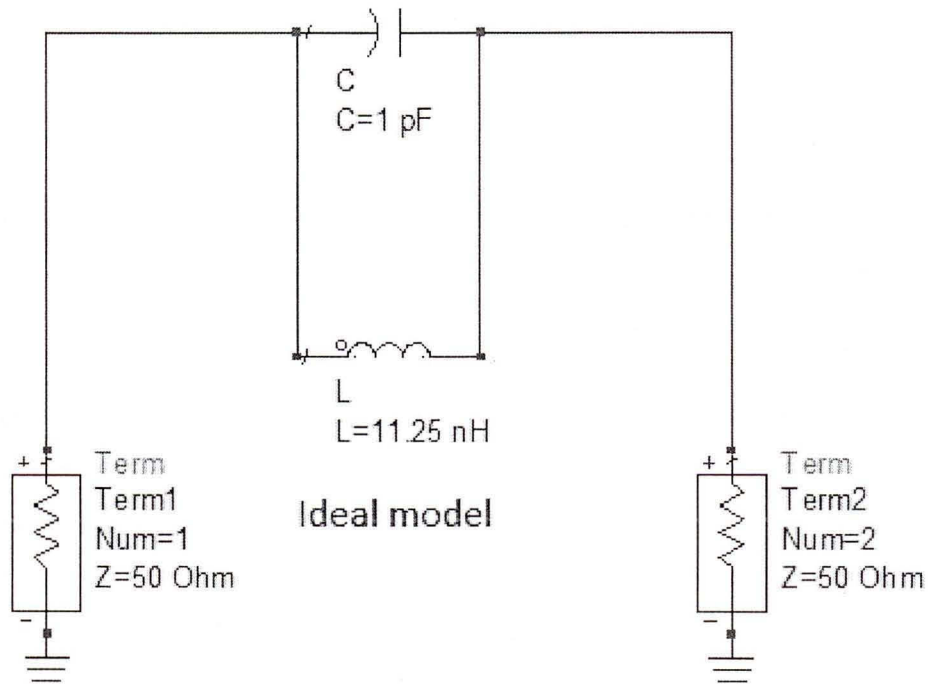


Figure 24: Ideal 1.5 GHz resonator design schematic diagram in ADS

The simulated result of the insertion loss of the ideal 1.5 GHz resonator is 63.58 dB as shown in Fig. 25. The return loss is near 0 dB. With ideal models and equation (1.9), the constructed ideal resonator design circuit has perfect performance.

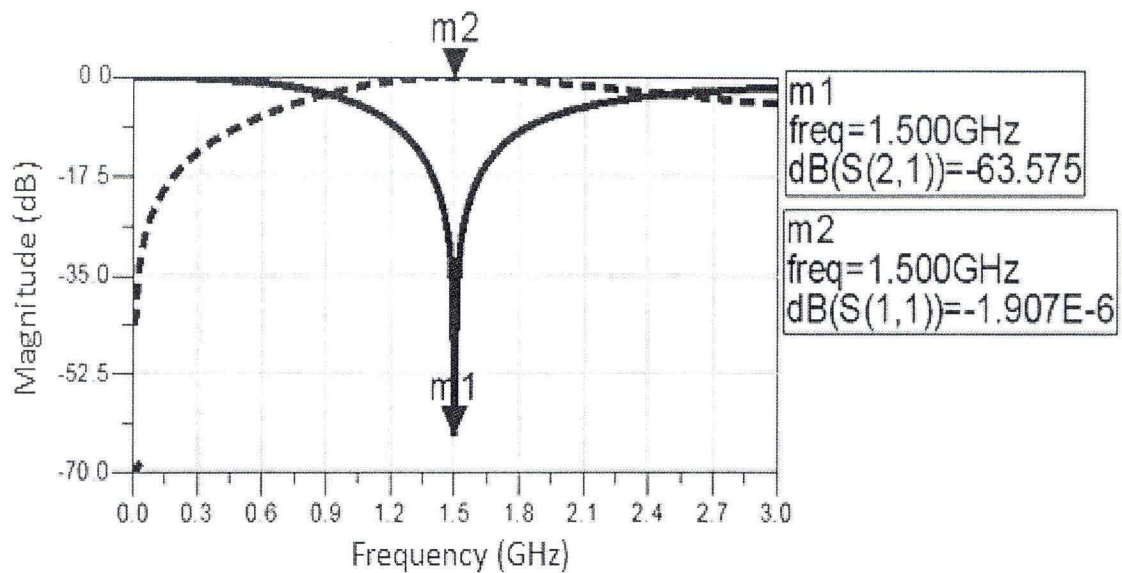


Figure 25: Simulated results of the ideal 1.5 GHz resonator design in ADS, solid line: insertion loss, and dot line: return loss

But if we used the same values calculated by equation (1.9) in the measured component models from Modelithics, the simulated result is totally different. I used the capacitor model of ATC600S and the inductor model of Coilcraft 0603HP modeled by Modelithics. With the structure shown in Fig. 26, the simulated result is shown in Fig. 27. By using the measured models, the insertion loss at 1.5 GHz is 13.85 dB which is far from the result of the ideal resonator 63.58 dB. To obtain an optimized insertion loss at 1.5 GHz, we used Tuning tool in ADS as shown in Fig. 28.

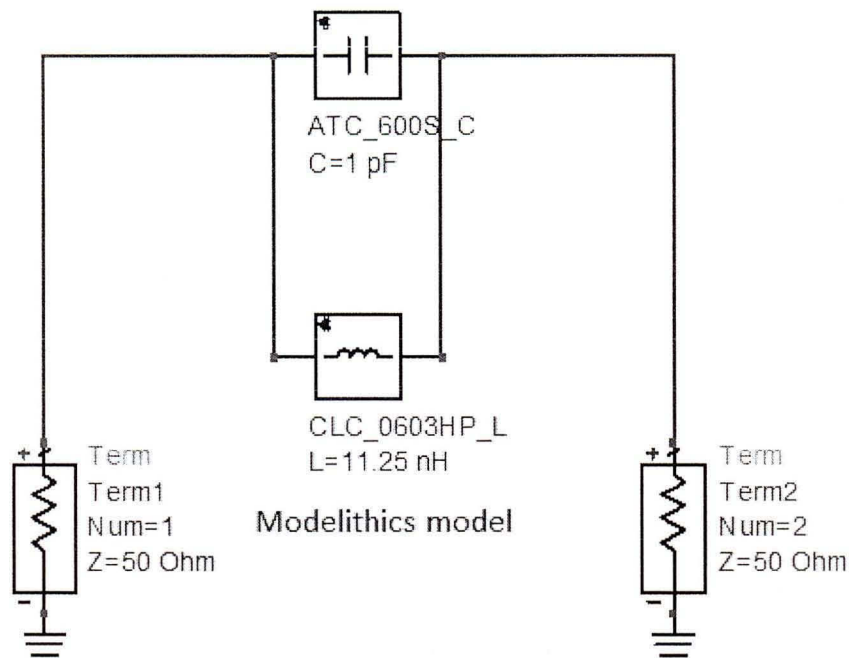


Figure 26: 1.5 GHz resonator circuit designed by using models from Modelithics compared with the ideal resonator circuit shown in Fig. 24

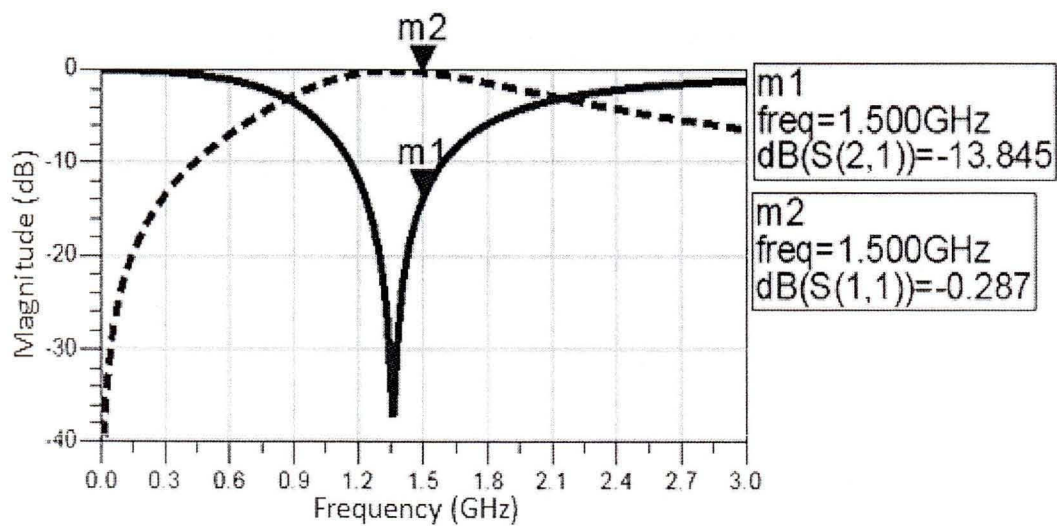


Figure 27: Simulated result of the 1.5 GHz resonator circuit designed by using models from Modelithics with the same value as the ideal 1.5 GHz resonator design, solid line: insertion loss, and dot line: return loss

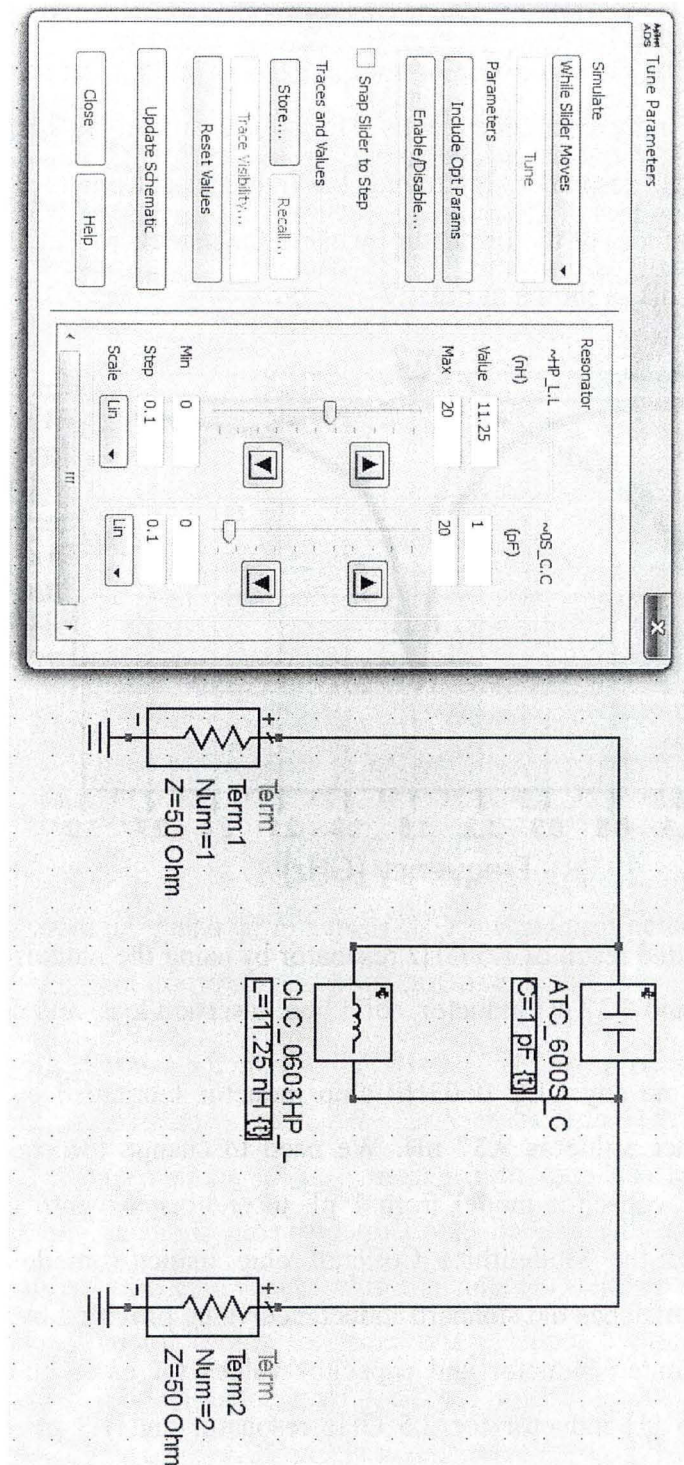


Figure 28: Tuning tool in ADS used to adjust the variable capacitance and inductance of capacitor and inductor models, respectively

To design the 1.5 GHz resonator using models provided by Modelithics, we used Tuning tool in ADS. By using Tuning tool, we can adjust the capacitance of capacitor and the inductance of inductor independently. Here, for example, we keep the capacitance as 1 pF for the 1.5 GHz resonator. By tuning the inductance from 11.25 nH to 9.37 nH, the minimum insertion loss of the resonator by using the models of Modelithics at 1.5 GHz can reach up to 27.50 dB as shown in Fig. 29.

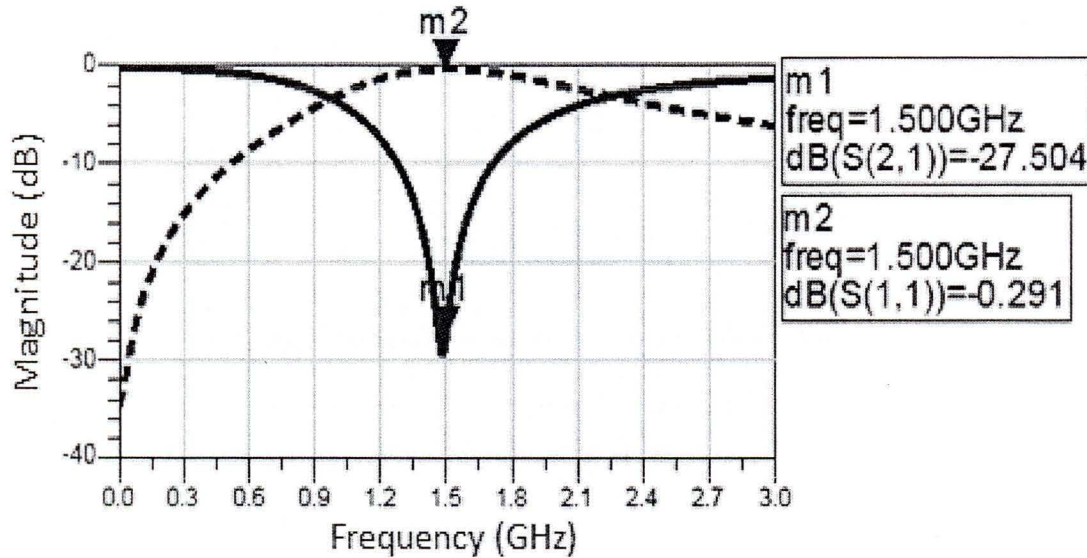


Figure 29: Simulated result of 1.5 GHz resonator by using the models of Modelithics with 1 pF capacitor and 9.37 nH inductor, solid line: insertion loss, and dot line: return loss .

But there's no any CLC 0603HP chip inductor fabricated by Coilcraft having the standard inductance value as 9.37 nH. We need to change the capacitance value of the Modelithics ATC capacitor model from 1 pF to another standard capacitance value and tune the value of the Modelithics Coilcraft chip inductor model to see if the tuned inductance value matches the standard inductance value provided by Coilcraft. In practical case, there are limited inductor and capacitor values for us to choose. I choose 0.8 pF capacitor and 3.6 nH inductor for 2.5 GHz resonator and 1.8 pF capacitor and 5.1 nH inductor for 1.5 GHz resonator as shown in Fig. 30.

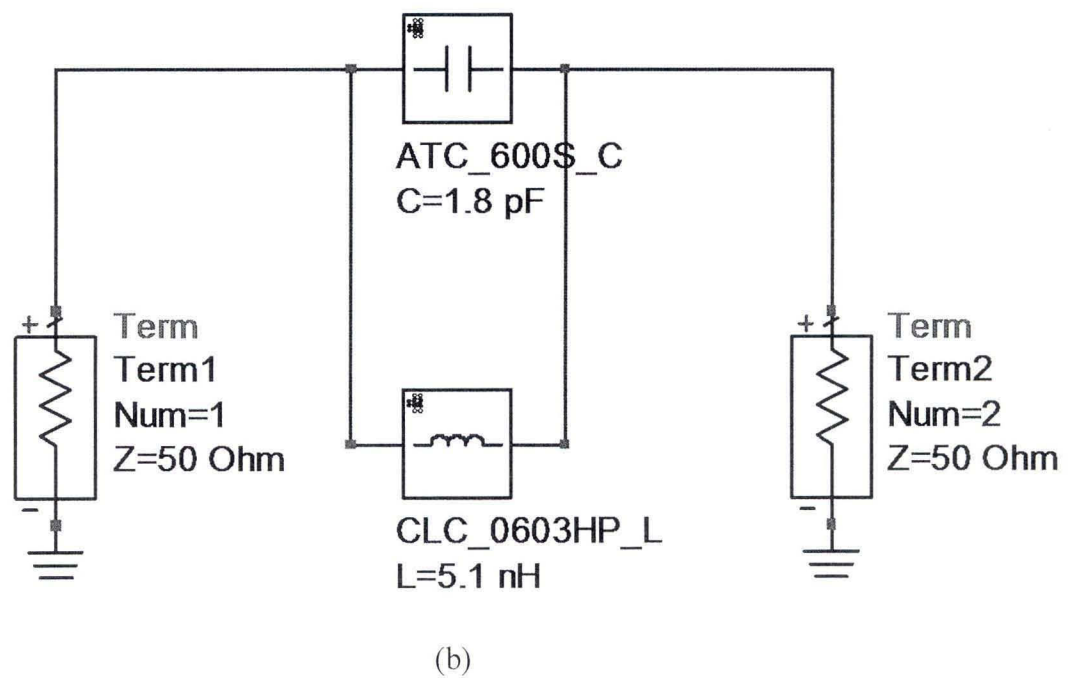
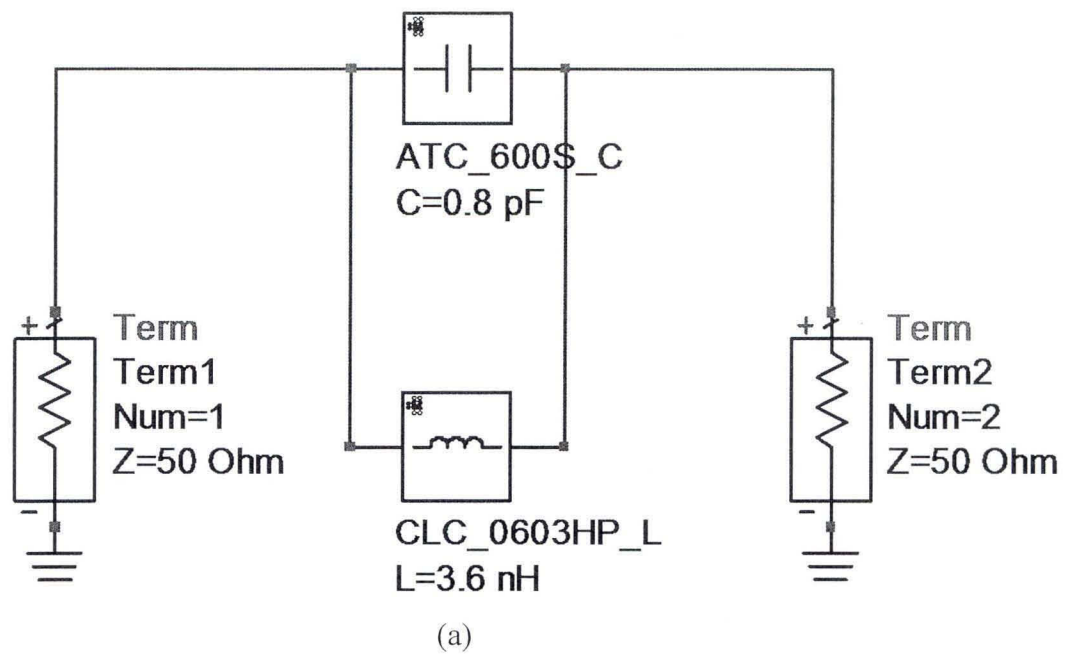
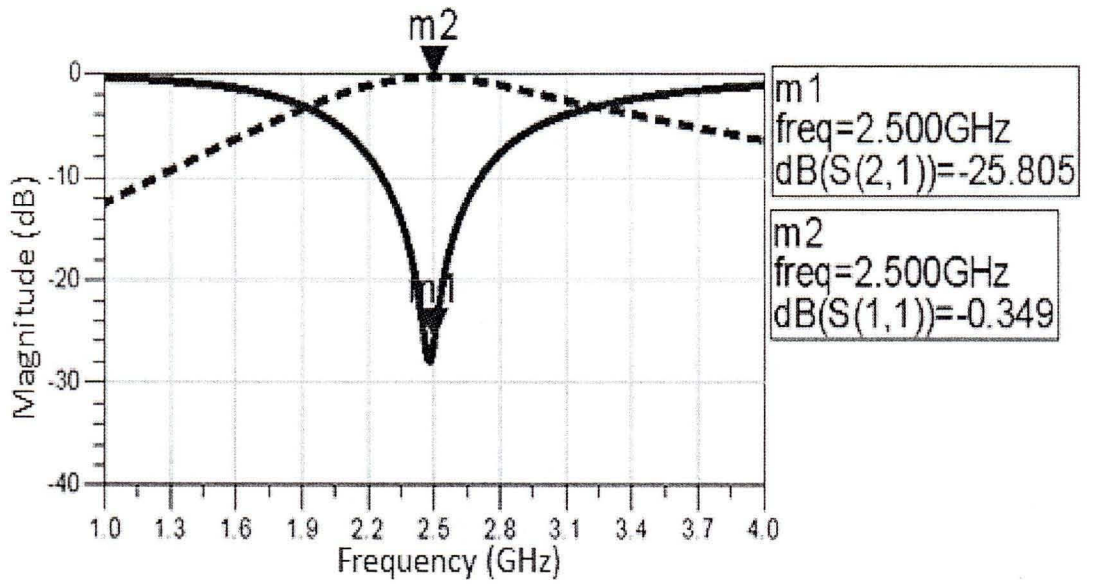
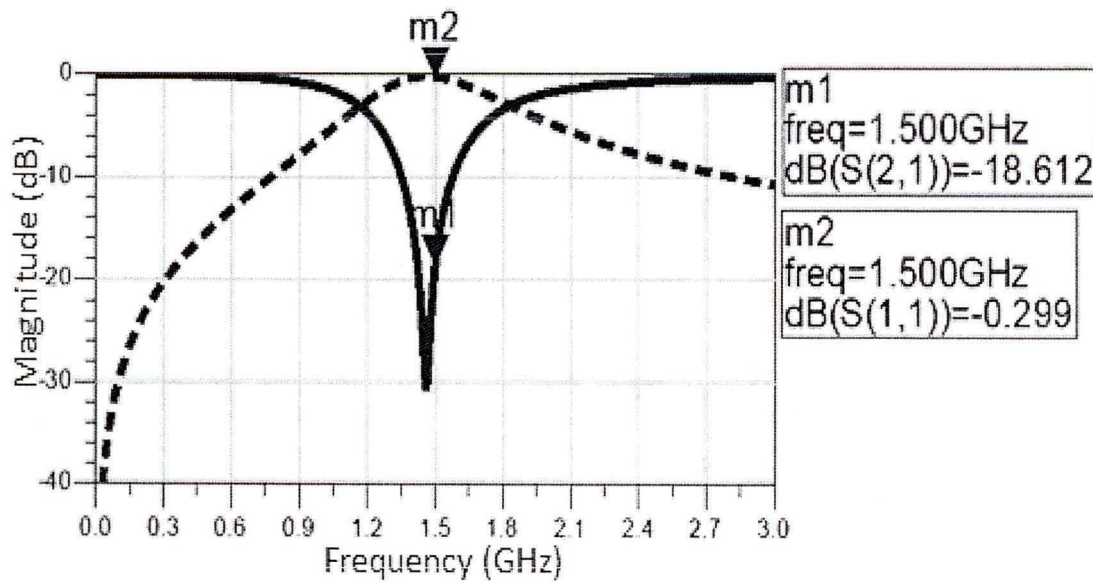


Figure 30: Resonator designed for (a): 2.5 GHz and (b): 1.5 GHz by using existent component values from manufacturers

The simulated results of (a) and (b) in Fig. 30 are shown in Fig. 31 (a) and (b), respectively.



(a)



(b)

Figure 31: Simulated results of resonators designed for (a): 2.5 GHz and (b): 1.5 GHz by using existent component values from manufactures, solid line: insertion loss, and dot line: return loss

The simulated result of the resonator in Fig. 32 is shown in Fig. 33.

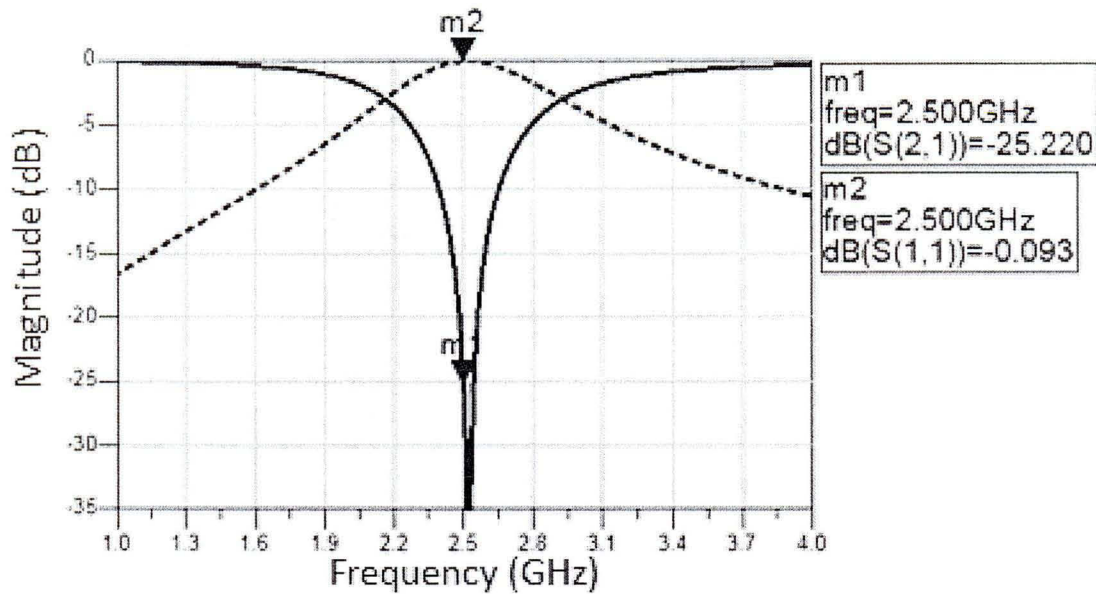


Figure 33: Simulated result of 2.5 GHz resonator by using microstrip line type inductor instead of chip inductor, solid line: insertion loss, and dot line: return loss

By using momentum simulation in ADS, we got the similar simulated results as the simulated results shown in Fig. 33 which applied ADS schematic simulation. The momentum simulation design schematic diagram with the measured Modelithics model is shown in Fig. 34. The simulated result of momentum simulation of 2.5 GHz resonator is shown in Fig. 35. Here, I use mesh density 100 and arc resolution 5 with Momentum MW model type. The substrate used is TLX-8 from Taconic. At 2.5 GHz, the simulated results in Fig. 35 show the return loss is 0.07 dB and the insertion loss is more than 33 dB. Signal generated at 2.5 GHz is blocked effectively by this mentioned microstrip type resonator.

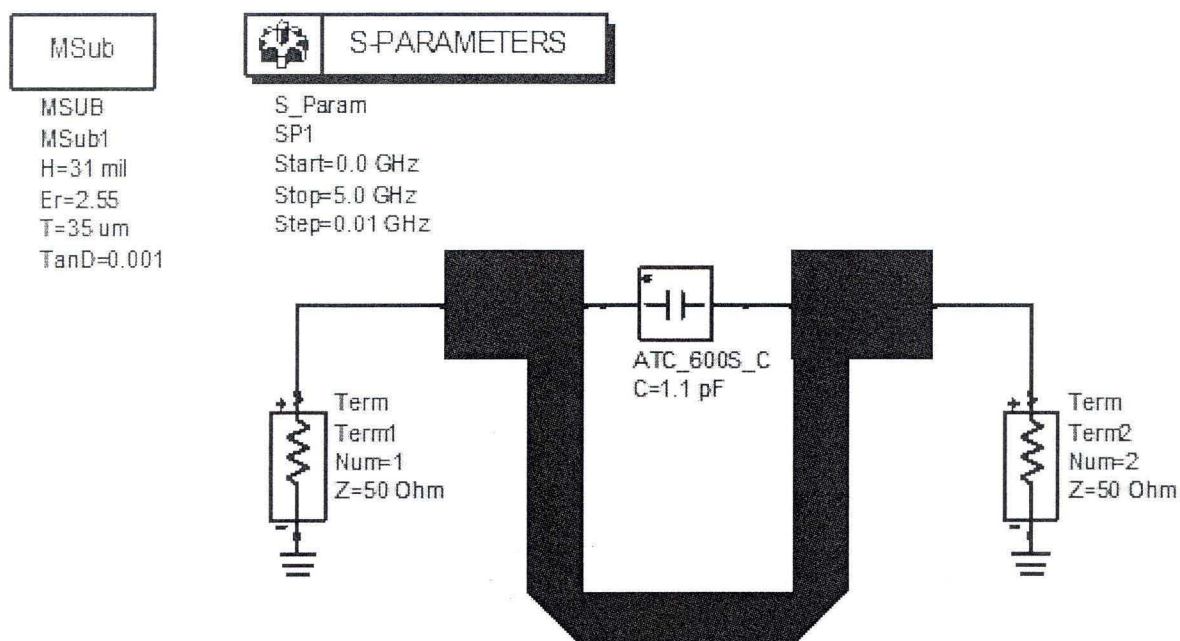


Figure 34: Schematic diagram of 2.5 GHz resonator using momentum model

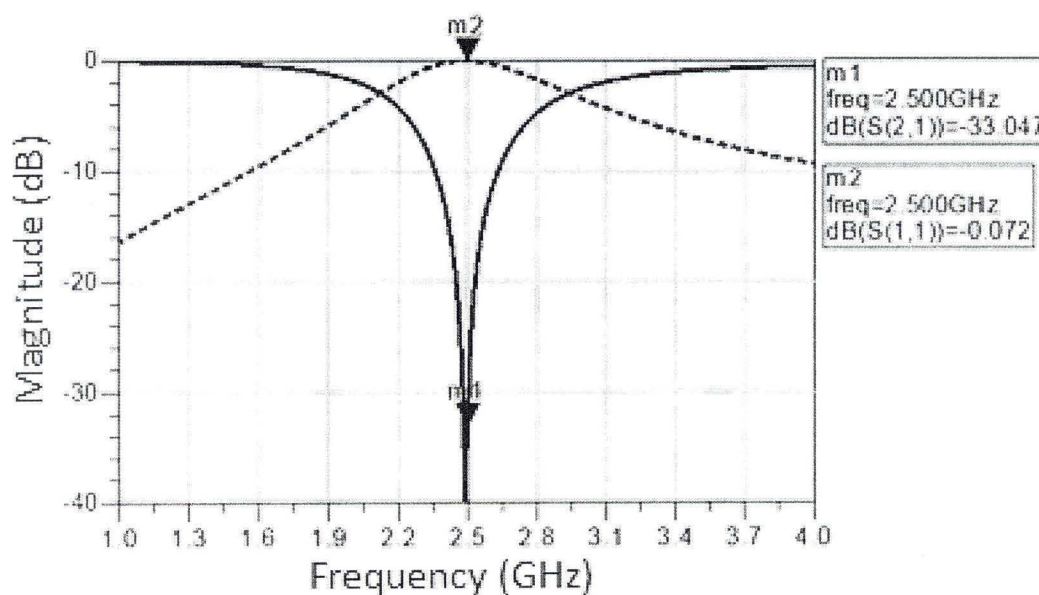


Figure 35: Simulated result of momentum model 2.5 GHz resonator, solid line: insertion loss, dot line: return loss

In practice, because microstrip type resonator using microstrip line type inductor instead of chip inductor, we can adjust the width and length of the microstrip line easily, so we can have any inductance value that we need and do not need to consider the limit standard values of chip inductors provided by inductor manufacturers. However, the structure of the microstrip type resonator is more complex and it takes more design space than the structure of the resonator using chip inductor.

c) Multiband Pi-shaped structure with resonators (Wang *et al.*, 2012 a)

In this part, a dual-band Pi-shaped structure with resonators, a tri-band Pi-shaped structure with resonators, and a general multiband (n-band) Pi-shaped structure with resonators are presented. This kind of multiband Pi-shaped structure performances like a multiband quarter wavelength transmission line. By adding resonators at both end of the series microstrip line of conventional Pi-shaped structure which consists of one series microstrip line and two open-circuited stubs as shown in Fig. 36, the proposed dual-band, tri-band, and multiband (n-band) Pi-shaped structures with resonators are achieved. In Fig. 36, Z_1 is the characteristic impedance of the series microstrip line, l_1 is the length of the series microstrip line, Z_2 is the characteristic impedance of the two open-circuited stubs, and l_2 is the length of the two open-circuited stubs.

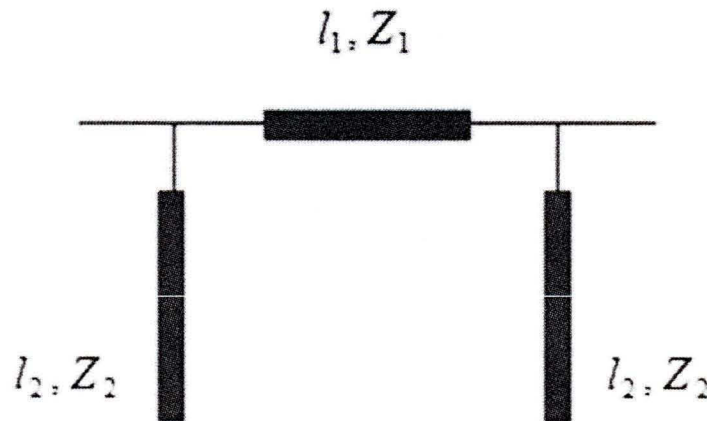


Figure 36: Conventional Pi-shaped structure consists of one series microstrip line and two open-circuited stubs

In order to calculate the length and characteristic impedance of stubs we used ABCD matrix which allows simplifying the calculation (Aflaki *et al.*, 2010). The two-port series transmission line is shown in Fig. 37 (Pozar, 2005: 185). The ABCD matrix of the two-port transmission line can be expressed with equation (1.10) (Pozar, 2005: 185) and equation (1.11) (Pozar, 2005: 52).

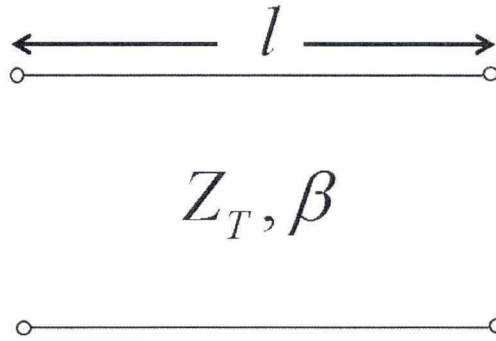


Figure 37: Two-port network consisting of one transmission line

$$\begin{bmatrix} A & B \\ C & D \end{bmatrix} = \begin{bmatrix} \cos \beta l & jZ_T \sin \beta l \\ jY_T \sin \beta l & \cos \beta l \end{bmatrix} \quad (1.10)$$

where Z_T is the characteristic impedance of the transmission line, Y_T is the characteristic admittance of the transmission line, and l is the length of the transmission line.

$$\beta = \frac{2\pi}{\lambda} \quad (1.11)$$

where λ is the wavelength.

When the transmission line is quarter wavelength transmission line, we can deduce:

$$l = \frac{\lambda}{4} \Rightarrow \beta l = \left(\frac{2\pi}{\lambda}\right)\left(\frac{\lambda}{4}\right) = \frac{\pi}{2} \quad (1.12)$$

The ABCD matrix of quarter wavelength transmission line can be expressed by equation (1.13).

$$\begin{aligned} \begin{bmatrix} A & B \\ C & D \end{bmatrix} &= \begin{bmatrix} \cos \beta l & jZ_T \sin \beta l \\ jY_T \sin \beta l & \cos \beta l \end{bmatrix} = \begin{bmatrix} \cos \frac{\pi}{2} & jZ_T \sin \frac{\pi}{2} \\ jY_T \sin \frac{\pi}{2} & \cos \frac{\pi}{2} \end{bmatrix} \\ &= \begin{bmatrix} 0 & jZ_T \\ jY_T & 0 \end{bmatrix} \end{aligned} \quad (1.13)$$

where Z_T is the characteristic impedance of the transmission line, Y_T is the characteristic admittance of the transmission line.

The two-port network consisting of one shunt admittance is shown in Fig. 38 (Pozar, 2005: 185). Its ABCD matrix is expressed by equation (1.14) (Pozar, 2005: 185).

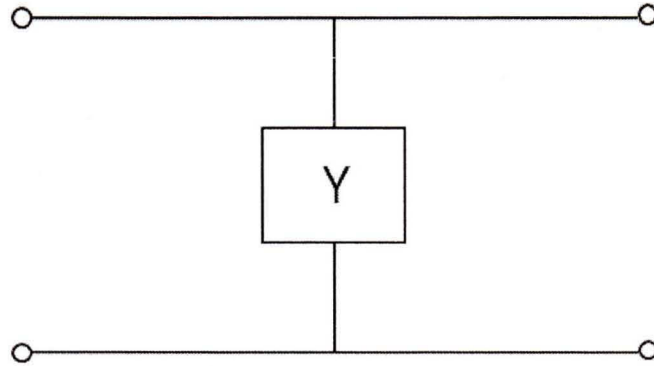


Figure 38: Two-port network consisting of one shunt admittance

$$\begin{bmatrix} A & B \\ C & D \end{bmatrix} = \begin{bmatrix} 1 & 0 \\ Y & 1 \end{bmatrix} \quad (1.14)$$

where Y is the admittance of the shunt circuit.

As shown in Fig. 36, we used open-circuited stub in the conventional Pi-shaped structure. Fig. 39 shows the open-circuited transmission line (Gonzalez, 1997: 16). The

impedance of the open-circuited transmission line is shown in equation (1.15) (Gonzalez, 1997: 16).

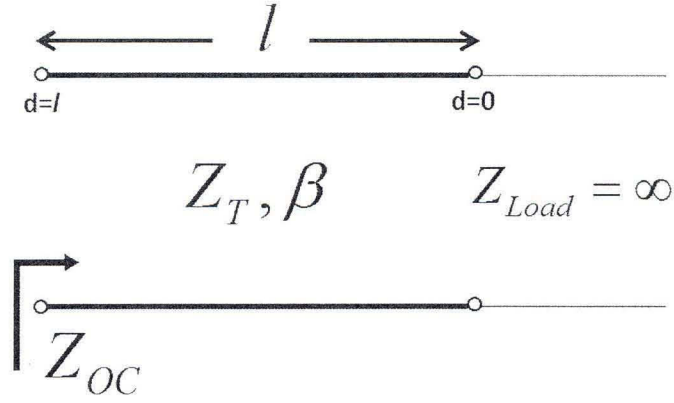


Figure 39: Open-circuited transmission line

$$Z_{OC}(d=l) = -jZ_T \cot \beta l \quad (1.15)$$

where Z_{OC} is the impedance of the open-circuited transmission line, Z_T is the characteristic impedance of the transmission line, l is the length of the transmission line, and Z_{Load} is the characteristic impedance of the load transmission line.

We can deduce the ABCD matrix of shunt open-circuited stub is:

$$\begin{bmatrix} A & B \\ C & D \end{bmatrix} = \begin{bmatrix} 1 & 0 \\ Y_{OC} & 1 \end{bmatrix} = \begin{bmatrix} 1 & 0 \\ \frac{1}{Z_{OC}} & 1 \end{bmatrix} = \begin{bmatrix} 1 & 0 \\ jY_T \tan \beta l & 1 \end{bmatrix} \quad (1.16)$$

where Y_T is the characteristic admittance of the transmission line, l is the length of the transmission line.

The conventional Pi-shaped circuit shown in Fig. 36 consisting of two identical shunt open-circuited transmission lines and one series transmission line can be expressed by ABCD matrix as shown in equation (1.17).

$$\begin{bmatrix} A & B \\ C & D \end{bmatrix} = \begin{bmatrix} 1 & 0 \\ jY_2 \tan \beta l_2 & 1 \end{bmatrix} \begin{bmatrix} \cos \beta l_1 & jZ_1 \sin \beta l_1 \\ jY_1 \sin \beta l_1 & \cos \beta l_1 \end{bmatrix} \begin{bmatrix} 1 & 0 \\ jY_2 \tan \beta l_2 & 1 \end{bmatrix} \quad (1.17)$$

where Y_1 is the characteristic admittance of the series transmission line, Z_1 is the characteristic impedance of the series transmission line, l_1 is the length of the series transmission line, Y_2 is the characteristic admittance of the shunt open-circuited transmission line, and l_2 is the length of the shunt open-circuited transmission line.

c.1) Principle of dual-band Pi-shaped structure

Resonance is obtained by using capacitor and inductor in parallel. The value of capacitor and inductor can be easily chosen to make a resonator to block the signal generated at the specific frequency. Before analyzing the whole topology of the dual-band Wilkinson power divider, we should analyze the dual-band Pi-shaped structure with resonators first as shown in Fig. 40. At frequency f_1 , the initial proposed dual-band Pi-shaped structure becomes a simple transmission line (Fig. 40 (a)), because the signal at frequency f_1 is blocked by the resonator f_1 at each side of the dual-band Pi-shaped structure. At frequency f_2 , because the ideal resonator f_1 is hypothesized to pass signal without any power loss and phase delay, the Pi-shaped structure transforms to the Pi-shaped circuit with open-circuited stubs whose characteristic impedance is Z_2 and length is l_2 (Fig. 40 (b)). In the design procedure, at frequency f_2 the phase and impedance of the LC resonator f_1 should be considered. The parameter Z_2 and l_2 have to be synthesized, so that the Pi-shaped structure with resonators (Fig. 40) can perform as a quarter wavelength transmission line well.

To design a dual-band Pi-shaped quarter wavelength transmission line for dual-band Wilkinson power divider, at frequency f_1 , the length of the series microstrip line l_1 is chosen

as $\lambda_1/4$, λ_1 is the wavelength of frequency f_1 . The characteristic impedance Z_1 of the series microstrip line is 70.7 Ohm.

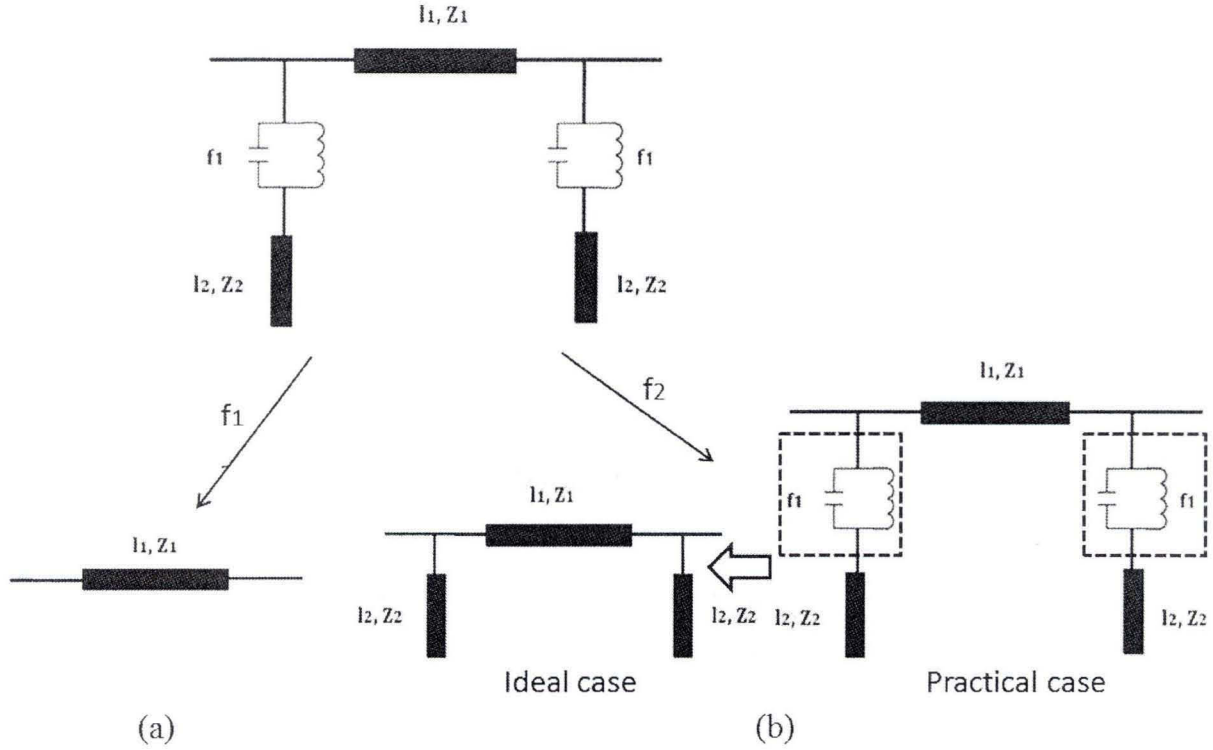


Figure 40: Principle of dual-band quarter wavelength transmission line, (a): at frequency f_1 , and (b): at frequency f_2

Theoretically, we use ideal resonator f_1 which is considered as a short circuit at frequency f_2 . According to equation (1.17), the ideal equivalent Pi-shaped structure shown in Fig. 40 (b) at frequency f_2 can be expressed with ABCD matrix as:

$$\begin{bmatrix} A & B \\ C & D \end{bmatrix} = \begin{bmatrix} 1 & 0 \\ jY_2 \tan \beta_2 l_2 & 1 \end{bmatrix} \begin{bmatrix} \cos \beta_2 l_1 & jZ_1 \sin \beta_2 l_1 \\ jY_1 \sin \beta_2 l_1 & \cos \beta_2 l_1 \end{bmatrix} \begin{bmatrix} 1 & 0 \\ jY_2 \tan \beta_2 l_2 & 1 \end{bmatrix} \quad (1.18)$$

where $\beta_2 = \frac{2\pi}{\lambda_2}$, $Z_1 = 70.7\Omega$, $l_1 = \frac{\lambda_1}{4}$.

λ_1 is the wavelength of frequency f_1 and λ_2 is the wavelength of frequency f_2 .

According to equation (1.13), at frequency f_2 , ABCD matrix of a quarter wavelength transmission line can be expressed as:

$$\begin{bmatrix} A & B \\ C & D \end{bmatrix} = \begin{bmatrix} 0 & jZ_{02} \\ jY_{02} & 0 \end{bmatrix} \quad (1.19)$$

where Z_{02} is the characteristic impedance of the quarter wavelength transmission line at frequency f_2 .

The length of the ideal equivalent Pi-shaped structure (Fig. 40) should be $\lambda_2/4$ at frequency f_2 . To do that, we equalize the equations (1.18) and (1.19). We can deduce:

$$\begin{aligned} A &= \cos \beta_2 l_1 - Y_2 Z_1 \tan \beta_2 l_2 \sin \beta_2 l_1 = 0 \\ \Rightarrow Z_1 \tan \beta_2 l_1 &= Z_2 \cot \beta_2 l_2 \end{aligned} \quad (1.20)$$

$$\begin{aligned} B &= jZ_1 \sin \beta_2 l_1 = jZ_{02} \\ \Rightarrow Z_{02} &= Z_1 \sin \beta_2 l_1 \end{aligned} \quad (1.21)$$

$$\begin{aligned} C &= jY_2 \tan \beta_2 l_2 \cos \beta_2 l_1 + jY_1 \sin \beta_2 l_1 \\ &- jY_2 Y_2 Z_1 \tan \beta_2 l_2 \tan \beta_2 l_2 \sin \beta_2 l_1 + jY_2 \tan \beta_2 l_2 \cos \beta_2 l_1 = jY_{02} \end{aligned} \quad (1.22)$$

$$\begin{aligned} D &= \cos \beta_2 l_1 - Y_2 Z_1 \tan \beta_2 l_2 \sin \beta_2 l_1 = 0 \\ \Rightarrow Z_1 \tan \beta_2 l_1 &= Z_2 \cot \beta_2 l_2 \end{aligned} \quad (1.23)$$

where $\beta_2 = \frac{2\pi}{\lambda_2}$, $Z_1 = 70.7\Omega$, $l_1 = \frac{\lambda_1}{4}$.

We can deduce:

$$\Rightarrow Z_1 \tan \beta_2 l_1 = Z_2 \cot \beta_2 l_2 \quad (1.24)$$

$$\Rightarrow Z_{02} = Z_1 \sin \beta_2 l_1 \quad (1.25)$$

where $\beta_2 = \frac{2\pi}{\lambda_2}$, $Z_1 = 70.7\Omega$, $l_1 = \frac{\lambda_1}{4}$.

Equation (1.24) which has 2 unknowns permits to calculate the stub length by setting $Z_2 = 50 \text{ Ohm}$ as a starting value, l_2 can be found. And Z_{02} can be calculated by equation (1.25), i.e. 57.19 Ohm of the dual-band Wilkinson power divider proposed in this chapter as setting the frequency f_1 to 3.6 GHz and the frequency f_2 to 2.5 GHz . The value of Z_{02} is different than the theoretical impedance 70.7 Ohm . As the impedance condition is not satisfying perfectly for frequency f_2 , we can take the best trade-off by little bit increasing the value of Z_1 to obtain a better performance at frequency f_2 .

c.2) Principle of tri-band Pi-shaped structure

Before analyzing the whole topologies of the proposed tri-band Wilkinson power divider and the tri-band rat-race coupler, we should grasp the gist of the tri-band quarter wavelength Pi-shaped structure with resonators as shown in Fig. 41. This tri-band quarter wavelength Pi-shaped structure consists of one series microstrip line, four shunt open-circuited transmission lines, and four resonators. Resonator f_1 is designed to block the signal at frequency f_1 and resonator f_2 is designed to block the signal at frequency f_2 . Theoretically, in Fig. 41, we consider resonator f_1 and resonator f_2 are ideal resonators. That means, at frequency f_2 resonator f_1 has no power loss and phase delay, while at frequency f_1 , it provides infinite impedance. The same is supposed for resonator f_2 . In the proposed tri-band Wilkinson power divider and the tri-band rat-race coupler, this proposed tri-band Pi-shaped circuit (Fig. 41) acts as a tri-band quarter wavelength transmission line at each operating frequency.

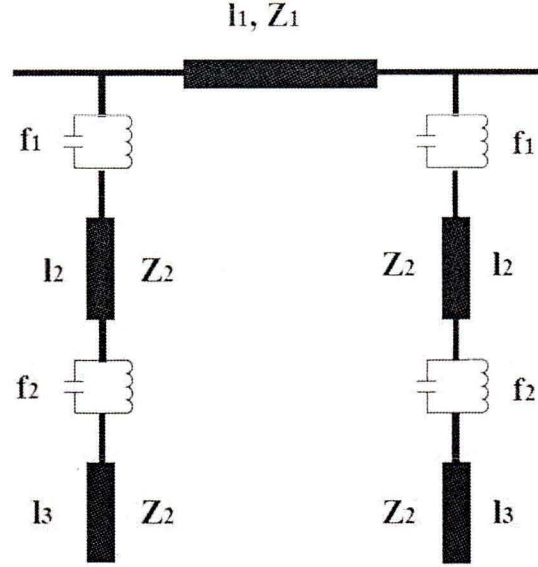


Figure 41: Tri-band Pi-shaped structure with resonators

The line l_1 is the microstrip line measured quarter electrical wavelength at frequency f_1 with the characteristic impedance corresponding at 70.7 Ohm. At both ends of line l_1 , we put one stub with characteristic impedance Z_2 and length l_2 between the parallel type resonator f_1 and resonator f_2 . Resonator f_1 is specially designed to block signal generated at frequency f_1 , the same as resonator f_2 . Behind resonator f_2 , we put one open-circuited stub with characteristic impedance Z_2 and length l_3 .

Fig. 42 shows the principle of the proposed tri-band Pi-shaped structure. At frequency f_1 , signal is blocked by the first resonator f_1 , the initial proposed structure (Fig. 41) becomes a simple transmission line (Fig. 42 (a)). At frequency f_2 it transforms to Pi-shaped line with characteristic impedance Z_2 and length l_2 (Fig. 42 (b)), because the signal at frequency f_2 can go through the first resonator f_1 but is blocked at the second resonator f_2 . Finally the same operation is repeated at frequency f_3 , the first open-circuited stub joins to the second open-circuited stub to be considered as one longer open-circuited stub which has the length (l_2+l_3) as shown in Fig. 42 (c).

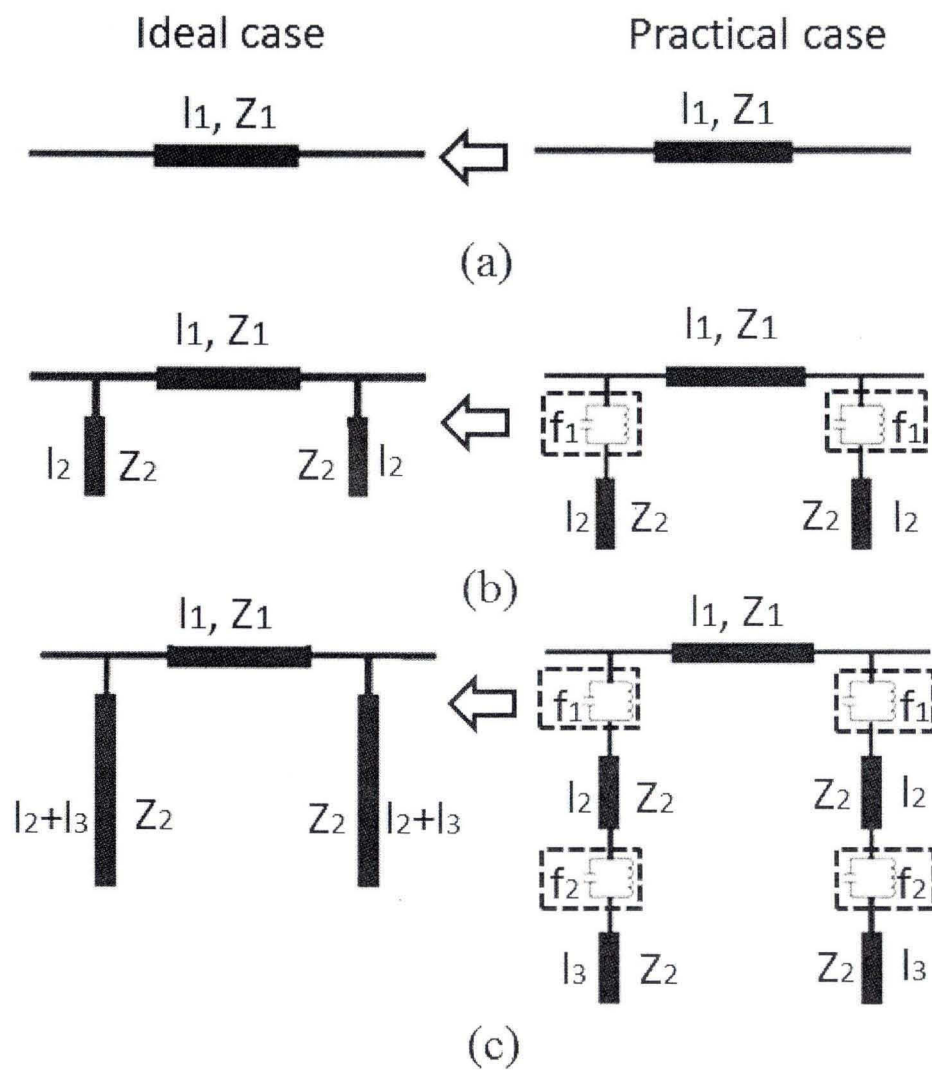
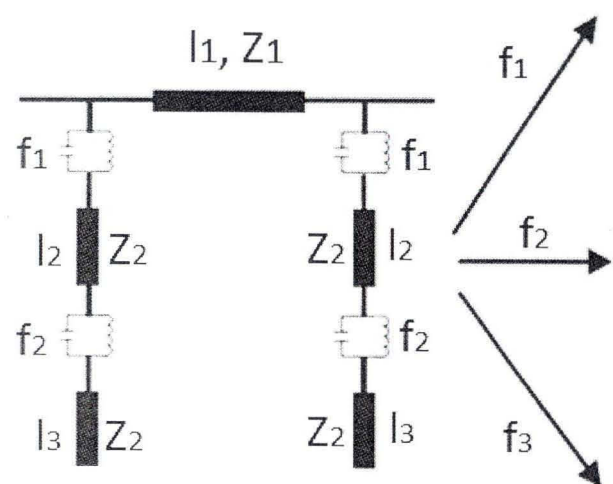


Figure 42: Principle of the proposed tri-band Pi-shaped structure with resonators

In order to calculate the length and characteristic impedance of stubs we use ABCD matrix which allows simplifying the calculation.

At frequency f_l , the signal is blocked by the resonator f_l as shown in Fig. 41, the proposed tri-band Pi-shaped structure becomes to one simple microstrip transmission line as shown in Fig. 42 (a). To apply this tri-band Pi-shaped circuit in tri-band Wilkinson power divider or tri-band rat-race coupler as the tri-band quarter wavelength transmission line which has characteristic impedance 70.7 Ohm, we set $l_l = \lambda_l/4$ and $Z_l = 70.7$ Ohm, where λ_l is the wavelength of frequency f_l .

At frequency f_2 , according to equation (1.17), the equivalent circuit shown in Fig. 42 (b) with symmetrical structure at both ends of line l_l corresponds to the matrix below:

$$\begin{bmatrix} A_2 & B_2 \\ C_2 & D_2 \end{bmatrix} = \begin{bmatrix} 1 & 0 \\ jY_2 \tan \beta_2 l_2 & 1 \end{bmatrix} \begin{bmatrix} \cos \beta_2 l_1 & jZ_1 \sin \beta_2 l_1 \\ jY_1 \sin \beta_2 l_1 & \cos \beta_2 l_1 \end{bmatrix} \begin{bmatrix} 1 & 0 \\ jY_2 \tan \beta_2 l_2 & 1 \end{bmatrix} \quad (1.26)$$

where $\beta_2 = \frac{2\pi}{\lambda_2}$, $Z_1 = 70.7\Omega$, $l_1 = \frac{\lambda_1}{4}$.

λ_1 is the wavelength of frequency f_l and λ_2 is the wavelength of frequency f_2 .

At frequency f_2 , according to equation (1.13), ABCD matrix of a quarter wavelength transmission line can be expressed as:

$$\begin{bmatrix} A_2 & B_2 \\ C_2 & D_2 \end{bmatrix} = \begin{bmatrix} 0 & jZ_{02} \\ jY_{02} & 0 \end{bmatrix} \quad (1.27)$$

where Z_{02} is the characteristic impedance of the quarter wavelength transmission line at frequency f_2 .

Ideally the equivalent electrical length of the proposed Pi-shaped circuit should be quarter wavelength at frequency f_2 . To do that, we equalize the equations (1.26) and (1.27).

We can deduce:

$$\begin{aligned} A_2 &= \cos \beta_2 l_1 - Y_2 Z_1 \tan \beta_2 l_2 \sin \beta_2 l_1 = 0 \\ \Rightarrow Z_1 \tan \beta_2 l_1 &= Z_2 \cot \beta_2 l_2 \end{aligned} \quad (1.28)$$

$$\begin{aligned} B_2 &= jZ_1 \sin \beta_2 l_1 = jZ_{02} \\ \Rightarrow Z_{02} &= Z_1 \sin \beta_2 l_1 \end{aligned} \quad (1.29)$$

$$\begin{aligned} C_2 &= jY_2 \tan \beta_2 l_2 \cos \beta_2 l_1 + jY_1 \sin \beta_2 l_1 \\ &- jY_2 Y_2 Z_1 \tan \beta_2 l_2 \tan \beta_2 l_2 \sin \beta_2 l_1 + jY_2 \tan \beta_2 l_2 \cos \beta_2 l_1 = jY_{02} \end{aligned} \quad (1.30)$$

$$\begin{aligned} D_2 &= \cos \beta_2 l_1 - Y_2 Z_1 \tan \beta_2 l_2 \sin \beta_2 l_1 = 0 \\ \Rightarrow Z_1 \tan \beta_2 l_1 &= Z_2 \cot \beta_2 l_2 \end{aligned} \quad (1.31)$$

where $\beta_2 = \frac{2\pi}{\lambda_2}$, $Z_1 = 70.7\Omega$, $l_1 = \frac{\lambda_1}{4}$.

We can deduce:

$$\Rightarrow Z_1 \tan \beta_2 l_1 = Z_2 \cot \beta_2 l_2 \quad (1.32)$$

$$\Rightarrow Z_{02} = Z_1 \sin \beta_2 l_1 \quad (1.33)$$

where $\beta_2 = \frac{2\pi}{\lambda_2}$, $Z_1 = 70.7\Omega$, $l_1 = \frac{\lambda_1}{4}$.

Similarly, at frequency f_3 , according to equation (1.17), the equivalent circuit shown in Fig. 42 (c) with symmetrical structure at both ends of line l_1 corresponds to the ABCD matrix below:

$$\begin{bmatrix} A_3 & B_3 \\ C_3 & D_3 \end{bmatrix} = \begin{bmatrix} 1 & 0 \\ jY_2 \tan \beta_3(l_2 + l_3) & 1 \end{bmatrix} \begin{bmatrix} \cos \beta_3 l_1 & jZ_1 \sin \beta_3 l_1 \\ jY_1 \sin \beta_3 l_1 & \cos \beta_3 l_1 \end{bmatrix} \begin{bmatrix} 1 & 0 \\ jY_2 \tan \beta_3(l_2 + l_3) & 1 \end{bmatrix} \quad (1.34)$$

where $\beta_3 = \frac{2\pi}{\lambda_3}$, $Z_1 = 70.7\Omega$, $l_1 = \frac{\lambda_1}{4}$.

λ_1 is the wavelength of frequency f_1 and λ_3 is the wavelength of frequency f_3 .

At frequency f_3 , according to equation (1.13), ABCD matrix of a quarter wavelength transmission line can be expressed as:

$$\begin{bmatrix} A_3 & B_3 \\ C_3 & D_3 \end{bmatrix} = \begin{bmatrix} 0 & jZ_{03} \\ jY_{03} & 0 \end{bmatrix} \quad (1.35)$$

where Z_{03} is the characteristic impedance of the quarter wavelength transmission line at frequency f_3 .

By equalizing the equations (1.34) and (1.35), we can deduce:

$$\begin{aligned} A_3 &= \cos \beta_3 l_1 - Y_2 Z_1 \tan \beta_3(l_2 + l_3) \sin \beta_3 l_1 = 0 \\ \Rightarrow Z_1 \tan \beta_3 l_1 &= Z_2 \cot \beta_3(l_2 + l_3) \end{aligned} \quad (1.36)$$

$$\begin{aligned} B_3 &= jZ_1 \sin \beta_3 l_1 = jZ_{03} \\ \Rightarrow Z_{03} &= Z_1 \sin \beta_3 l_1 \end{aligned} \quad (1.37)$$

$$\begin{aligned}
C_3 &= jY_2 \tan \beta_3(l_2 + l_3) \cos \beta_3 l_1 + jY_1 \sin \beta_3 l_1 \\
&- jY_2 Y_2 Z_1 \tan \beta_3(l_2 + l_3) \tan \beta_3(l_2 + l_3) \sin \beta_3 l_1 \\
&+ jY_2 \tan \beta_3(l_2 + l_3) \cos \beta_3 l_1 = jY_{03}
\end{aligned} \tag{1.38}$$

$$\begin{aligned}
D_3 &= \cos \beta_3 l_1 - Y_2 Z_1 \tan \beta_3(l_2 + l_3) \sin \beta_3 l_1 = 0 \\
\Rightarrow Z_1 \tan \beta_3 l_1 &= Z_2 \cot \beta_3(l_2 + l_3)
\end{aligned} \tag{1.39}$$

where

$$\beta_3 = \frac{2\pi}{\lambda_3}, \quad Z_1 = 70.7\Omega, \quad l_1 = \frac{\lambda_1}{4}.$$

Similarly for frequency f_3 , we can deduce:

$$\Rightarrow Z_1 \tan \beta_3 l_1 = Z_2 \cot \beta_3(l_2 + l_3) \tag{1.40}$$

$$\Rightarrow Z_{03} = Z_1 \sin \beta_3 l_1 \tag{1.41}$$

where

$$\beta_3 = \frac{2\pi}{\lambda_3}, \quad Z_1 = 70.7\Omega, \quad l_1 = \frac{\lambda_1}{4}.$$

Equation (1.32), which have 2 unknowns, permits to calculate the stub length by setting $Z_2 = 50 \text{ Ohm}$ as a starting value, l_2 can be found. And Z_{02} can be calculated by equation (1.33). With the same manner using equation (1.40) and (1.41) we can find the value of $(l_2 + l_3)$ and Z_{03} . The values of Z_{02} and Z_{03} will be not equal to 70.7 Ohm . As the impedance condition is not satisfied perfectly for each operation frequency, we can make the best trade-off by little bit increasing the value of Z_l to obtain the best performance for tri-band operation.

In fact, the stubs at both sides of transmission line l_l adapt the length of the whole Pi-shaped circuit to have corresponding electrical length of $\lambda_2/4$ and $\lambda_3/4$ at frequency f_2 and frequency f_3 , respectively. Therefore we satisfied the condition of Wilkinson power divider or rat-race coupler for three distinctive frequencies at the meantime.

c.3) Principle of general multiband (n-band) Pi-shaped structure

The topology of the proposed general multiband (n-band, $n \geq 2$) Pi-shaped structure is shown in Fig. 43. Parallel LC resonator f_x ($x=1, 2, \dots, n-1$) used in the proposed Pi-shaped circuit blocks signal generated at frequency f_x ($x=1, 2, \dots, n-1$), where $f_1 > \dots > f_{n-1}$. Theoretically, we assume resonator f_x as an ideal resonator. That means, at frequency f_x , resonator f_x provides infinite impedance, while at other frequencies it has no power loss and phase delay just like a short circuit.

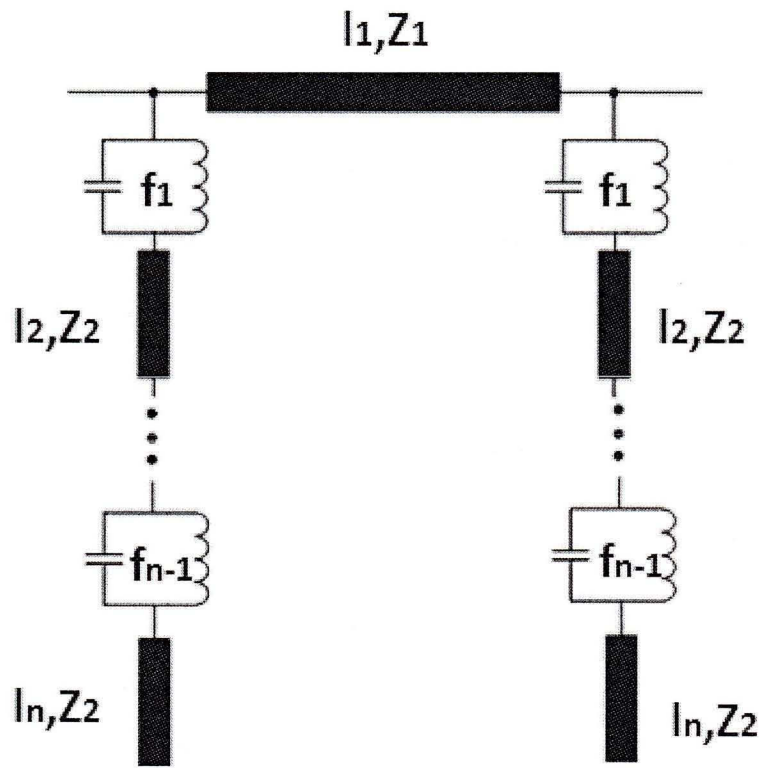


Figure 43: Multiband Pi-shaped structure with resonators

In Fig. 43, at frequency f_x ($x=1, 2, \dots, n-1$), signal is blocked by the resonator f_x and passing through resonator f_y ($y=0, 1, \dots, x-1$). The resonator f_0 means there's no resonator. For example, in tri-band case, we set $n=3$, there are three distinctive frequencies frequency f_1 , frequency f_2 , and frequency f_3 . At frequency f_1 , signal is blocked by the resonator f_1 and passing through resonator f_0 (the resonator f_0 means there's no resonator); at frequency f_2 ,

signal is blocked by the resonator f_2 , and passing through resonator f_1 . At frequency f_3 , signal is blocked by the resonator f_3 which is like open circuit at frequency f_3 and passing through resonator f_1 and resonator f_2 .

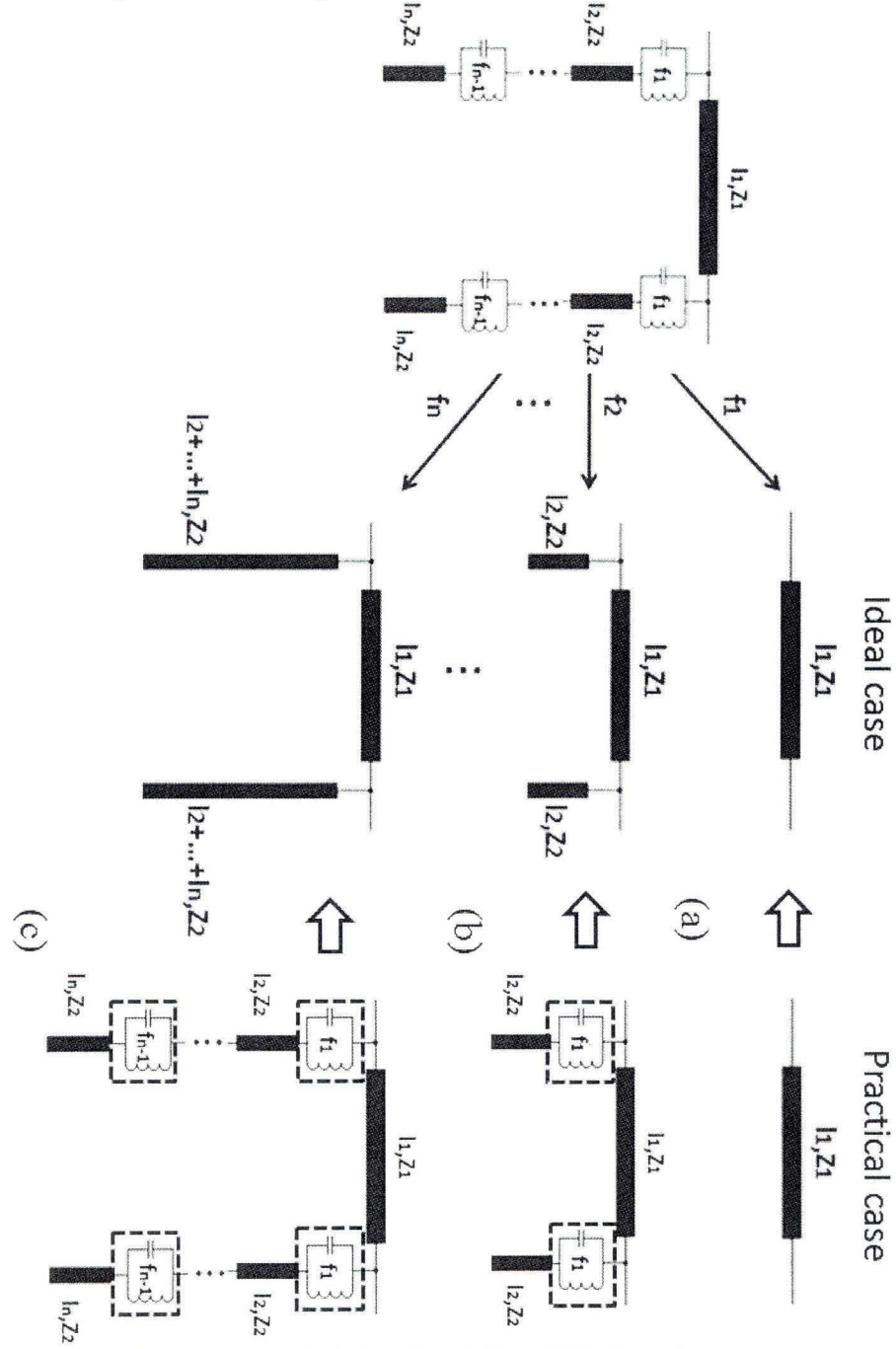


Figure 44: Principle of multiband Pi-shaped structure

Fig. 44 shows the principle of the proposed multiband Pi-shaped structure. At different frequency, the proposed multiband Pi-shaped structure becomes the equivalent circuit as shown in Fig. 44. For example, for frequency f_1 , signal at frequency f_1 is blocked by the first resonator f_1 and the initial proposed structure (Fig. 43) becomes a transmission line (Fig. 44 (a)). For frequency f_2 , because the signal at frequency f_2 can go through the first resonator and be blocked at the second resonator f_2 , our proposed multiband Pi-shaped structure (Fig. 43) transforms to the Pi-shaped line with characteristic impedance Z_2 and length l_2 (Fig. 44 (b)). Finally, the same operation is repeated for frequency f_n ($n \geq 2$), the first stub is combined to the $(n-1)^{\text{th}}$ stub to be considered as one combined open-circuit stub (Fig. 44 (c)) which has the characteristic impedance Z_2 and length $(l_2+l_3+\dots+l_n)$.

According to equation (1.17), for the proposed multiband Pi-shaped structure at frequency f_n ($n \geq 2$), the equivalent circuit (Fig. 44 (c)) with the symmetrical structure $(l_2+l_3+\dots+l_n, Z_2)$ at both ends of the line l_1 corresponds to the matrix below:

$$\begin{bmatrix} A_n & B_n \\ C_n & D_n \end{bmatrix} = \begin{bmatrix} 1 & 0 \\ jY_2 \tan \beta_n (l_2 + l_3 + \dots + l_n) & 1 \end{bmatrix} \begin{bmatrix} \cos \beta_n l_1 & jZ_1 \sin \beta_n l_1 \\ jY_1 \sin \beta_n l_1 & \cos \beta_n l_1 \end{bmatrix} \cdot \begin{bmatrix} 1 & 0 \\ jY_2 \tan \beta_n (l_2 + l_3 + \dots + l_n) & 1 \end{bmatrix} \quad (1.42)$$

where $\beta_n = \frac{2\pi}{\lambda_n}$, $Z_1 = 70.7 \Omega$, $l_1 = \frac{\lambda_1}{4}$.

λ_1 is the wavelength of frequency f_1 and λ_n is the wavelength of frequency f_n .

For frequency f_n , according to equation (1.13), ABCD matrix of a quarter wavelength transmission line can be expressed as:

$$\begin{bmatrix} A_n & B_n \\ C_n & D_n \end{bmatrix} = \begin{bmatrix} 0 & jZ_{0n} \\ jY_{0n} & 0 \end{bmatrix} \quad (1.43)$$

where Z_{0n} is the characteristic impedance of the quarter wavelength transmission line at frequency f_n .

Ideally the equivalent length of the proposed Pi-shaped circuit should be $\lambda_n/4$ at frequency f_n . To do that, we equalize the equations (1.42) and (1.43). We can deduce:

$$\begin{aligned} A_n &= \cos \beta_n l_1 - Y_2 Z_1 \tan \beta_n (l_2 + l_3 + \dots + l_n) \sin \beta_n l_1 = 0 \\ \Rightarrow Z_1 \tan \beta_n l_1 &= Z_2 \cot \beta_n (l_2 + l_3 + \dots + l_n) \end{aligned} \quad (1.44)$$

$$\begin{aligned} B_n &= jZ_1 \sin \beta_n l_1 = jZ_{0n} \\ \Rightarrow Z_{0n} &= Z_1 \sin \beta_n l_1 \end{aligned} \quad (1.45)$$

$$\begin{aligned} C_n &= jY_2 \tan \beta_n (l_2 + l_3 + \dots + l_n) \cos \beta_n l_1 + jY_1 \sin \beta_n l_1 \\ &\quad - jY_2 Y_2 Z_1 \tan \beta_n (l_2 + l_3 + \dots + l_n) \tan \beta_n (l_2 + l_3 + \dots + l_n) \sin \beta_n l_1 \\ &\quad + jY_2 \tan \beta_n (l_2 + l_3 + \dots + l_n) \cos \beta_n l_1 = jY_{0n} \end{aligned} \quad (1.46)$$

$$\begin{aligned} D_n &= \cos \beta_n l_1 - Y_2 Z_1 \tan \beta_n (l_2 + l_3 + \dots + l_n) \sin \beta_n l_1 = 0 \\ \Rightarrow Z_1 \tan \beta_n l_1 &= Z_2 \cot \beta_n (l_2 + l_3 + \dots + l_n) \end{aligned} \quad (1.47)$$

where

$$\beta_n = \frac{2\pi}{\lambda_n}, \quad Z_1 = 70.7 \text{ Ohm}, \quad l_1 = \frac{\lambda_1}{4}.$$

We can deduce:

$$\Rightarrow Z_1 \tan \beta_n l_1 = Z_2 \cot \beta_n (l_2 + l_3 + \dots + l_n) \quad (1.48)$$

$$\Rightarrow Z_{0n} = Z_1 \sin \beta_n l_1 \quad (1.49)$$

where $\beta_n = \frac{2\pi}{\lambda_n}$, $Z_1 = 70.7 \text{ Ohm}$, $l_1 = \frac{\lambda_1}{4}$.

In equation (1.48), by giving $Z_2 = R \text{ Ohm}$, we can calculate the shunt open-circuited stub length $(l_2 + l_3 + \dots + l_n)$ ($n \geq 2$). To satisfy $Z_{0n} = 70.7 \text{ Ohm}$, we can make a trade-off with Z_1 to obtain the best performance of multiband operation by using equation (1.49).

1.2.6 New dual-band Wilkinson power divider (Wang *et al.*, 2011 a)

In this section, we propose a new dual-band Wilkinson power divider using the proposed dual-band Pi-shaped quarter wavelength structure with lumped component resonators. It has been published by me in (Wang *et al.*, 2011 a). This proposed dual-band Wilkinson power divider structure is based on the prototype of the conventional Wilkinson power divider working at higher frequency f_1 (3.6 GHz). In order to work simultaneously at lower frequency f_2 (2.5 GHz) as well, we add open-circuited stubs connected with resonators on the initial Wilkinson power divider. Further, one of the open-circuited stubs can be shared with its adjacent Pi-shaped circuit and all of the open-circuited stubs are putted inside the proposed dual-band Wilkinson power divider to minimize the design space.

The proposed topology of the dual-band Wilkinson power divider is shown in Fig. 45. We make the parallel resonators embedded in Pi-shaped microstrip line. The principle of dual-band Pi-shaped structure has been discussed in section 1.2.5 (c.1). As shown in Fig. 40, the Pi-shaped structure with resonators will transfer to the equivalent circuit of Fig. 40 (a) and (b) at frequency f_1 and f_2 , respectively. The two equivalent circuits of Fig. 40 (a) and (b) are equal to the quarter wavelength transmission line at frequency f_1 and f_2 , respectively.

So by using the Pi-shaped structure with resonators in Wilkinson power divider, it will become the quarter wavelength transmission line at each operating frequency. So the concurrent dual-band Wilkinson power divider is realized.

In the design, we use the measurement model of Modelithics Ins. The models of capacitor and inductor of Modelithics include the parasite effect of components because it is a measurement model. As discussed in Section 1.2.5 (a) and (b), the comparison between ideal models and Modelithics models has been shown.

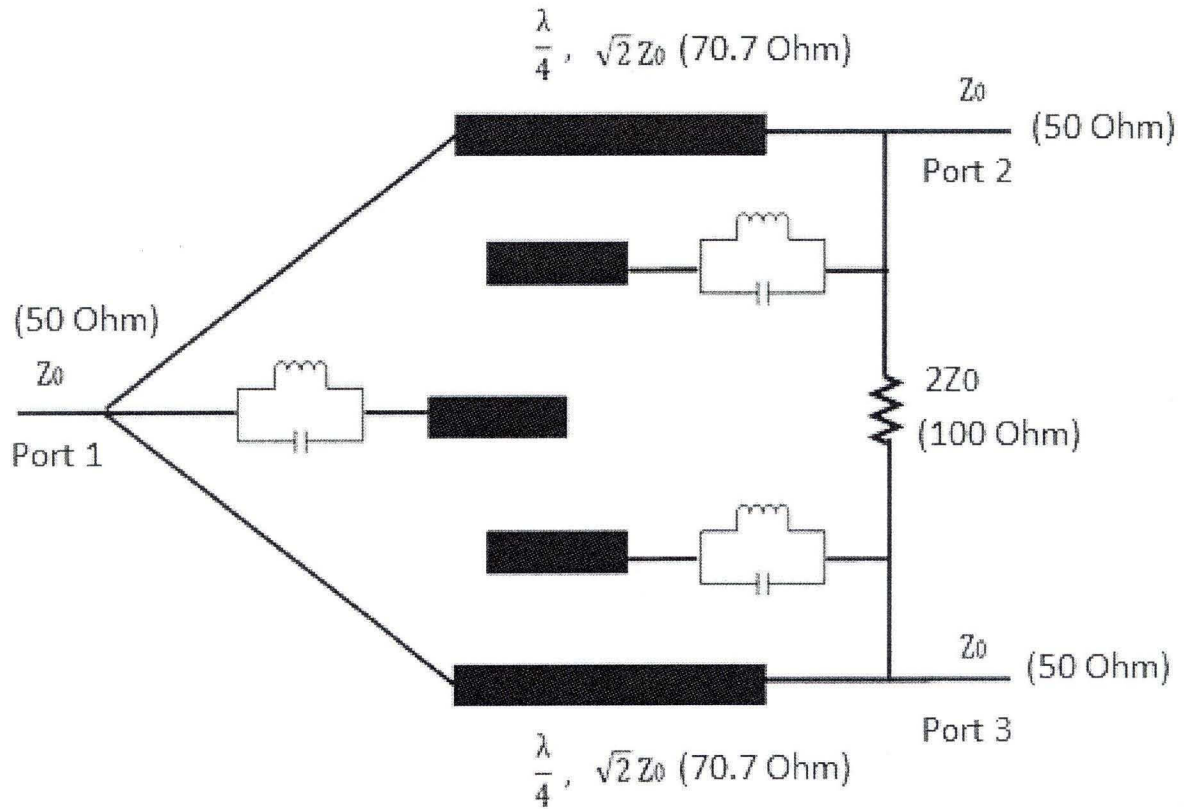


Figure 45: Proposed topology of dual-band Wilkinson power divider

a) ADS design of dual-band Pi-shaped structure

Taking 2.5 GHz and 3.6 GHz as the two operation frequencies for example, the dual-band Pi-shaped structure design schematic diagram in ADS is shown in Fig. 46.

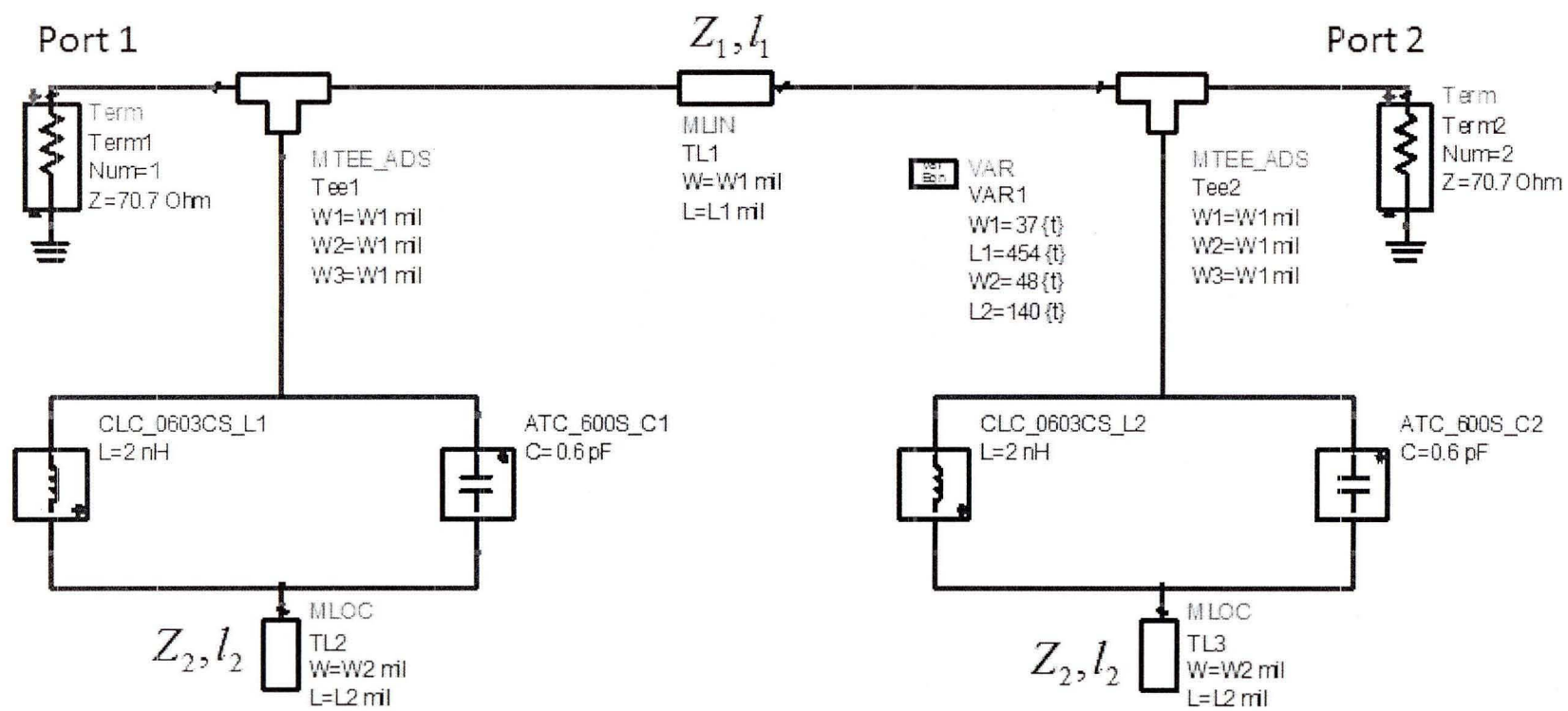


Figure 46: The designed schematic diagram of dual-band Pi-shaped structure

In Fig. 46, we set the reference impedance in ADS of the two ports in each end of the proposed dual-band Pi-shaped structure to 70.7 Ohm. The reference impedance of this dual-band Pi-shaped circuit now is 70.7 Ohm instead of 50 Ohm. The resonator circuit shown in Fig. 47 is designed for blocking signal at 3.6 GHz. The capacitance of the capacitor is 0.6 pF using model ATC600S and the inductance of the inductor is 2 nH using model CLC0603CS. The simulated result of this circuit is shown in Fig. 48.

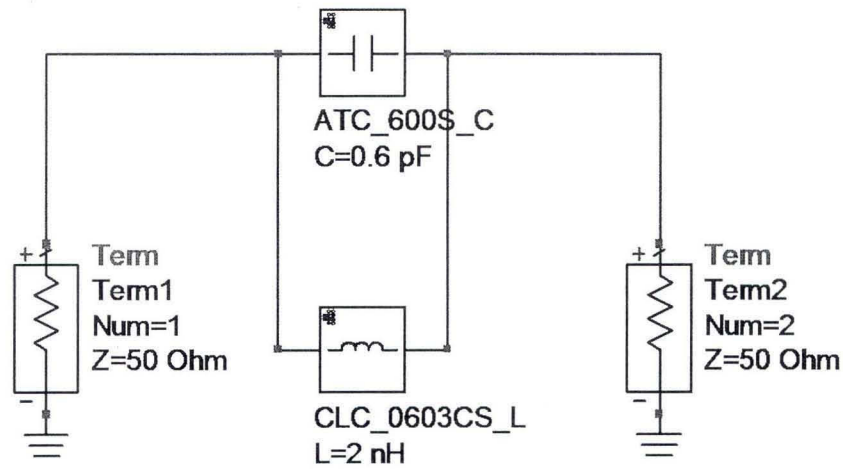


Figure 47: 3.6 GHz resonator circuit in ADS using models of Modelithics

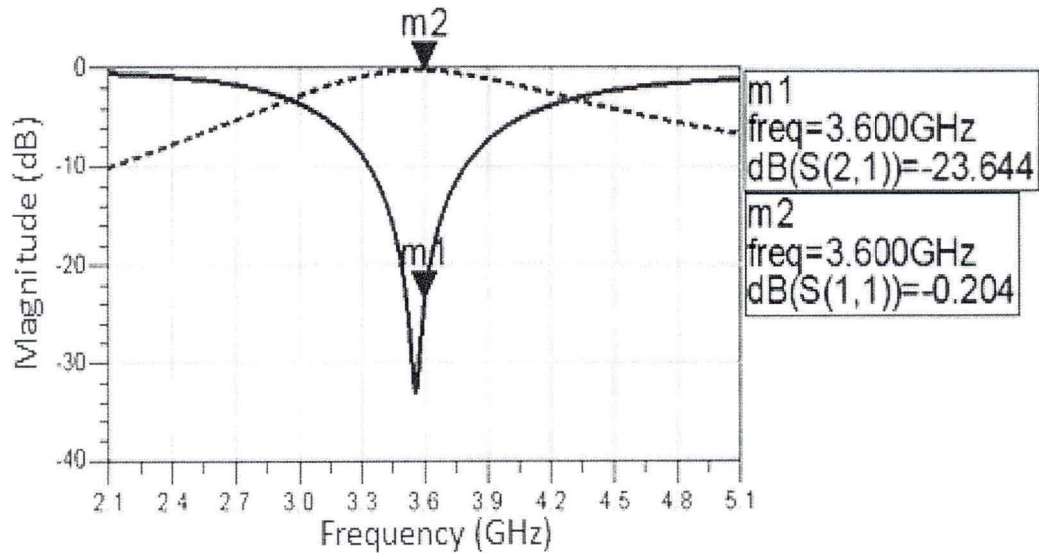


Figure 48: Simulated result of 3.6 GHz resonator circuit in ADS, solid line: insertion loss, and dot line: return loss

As Fig. 48 shows us, at 3.6 GHz, the signal is blocked effectively while the signal generated at 2.5 GHz passing through the proposed parallel resonator. With equation (1.24) and equation (1.25), we can set all the parameters as shown below:

$$\begin{aligned} f_1 &= 3.6\text{GHz}, \quad f_2 = 2.5\text{GHz}, \quad \lambda_1 = \frac{c}{f_1}, \quad \lambda_2 = \frac{c}{f_2}, \\ \beta_2 &= \frac{2\pi}{\lambda_2}, \quad Z_1 = 70.7\text{Ohm}, \quad l_1 = \frac{\lambda_1}{4}, \quad c = 3 \times 10^8. \end{aligned} \quad (1.50)$$

At 3.6 GHz, the proposed Pi-shaped structure becomes a simple series microstrip line with length l_1 and characteristic impedance Z_1 as shown in Fig. 40 (a). At 2.5 GHz, the proposed Pi-shaped structure becomes the normal Pi-shaped structure as shown in Fig. 40 (b). The normal Pi-shaped structure in Fig. 40 (b) is equal to the simple series microstrip line with electrical length $\lambda_2/4$ and impedance Z_{02} as shown in Fig. 49 (b).

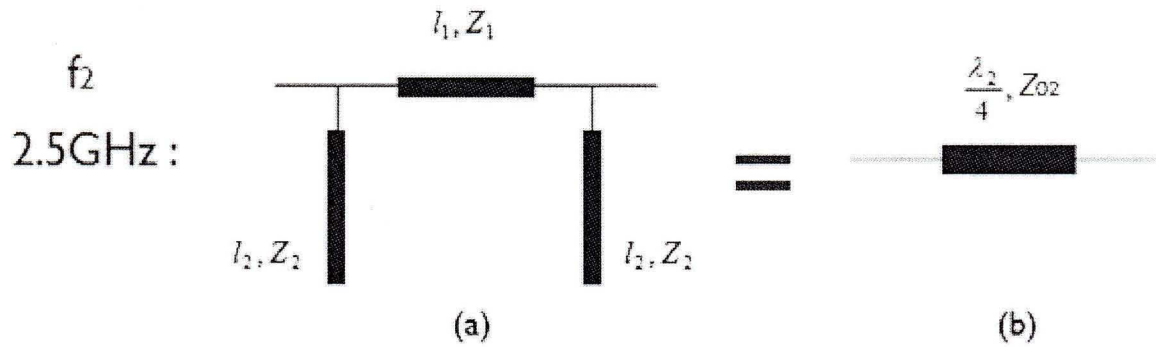


Figure 49: Equivalent circuit of Pi-shaped circuit at 2.5 GHz, (a): Pi-shaped circuit, (b): equivalent quarter wavelength microstrip line

From equation (1.25), we can calculate $Z_{02} = 62.71$ Ohm. If we want Z_{02} to be 70.7 Ohm instead of 62.71 Ohm, we should increase the value of Z_1 . The value of Z_1 is no longer 70.7 Ohm. There's a trade-off between choosing the value of Z_{02} and Z_1 .

To make the length of the whole dual-band Pi-shaped circuit as quarter wavelength at two operation frequencies 2.5 GHz and 3.6 GHz, we can tune the length of l_1 (Fig. 46) as shown in Fig. 50.

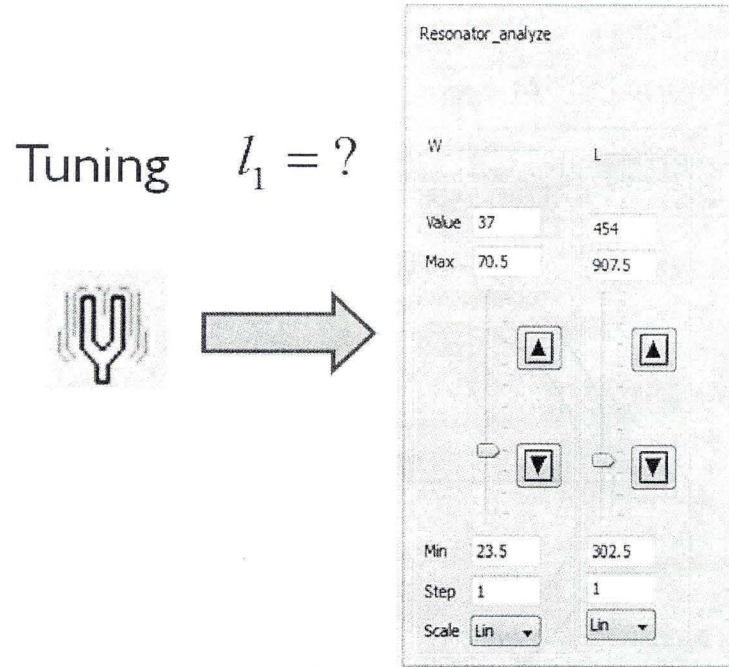


Figure 50: Tuning the length of l_1 in Fig. 46

The tuning phase simulation result of the circuit in Fig. 46 is shown in Fig. 51.

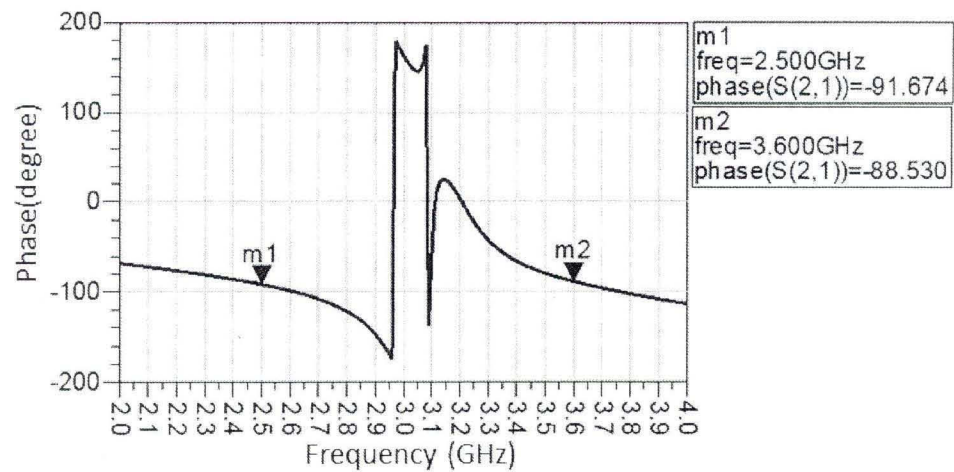


Figure 51: Simulated result of tuning the length of l_1 shown in Fig. 46

As Fig. 51 shows us, after tuning the length of l_1 , the phases of the signal generated at 2.5 GHz and 3.6 GHz are -91.67° and -88.53° , respectively. As mentioned before, to make sure the impedances at both 2.5 GHz and 3.6 GHz are 70.7 Ohm, we make a best trade-off by tuning Z_L . Here, we tune the width of the series microstrip line as shown in Fig. 46. The simulated result is shown in Fig. 52.

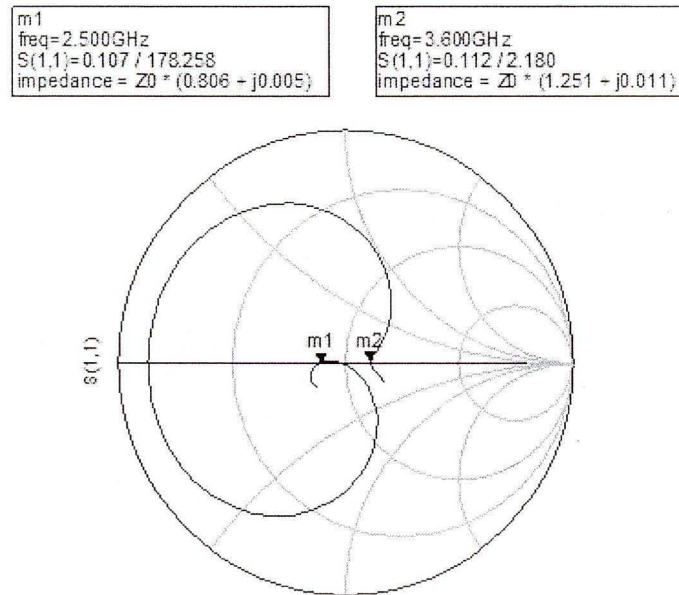


Figure 52: S_{11} simulated result of the dual-band Pi-shaped structure in Fig. 46 with characteristic impedance 70.7 Ohm

By analyzing the dual-band Pi-shaped structure shown in Fig. 46 and tuning the length and width of its series microstrip line, the lengths of the whole circuit shown in Fig. 46 at both 2.5 GHz and 3.6 GHz are near quarter wavelength. The whole characteristic impedances of the proposed dual-band Pi-shaped structure at both 2.5 GHz and 3.6 GHz are 56.98 Ohm and 88.45 Ohm, respectively. The dual-band quarter wavelength transmission line with characteristic impedance 70.7 Ohm is achieved. By equation (1.24), if we increase the value Z_2 or reduce the width of the open-circuited stub, we should increase the length of the open-circuited stub l_2 to keep equation (1.24) valid. That means thinner stub relates to longer stub length. The insertion loss and return loss of the circuit shown in Fig. 46 are shown in Fig. 53.

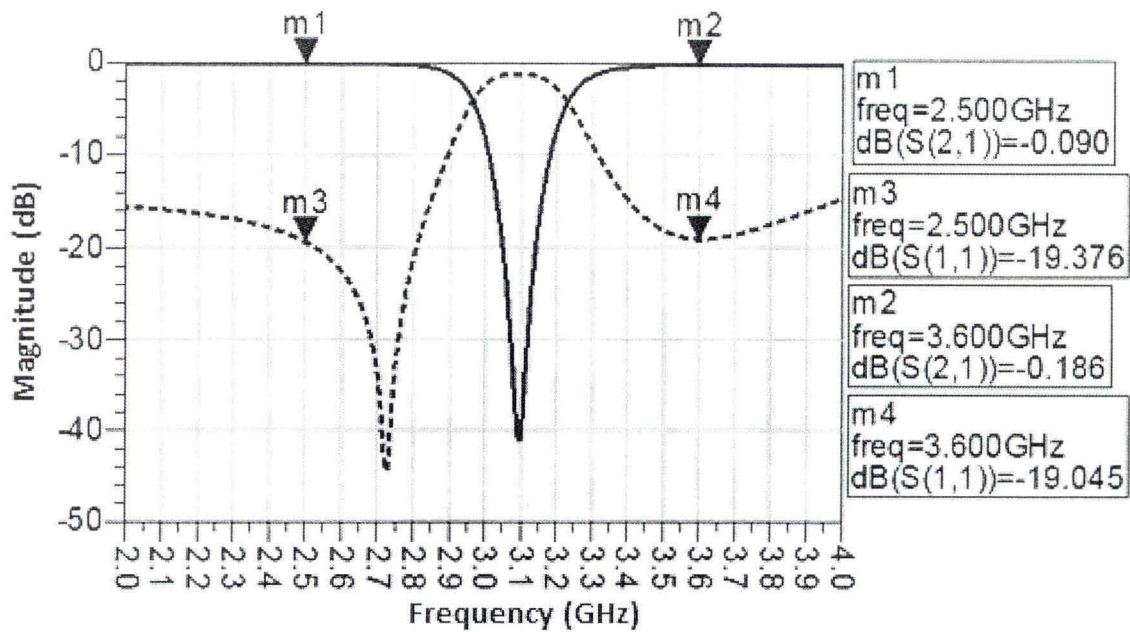


Figure 53: Simulated results of dual-band Pi-shaped structure in Fig. 46, solid line: insertion loss, and dot line: return loss

b) Dual-band Wilkinson power divider design, fabrication, and measurement

The topology of the proposed dual-band Wilkinson power divider is already shown in Fig. 45. Dual-band Pi-shaped structure is employed as dual-band quasi quarter wavelength transmission line with characteristic impedance 70.7 Ohm at both 2.5 GHz and 3.6 GHz. By combining two dual-band Pi-shaped structures together with 100 Ohm resistor, sharing the open-circuited stub with the adjacent Pi-shaped circuit, and putting all of the stubs inside the divider itself, the proposed compact dual-band Wilkinson power divider is achieved. The ADS momentum simulation circuit is shown in Fig. 54.

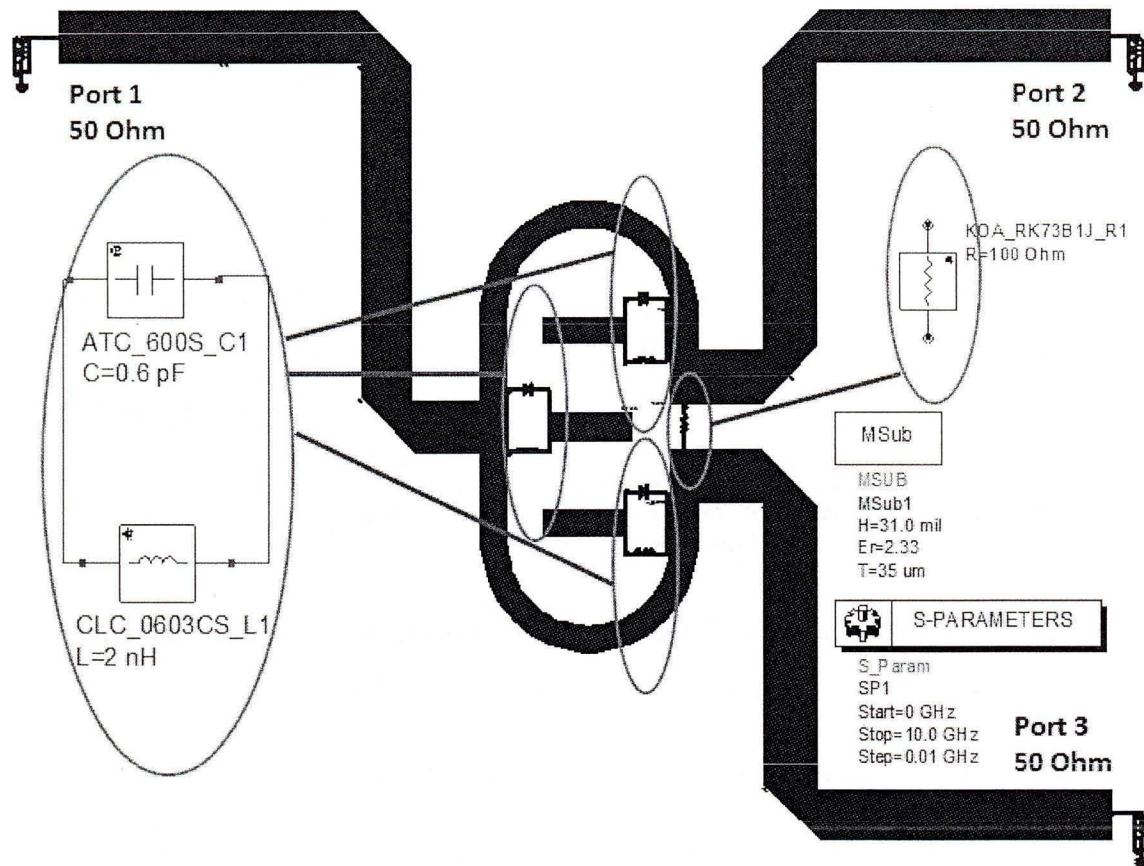


Figure 54: ADS Momentum simulation circuit of the proposed dual-band Wilkinson power divider

The fabricated circuit of the proposed dual-band Wilkinson power divider is shown in Fig. 55. The circuit is designed and fabricated on substrate RT/duroid[®] 5870 from ROGERS with dielectric constant of 2.33 and standard thickness 31 mil.

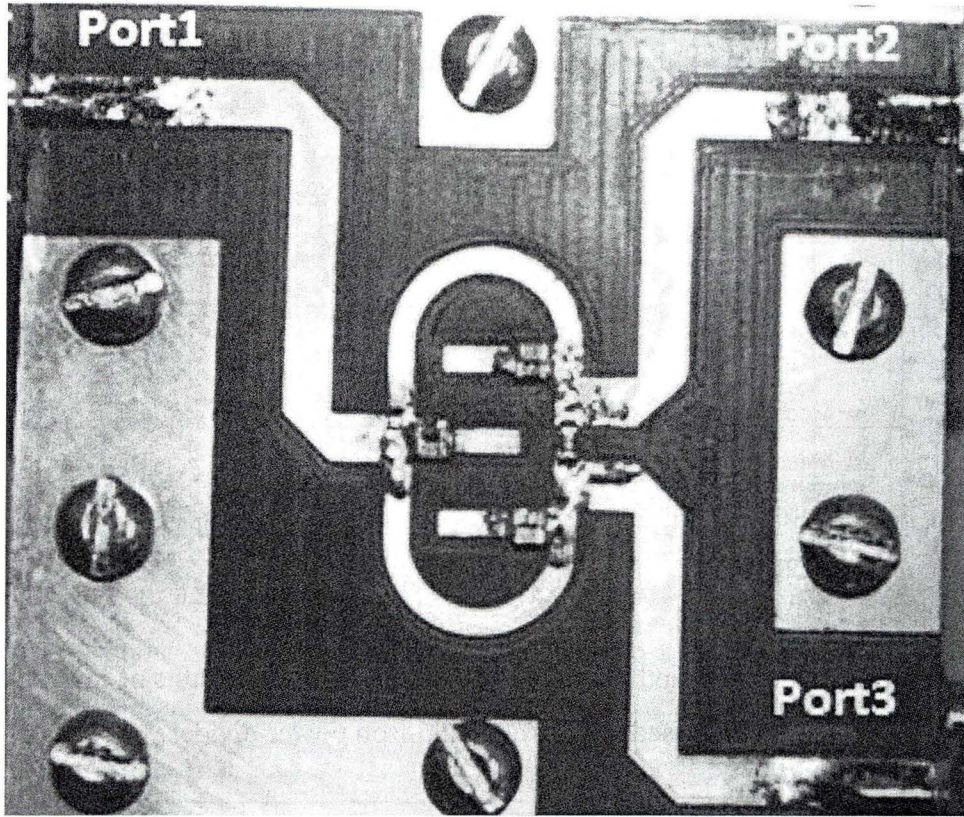


Figure 55: Fabricated circuit of the proposed dual-band Wilkinson power divider

All the results of simulation and measurement are compared in Fig. 56 to Fig. 59. Simulated results are in good agreement with measured results. Input and output return loss is less than 18.3 dB and 19.2 dB, respectively. Insertion loss is better than 3.9 dB and output isolation is less than 23.4 dB at two frequencies 2.5 GHz and 3.6 GHz. In Fig. 60, the measured phase difference between two output ports is less than 3.9° .

The measured results of the proposed dual-band Wilkinson power divider are shown in Table 1 in detail. The ideal insertion loss of S_{21} and S_{31} is -3 dB with return loss S_{11} , S_{22} , and S_{33} , and isolation S_{32} less than -10 dB. The ideal phase difference between two output ports is 0° . The design objective of the proposed dual-band Wilkinson power divider is also shown in Table 1.

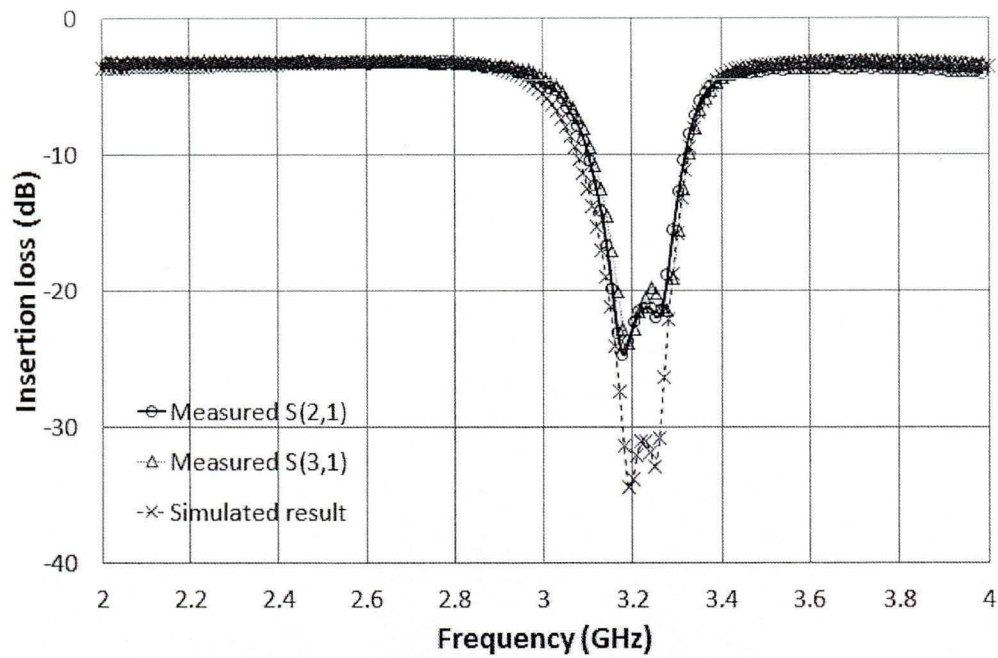


Figure 56: Simulated (cross) and measured (round and triangle) results of insertion loss of the proposed dual-band Wilkinson power divider

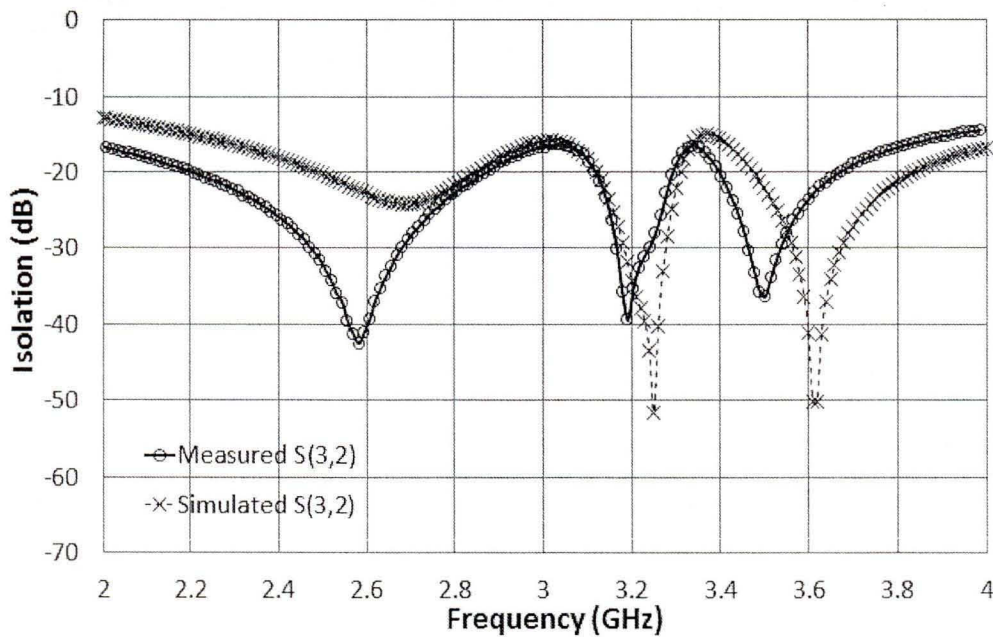


Figure 57: Simulated (cross) and measured (round) results of output port isolation of the proposed dual-band Wilkinson power divider

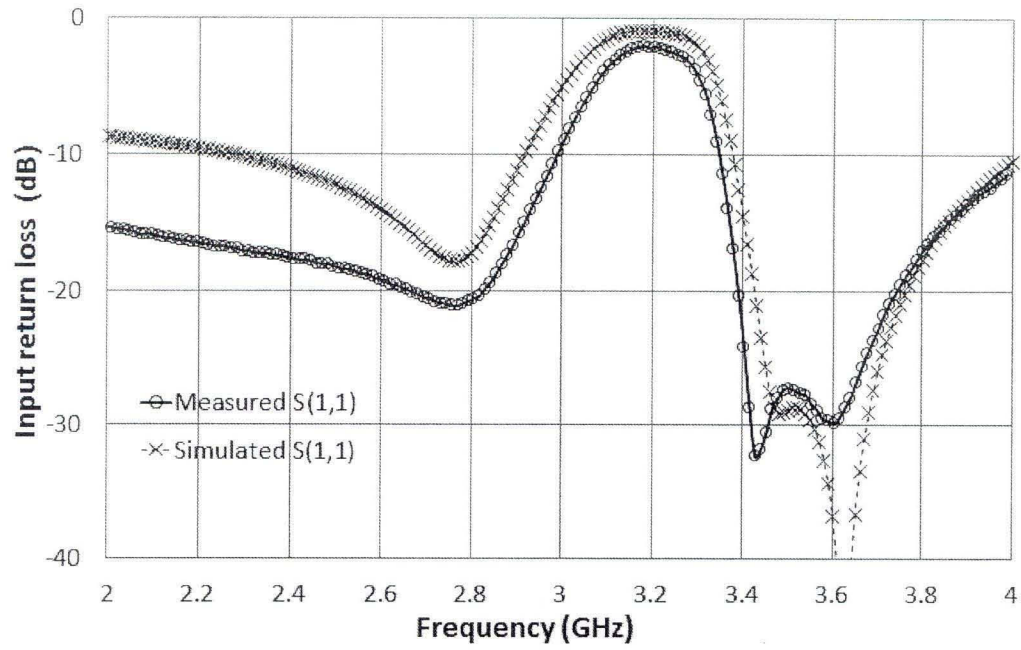


Figure 58: Simulated (cross) and measured (round) results of input return loss of the proposed dual-band Wilkinson power divider

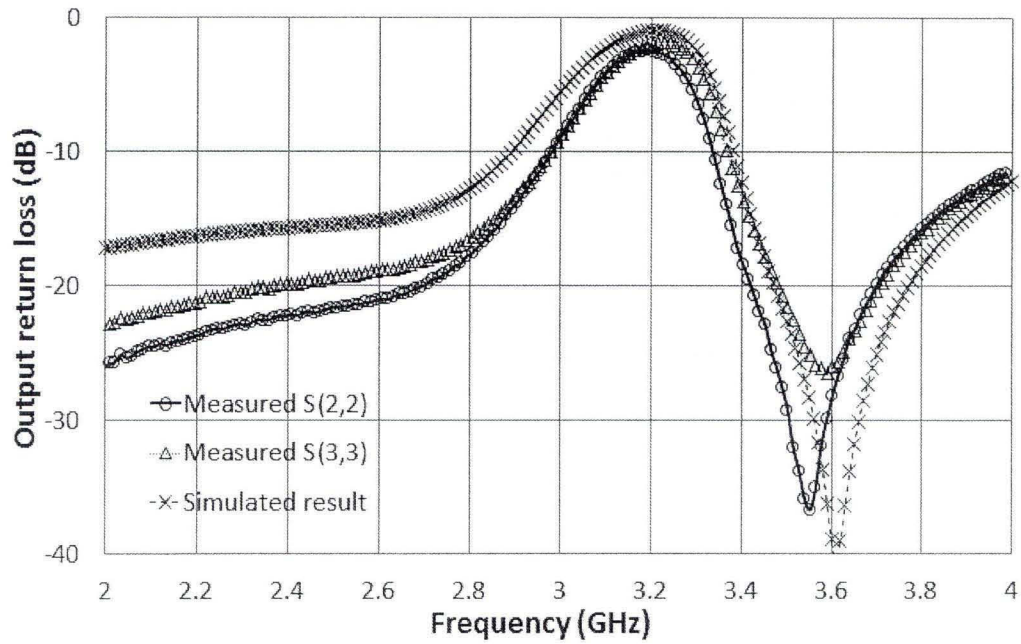


Figure 59: Simulated (cross) and measured (round and triangle) results of output return loss of the proposed dual-band Wilkinson power divider

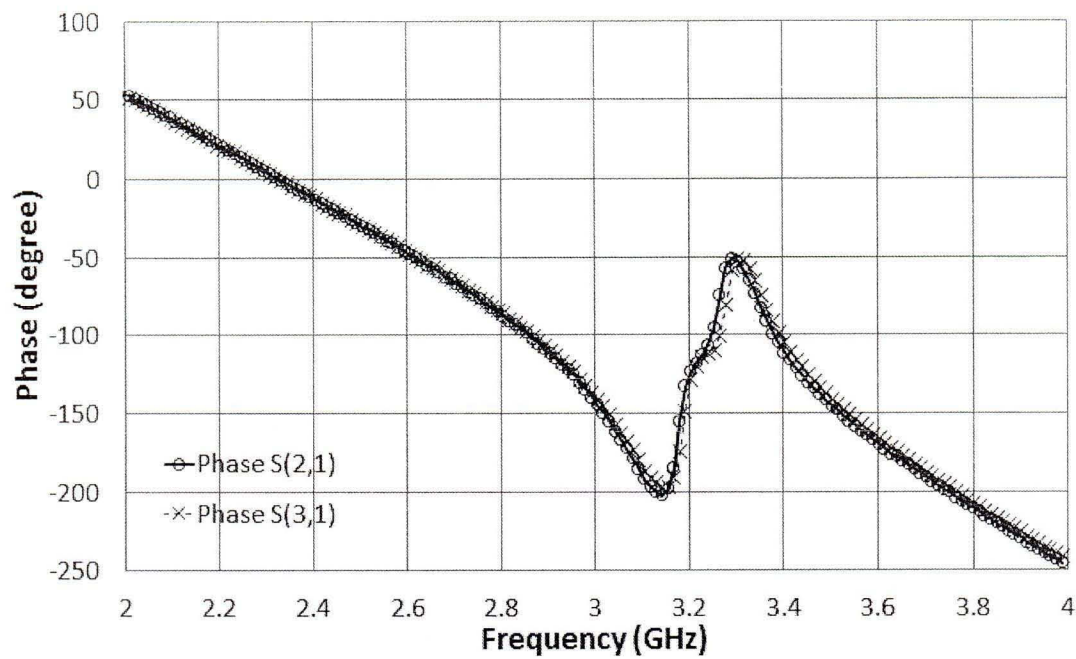


Figure 60: Measured phases of two output ports of the proposed dual-band Wilkinson power divider, round: Port 2, cross: Port3

Table 1: Measured results of the proposed dual-band Wilkinson power divider

Measured results of dual-band Wilkinson power divider							
Freq (GHz)	S ₂₁ (dB)	S ₃₁ (dB)	S ₃₂ (dB)	S ₁₁ (dB)	S ₂₂ (dB)	S ₃₃ (dB)	$\angle S_{21} - \angle S_{31}$ (°)
2.5	-3.29	-3.08	-32.97	-18.38	-21.60	-19.28	-0.47
3.6	-3.81	-3.27	-23.47	-29.91	-28.17	-25.93	-3.81
Design objective	-3	-3	<-15	<-10	<-10	<-10	0

The measured results of the dual-band Wilkinson power divider is compared with other references in Table 2.

Table 2: Comparison of the dual-band Wilkinson power divider in this work and other references

	This work		Ref. (Lee <i>et al.</i> , 2008)		Ref. (Srisathit <i>et al.</i> , 2003)		Ref. (Cheng <i>et al.</i> , 2007)	
	Frequency (GHz)		Frequency (GHz)		Frequency (GHz)		Frequency (GHz)	
	2.5	3.6	0.75	1.75	0.9	1.8	0.95	2.55
S ₂₁ (dB)	-3.29	-3.81	-3.12	-3.24	-3.40	-3.70	-3.30	-3.30
S ₃₁ (dB)	-3.08	-3.27	-3.13	-3.31	-3.40	-3.70	-3.30	-3.30
S ₃₂ (dB)	-32.97	-23.47	-20.00	-20.00	-14.50	-11.00	-25.00	-25.00
S ₁₁ (dB)	-18.38	-29.91	-24.00	-27.00	-26.10	-21.20	-22.00	-22.00
S ₂₂ (dB)	-21.60	-28.17	-20.00	-20.00	-14.20	-19.70	-22.00	-22.00
S ₃₃ (dB)	-19.28	-25.93	-20.00	-20.00	-15.80	-19.50	-22.00	-22.00
$\angle S_{21} - \angle S_{31}$ (°)	-0.47	-3.81	-	-	1.20	2.70	-	-

c) Conclusion

In this section we proposed one dual-band Wilkinson power divider employing resonators in conventional Pi-shaped structure. By analyzing the principle of the proposed dual-band Pi-shaped quarter wavelength transmission line, one dual-band Wilkinson power divider is designed, fabricated and tested to demonstrate this method. Because the proposed dual-band Wilkinson power divider is designed based on the conventional Wilkinson power divider structure at higher frequency such as 3.6 GHz, compared with lower operation frequency such as 2.5 GHz, the size of our proposed dual-band Wilkinson power divider is smaller. By sharing one open-circuited stub with the adjacent Pi-shaped circuit and putting all the open-circuited stubs inside the dual-band Wilkinson power divider, compactness of this circuit is kept efficiently. At two specific designed frequencies, measured results are in good agreement with simulated results. This design method proposed in this section can be easily applied in dual-band applications.

1.2.7 New tri-band Wilkinson power divider and new tri-band rat-race coupler (Wang *et al.*, 2012 a; Wang *et al.*, 2011 b; Wang *et al.*, 2011 c)

This section presents a new method by using multiband Pi-shaped structure with resonators to design a new tri-band Wilkinson power divider and a new tri-band rat-race coupler which have been published by me in (Wang *et al.*, 2012 a; Wang *et al.*, 2011 b; Wang *et al.*, 2011 c). We employ the conventional Wilkinson power divider and rat-race coupler structure working at higher frequency f_1 (2.5GHz) as the basic design. In order to achieve good performance at the other two frequencies, we use an open-circuited stub connected with a resonator for the middle frequency f_2 (1.5GHz) and cascade another open-circuited stub with a resonator for the lower frequency f_3 (1GHz). As shown in Fig. 42, the Pi-shaped structure with resonators will transfer to the equivalent circuit of Fig. 42 (a), (b), and (c) at frequency f_1 , f_2 , and f_3 , respectively. The proposed new topologies of the tri-band Wilkinson power divider and the tri-band rat-race coupler are shown in Fig. 61 and Fig. 62, respectively. By applying stubs with resonators in a conventional Pi-shaped structure and putting them inside the proposed tri-band Wilkinson power divider and tri-band rat-race coupler, topologies are kept compactness.

The design methods of the proposed tri-band Wilkinson power divider and tri-band rat-race coupler are analyzed by employing 2.5D EM simulator and these simulated results are in agreement with measured results.

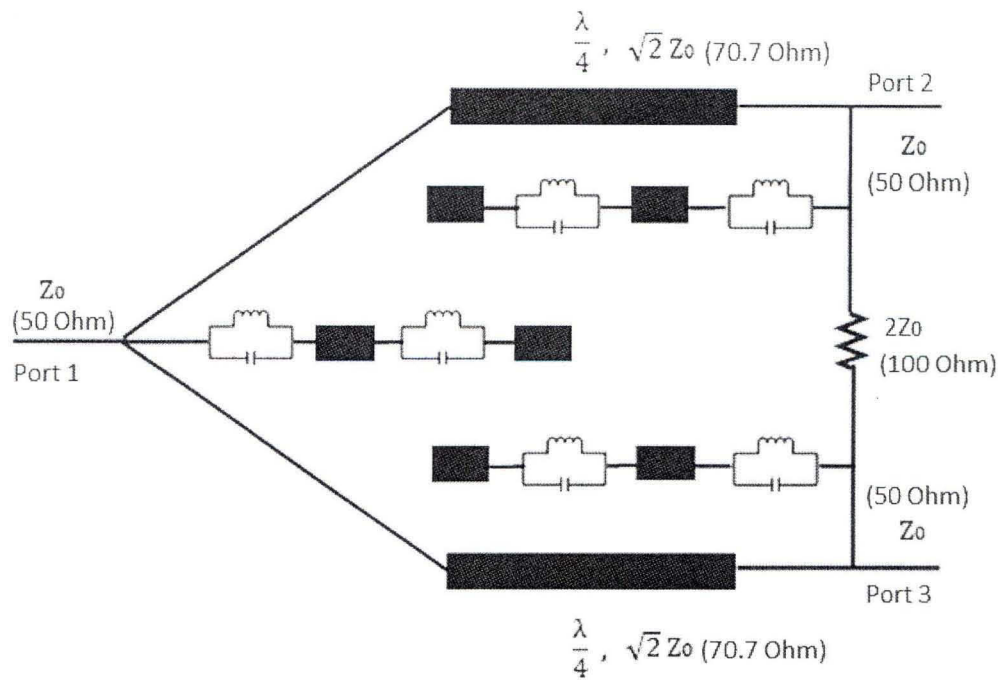


Figure 61: Proposed topology of tri-band Wilkinson power divider

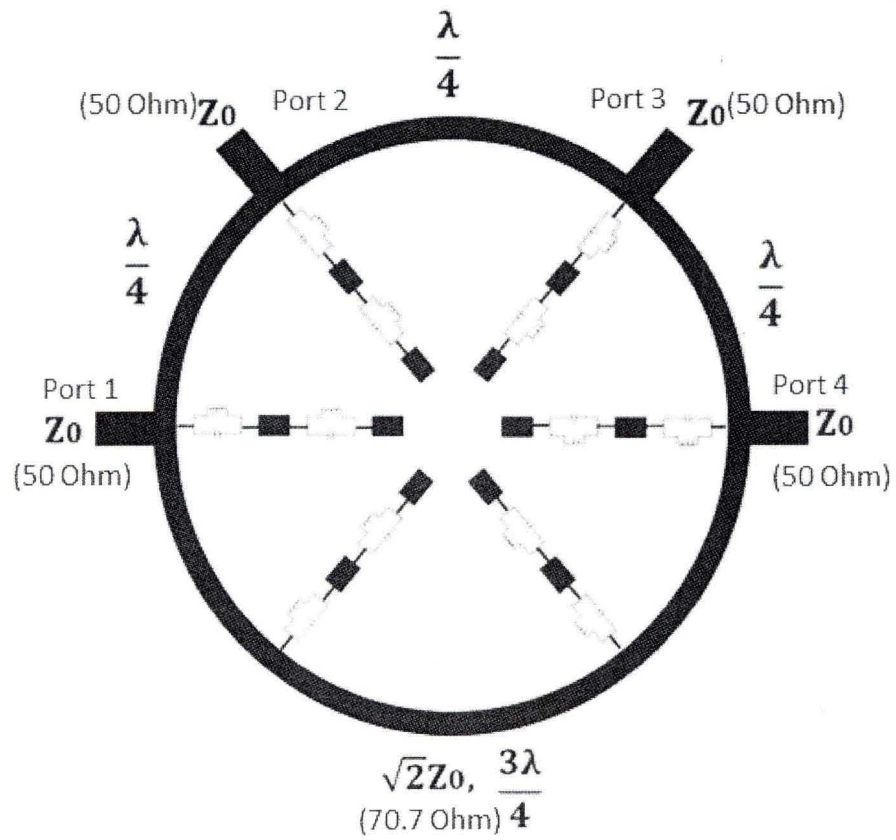


Figure 62: Proposed topology of tri-band rat-race coupler

a) ADS design of tri-band Pi-shaped structure

In this part, the three distinctive operation frequencies we choose are 1 GHz, 1.5 GHz, and 2.5 GHz. With the same analysis procedure as dual-band Pi-shaped structure explained in section 1.2.6 (a), according to equation (1.32) (1.33) (1.40) (1.41), we set:

$$\begin{aligned} f_1 = 2.5\text{GHz}, f_2 = 1.5\text{GHz}, f_3 = 1\text{GHz}, \lambda_1 = \frac{c}{f_1}, \lambda_2 = \frac{c}{f_2}, \lambda_3 = \frac{c}{f_3}, \\ \beta_2 = \frac{2\pi}{\lambda_2}, \beta_3 = \frac{2\pi}{\lambda_3}, Z_1 = 70.7\Omega, l_1 = \frac{\lambda_1}{4}, c = 3 \times 10^8. \end{aligned} \quad (1.51)$$

By calculating with the parameters above in equation (1.32) (1.33) (1.40) (1.41), we get:

$$\begin{aligned} Z_{02} &= 57.19\Omega \\ Z_{03} &= 41.56\Omega \end{aligned} \quad (1.52)$$

To satisfy the theoretical characteristic impedance 70.7 Ohm for each operation frequency, we can make a best trade-off by increasing the value of Z_l as equation (1.33) and (1.41) show us.

The designed schematic diagram of the proposed tri-band Pi-shaped structure in ADS is shown in Fig. 63. In this circuit, the reference impedance in ADS which is the impedance value at the center point of Smith chart in simulation result is 70.7 Ohm.

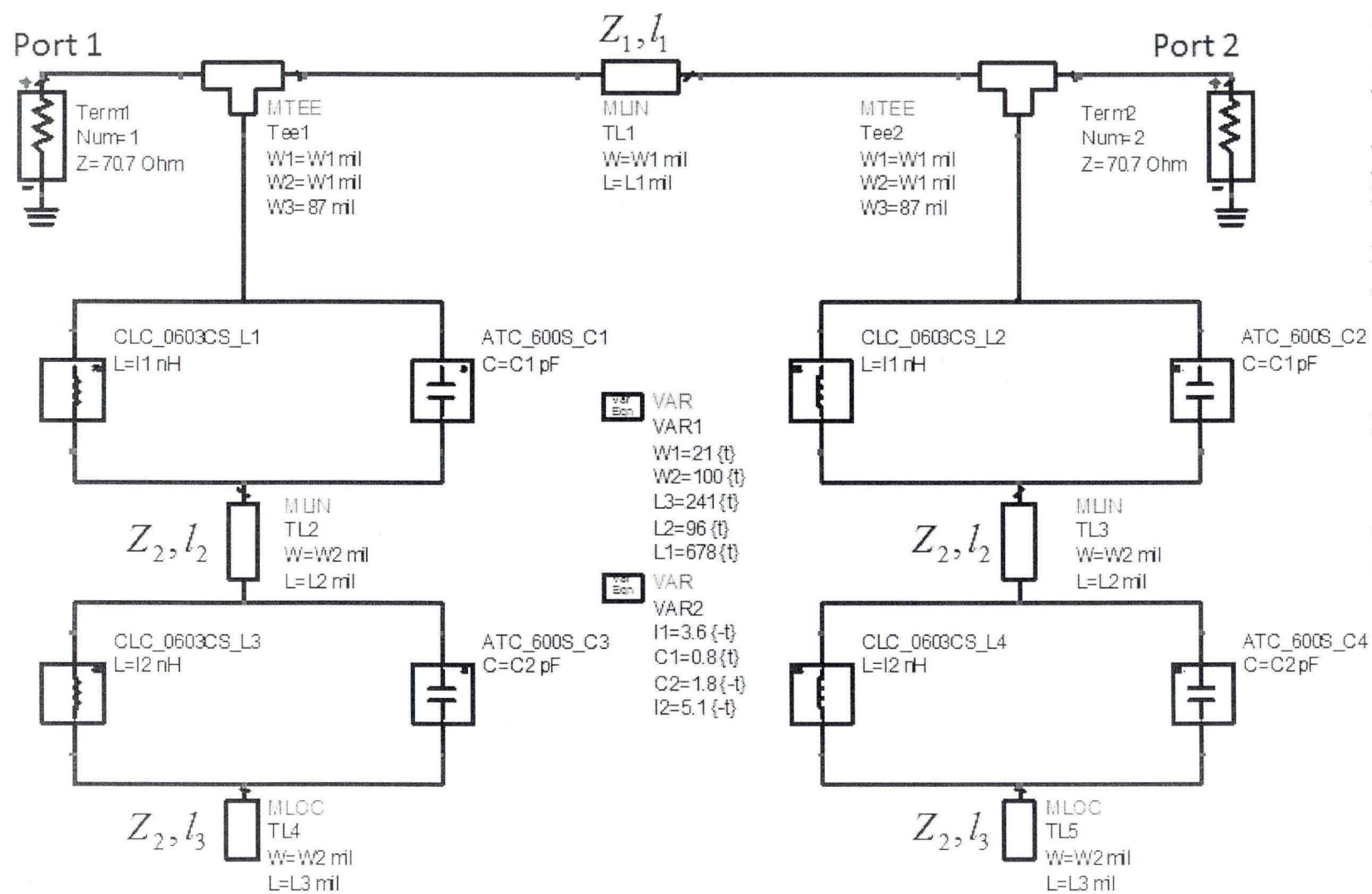


Figure 63: Designed schematic diagram of the proposed tri-band Pi-shaped structure

The capacitor and inductor models used in the design schematic diagram are the same as Fig. 30 for resonators working at 1.5 GHz and 2.5 GHz. By using Tuning tool in ADS as section 1.2.6 (a), based on calculation with equation (1.32) (1.33) (1.40) (1.41), slightly tuning the value of l_1 , l_2 , l_3 , Z_1 , and Z_2 , the simulated phase and impedance results are shown in Fig. 64 and Fig. 65, respectively.

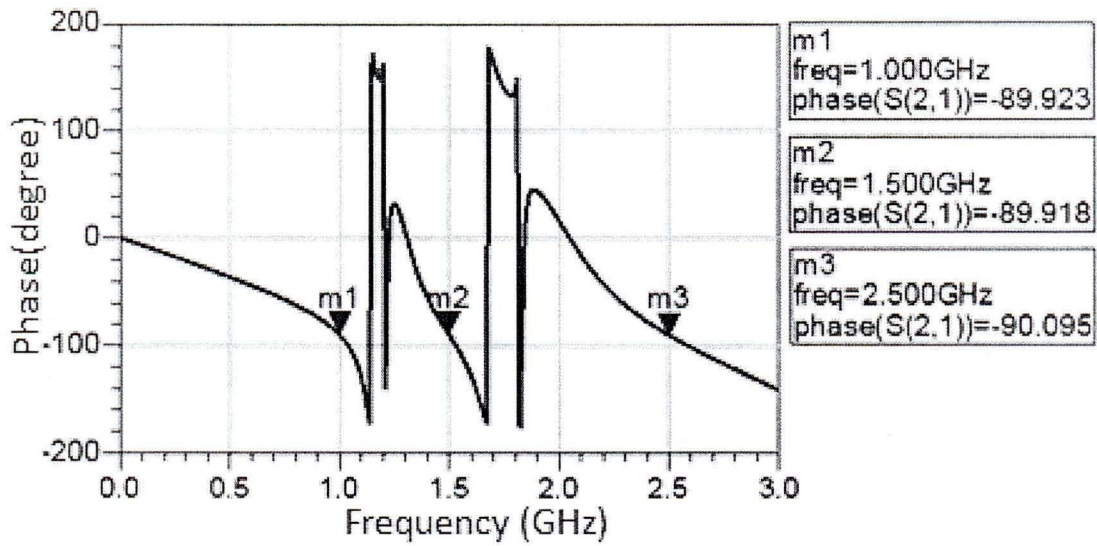


Figure 64: Phase simulated result of the proposed tri-band Pi-shaped structure

m1 freq=1.000GHz $S(1,1)=0.315 / 179.981$ impedance = $Z_0 * (0.521 + j1.195E-4)$	m2 freq=1.500GHz $S(1,1)=0.015 / 6.533$ impedance = $Z_0 * (1.030 + j0.004)$	m3 freq=2.500GHz $S(1,1)=0.316 / 0.060$ impedance = $Z_0 * (1.922 + j0.001)$
--	---	---

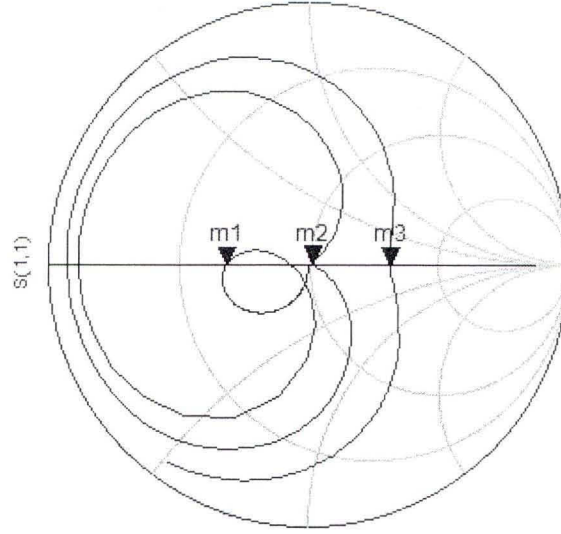


Figure 65: S_{11} simulated result of the tri-band Pi-shaped structure shown in Fig. 63 with reference impedance 70.7 Ohm in the center of Smith chart

The simulated result in Fig. 64 shows the phases of the whole proposed tri-band Pi-shaped structure are -89.92° , -89.92° , and -90.10° at 1GHz, 1.5 GHz, and 2.5 GHz, respectively. The impedances of the whole proposed tri-band Pi-shaped structure at the three operation frequencies are 36.83 Ohm at 1 GHz, 72.82 Ohm at 1.5 GHz, and 135.89 Ohm at 2.5 GHz. The simulated insertion loss and return loss results of the proposed tri-band Pi-shaped structure shown in Fig. 63 are shown in Fig. 66.

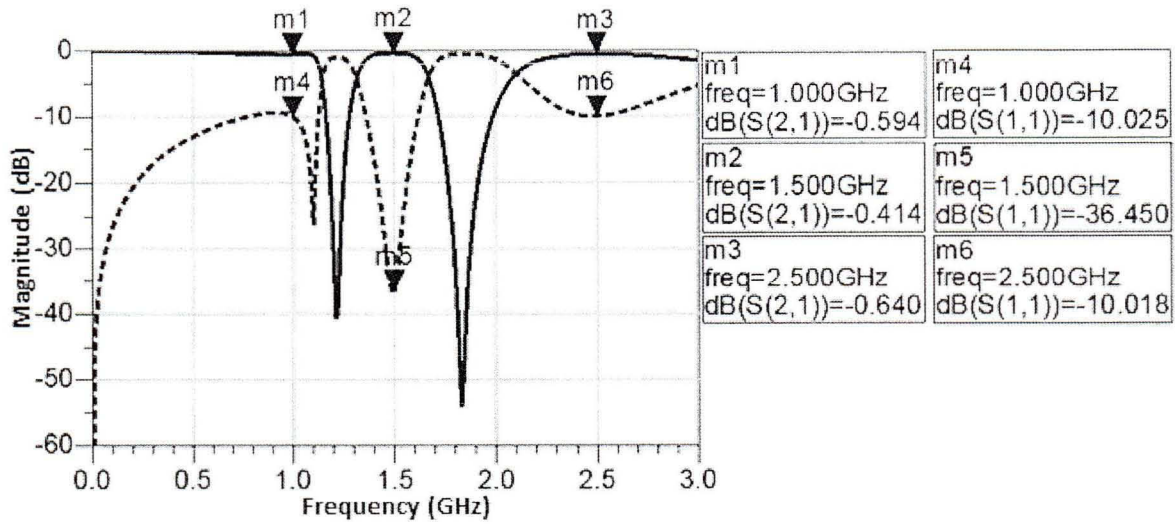


Figure 66: Simulated results of the proposed tri-band Pi-shaped structure, solid line: insertion loss, and dot line: return loss

With all the simulated results shown above, the proposed tri-band quarter wavelength transmission line with characteristic impedance 70.7 Ohm is achieved.

b) Tri-band Wilkinson power divider design, fabrication, and measurement

The quarter wavelength line is realized by arc of half circle form as most of Wilkinson power divider applications. The tri-band Wilkinson power divider structure is designed by connecting open-circuited stubs with parallel LC resonators in cascade in order to have appropriate quarter wavelength transmission line with characteristic impedance 70.7 Ohm at frequencies f_1 , f_2 and f_3 . As mentioned before, the respond of the ideal characteristic impedance 70.7 Ohm for each operation frequency band cannot be achieved at the same time. The impedance value is adjusted by tuning to approach the relative ideal case.

Combining two adjacent Pi-shaped lines as one, the number of open-circuited stub added on conventional Wilkinson power divider is reduced to three instead of four. The momentum simulation schematic diagram of the proposed tri-band Wilkinson power divider working at 1GHz, 1.5GHz, and 2.5GHz is shown in Fig. 67.

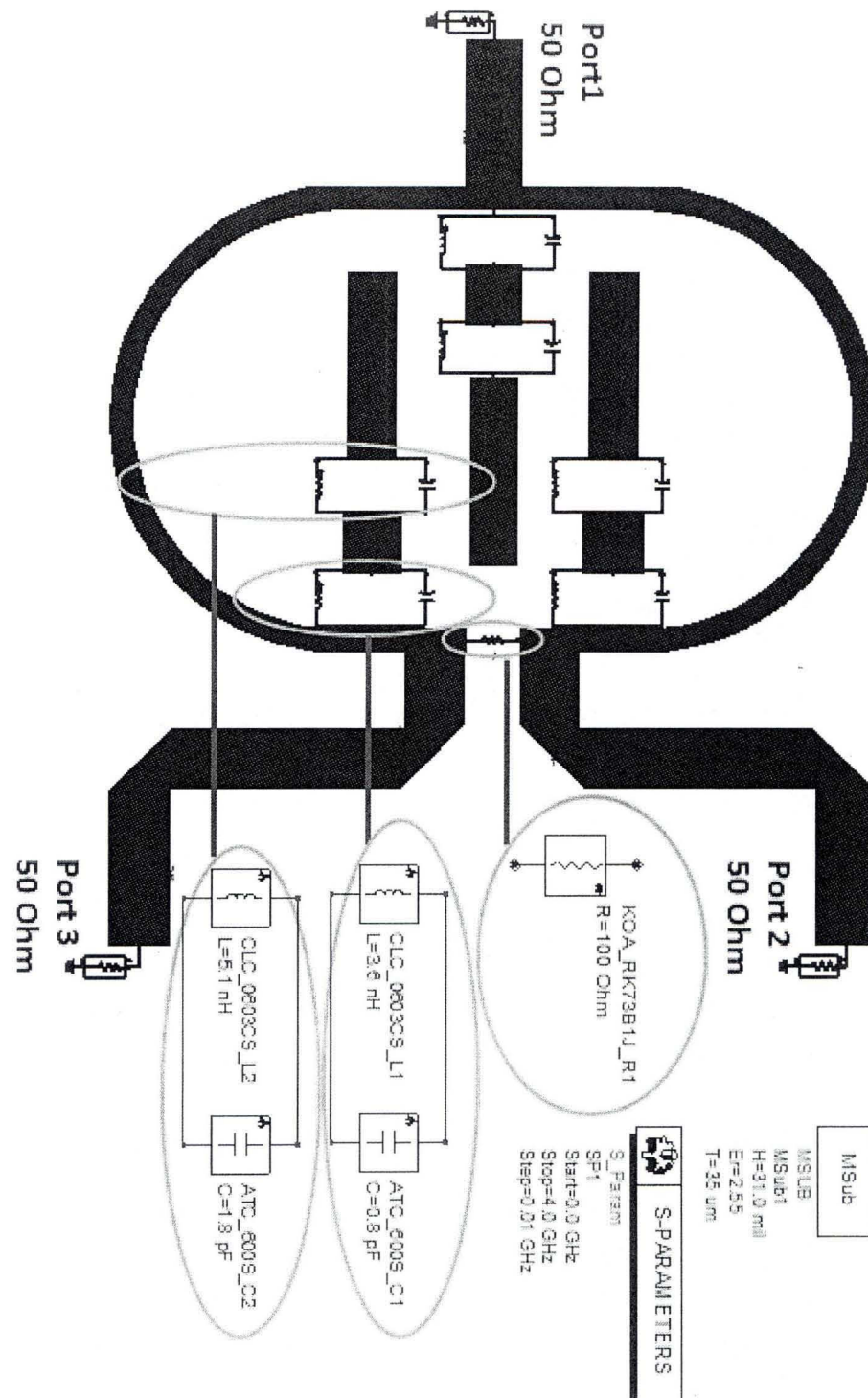


Figure 67: ADS Momentum simulation schematic diagram of the proposed tri-band Wilkinson power divider

The fabricated circuit of the proposed tri-band Wilkinson power divider is shown in Fig. 68. The circuit is designed and fabricated on substrate TLX-8 from TACONIC with dielectric constant of 2.55 and standard thickness 31 mil.

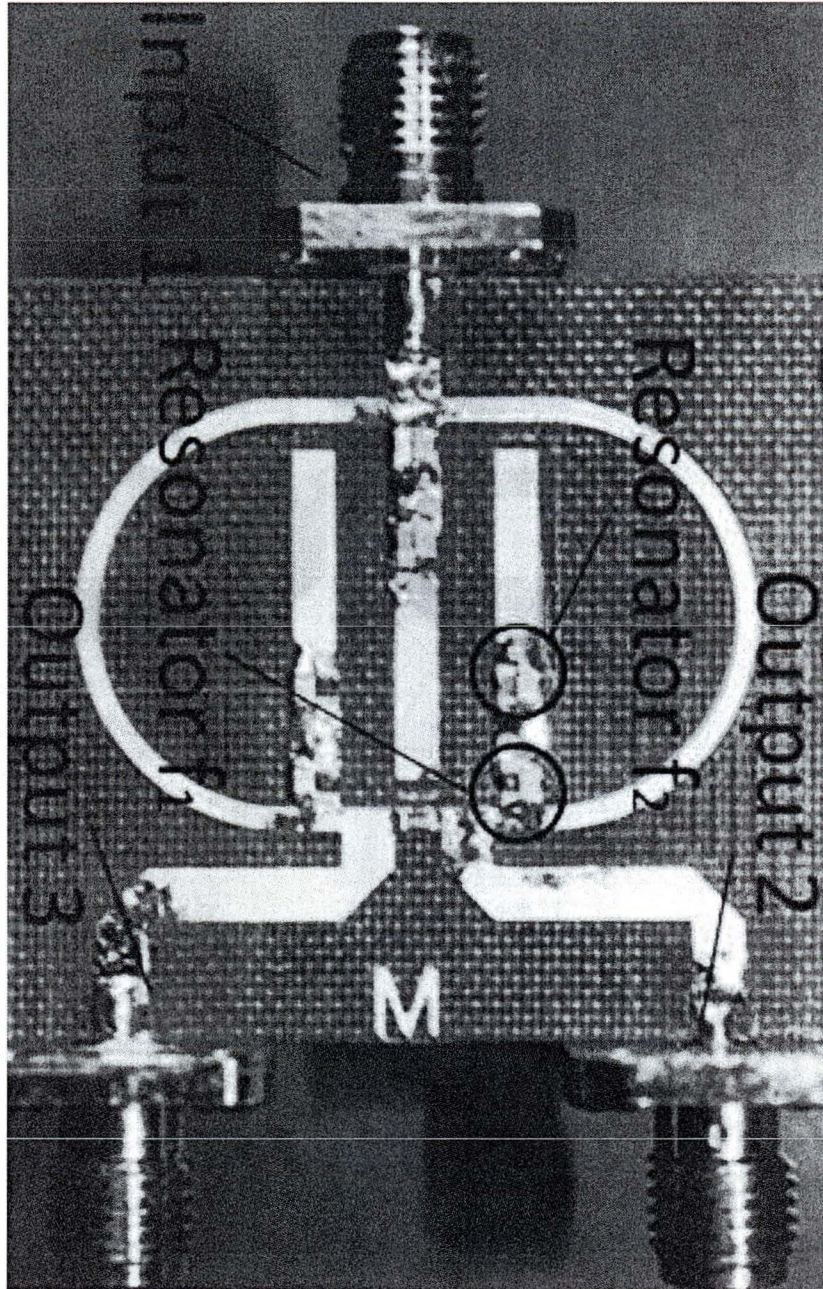


Figure 68: Fabricated circuit of the proposed tri-band Wilkinson power divider

All the results of measurement and simulation are compared in Fig. 69 to Fig. 72. Simulated results are found to be consistent with measured results. Input and output return loss is more than 12.2 dB and 13.4 dB respectively, insertion loss is better than 3.8 dB, and output isolation is better than 19.9 dB for three frequencies 1 GHz, 1.5 GHz, and 2.5 GHz. In Fig. 73, the measured phase difference between two output ports is less than 2.1° .

The measured results of the proposed tri-band Wilkinson power divider are shown in Table 3 in detail. The ideal insertion loss of S_{21} and S_{31} is -3 dB with return loss S_{11} , S_{22} , and S_{33} , and isolation S_{32} less than -10 dB. The ideal phase difference between two output ports is 0° . The design objective of the proposed tri-band Wilkinson power divider is also shown in Table 3.

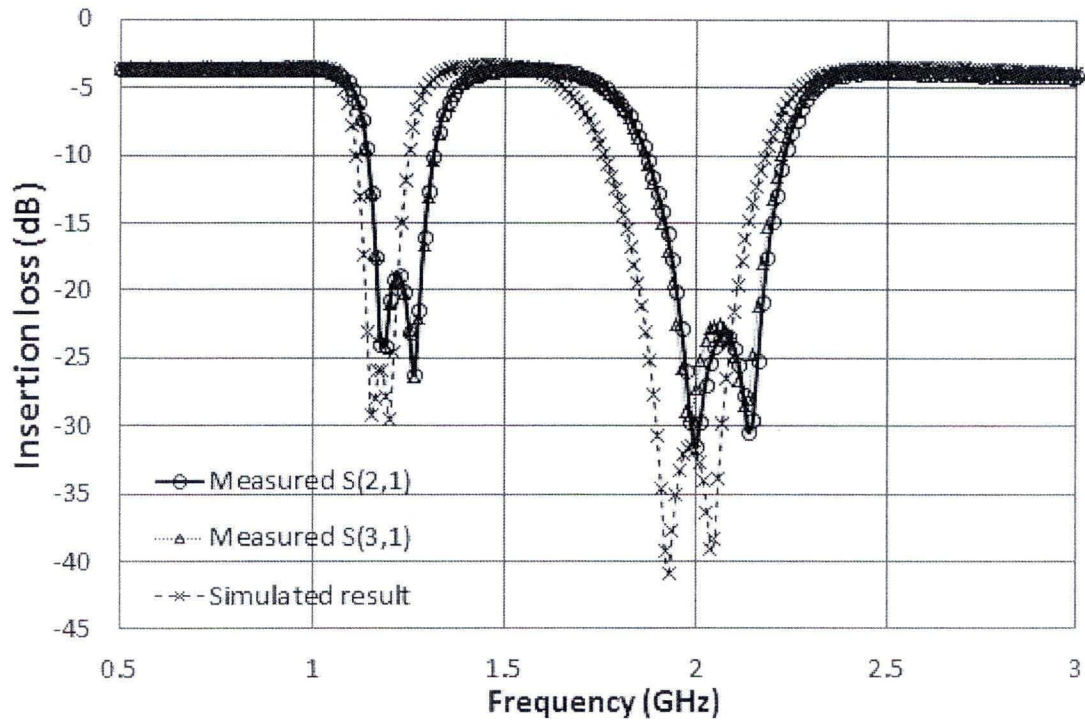


Figure 69: Simulated (cross) and measured (round and triangle) results of insertion loss of the proposed tri-band Wilkinson power divider

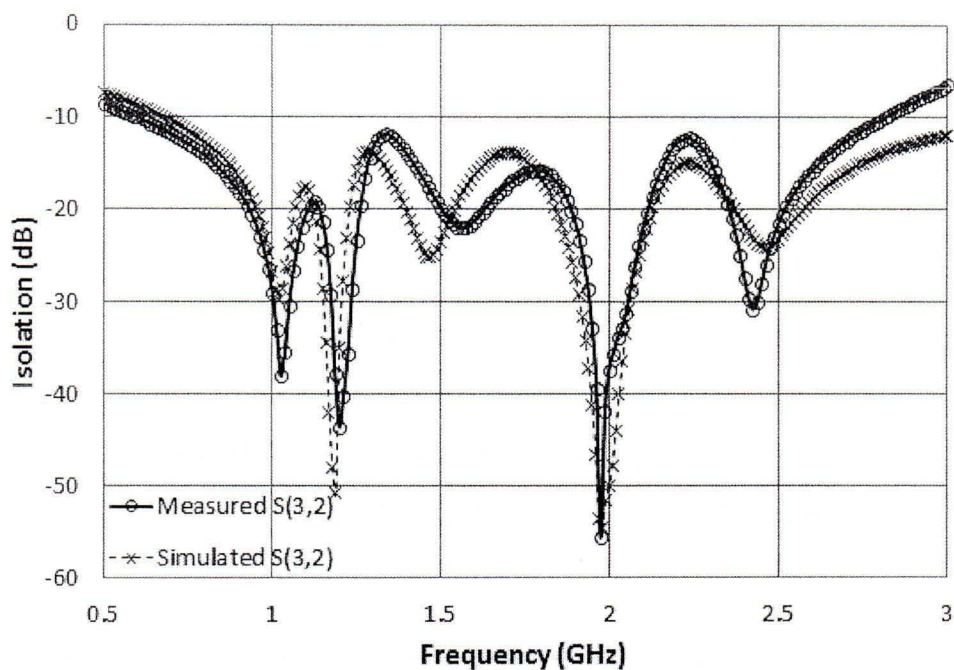


Figure 70: Simulated (cross) and measured (round) results of output port isolation of the proposed tri-band Wilkinson power divider

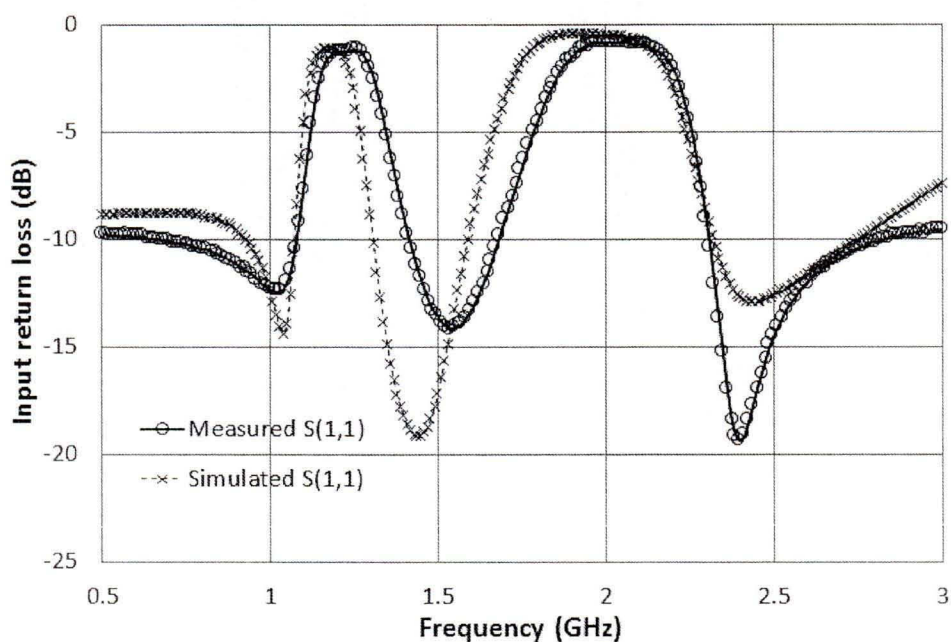


Figure 71: Simulated (cross) and measured (round) results of input return loss of the proposed tri-band Wilkinson power divider

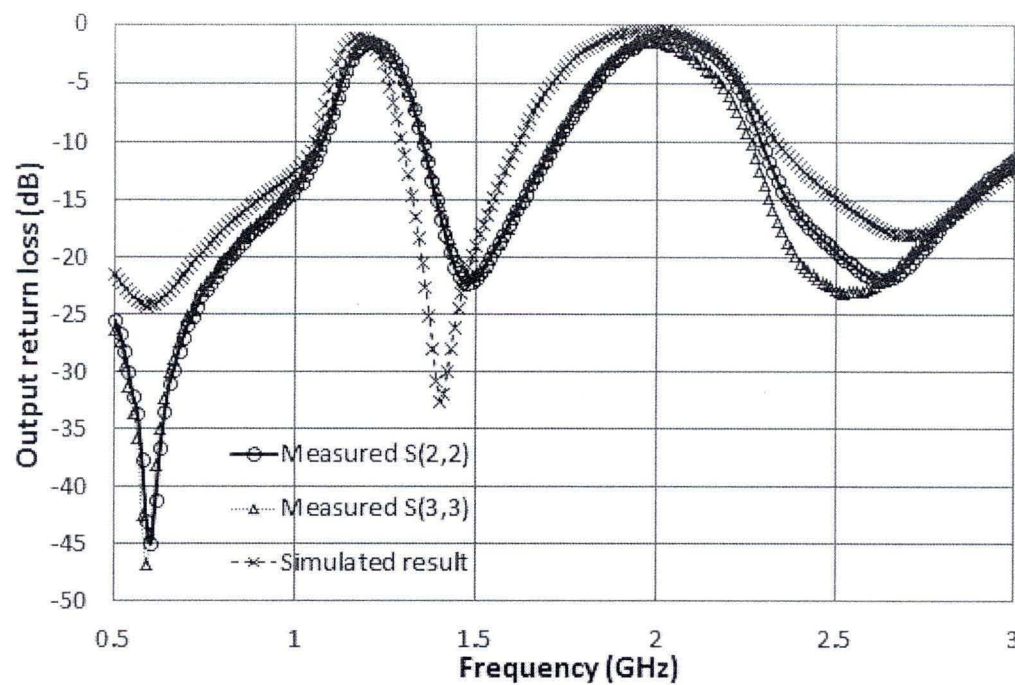


Figure 72: Simulated (cross) and measured (round and triangle) results of output return loss of the proposed tri-band Wilkinson power divider

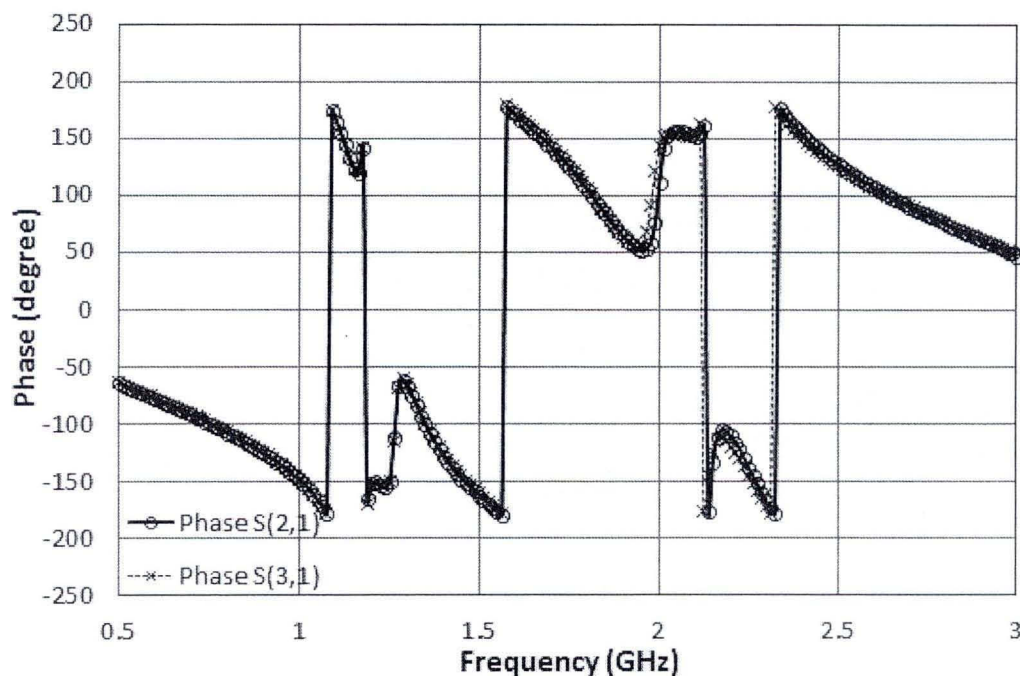


Figure 73: Measured phases of two output ports of the proposed tri-band Wilkinson power divider, round: *Port 2*, cross: *Port 3*

Table 3: Measured results of the proposed tri-band Wilkinson power divider

Measured results of tri-band Wilkinson power divider							
Freq (GHz)	S ₂₁ (dB)	S ₃₁ (dB)	S ₃₂ (dB)	S ₁₁ (dB)	S ₂₂ (dB)	S ₃₃ (dB)	$\angle S_{21} - \angle S_{31}$ (°)
1	-3.58	-3.59	-29.05	-12.29	-13.89	-13.43	-0.28
1.5	-3.64	-3.64	-19.93	-13.56	-21.82	-21.53	-2.09
2.5	-3.78	-3.74	-21.65	-14.49	-19.49	-22.78	1.65
Design objective	-3	-3	<-15	<-10	<-10	<-10	0

The tri-band Wilkinson power divider is compared with another reference as shown in Table 4. Compared with the reference (Chongcheawchamnan *et al.*, 2006), the size of the tri-band Wilkinson power divider in this work is 29 mm by 32 mm, while the size of the tri-band Wilkinson power divider presented in the reference is 31 mm by 55 mm.

Table 4: Comparison of the tri-band Wilkinson power divider and another reference

	This work			Ref. (Chongcheawchamnan <i>et al.</i> , 2006)		
	Frequency (GHz)			Frequency (GHz)		
	1	1.5	2.5	0.9	1.17	2.43
S ₂₁ (dB)	-3.58	-3.64	-3.78	-3.40	-3.40	-3.40
S ₃₁ (dB)	-3.59	-3.64	-3.74	-3.40	-3.40	-3.40
S ₃₂ (dB)	-29.05	-19.93	-21.65	-30.00	-25.00	-20.00
S ₁₁ (dB)	-12.29	-13.56	-14.49	-20.00	-20.00	-20.00
S ₂₂ (dB)	-13.89	-21.82	-19.49	-20.00	-20.00	-20.00
S ₃₃ (dB)	-13.43	-21.53	-22.78	-20.00	-20.00	-20.00
$\angle S_{21} - \angle S_{31}$ (°)	-0.28	-2.09	1.65	0.20	0.45	1.50

c) Tri-band rat-race coupler design, fabrication, and measurement

To design the tri-band rat-race coupler, we used resonators using microstrip line type inductor instead of chip inductor as mentioned in section 1.2.5 (b.2). With the circle shape of the conventional rat-race coupler, in simulation it's possible for us to use microstrip line type inductor inside the proposed tri-band rat-race coupler itself. Parasitic effect and tolerance of manufactured inductor can be avoided. We designed the tri-band rat-race coupler by using the substrate TLX-8 from TACONIC with dielectric constant 2.55 and standard thickness 31mil. The ADS momentum simulation circuit of the proposed tri-band rat-race coupler working at frequencies 1 GHz, 1.5 GHz, and 2.5 GHz is shown in Fig. 74.

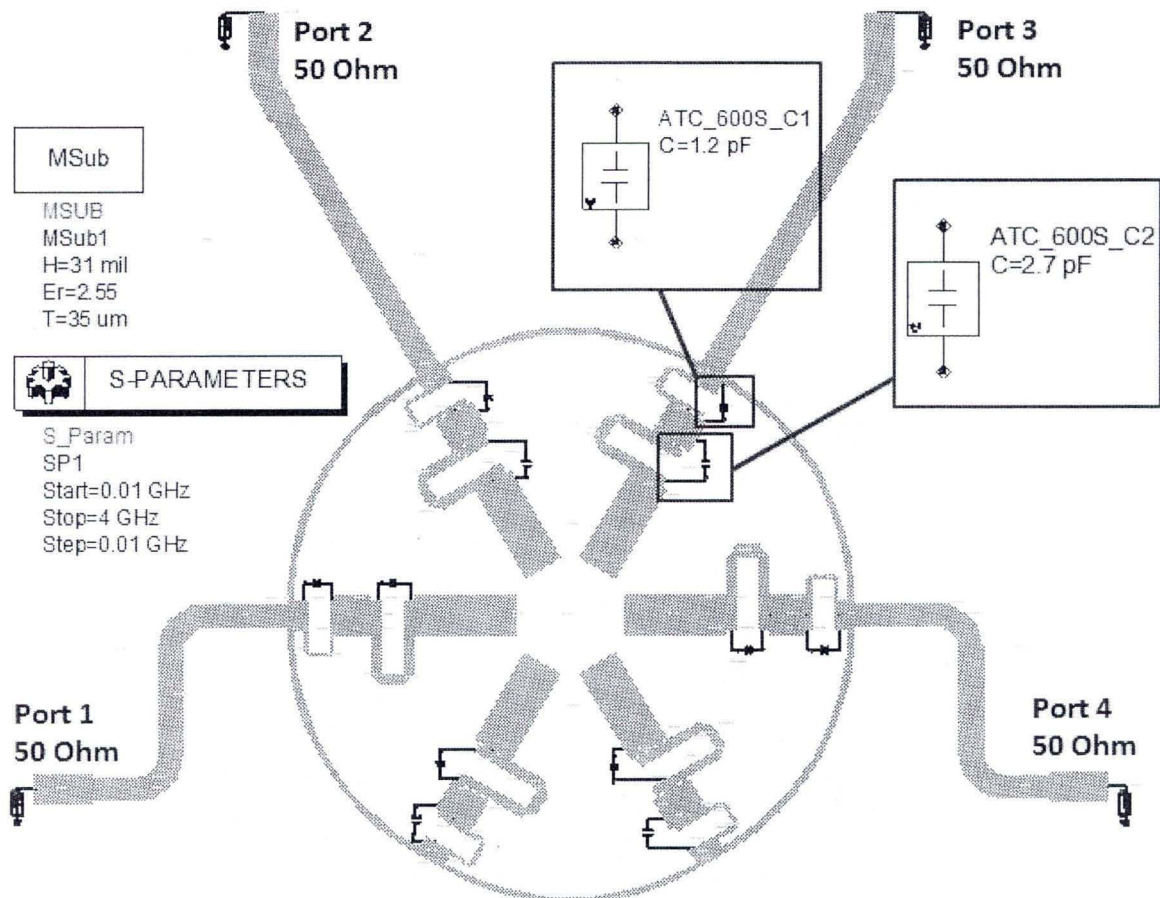


Figure 74: ADS momentum simulation circuit of the proposed tri-band rat-race coupler

By combining the open-circuited stub of two adjacent Pi-shaped lines as one, the number of these open-circuited stubs added in conventional rat-race coupler is reduced to six instead of twelve. Because our proposed structure is based on the conventional rat-race coupler for 2.5 GHz, the size of our proposed tri-band rat-race coupler is 84% smaller than conventional rat-race coupler designed for 1 GHz. The fabricated tri-band rat-race coupler is shown in Fig. 75. The measured and simulated results are compared in Fig. 76 to Fig. 82. For three frequencies (1 GHz, 1.5 GHz, and 2.5 GHz), insertion loss is better than 4 dB. The reflection coefficient is better than 10 dB and the isolation between *Port 1* and *Port 3*, *Port 2* and *Port 4* is better than 26 dB and 22dB, respectively. In phase difference $\angle S_{23} - \angle S_{43}$ is less than 2.3° . Out of phase difference $\angle S_{21} - \angle S_{41}$ is less than 183.8° .

The measured results of the proposed tri-band rat-race coupler are shown in Table 5 in detail. The ideal in phase insertion loss of S_{23} and S_{34} , and out of phase insertion loss of S_{21} and S_{41} , is -3 dB. The return loss of S_{11} , S_{22} , S_{33} , and S_{44} , and the isolation of S_{31} and S_{42} , are less than -10 dB. The ideal phase difference between in phase output ports ($\angle S_{23} - \angle S_{43}$) is 0° . The ideal phase difference between out of phase output ports ($\angle S_{21} - \angle S_{41}$) is 180° . The design objective of the proposed tri-band rat-race coupler is also shown in Table 5.

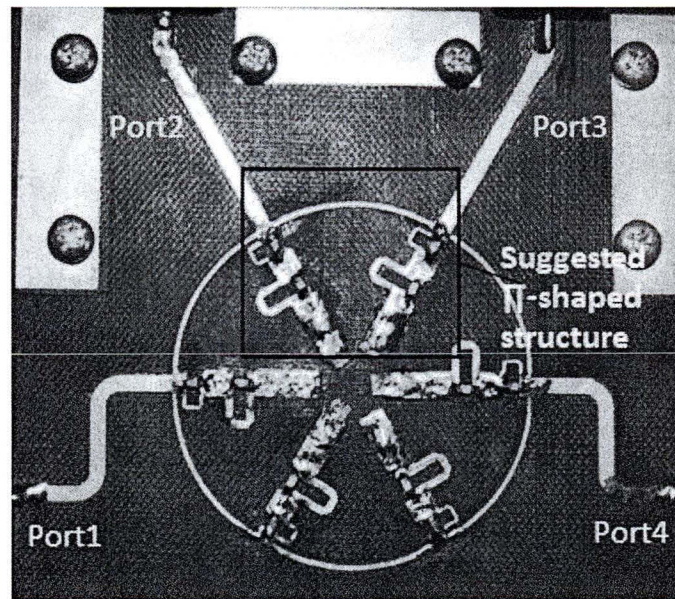


Figure 75: Fabricated circuit of the proposed tri-band rat-race coupler

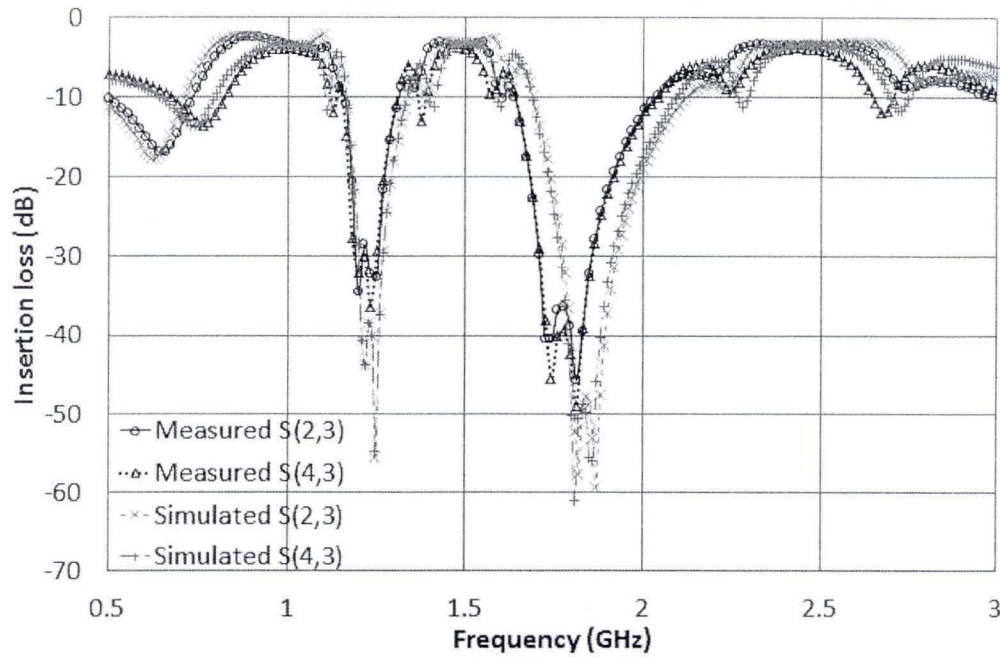


Figure 76: Simulated and measured results of insertion loss of S_{23} and S_{43} of the proposed tri-band rat-race coupler

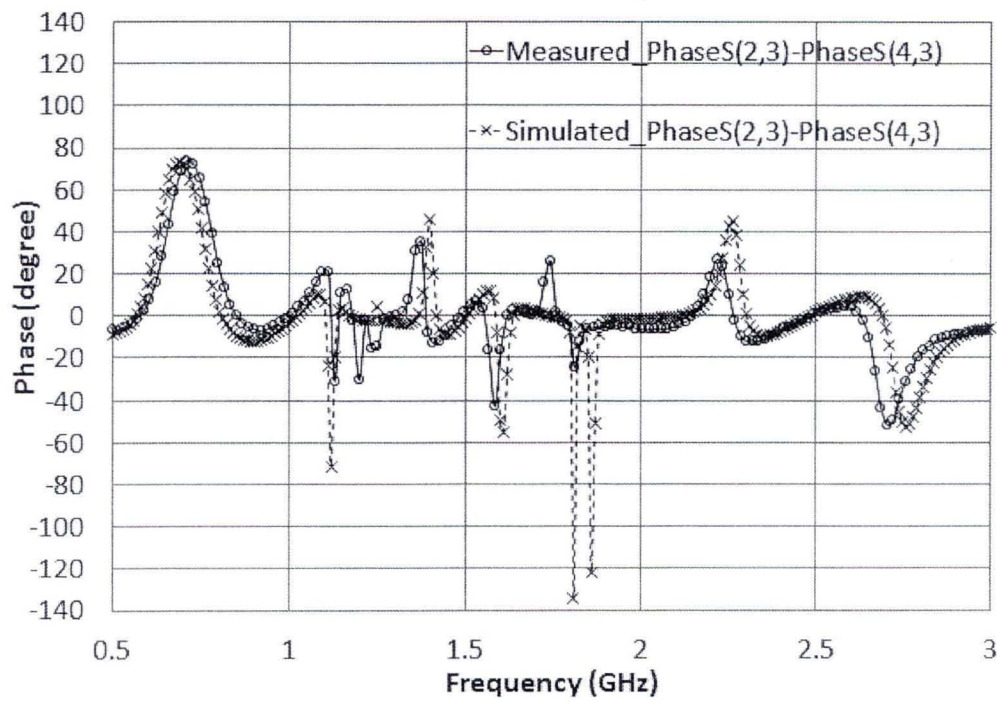


Figure 77: Simulated and measured results of $\angle S_{23} - \angle S_{43}$ of the proposed tri-band rat-race coupler

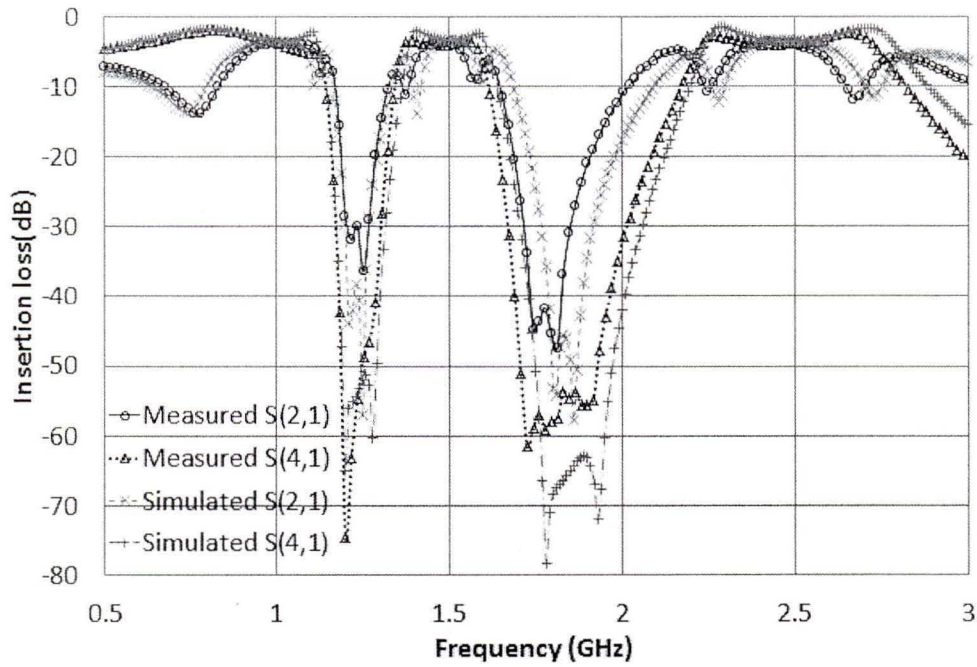


Figure 78: Simulated and measured results of insertion loss of S_{21} and S_{41} of the proposed tri-band rat-race coupler

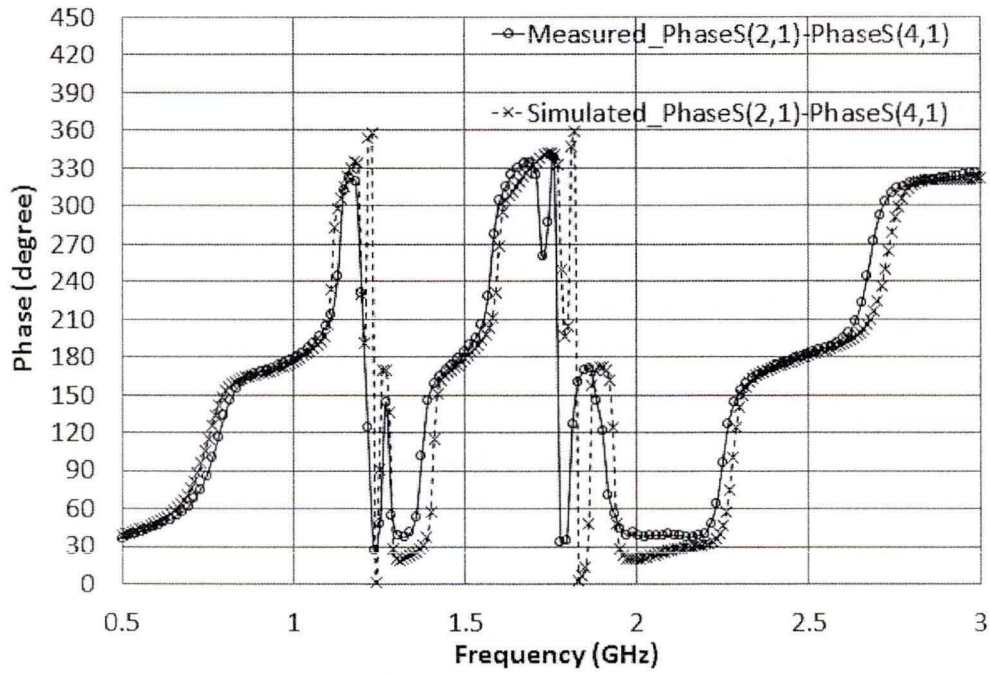


Figure 79: Simulated and measured results of $\angle S_{21} - \angle S_{41}$ of the proposed tri-band rat-race coupler

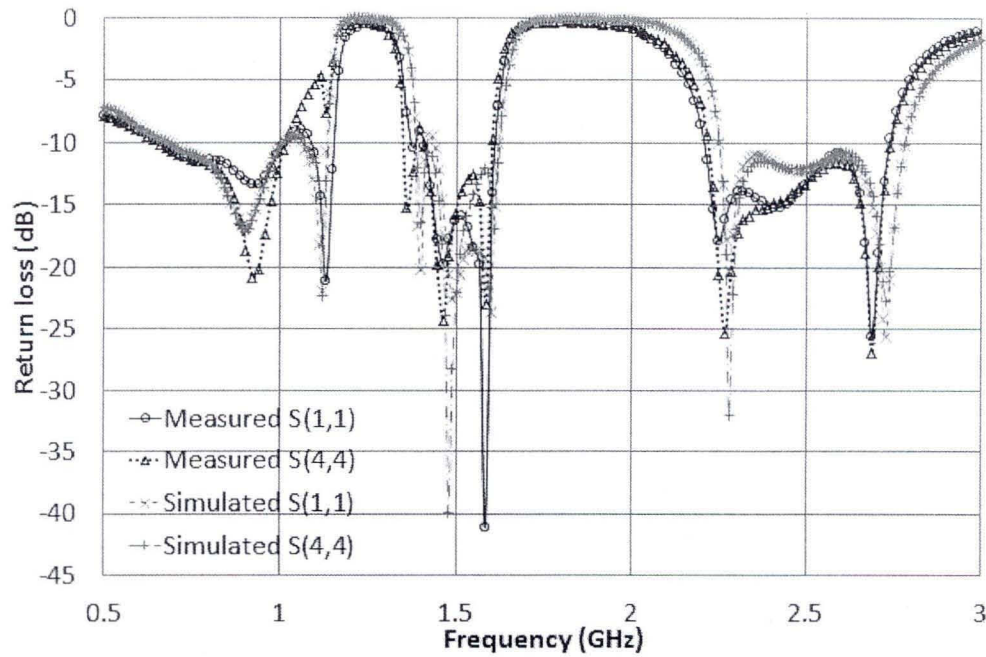


Figure 80: Simulated and measured results of return loss of *Port 1* and *Port 4* of the proposed tri-band rat-race coupler

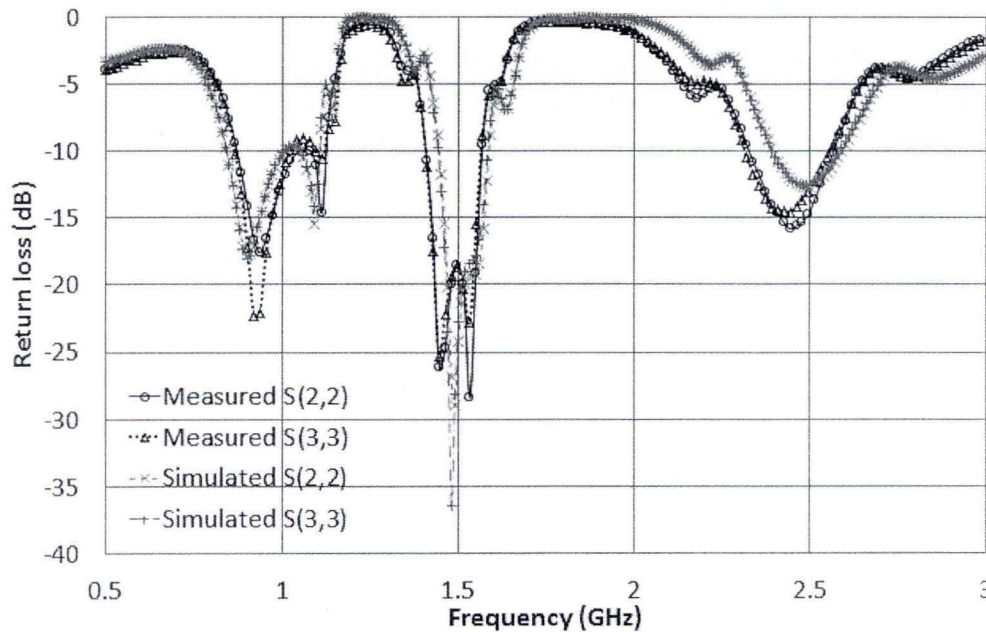


Figure 81: Simulated and measured results of return loss of *Port 2* and *Port 3* of the proposed tri-band rat-race coupler

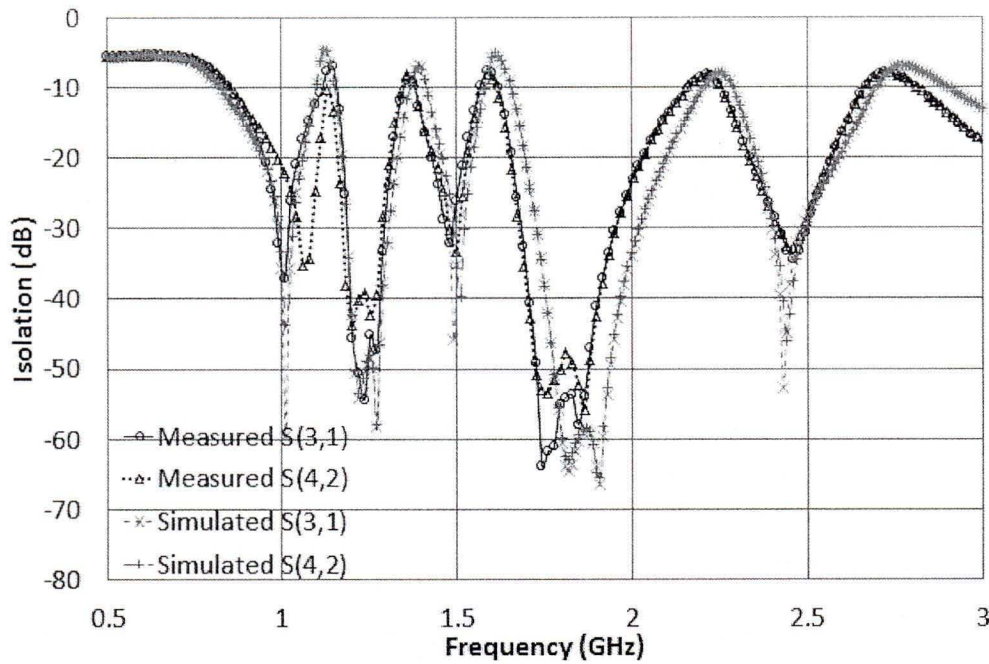


Figure 82: Simulated and measured results of isolation of S_{31} and S_{42} of the proposed tri-band rat-race coupler

Table 5: Measured results of the proposed tri-band rat-race coupler

Measured results of tri-band rat-race coupler						
Freq (GHz)	S_{23} (dB)	S_{43} (dB)	$\angle S_{23} - \angle S_{43}$ (°)	S_{21} (dB)	S_{41} (dB)	$\angle S_{21} - \angle S_{41}$ (°)
1	-3.58	-3.84	1.02	-3.77	-3.88	180.31
1.5	-3.59	-4.00	2.32	-3.87	-4.04	183.84
2.5	-3.47	-4.03	1.14	-3.92	-3.87	181.87
Design objective	-3	-3	0	-3	-3	180
Freq (GHz)	S_{11} (dB)	S_{44} (dB)	S_{22} (dB)	S_{33} (dB)	S_{31} (dB)	S_{42} (dB)
1	-10.16	-10.59	-11.77	-10.82	-37.13	-22.13
1.5	-16.23	-15.80	-18.46	-18.63	-26.09	-33.31
2.5	-13.38	-13.31	-14.75	-13.10	-30.59	-29.00
Design objective	<-10	<-10	<-10	<-10	<-15	<-15

Table 6: Comparison of the tri-band rat-race coupler and another reference

	This work			Ref. Lin <i>et al.</i> , 2004	
	Frequency (GHz)			Frequency (GHz)	
	1	1.5	2.5	1.54	3.43
$S_{21}(\text{dB})$	-3.77	-3.87	-3.92	-4.10	-3.80
$S_{41}(\text{dB})$	-3.88	-4.04	-3.87	-4.10	-4.00
$S_{11}(\text{dB})$	-10.16	-16.23	-13.38	-12.20	-22.50
$S_{42}(\text{dB})$	-22.13	-33.31	-29.00	-31.00	-32.80
$\angle S_{21} - \angle S_{41} (^\circ)$	180.31	183.84	181.87	176.20	-182.24

The tri-band rat-race coupler in this work is compared with the dual-band rat-race coupler in another reference as shown in Table 6.

d) Conclusion

A simple and compact tri-band Wilkinson power divider and tri-band rat-race coupler working at 1 GHz, 1.5 GHz and 2.5 GHz have been presented in this section. By adding four resonators in conventional Pi-shaped structure to block the signal generated at its corresponding frequency, tri-band quarter wavelength transmission line is achieved. By employing tri-band Pi-shaped circuits with resonators, one compact tri-band Wilkinson power divider and one compact tri-band rat-race coupler are designed, fabricated for 1GHz, 1.5 GHz, and 2.5 GHz to demonstrate the proposed tri-band design method. In addition, because we designed the proposed tri-band Wilkinson power divider and tri-band rat-race coupler based on the highest frequency of 2.5 GHz, comparing to 1 GHz conventional Wilkinson power divider and rat-race coupler, the size of our tri-band circuits is smaller. The excellence performance of the proposed tri-band circuits is investigated by both simulation and measurement, reasonably good agreement is seen. The tri-band design method proposed in this section can be widely applied for tri-band applications.

1.2.8 Conclusion

This chapter presents a novel multiband Pi-shaped structure. By adding resonator in conventional Pi-shaped structure to block the signal generated at its corresponding frequency, multiband quarter wavelength transmission line is achieved. Dual-band Wilkinson power divider, tri-band Wilkinson power divider, and tri-band rat-race coupler are designed and fabricated to demonstrate the proposed multiband Pi-shaped structure. The excellence performance of the proposed multiband circuits is investigated both by simulation and measurement. Simulated results are in good agreement with measured results. The multiband design method proposed in this chapter can be widely applied for multiband applications.

The contributions of this chapter are listed below:

1: An original multiband Pi-shaped quarter wavelength transmission line is presented and analyzed in section 1.2.5. It can be used in dual-band and tri-band applications of Wilkinson power divider, rat-race coupler, and PAs.

2: A new dual-band Wilkinson power divider, a new tri-band Wilkinson power divider, and a new tri-band rat-race coupler are designed, fabricated, and tested. They can be employed for dual-band and tri-band applications.

3: The method about keeping the compactness of the proposed multiband circuits is presented. The size of the proposed multiband passive components, such as dual-band Wilkinson power divider, tri-band Wilkinson power divider, and tri-band rat-race coupler, is reduced by sharing the open-circuited stub with resonators of two adjacent multiband Pi-shaped structures as one and making all open-circuited stubs with resonators inside the demonstrated multiband components themselves.

My original publications related to this chapter are listed below:

- [1] **Zhebin Wang** and Chan-Wang Park, “Multiband Pi-shaped Structure with Resonators for Tri-band Wilkinson Power Divider and Tri-band Rat-Race Coupler,” IEEE MTT-S International Microwave Symposium Digest, pp. 1-3, Montréal, Canada, 17-22 June 2012.
- [2] **Zhebin Wang**, Jae Sik Jang, and Chan-Wang Park, “Compact Dual-Band Wilkinson Power Divider Using Lumped Component Resonators and Open-Circuited Stubs,” The 12th Annual IEEE Wireless and Microwave Technology (WAMI) Conference, pp. 1-4, Clearwater, FL., U.S.A., 18-19 April 2011.
- [3] **Zhebin Wang**, Jae-Sik Jang, and Chan-Wang Park, “Tri-band Wilkinson Power Divider Using Resonators,” 2011 IEEE Radio and Wireless Symposium, pp. 287-290, Phoenix, AZ., U.S.A., 16-19 January 2011.

CHAPITRE 2

AMPLIFICATEUR DE PUISSANCE MULTIBANDE UTILISANT DES RÉSONATEURS DANS LES RÉSEAUX D'ADAPTATION

2.1 RÉSUMÉ

Ce chapitre présente une nouvelle méthode utilisant des résonateurs à la fois dans les réseaux d'adaptation (MNs) d'entrée et de sortie pour la conception d'amplificateur de puissance multibande. Pour l'amplificateur de puissance bibande, nous ajoutons des résonateurs parallèles entre la ligne microruban série et les stubs circuits ouverts à la fois dans les réseaux d'adaptation d'entrée et de sortie pour réaliser l'opération bibande. Avec la structure proposée, nous utilisons la structure conventionnelle de type L pour concevoir le réseau d'adaptation pour chaque fréquence de fonctionnement, ainsi la procédure de conception est plus facile. En utilisant un seul transistor sans aucun élément électronique ajustable ou un commutateur, deux nouveaux types d'amplificateur de puissance bibande de classe AB sont conçus et fabriqués pour démontrer la méthode bibande facile proposée. Pour l'amplificateur de puissance tribande, deux résonateurs parallèles en série combinés comme un élément pour choisir la fréquence sont utilisés pour chaque fréquence de fonctionnement. En appliquant cet élément de sélection de fréquences à la fois dans les réseaux d'adaptation d'entrée et de sortie, l'amplificateur de puissance tribande est réalisé avec un seul transistor. Avec l'élément de sélection de fréquences, nous pouvons utiliser la structure conventionnelle de type L pour concevoir le réseau d'adaptation tribande. Dans le processus de conception de l'amplificateur de puissance tribande, nous avons également proposé un nouveau réseau d'adaptation simplifié en utilisant le circuit de polarisation pour adapter l'impédance de la fréquence de fonctionnement la plus basse afin de réduire le nombre des groupes de résonateurs. Pour démontrer la méthode proposée, nous avons fabriqué et testé un amplificateur de puissance tribande. Les résultats mesurés montrent

d'excellentes performances des amplificateurs de puissance bibande et tribande. Les méthodes multibandes proposées de conception d'amplificateur de puissance peuvent être largement appliquées dans les applications multibandes.

2.2 MULTIBAND POWER AMPLIFIER USING RESONATORS IN MATCHING NETWORKS

2.2.1 Abstract

This chapter presents a novel method using resonators in both input and output matching networks (MN) to design multiband GaN HEMT power amplifier (PA). For the dual-band PA, at both input and output matching networks, we add parallel resonators between series microstrip lines and open-circuited stubs to realize the dual-band operation. With the proposed structure, we use the conventional L-type structure to design matching network for each operation frequency so that the design procedure is easier. By using just one transistor without any tunable electronic element or switch, two novel types of dual-band class AB PA are designed and fabricated to demonstrate the proposed simple dual-band method. For the tri-band PA, two parallel resonators in series combined as one frequency selection element are used for each operation frequency. By applying this frequency selection element in both input and output matching networks constructed with microstrip line, the tri-band PA is realized with only one transistor. With the proposed frequency selection element, we can use the conventional L-type structure to design matching network for three frequencies concurrently. In the process of designing the tri-band PA, we also proposed a new simplified load matching network using bias line to match the load impedance for the lowest operation frequency to reduce the number of resonator groups. To demonstrate the proposed method, we fabricated a concurrent tri-band PA and tested it. Measured results show the excellence performances of the proposed dual-band and tri-band PAs. The proposed multiband PA design method can be widely applied in multiband applications.

2.2.2 Introduction

With the trend of co-existence and interoperability between dissimilar standards, such as wireless local area networks (WLANS) and the global systems for mobile communication systems (GSM), multiband mobile and satellite communication system will be widely required in future wireless networks. PA is certainly required for multiband operation.

In previous works, to realize multiband operation, technologies of diplexers (Ryu *et al.*, 2009; Kunihiro *et al.*, 2004; Jou *et al.*, 2003), switched elements (Eo *et al.*, 2004; Yamamoto *et al.*, 2002; Adar *et al.*, 1998), and electronically tunable elements (Ujiie *et al.*, 2007) are explored for multiband PA design. Concurrent multiband operation is one of the important considerations in multiband PA design. Toggling between different matching networks and adjustment of tunable components are unable to offer simultaneous operation when the operation frequency changes (Negra *et al.*, 2008). To reduce the size of parallel PA circuit and to save component cost, especially for active component, we need to design a versatile matching network circuit to realize multiband operation concurrently.

In the same bias condition, different operation frequency could have different impedance point in Smith chart for the maximum power added efficiency (PAE) or the maximum output power according to the source pull and load pull simulations. Also, the source and load stability circles will be different when the operation frequency is different. Therefore, the conventional single band L-type matching network cannot be applied for multiband requirement. Our objective is to design a concurrent multiband PA working at two or three distinctive frequency bands using the simplest L-type matching network structure with resonators. To reduce the size of the circuit and to save component cost, especially for active component, we need to design a versatile matching network circuit to realize multiband operation concurrently.

2.2.3 Conventional power amplifier

a) Power amplifier

In general, a PA is used in the final stages of radar and radio transmitters to increase the radiated power level. Efficiency, gain, linearity, and thermal effects are the important considerations of RF or microwave PAs (Pozar, 2005: 570). The drain efficiency and power added efficiency (PAE) which includes the effect of input power are defined as shown below: (Pozar, 2001: 218; Gardiol, 1994: 150):

Drain efficiency:

$$\eta = \frac{P_{out}}{P_b} \times 100[\%] \quad (2.1)$$

PAE:

$$\eta_{PAE} = \frac{(P_{out} - P_{in})}{P_b} \times 100[\%] \quad (2.2)$$

where P_{out} is the output power, P_{in} is the input power, and P_b is the DC power supplied by the biasing sources.

Most small-signal and low-noise amplifiers operate as class A circuits, the transistor is biased to conduct over the entire range of the input signal cycle, but the drain efficiency of class A is as low as 50%. Class A amplifiers are inherently linear circuits (Pozar, 2005: 571; Cripps, 2006: 48, 137). Class AB is the class between class A and class B. In its operation, the conduct angle is between 180° and 360° . To keep its linearity class AB amplifier sacrifices some efficiency. The drain efficiency of class AB is more than 50% but less than 78.5% (class B level) (Pozar, 2005: 571; Cripps, 2006: 50, 141). The conduct angle of class C which has a big distortion is less than 180° . It has theoretical drain

efficiency up to 100%, but can only be used with constant envelope modulations. (Pozar, 2005: 571; Cripps, 2006: 54).

PAs require bias circuit to change DC (direct current) energy to RF (radio frequency) energy. The desirable feature of bias circuit is small RF leakage and broad bandwidth characteristics (Bahl, 2003: 377). The conventional bias circuit using lumped-element is shown in Fig. 83 (Bahl, 2003: 379). The shunt inductor L_B is used as a RF choke and the series capacitor C_B is used to isolate bias circuit from ground. We will use the conventional bias circuit in source pull, load pull, and stability simulation for the GaN transistor model CGH40010 of CREE Inc.

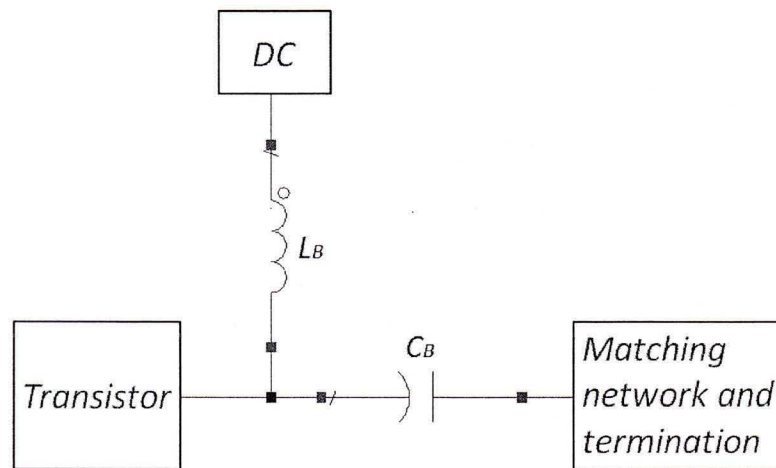


Figure 83: Conventional lumped-element bias circuit

b) Source pull and load pull simulation

We use source pull and load pull simulation to investigate the impedance points for the maximum PAE and maximum output power. The source pull and load pull simulation schematic diagrams are shown in Fig. 84 and Fig. 85, respectively. We use ideal inductor and capacitor models as shown in Fig. 83 in both source pull and load pull simulation and set $L_B = 1$ uH and $C_B = 1$ uF as a default. The simulated PAE curve and output power curve at 1 GHz, 1.5GHz, and 2.5 GHz are shown in Fig. 86 and Fig. 87, respectively. The step of the PAE curves is 1% and the step of the output power curves is 0.2 dBm.

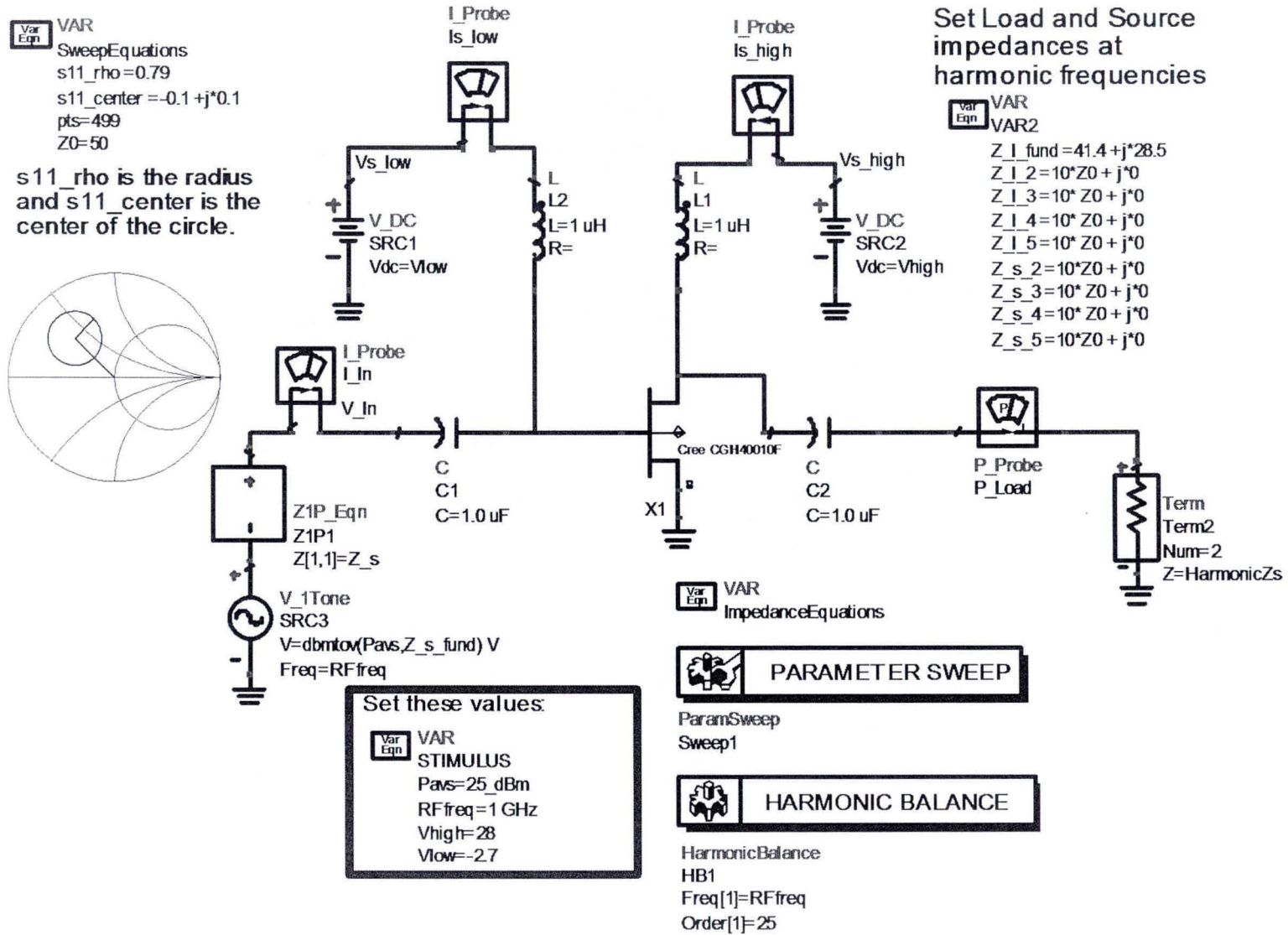


Figure 84: Source pull simulation schematic diagram of output power and PAE

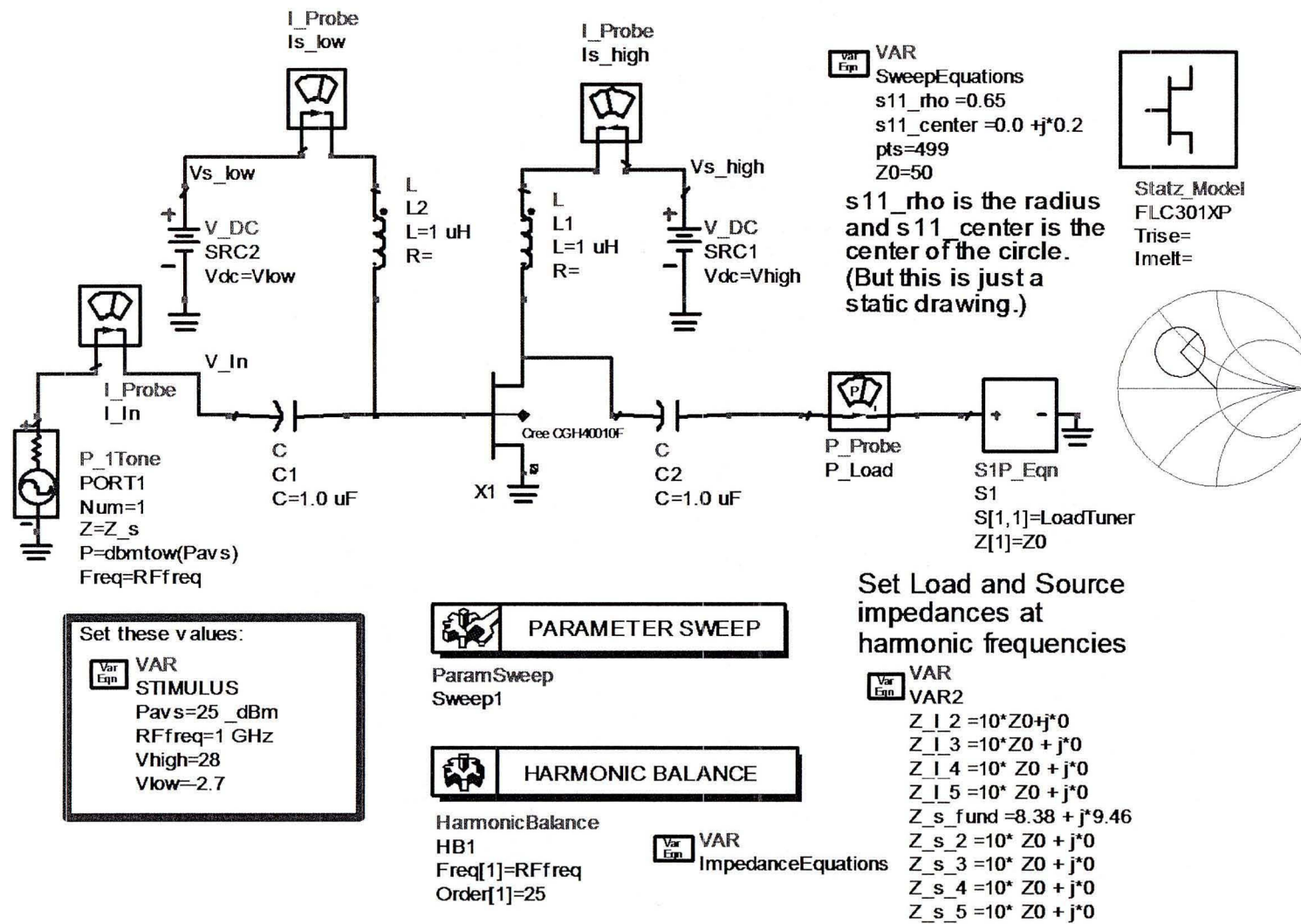


Figure 85: Load pull simulation schematic diagram of output power and PAE

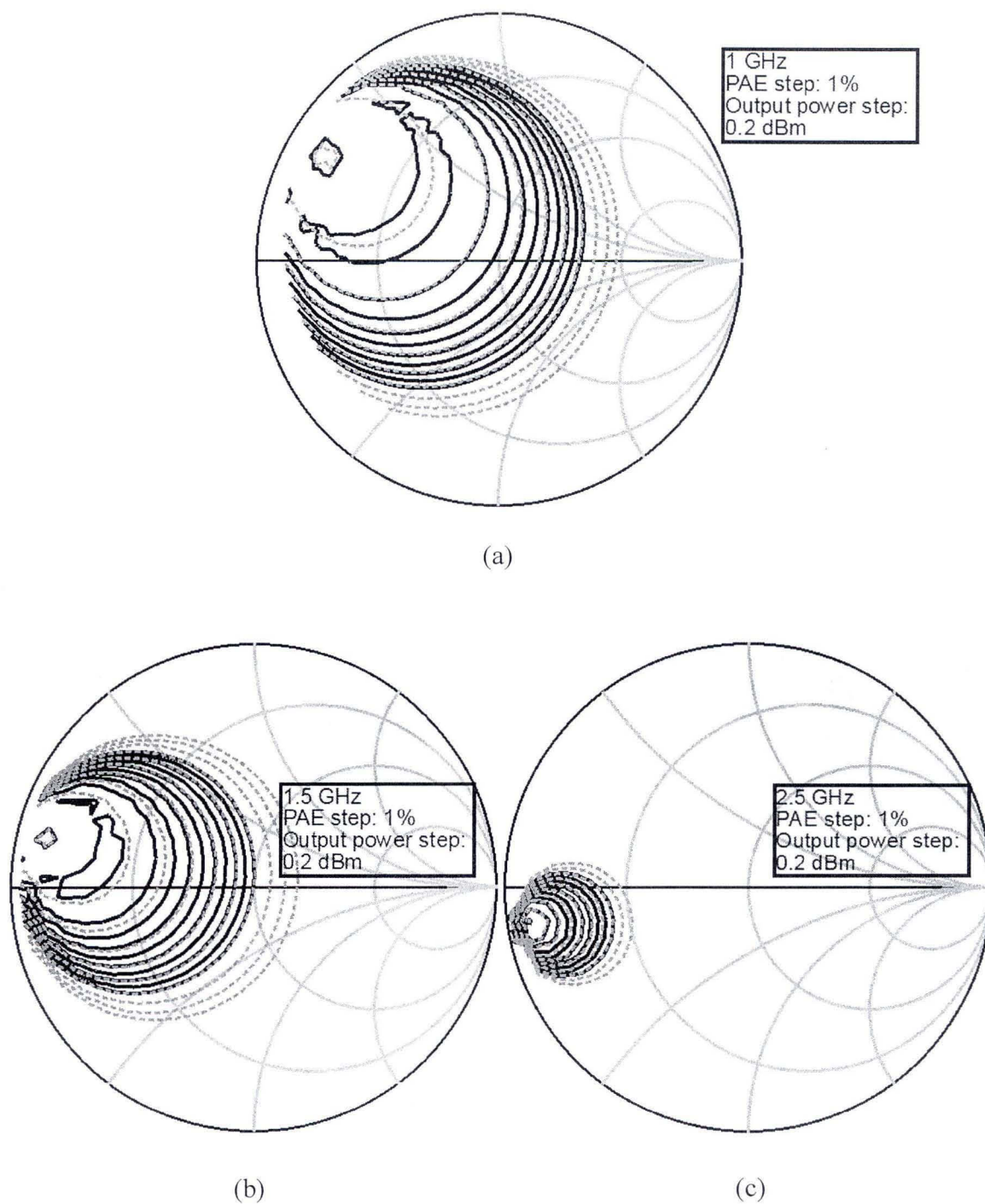


Figure 86: Simulated results of source pull simulation at (a): 1 GHz, (b): 1.5GHz, and (c): 2.5 GHz, solid line: PAE, and dot line: output power

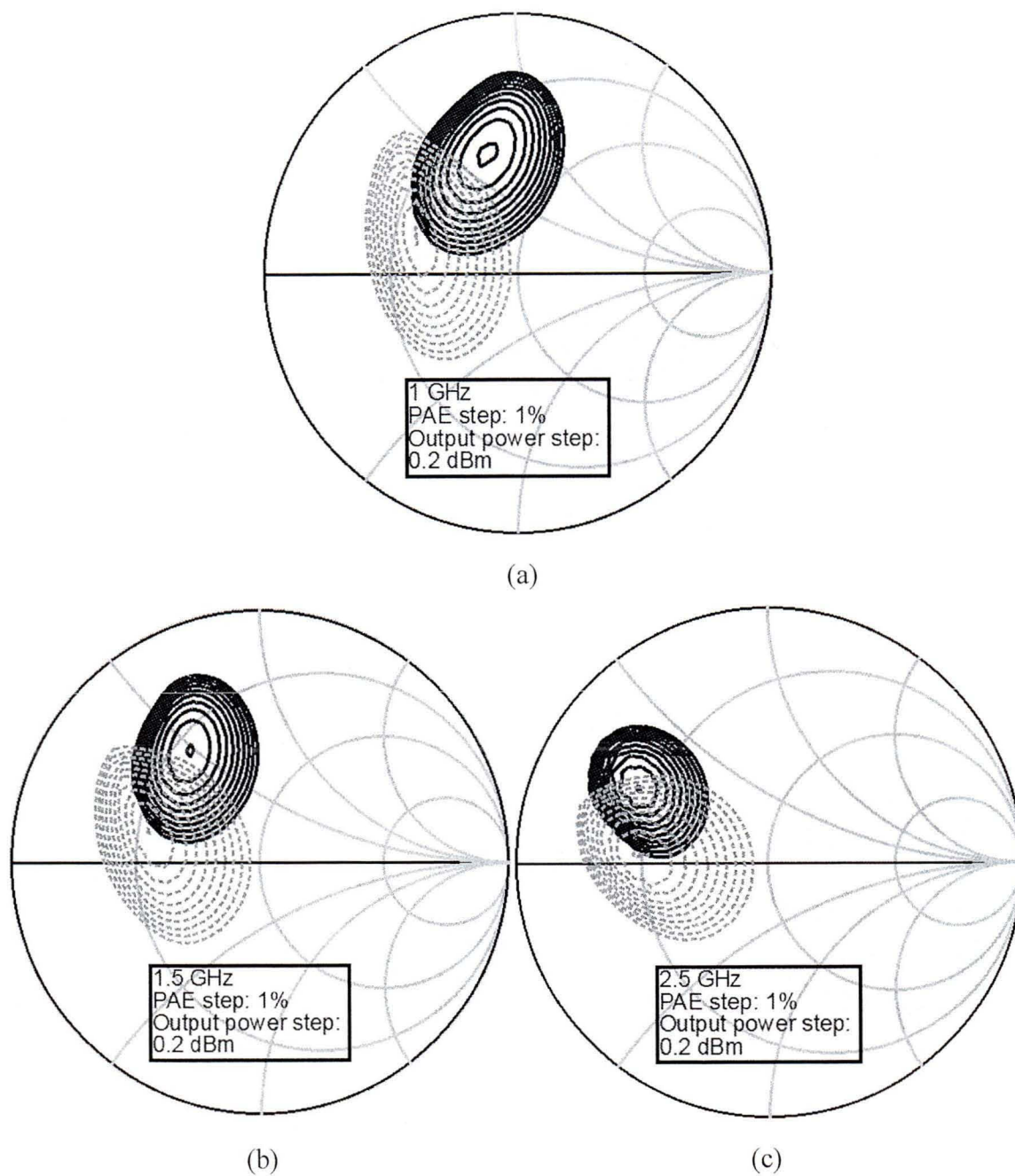


Figure 87: Simulated results of load pull simulation at (a): 1 GHz, (b): 1.5GHz, and (c): 2.5 GHz, solid line: PAE, and dot line: output power

c) Stability simulation

The stability of an amplifier is an important aspect that we should consider in a design and it can be determined from the S-parameter. In a two-port network, oscillations are possible when either the input or output port presents a negative resistance (Gonzalez, 1997: 217). Stability circle analysis is especially useful in the analysis of potentially unstable transistors (Gonzalez, 1997: 218). The stability simulation schematic diagram in ADS is shown in Fig. 88. The source and load simulated stability circle is shown in Fig. 89 at 1GHz, 1.5 GHz, and 2.5 GHz.

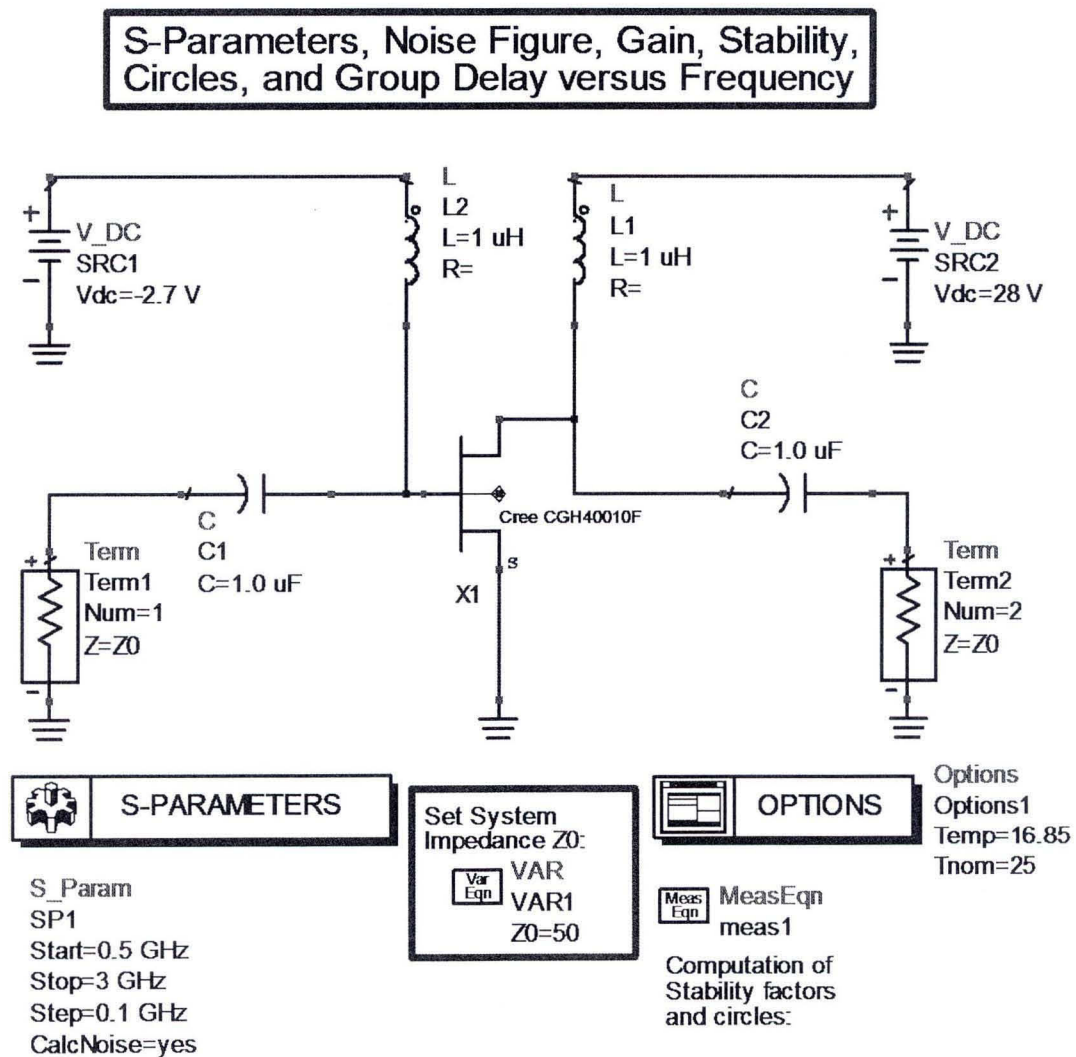


Figure 88: Stability simulation schematic diagram

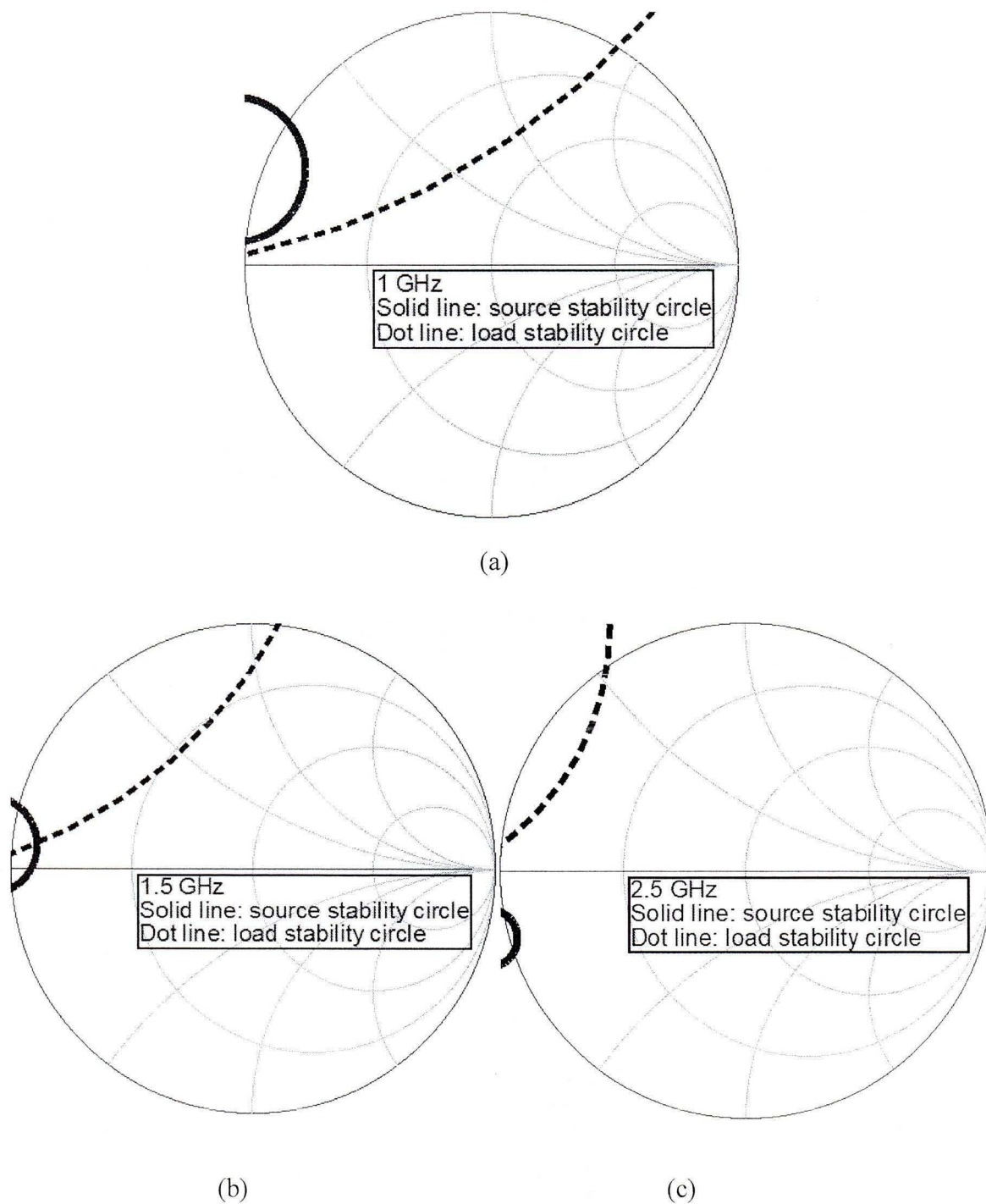


Figure 89: Source and load stability circles of CGH40010F_r6 model, (a): 1 GHz, (b): 1.5 GHz, (c): 2.5 GHz, solid line: source stability circle, and dot line: load stability circle

2.2.4 Problem, objective, and methodology

For multiband PA, with the same bias condition at the gate and drain side of the transistor, different frequencies could have different impedance points of matching network for the maximum PAE or maximum output power according to the source and load pull simulation as shown in Fig. 86 and Fig. 87, respectively. Source and load stability circles will be different at different frequencies as shown in Fig. 89. Conventional L-type matching network is shown in Fig. 90 to match source or load impedance to get the maximum PAE or output power. Because the physical length of microstrip line of conventional L-type matching network is fixed for one specific frequency, it cannot adapt to impedance matching at other frequencies. In other words, impedance matching using conventional L-type matching network for two or three distinctive frequencies is not independent.

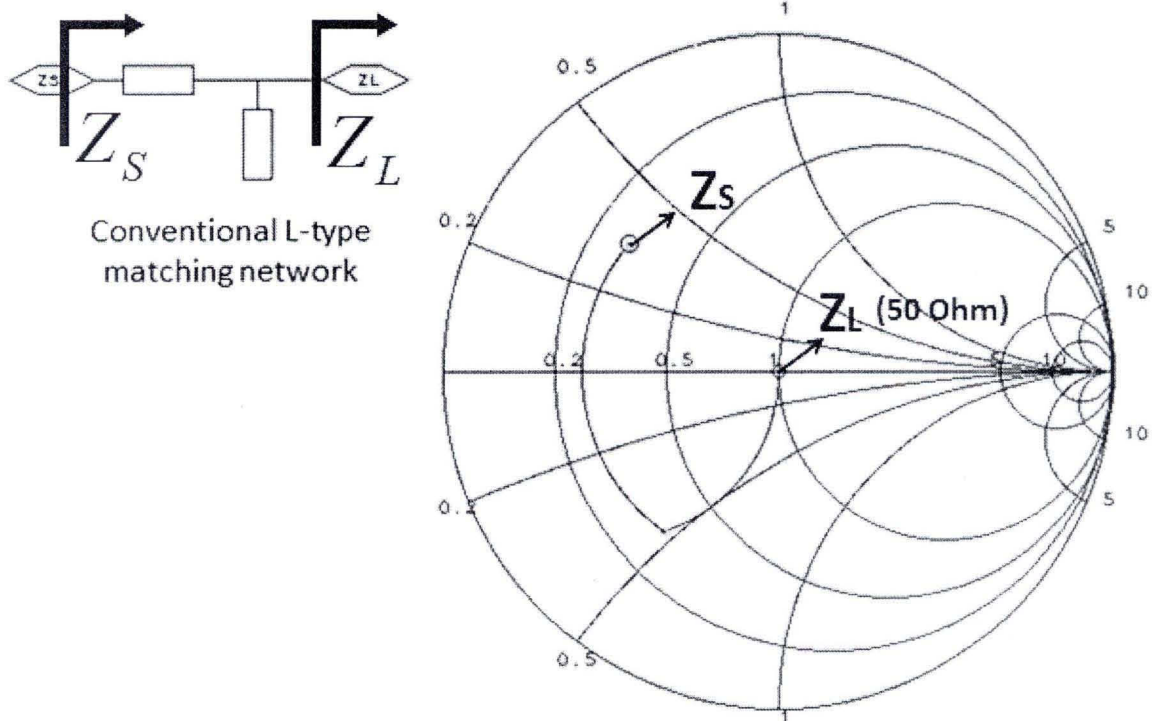


Figure 90: Conventional L-type matching network

In this chapter, my objective is to design multiband amplifiers for the requirements of multiband applications. To do that, I will propose one concurrent dual-band and one concurrent tri-band PAs by applying resonator as frequency selection element in both input and output matching networks instead of using diplexers, switches, or electronically tunable elements. The frequency selection element can reject undesired frequencies while passing the signal at the desired frequency. With these frequency selection elements, we can employ the simplest L-type matching network structure for dual-band or tri-band PA design. The design procedure of multiband PA is simplified. Because the proposed multiband matching network structure can realize multiband operation concurrently with only one transistor, the cost of active component can be saved.

2.2.5 Analysis and design of new multiband matching network with resonators

In this section, we proposed a new dual-band and a new tri-band matching networks which employ the parallel LC resonant circuits in the conventional L-type matching networks. At resonant frequency, the impedance of parallel resonant circuit becomes the largest and signal generated at this frequency is blocked by resonant effect. The resonant frequency can be easily calculated with equation (1.9). By adding resonators in matching network with conventional L-type structure, multiband matching network is achieved. The principles of the proposed dual-band or tri-band matching network are investigated and explained in this section. The new dual-band and tri-band matching networks have been published by me in (Wang *et al.*, 2011 d; Wang *et al.*, 2012 b).

a) Dual-band matching network with resonators (Wang *et al.*, 2011 d)

In Fig. 91, we show two parallel LC resonant circuits to block signal at frequency f_1 and frequency f_2 . With equation (1.9), the capacitance of capacitor and the inductance of inductor we choose for frequency f_1 and frequency f_2 are C_1 and L_1 , and C_2 and L_2 , respectively.

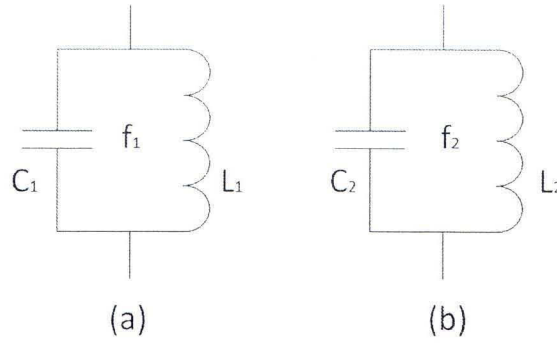


Figure 91: Parallel resonators, (a): the resonant circuit to block signal at frequency f_1 , and (b): the resonant circuit to block signal at frequency f_2

Fig. 93 shows the principle and topologies of input and output matching circuits in the proposed dual-band PA block diagram as shown in Fig. 92. At frequency f_1 , signal is blocked by resonant circuit f_1 as shown in Fig. 91 (a). In Fig. 93, the shunt stub with resonant circuit f_1 performs like an open circuit; the shunt stub with the resonant circuit f_2 performs like a normal shunt stub connected with the series microstrip line directly. Signal at frequency f_1 can pass resonant circuit f_2 and the open-circuited stub connected with resonant circuit f_2 affects the impedance of matching network with the series microstrip line. The same performance as the operation frequency is frequency f_2 . Both the input and output dual-band matching networks transform to equivalent L-type matching networks at frequency f_1 and frequency f_2 . In this chapter, frequency f_1 is 2.5 GHz and frequency f_2 is 1.5 GHz.

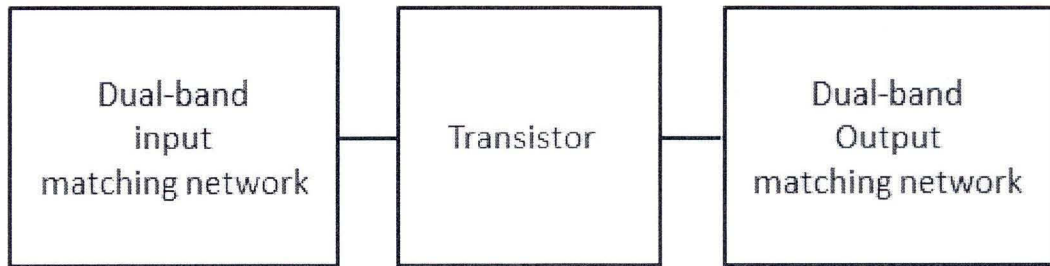


Figure 92: Block diagram of the proposed dual-band power amplifier

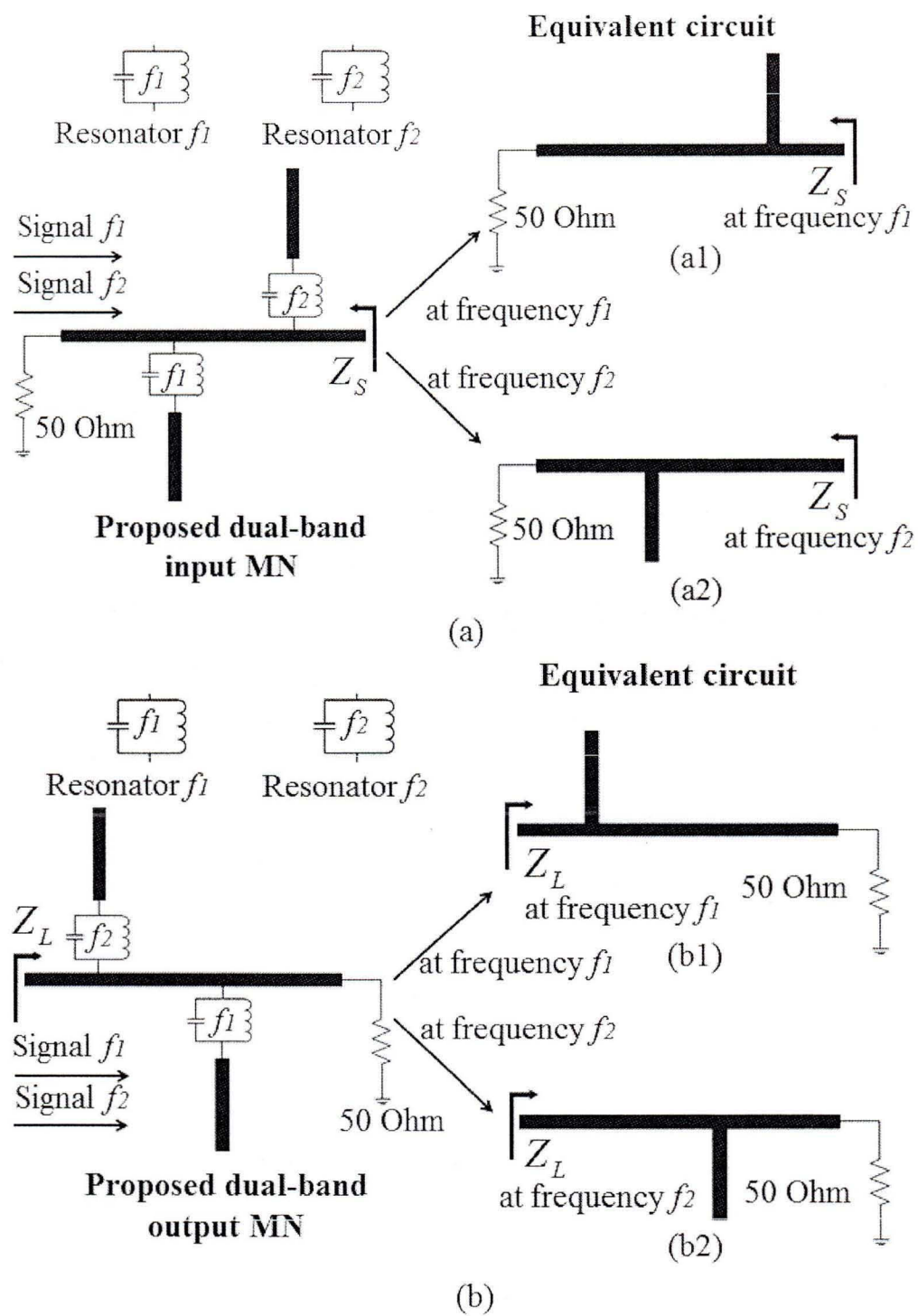


Figure 93: Principle and topologies of dual-band matching networks, (a): input matching network, and (b): output matching network

b) Tri-band matching network with resonator groups (Wang *et al.*, 2012 b)

To realize tri-band operation, we employ parallel resonator group (Fig. 94 (d)) as the frequency selection element in both input and output matching networks. As Fig. 94 (a) shows, one parallel resonator designed for frequency f_1 contains one capacitor C_1 and one inductor L_1 . The resonant frequency can be calculated by equation (1.9) where C is capacitance of capacitor and L is inductance of inductor. Fig. 94 (d) shows the topology of the proposed resonator group. At three distinctive frequencies, frequency f_x , frequency f_y , and frequency f_z , signal at frequency f_x is blocked by resonant circuit f_x and signal generated at frequency f_y is blocked by resonant circuit f_y . Signal generated at frequency f_z can pass through the resonator group (Fig. 94 (d)).

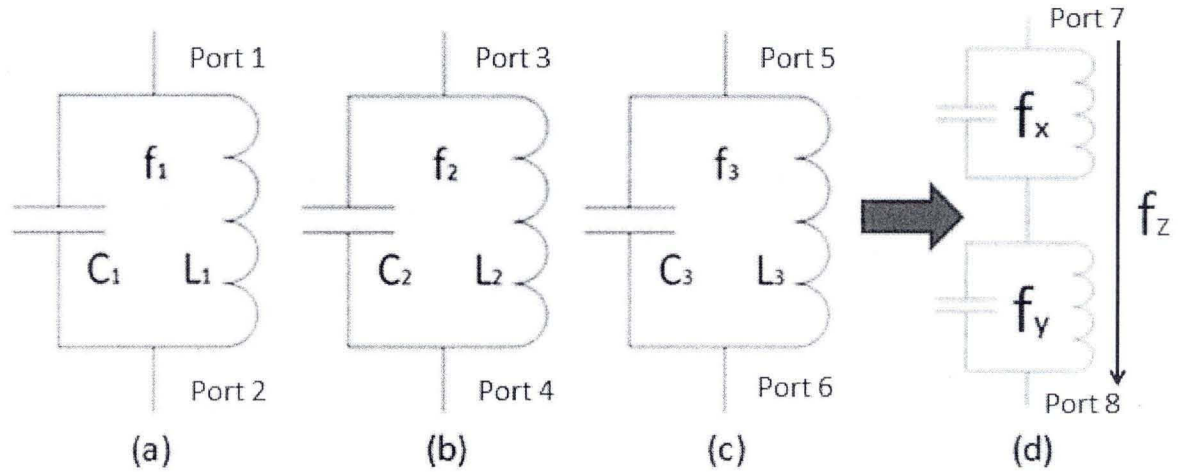


Figure 94: Parallel resonator circuits for (a): frequencies f_1 , (b): frequency f_2 , (c): frequency f_3 , and (d): resonator group

Fig. 95 shows the proposed principle and topologies of input and output tri-band matching networks by applying resonator groups. Each resonator group contains two parallel resonators. With these resonator groups, each shunt open-circuited microstrip stub in Fig. 95 can affect the signal generated at its corresponding frequency.

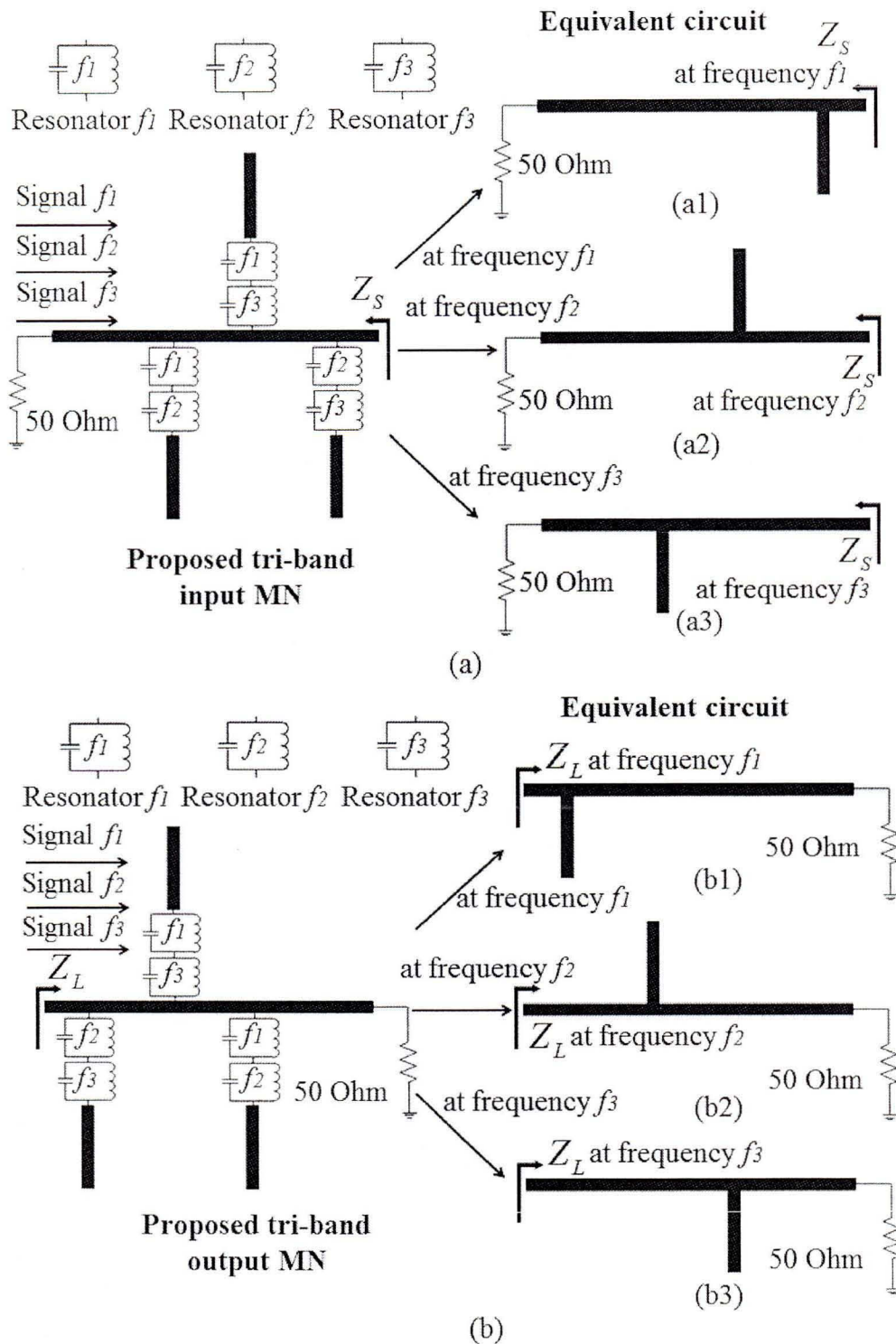


Figure 95: Principle and topologies of tri-band matching networks, (a): input matching network, and (b): output matching network

According to Fig. 95, the desired impedance point at each frequency can be matched to 50 Ohm with equivalent circuit concept independently. For example in Fig. 95 (a), the left side of the tri-band input matching network has two parallel resonators and one open-circuited stub. Signal at frequency f_3 can pass through this resonator group to the open-circuited stub directly while signal at frequency f_1 and frequency f_2 is blocked by the resonator group. The same idea is adapted for the middle and right side of the tri-band source matching circuit. With this characteristic, tri-band function in a single matching network with conventional L-type matching structure is realized. In this chapter, we choose 2.5 GHz as frequency f_1 , 1.5 GHz as frequency f_2 , and 1 GHz as frequency f_3 . The chosen source and load impedance points for 2.5 GHz, 1.5 GHz, and 1 GHz are shown in Fig. 96.

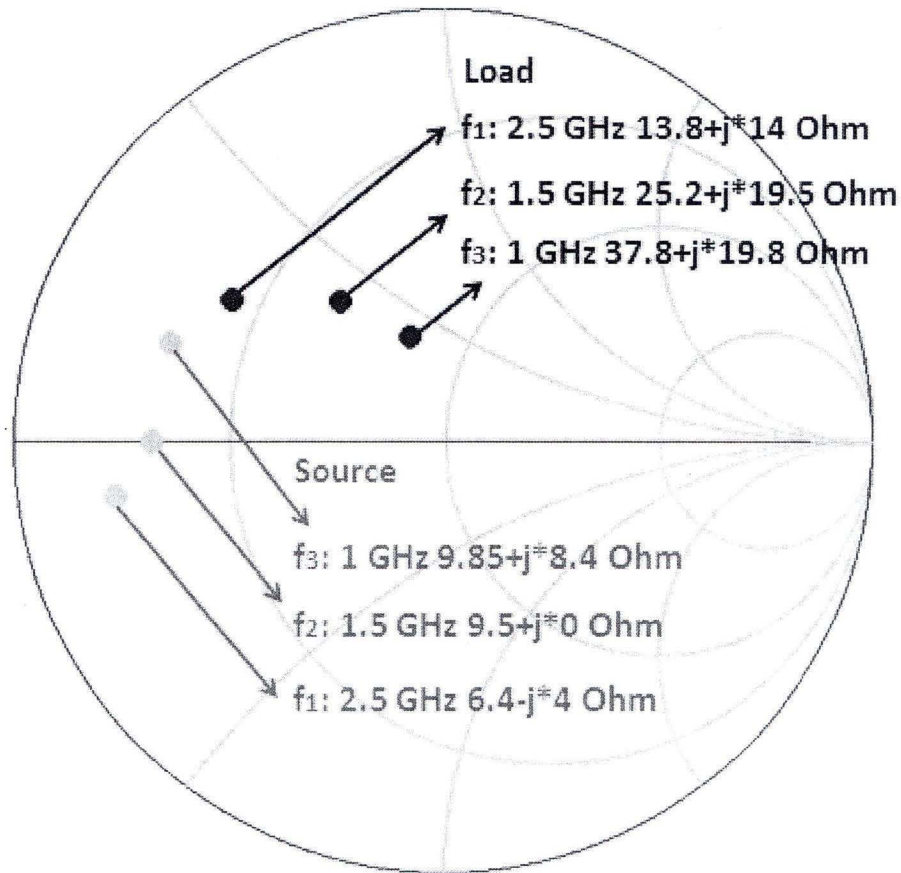


Figure 96: Desired source and load impedance points of CGH40010 at 2.5 GHz, 1.5 GHz, and 1 GHz

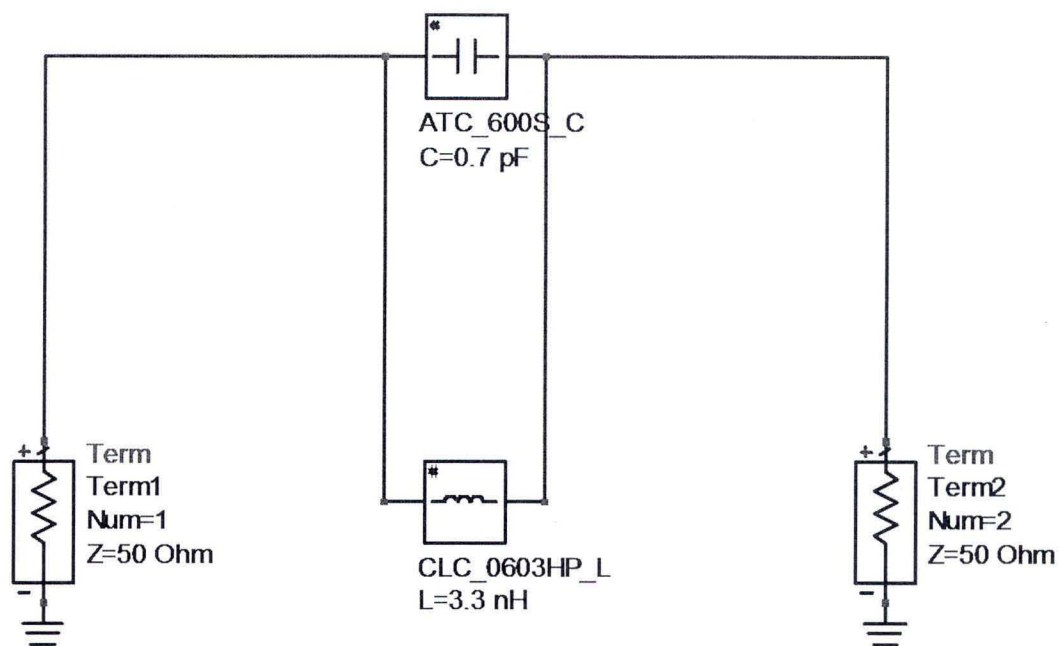
2.2.6 New concurrent dual-band power amplifier

a) Dual-band power amplifier with parallel resonator constructed with capacitor and inductor (Wang *et al.*, 2011 d)

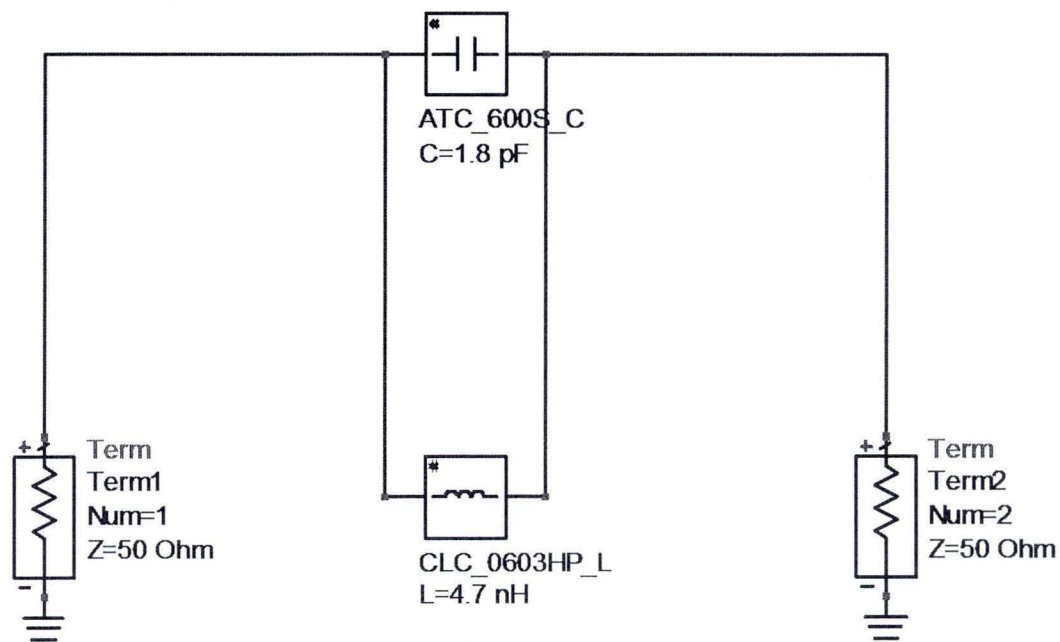
The new dual-band PA was published by me in (Wang *et al.*, 2011 d). To evaluate the proposed concept of dual-band matching network, we designed, fabricated, and tested one dual-band PA using parallel resonator which is constructed with one capacitor and one inductor in this section. To design the proposed dual-band class AB PA, we use 10 W GaN HEMT packaged transistor CGH40010 from CREE Inc. The circuit was designed and fabricated on a substrate TLX-8 from Taconic with dielectric constant of 2.55 and thickness of 31 mils.

We design the proposed dual-band GaN HEMT class AB PA by using ADS software of Agilent Technology. We choose source and load matching network impedance points near the centers of maximum PAE curves obtained by source pull and load pull simulations for 1.5 GHz and 2.5 GHz, respectively, as shown in Fig. 86 and Fig. 87. In Fig. 96, the source impedance values for 1.5 GHz and 2.5 GHz we choose are $9.5 + j0$ Ohm and $6.4 - j4$ Ohm, respectively. The load impedance values for 1.5 GHz and 2.5 GHz we choose are $25.2 + j 19.5$ Ohm and $13.8 + j 14$ Ohm, respectively.

The resonant circuits of the proposed dual-band PA designed for 2.5 GHz and 1.5 GHz are shown in Fig. 97. The simulated results of the resonant circuits in Fig. 97 are shown in Fig. 98. The design schematic diagrams of resonant circuit with open-circuited stub for 2.5 GHz and 1.5 GHz are shown in Fig. 99. The simulated results of the circuits in Fig. 99 are shown in Fig. 100.



(a)



(b)

Figure 97: Resonators designed for the proposed dual-band power amplifier, (a): 2.5 GHz and (b): 1.5 GHz

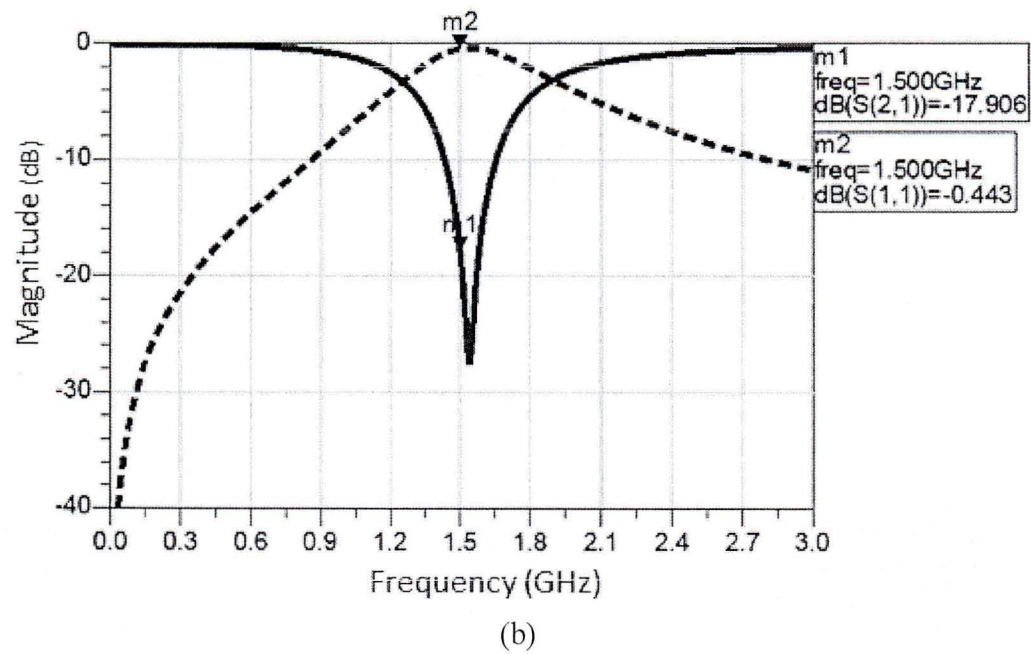
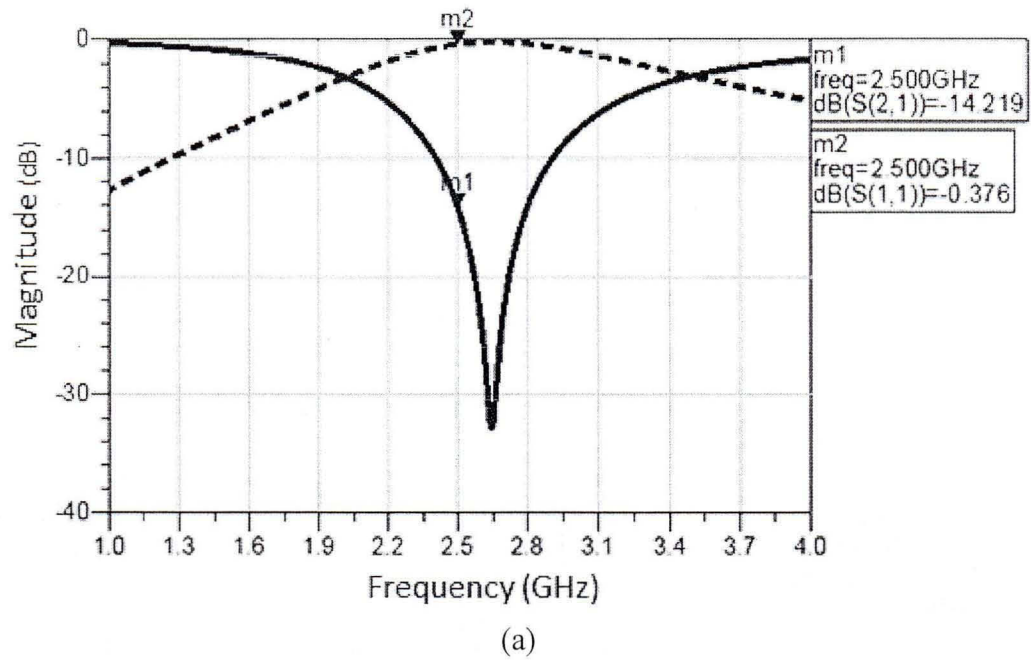
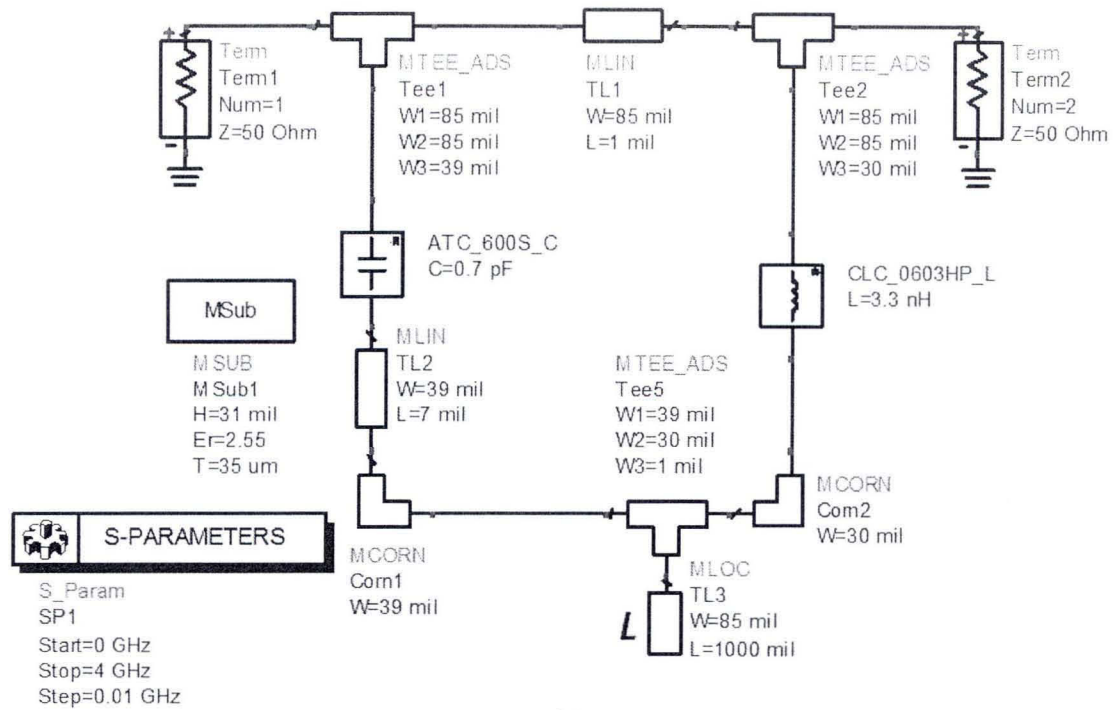
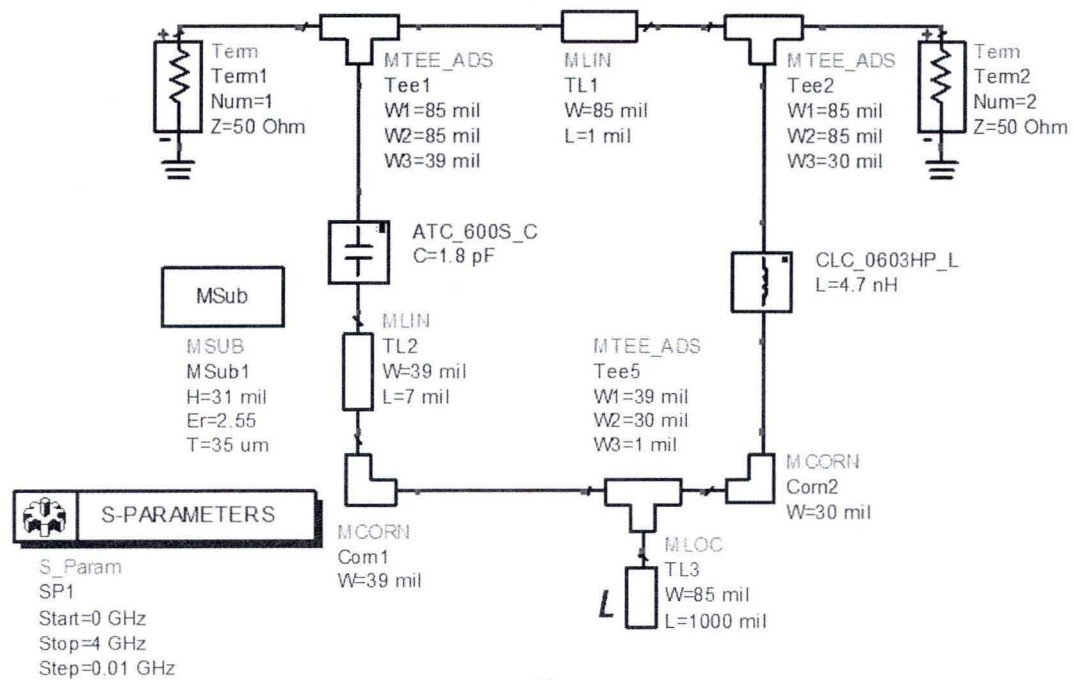


Figure 98: Simulated results of the resonators designed for the proposed dual-band power amplifier, (a): 2.5 GHz and (b): 1.5 GHz, solid line: insertion loss, and dot line: return loss



(a)



(b)

Figure 99: The design schematic diagrams of resonant circuit with open-circuited stub, (a): 2.5 GHz and (b): 1.5 GHz

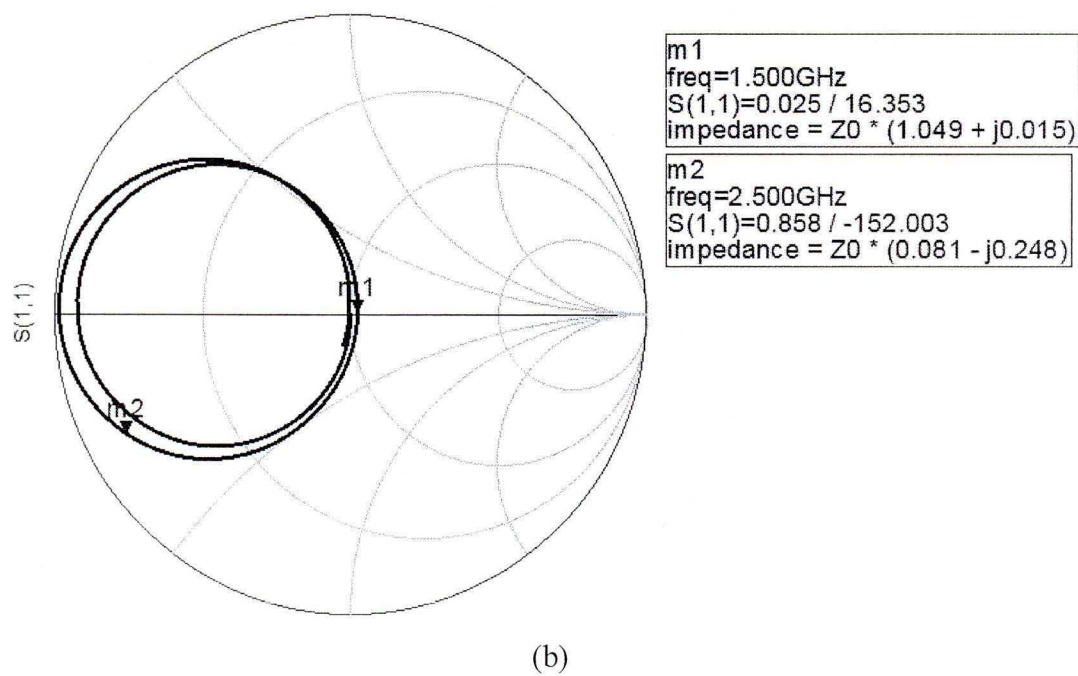
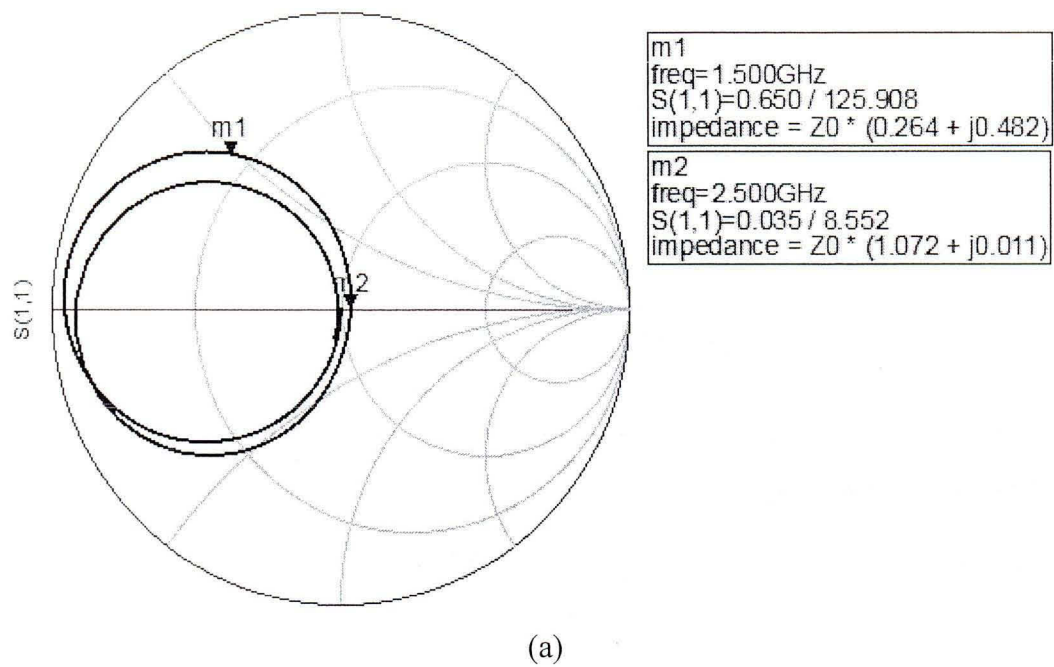


Figure 100: Simulated results of the resonant circuit with open-circuited stub shown in Fig. 99, (a): 2.5 GHz resonator and (b): 1.5 GHz resonator

Fig. 98 shows the insertion loss and return loss of the resonator consists of ATC 0.7 pF capacitor and Coilcraft 3.3 nH inductor are 14.22 dB and 0.38 dB, respectively; the insertion loss and return loss of the resonator with ATC 1.8 pF capacitor and Coilcraft 4.7 nH inductor are 17.91 dB and 0.44 dB, respectively. Signal generated at 1.5 GHz and 2.5 GHz is suppressed effectively by its corresponding resonator.

We connect the resonators with open-circuited stub as shown in Fig. 99 (L is the length of shunt open-circuited stub), no matter how we change the value of L at 2.5 GHz or 1.5 GHz, the impedance point stayed at the center of Smith chart as shown in Fig. 100. Signal at 2.5 GHz or 1.5 GHz is blocked by its corresponding resonator. The open-circuited stub cannot affect the impedance value of matching circuit at 2.5 GHz or 1.5 GHz.

The designed schematic diagrams of the proposed source and load matching networks of the dual-band class AB PA are shown in Fig. 101 and Fig. 102, respectively. The total layout of the proposed dual-band class AB PA is shown in Fig. 103.

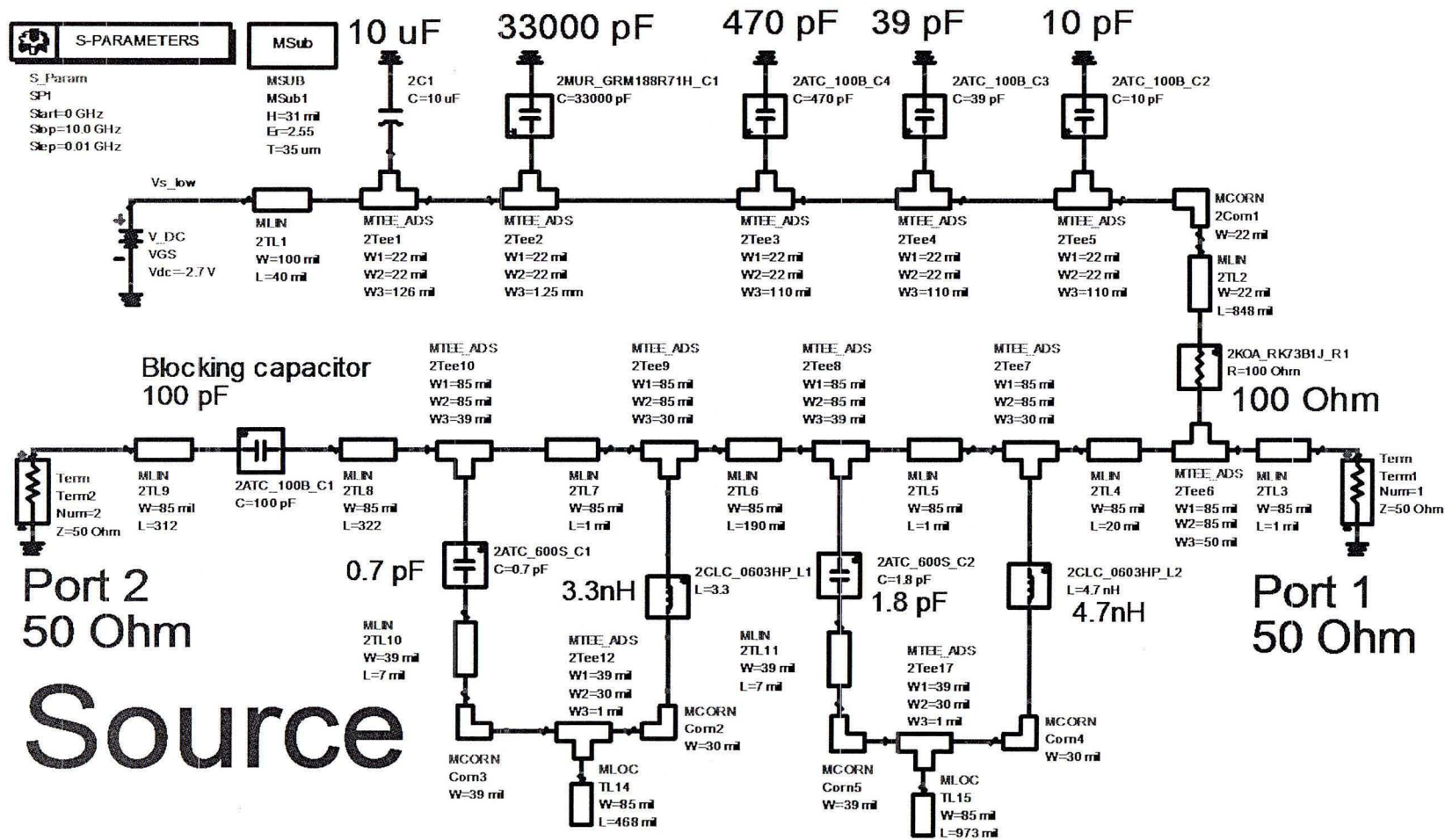


Figure 101: The design schematic diagram of the source matching network of the proposed dual-band power amplifier

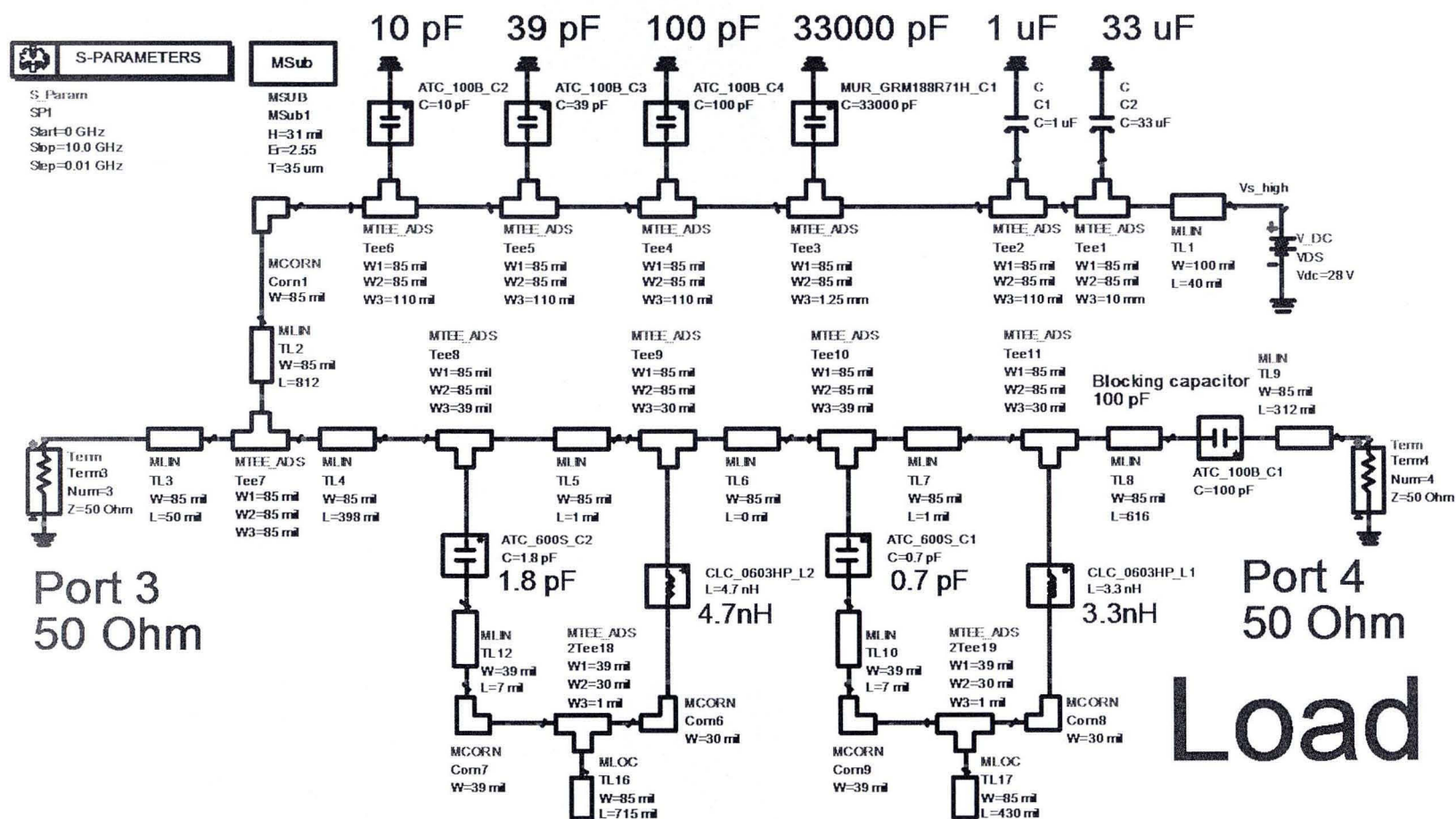


Figure 102: The design schematic diagram of the load matching network of the proposed dual-band power amplifier

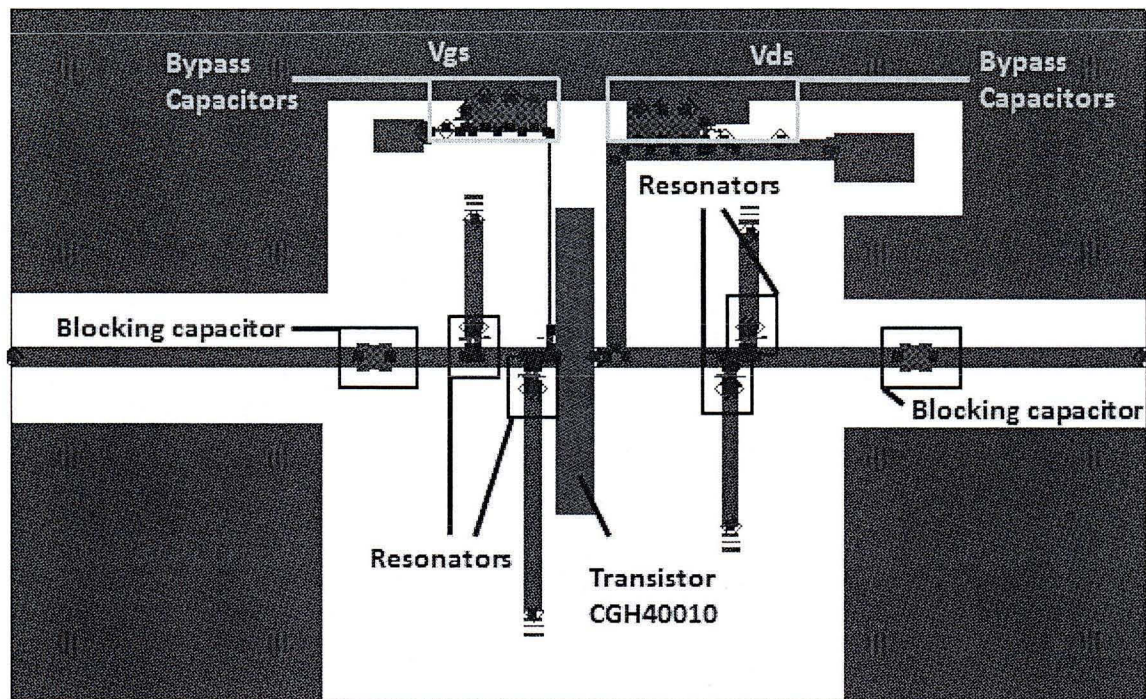


Figure 103: Layout of the proposed dual-band class AB power amplifier

Fig. 104 shows the simulated impedance results of the input and output matching networks shown in Fig. 101 and Fig. 102, respectively. Mark $m1$ and mark $m2$ show the impedance points of input matching network at 1.5 GHz and 2.5 GHz, respectively. Mark $m3$ and mark $m4$ show the impedance points of output matching network at 1.5 GHz and 2.5GHz, respectively. All the impedance values of input and output matching networks are for the operation of dual-band class AB PA.

From Fig. 104 we notice that we can obtain the desired impedance points for impedance matching at different frequencies by employing just one simple matching network using resonators.

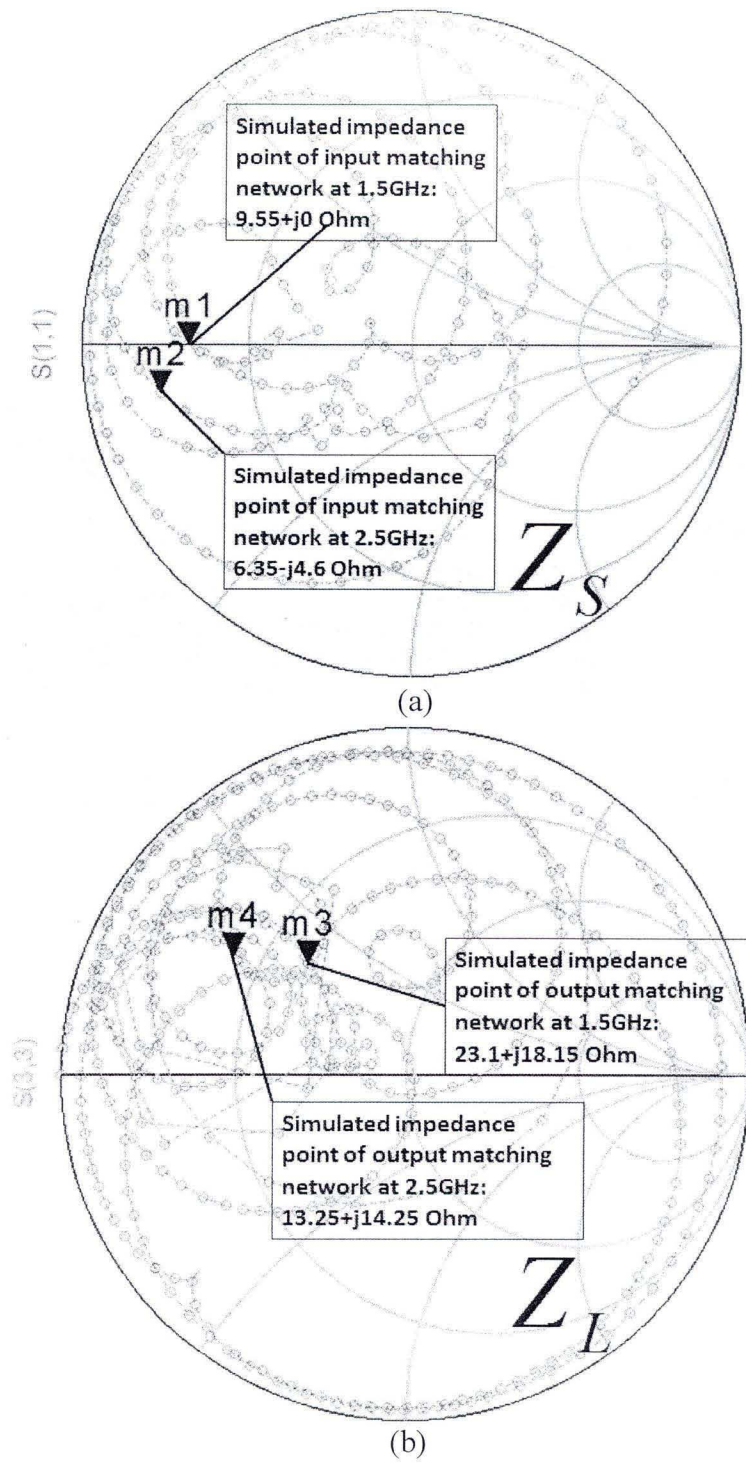


Figure 104: Simulated impedance results of the proposed dual-band matching networks, (a): input matching network, and (b): output matching network with 0.01 GHz step

For testing this dual-band PA, we used Anritsu signal generator MG3700A, Agilent signal analyzer N9020A, one 20 dB attenuator, and one 40 dB ZHL-4240W pre-amplifier from Mini-Circuits. The test setup diagram is shown in Fig. 105.

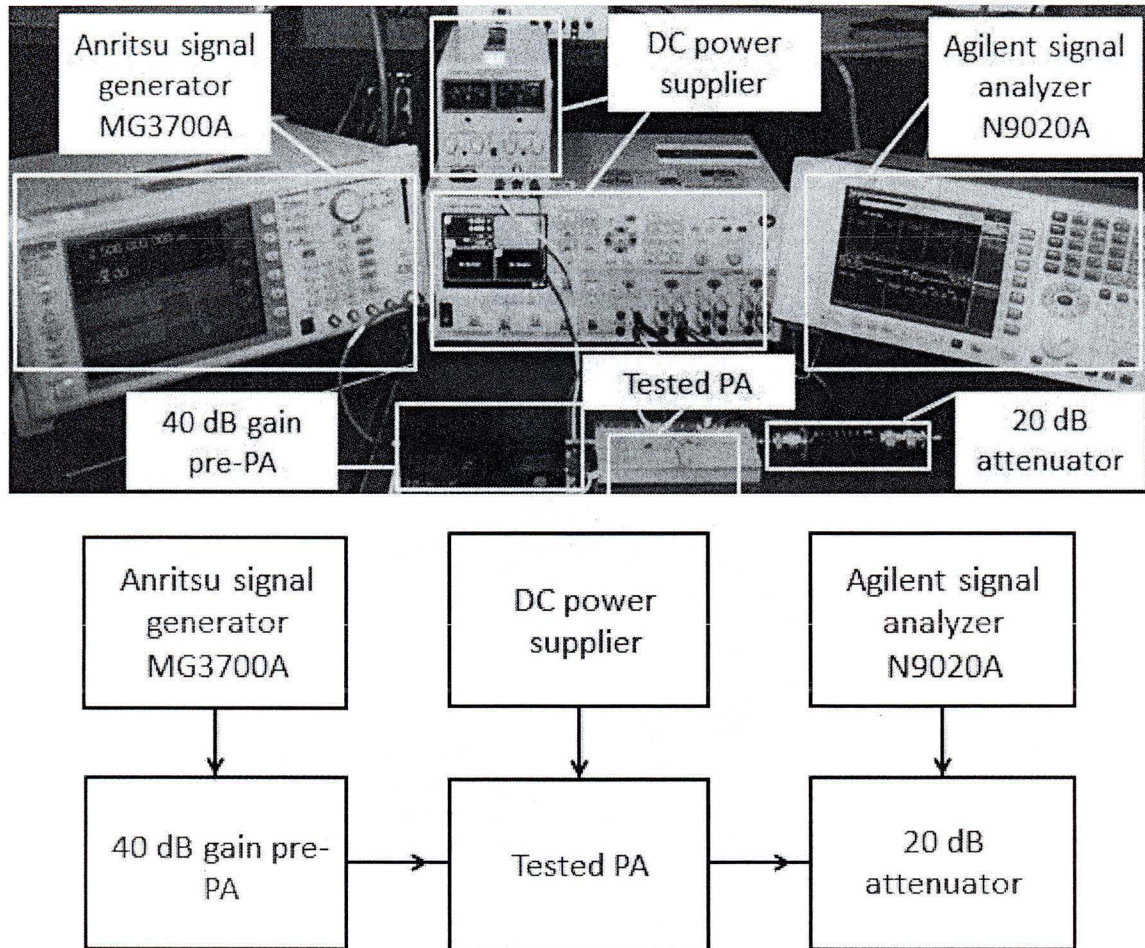


Figure 105: The test setup diagram of the proposed dual-band power amplifier

The fabricated dual-band GaN HEMT class AB PA is shown in Fig. 106. Resonator f_1 inserted in both input and output matching networks indicates the resonant circuit (a) of Fig. 91 to block the signal at frequency f_1 ; the same, Resonator f_2 shown in Fig. 106 indicates the resonant circuit (b) of Fig. 91 to block signal at frequency f_2 .

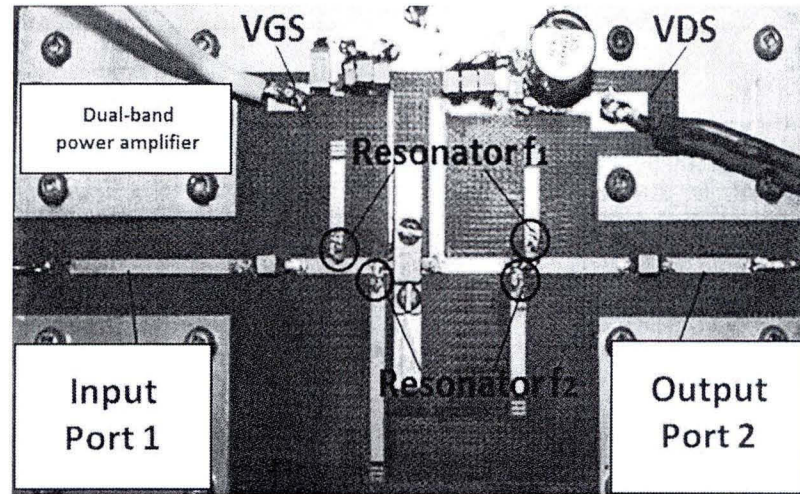


Figure 106: Fabricated dual-band class AB power amplifier using resonators constructed by chip capacitor and chip inductor

The best performance of the fabricated dual-band PA is measured at 1.5 GHz and 2.4 GHz. Fig. 107 shows the comparison between the simulated and measured results of PAE versus output power at 1.5 GHz and 2.4 GHz, respectively. From measured results, at 1.5 GHz ((a) of Fig. 107), the maximum PAE can reach 55.63% with 40.30 dBm output power. At 2.4 GHz ((b) of Fig. 107), the maximum PAE is 40.25% with 39.05 dBm output power.

Fig. 108 shows output power versus frequency curve from 1GHz to 3 GHz. According to this figure we notice that, from 1 GHz to 2 GHz, the peak value is 40.30 dBm at 1.5 GHz. From 2GHz to 3GHz, the peak value is 39.05 dBm at 2.4 GHz. In output power aspect, the proposed dual-band PA has the best performance at 1.5 GHz and 2.4 GHz, respectively. Fig. 109 shows the measured AM-AM curves at 1.5 GHz and 2.4 GHz.

Fig. 110 shows PAE versus frequency curve from 1 GHz to 3 GHz. According to this figure, the maximum PAE is 55.63% at 1.5 GHz from 1GHz to 2GHz. From 2GHz to 3GHz, at 2.4 GHz, we found the maximum PAE is 40.25%. In the PAE aspect, also the proposed dual-band PA got the best results at 1.5 GHz and 2.4 GHz, respectively.

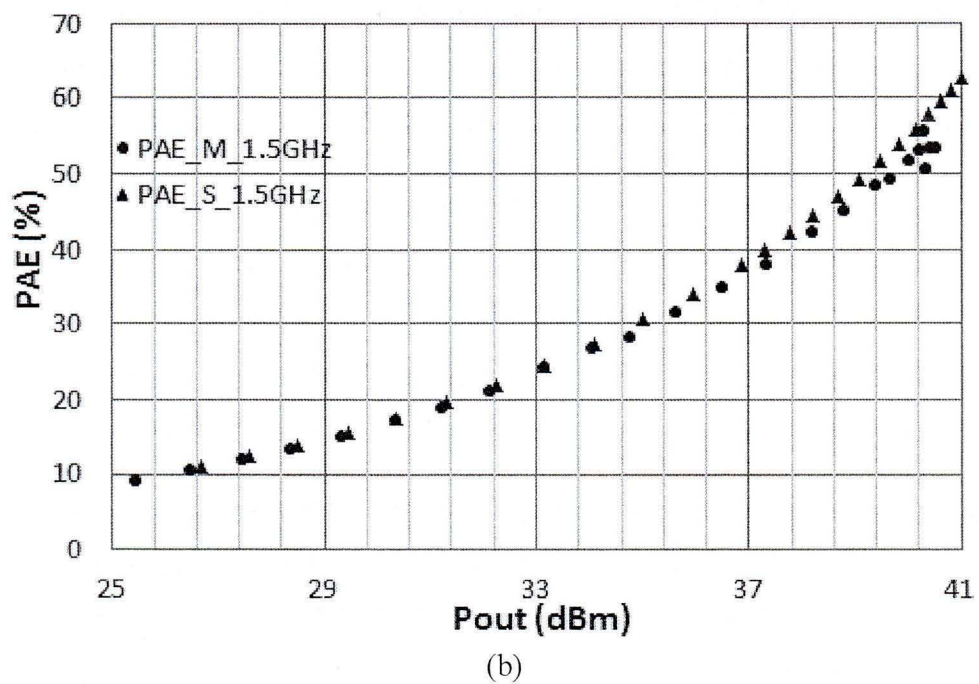
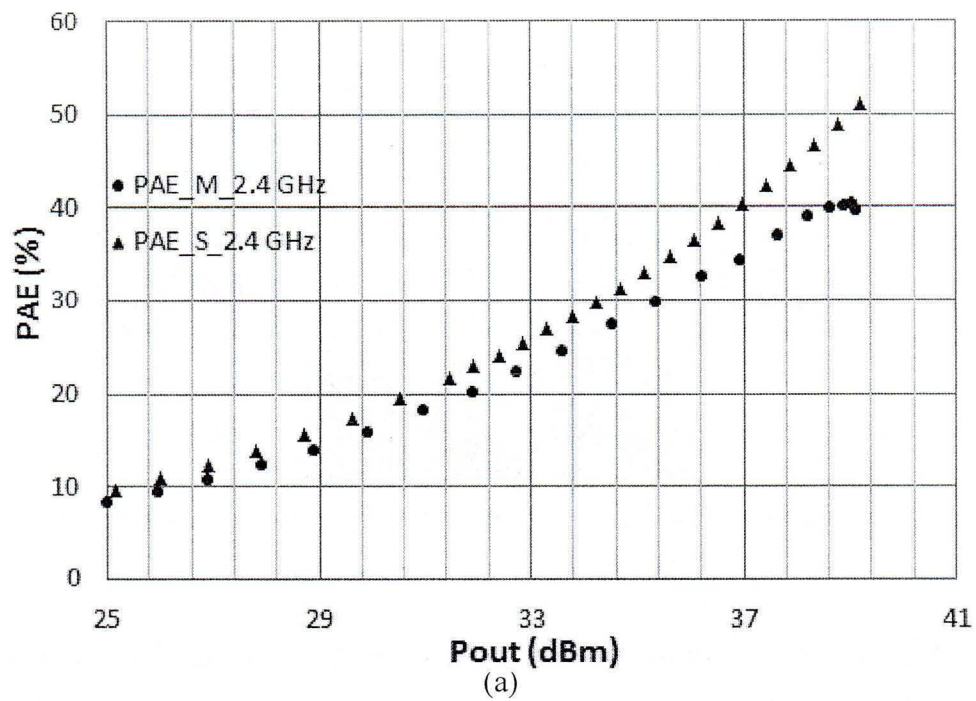


Figure 107: Measured (round point) and simulated (triangular point) results of PAE versus output power of the proposed dual-band power amplifier, (a): 2.4 GHz, and (b): 1.5 GHz

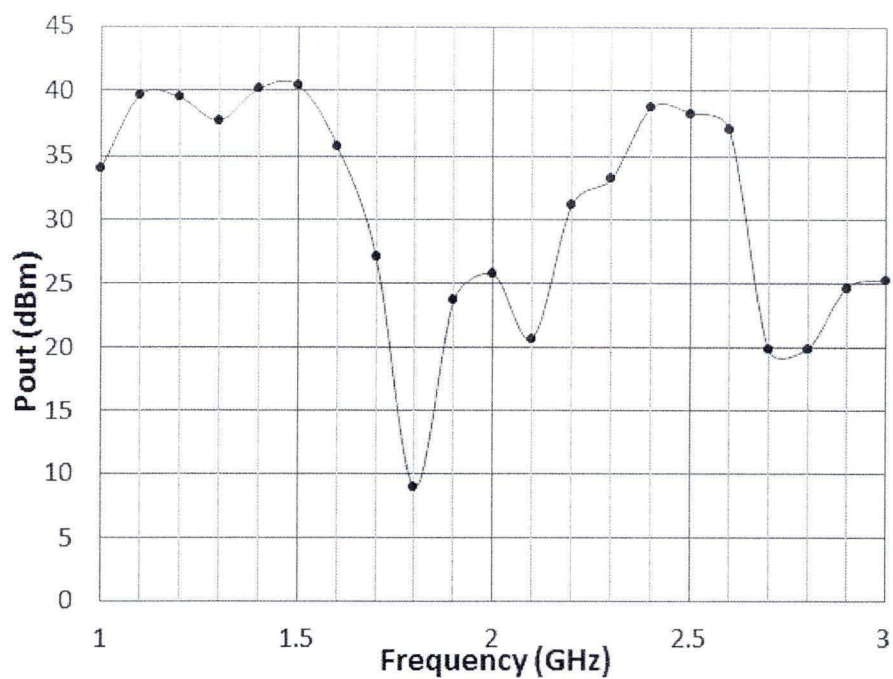


Figure 108: Measured output power versus frequency of the proposed dual-band power amplifier

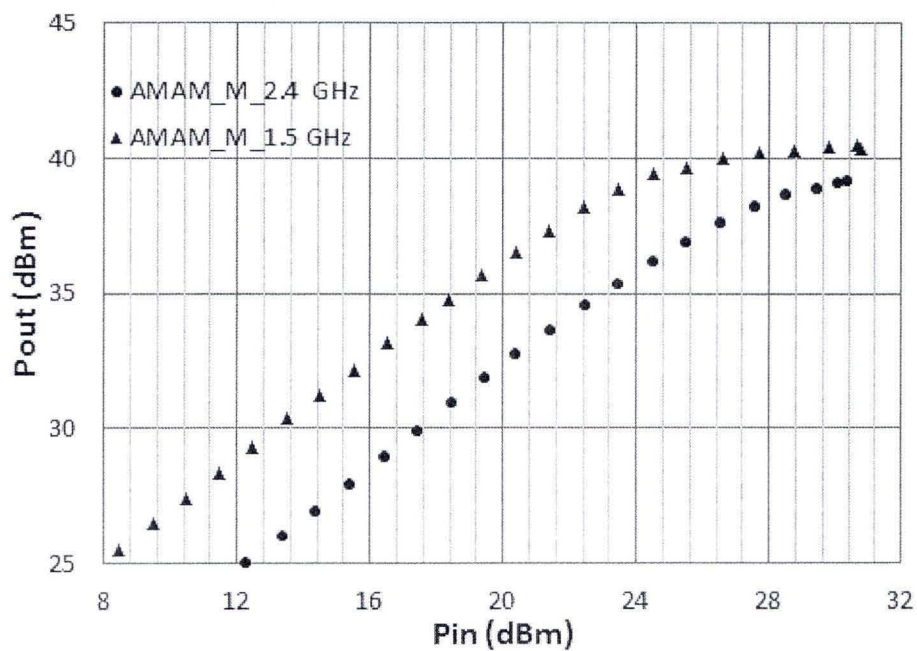


Figure 109: Measured AM-AM curves at 2.4 GHz (round point) and 1.5 GHz (triangular point) of the proposed dual-band power amplifier

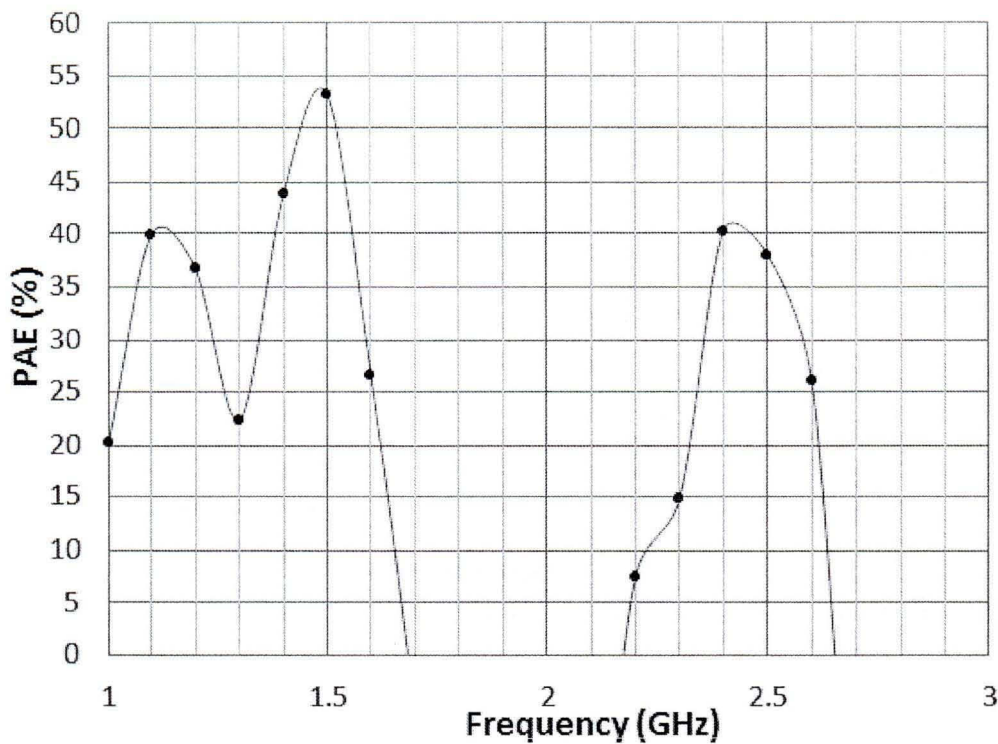
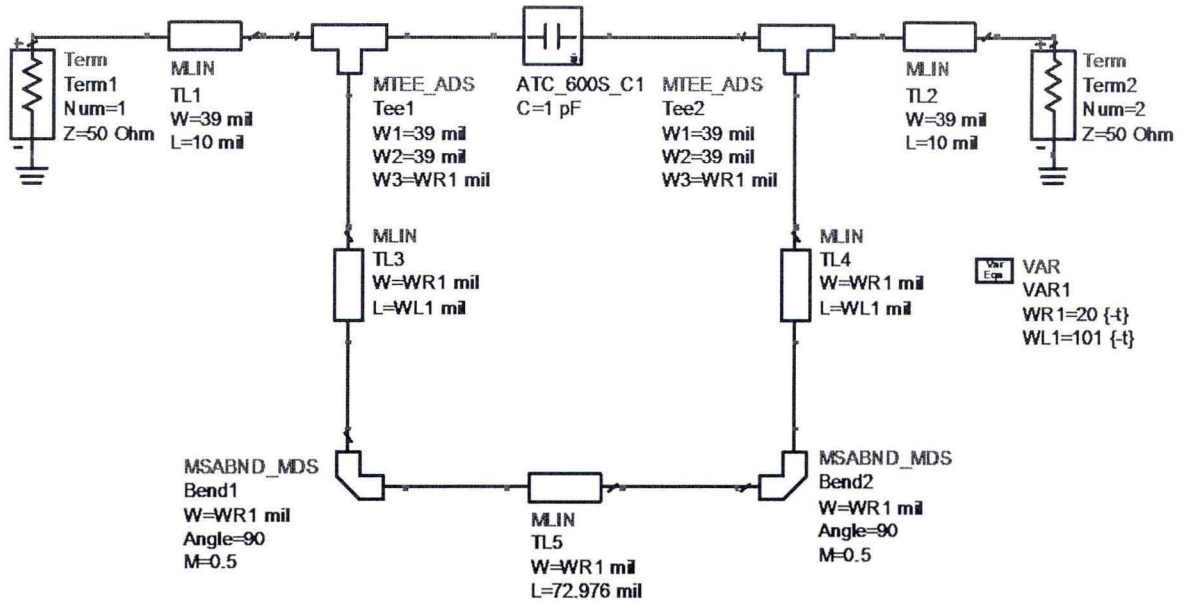


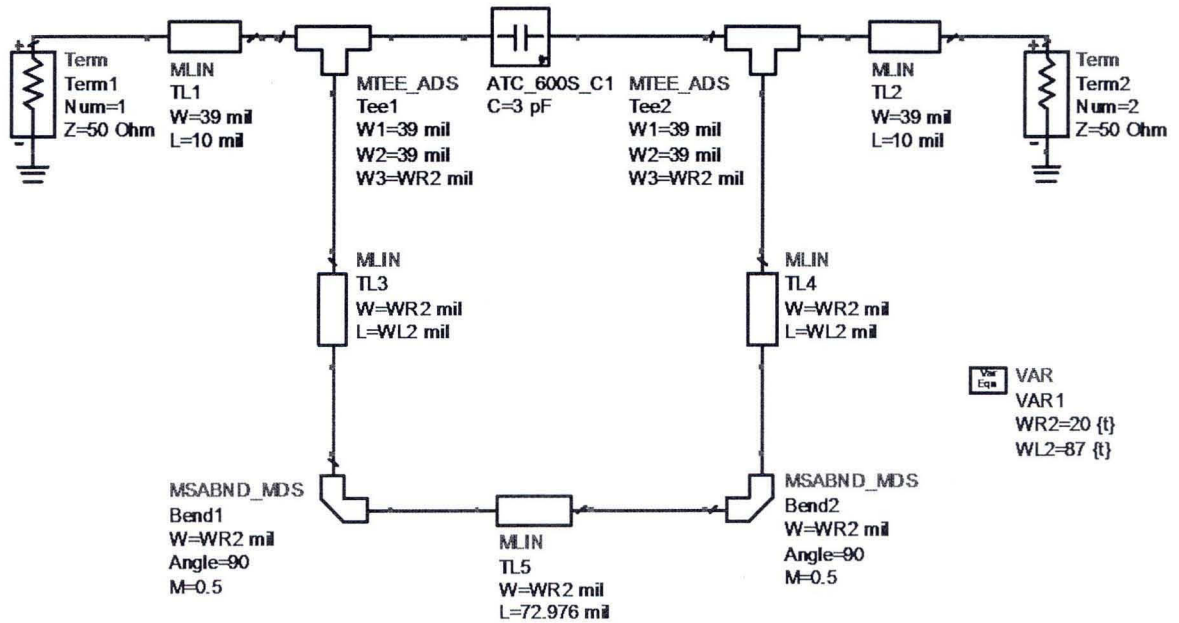
Figure 110: Measured PAE versus frequency of the proposed dual-band power amplifier

b) Dual-band power amplifier with parallel resonator constructed with chip capacitor and microstrip line type inductor

In this part, we propose one new dual-band class AB GaN HEMT PA using relative thin microstrip line as a part of resonator instead of using inductor. The advantages of using microstrip line type inductor in resonator have been mentioned in section 1.2.5 (b.2), such limitless inductance value. The substrate we used for the proposed dual-band PA in this part is TLX-8 from Taconic with dielectric constant of 2.55 and thickness of 31 mils. The ADS schematic diagrams of the resonator constructed by capacitor and microstrip line designed at 2.5 GHz and 1.5 GHz are shown in Fig. 111. The simulated results are shown in Fig. 112.

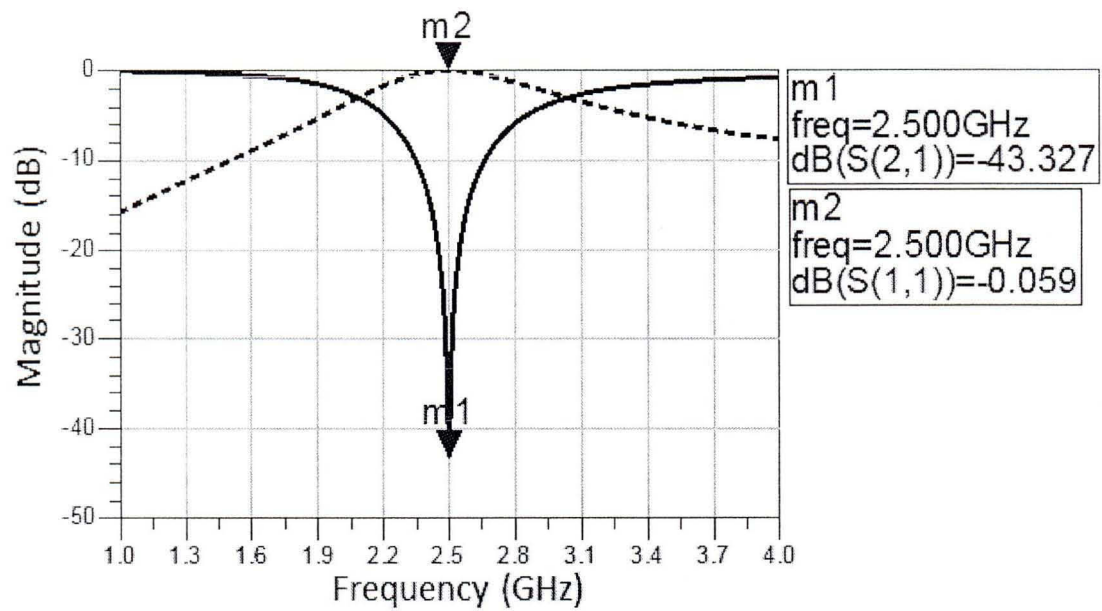


(a)

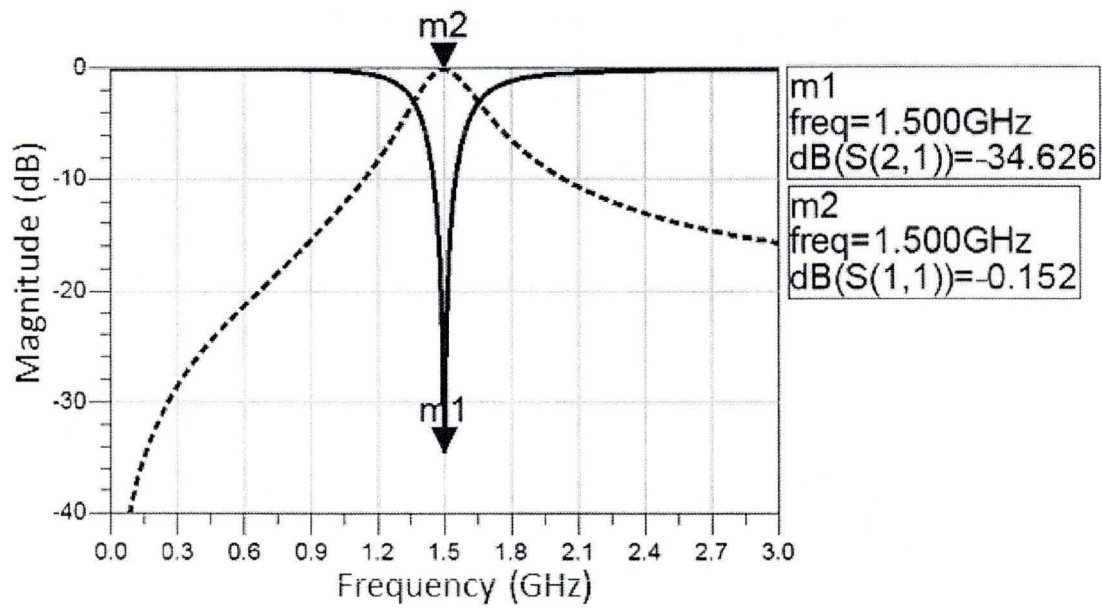


(b)

Figure 111: Resonator consists of capacitor and microstrip line, (a) 2.5 GHz resonator, (b) 1.5 GHz resonator



(a)



(b)

Figure 112: Simulated results of resonator that consists of capacitor and microstrip line, (a) 2.5 GHz, (b) 1.5 GHz

With the principle of dual-band matching network discussed in section 2.2.5 (a), the ADS momentum design schematic diagrams of source and load matching networks using resonator constructed by chip capacitor and microstrip line type inductor are shown in Fig. 113 and Fig. 114, respectively.

The simulated results of the proposed dual-band source and load matching networks using microstrip line type inductor are shown in Fig. 115 (a) and Fig. 115 (b), respectively. The desired source impedance of the proposed dual-band PA is $9.5+j0$ Ohm at 1.5 GHz and $6.4-j4$ Ohm at 2.5 GHz. The desired load impedance of the proposed dual-band PA is $25.2+j19.5$ Ohm at 1.5 GHz and $13.8+j14$ Ohm at 2.5 GHz. Mark *m1* ($9.45-j0.15$ Ohm) and mark *m2* ($6.35-j4.15$ Ohm) show the simulated impedance points of the input matching network (Fig. 113) at 1.5 GHz and 2.5 GHz, respectively. Mark *m3* ($23+j16.6$ Ohm) and mark *m4* ($13.2+j12.95$ Ohm) show the impedance points of the output matching network (Fig. 114) at 1.5 GHz and 2.5GHz, respectively. As shown in Fig. 115 (b), with the dual-band load matching network structure shown in Fig. 114, we can't match the load impedance points to the desired impedance matching points of $25.2+j19.5$ Ohm and $13.8+j14$ Ohm for 1.5 GHz and 2.5 GHz perfectly. To solve this problem, an adjusted dual-band load matching network is proposed in Fig. 116. For this adjusted dual-band load matching network, we add another dual-band matching network at the end of the structure of the load matching network shown in Fig. 114. With the structure shown in Fig. 116, at 1.5 GHz we first match the impedance from $25.2+j19.5$ Ohm to 26.35 Ohm instead of 50 Ohm, then we match the impedance from 26.35 Ohm to 50 Ohm. At 2.5 GHz, because the resonator with 1 pF capacitor has 2.5 GHz resonant frequency, the added dual-band matching network is equal to 50 Ohm transmission line, we can match the impedance of the adjusted dual-band load matching network from $13.8+j14$ Ohm to 50 Ohm directly. The load impedance matching at 1.5 GHz and 2.5 GHz is achieved perfectly by using the proposed adjusted dual-band load matching network shown in Fig. 116. The simulated result of the adjusted dual-band load matching network is shown in Fig. 117.

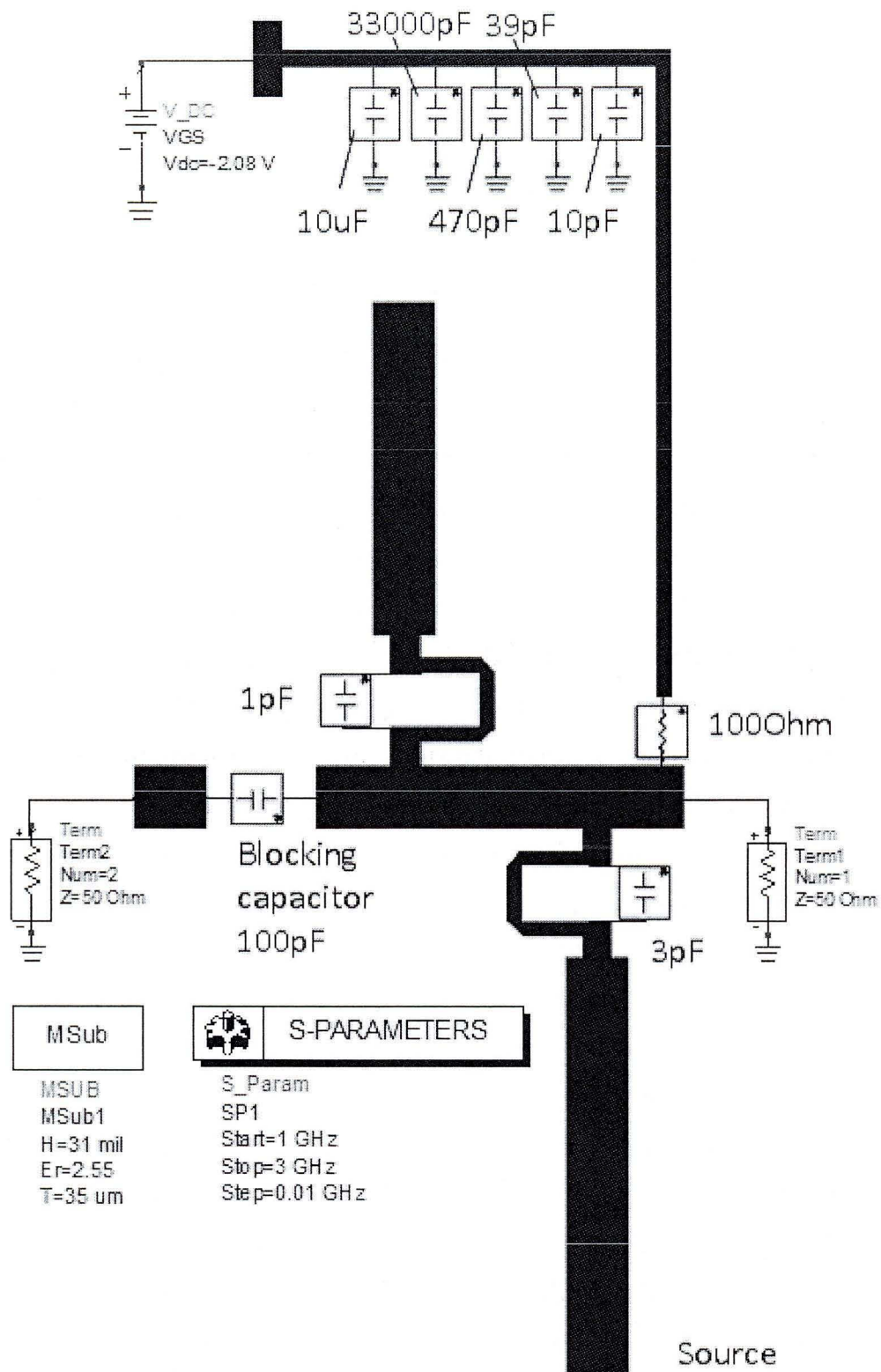


Figure 113: ADS momentum design schematic diagram of the proposed dual-band source matching network using resonators with microstrip line type inductor

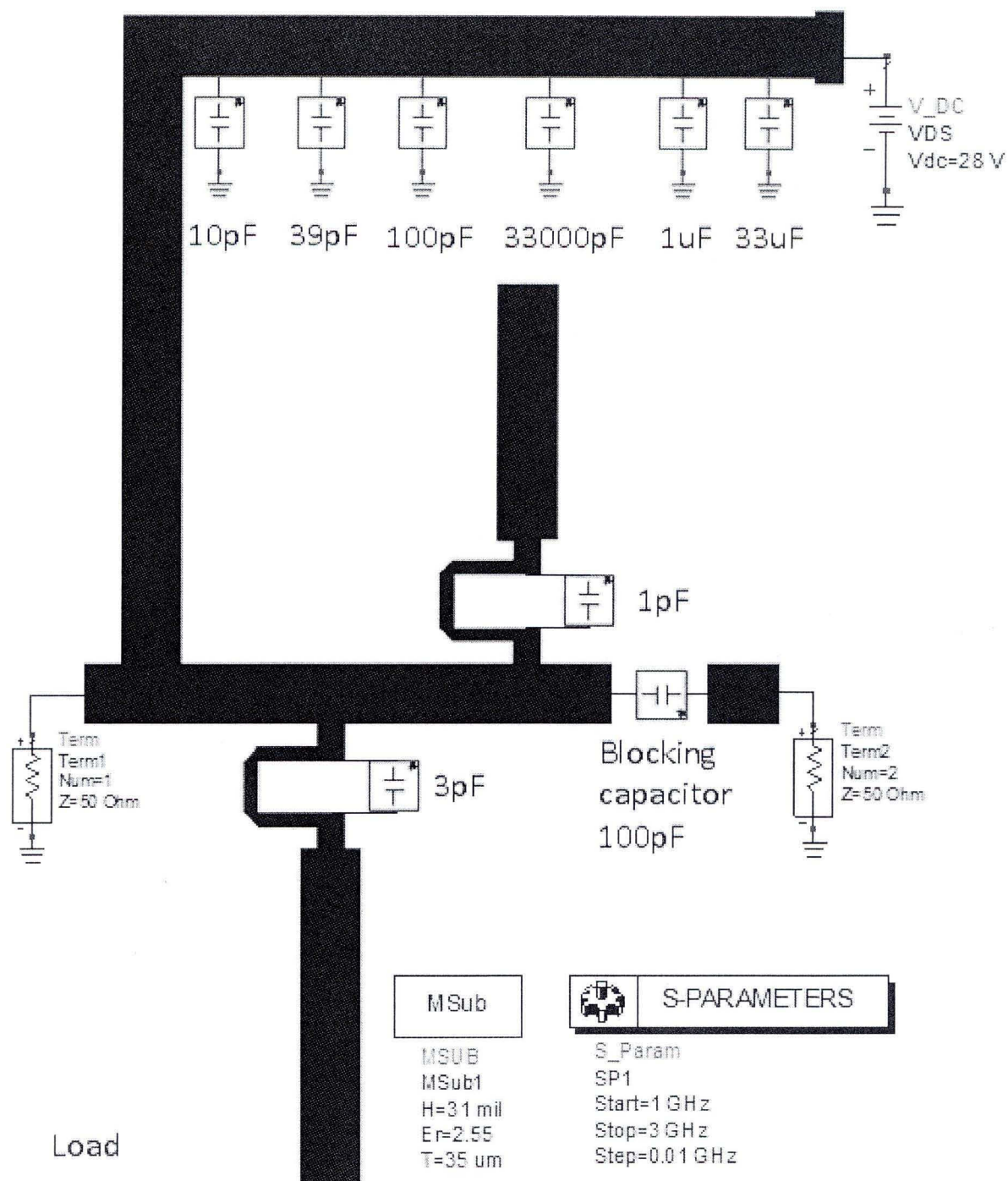


Figure 114: ADS momentum design schematic diagram of the proposed dual-band load matching network using resonators with microstrip line type inductor

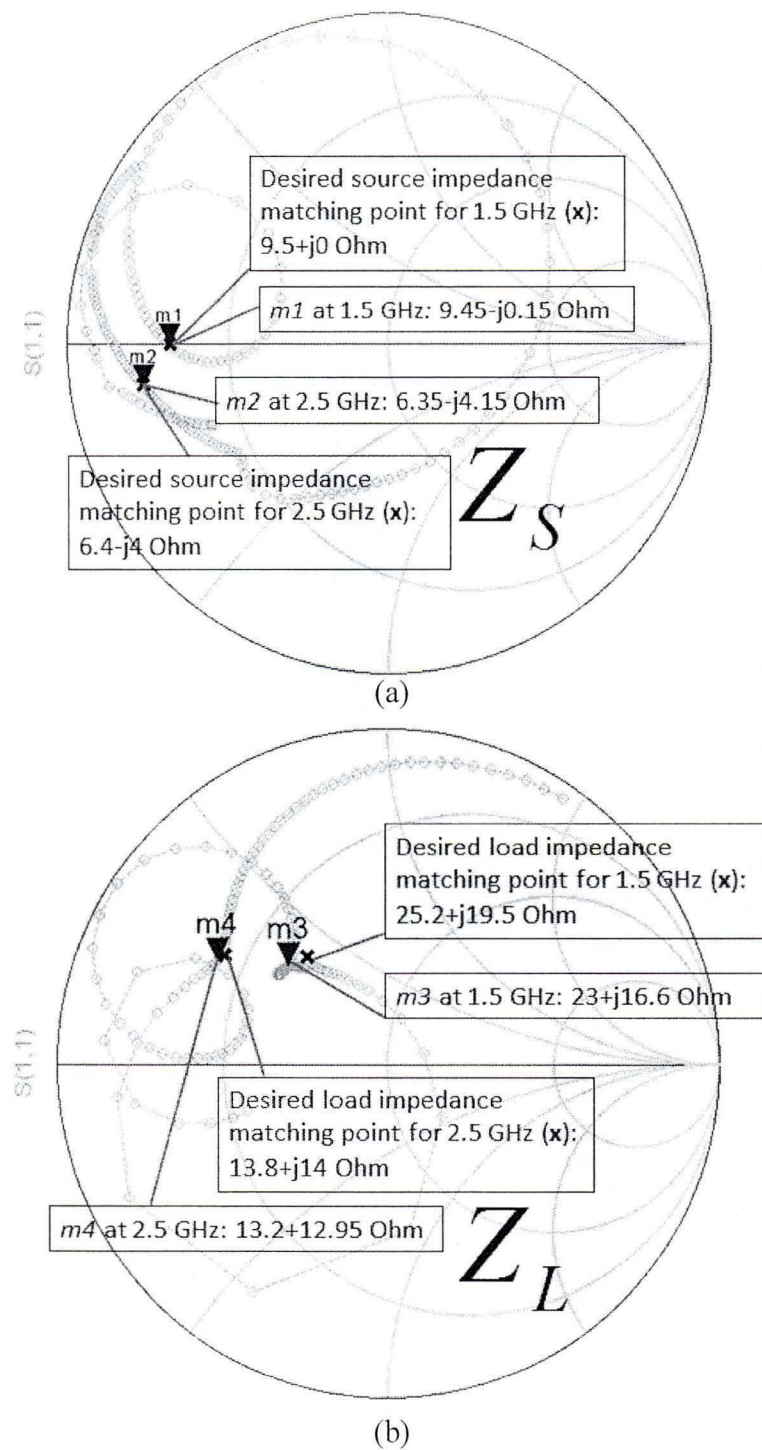


Figure 115: Simulated results of the proposed dual-band matching networks using resonators with microstrip line type inductor, (a) source, and (b) load, with 0.01 GHz step

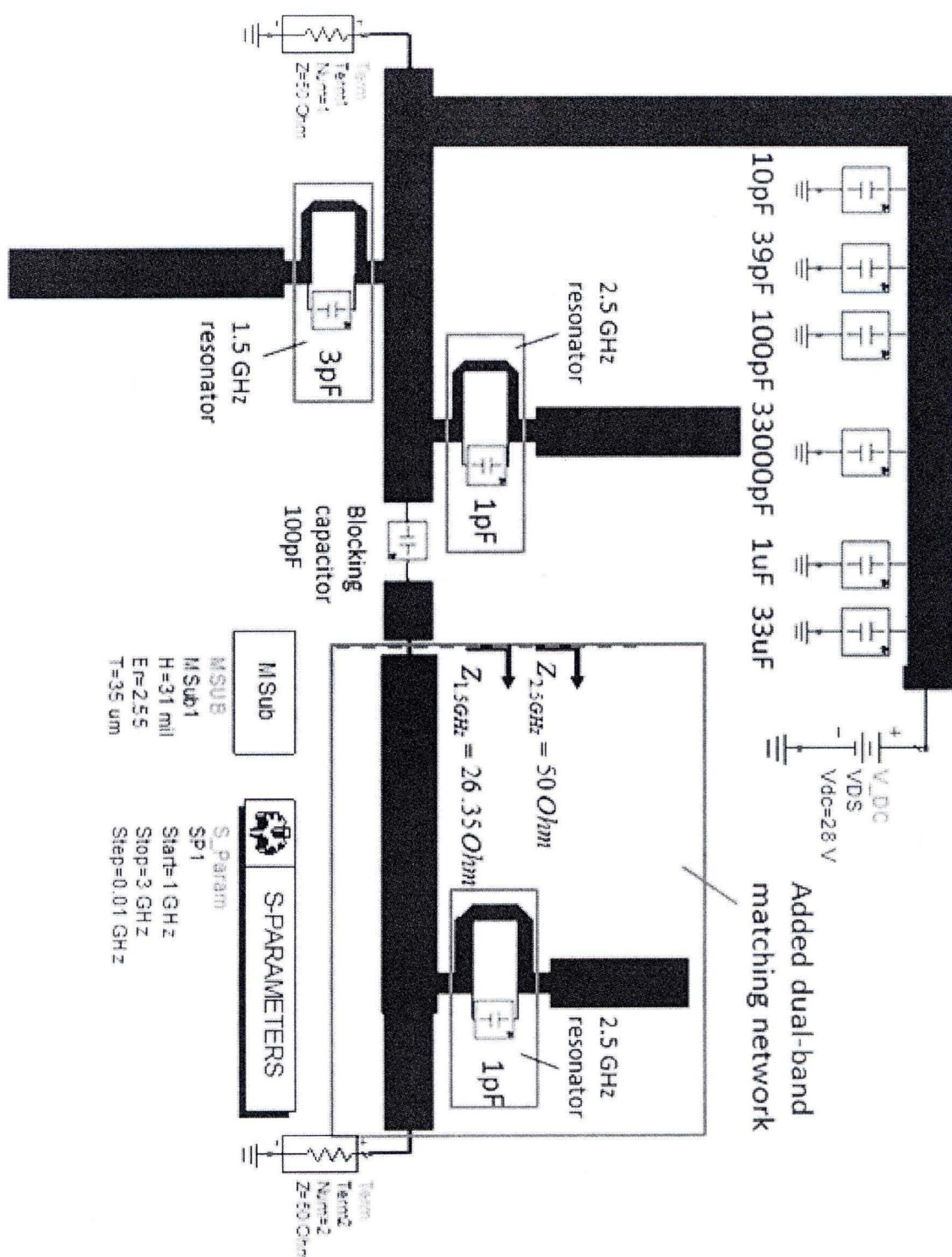


Figure 116: The adjusted dual-band load matching network by adding another dual-band matching network after the structure shown in Fig. 114

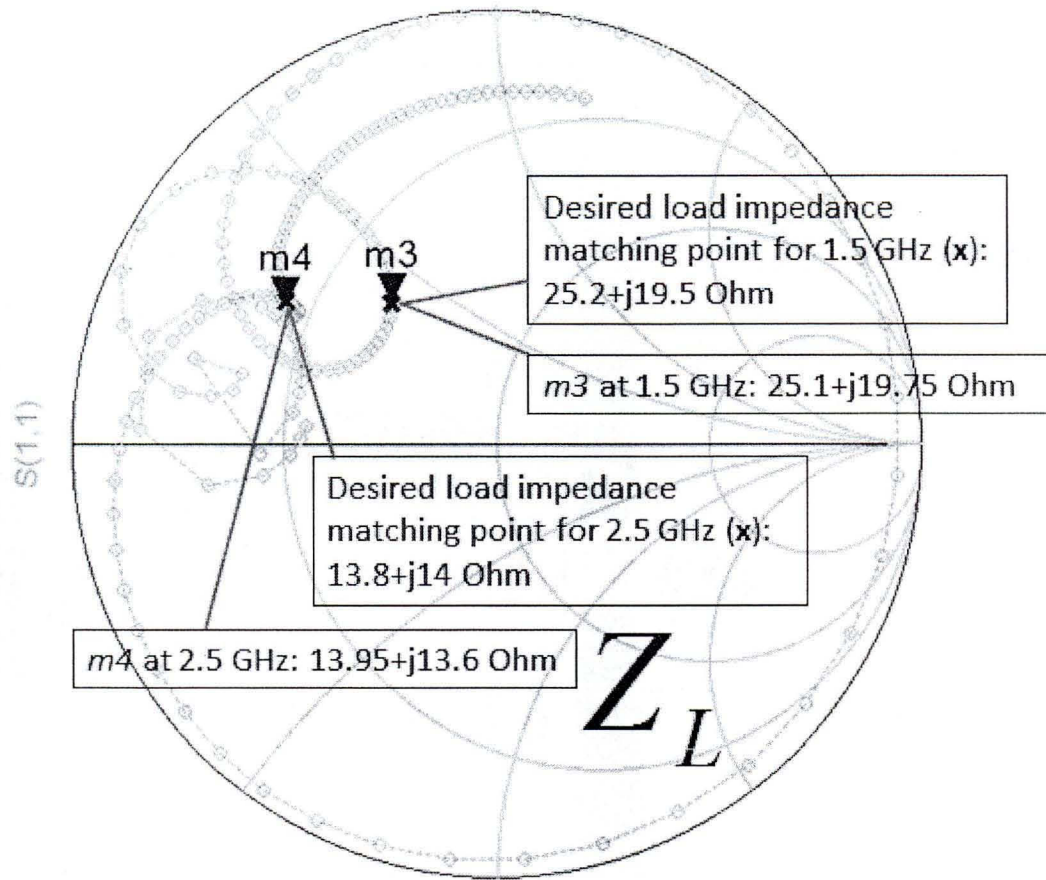


Figure 117: Simulated results of the adjusted dual-band load matching network with frequency step 0.01 GHz

The total layout of the proposed dual-band class AB GaN HEMT PA is shown in Fig. 118. The fabricated dual-band PA circuit is shown in Fig. 119. The transistor embedded in this dual-band PA is CGH40010P with $V_{gs} = -2.7$ V and $V_{ds} = 28$ V. The proposed dual-band PA is measured by the signal generator of R&S SMBV100A and the signal analyzer of R&S FSV. DC power analyzer N6705B from Agilent is used for supplying both V_{gs} and V_{ds} DC power and for measuring the current value. The measured results of the proposed dual-band PA in this part are shown in Fig. 120 to Fig. 122.

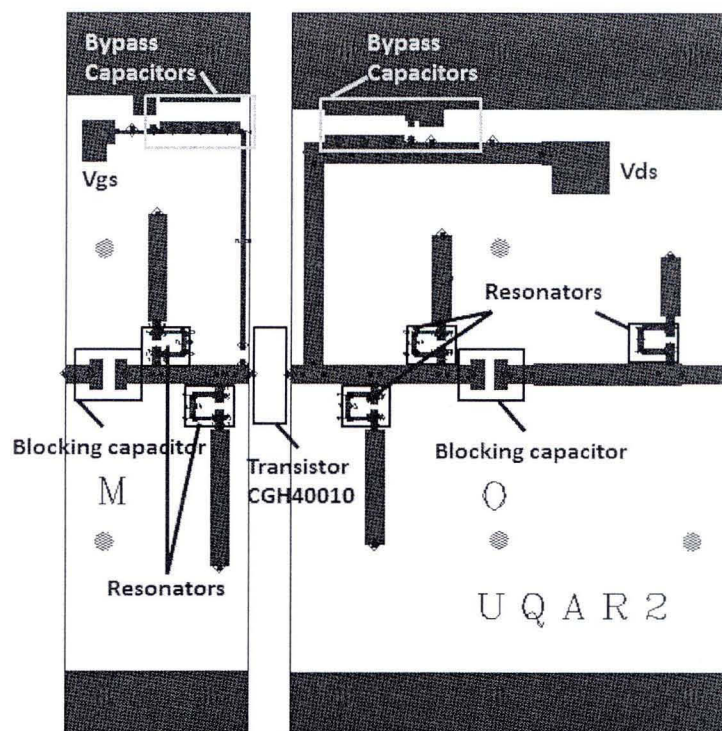


Figure 118: Total layout of the proposed dual-band power amplifier using resonators with microstrip line

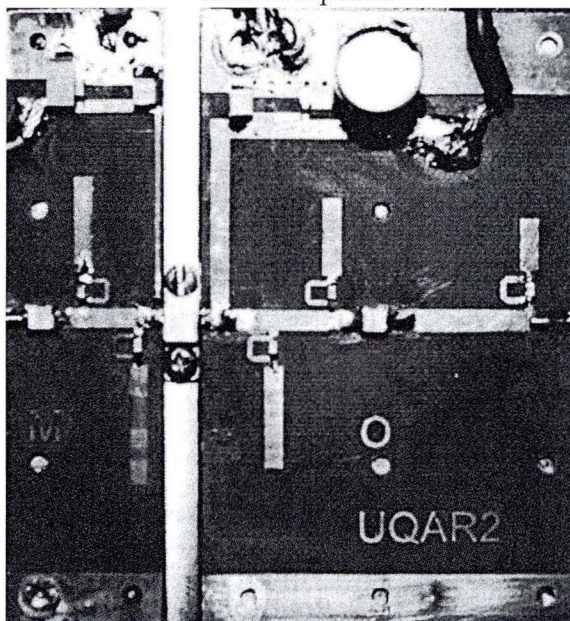


Figure 119: Fabricated circuit of the proposed dual-band power amplifier using resonators with microstrip line

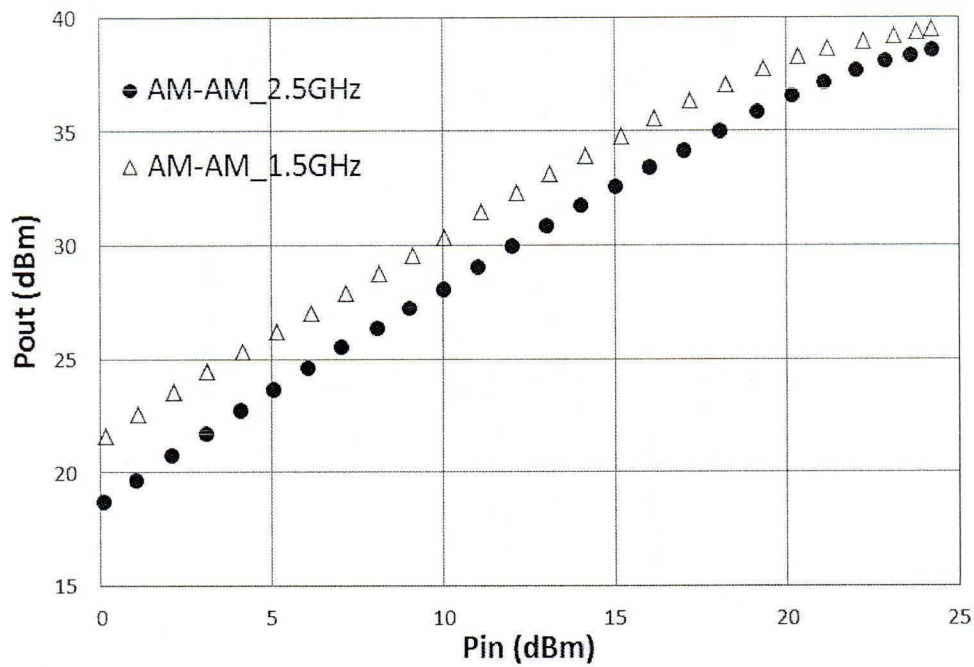


Figure 120: Measured AM-AM curves at 2.5 GHz (round point) and 1.5 GHz (triangular point) of the proposed dual-band power amplifier shown in Fig. 119

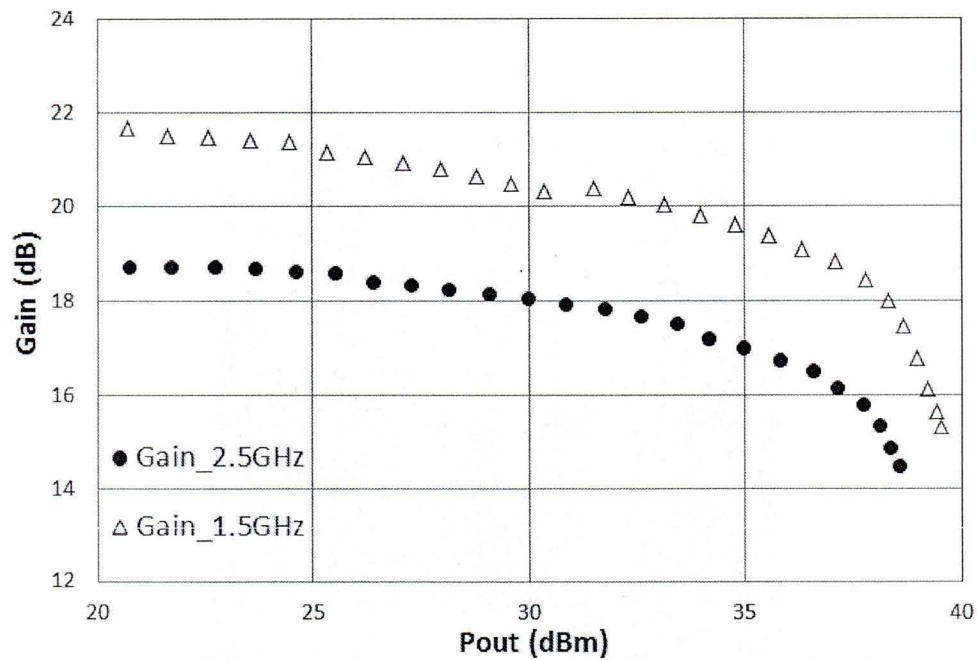


Figure 121: Measured gain curves at 2.5 GHz (round point) and 1.5 GHz (triangular point) of the proposed dual-band power amplifier shown in Fig. 119

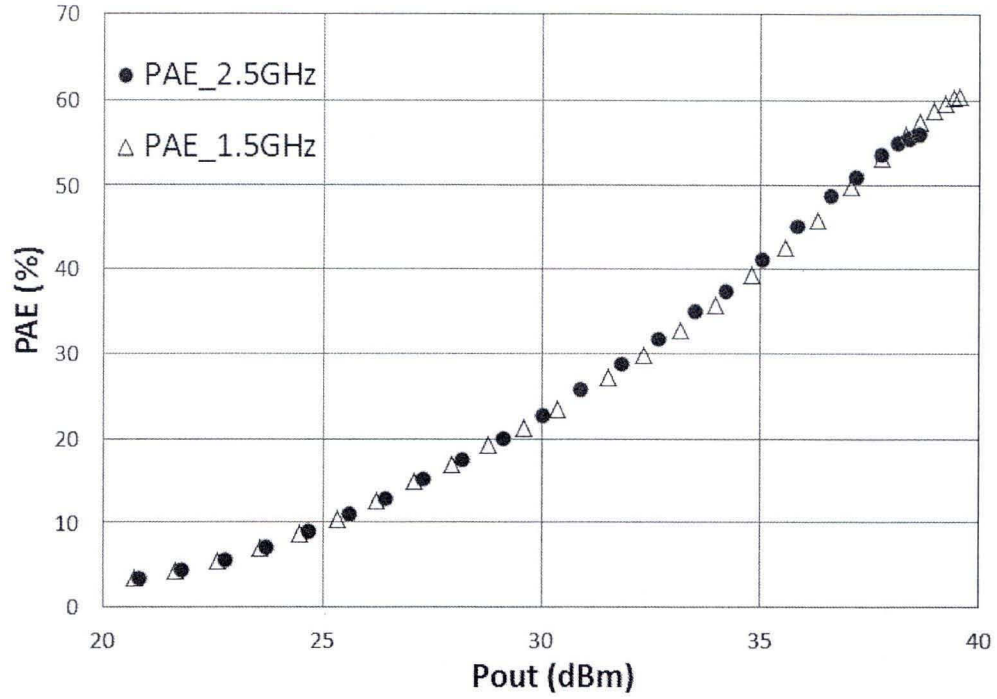


Figure 122: Measured PAE curves at 2.5 GHz (round point) and 1.5 GHz (triangular point) of the proposed dual-band power amplifier shown in Fig. 119

According to Fig. 120 to Fig. 122, the maximum measured output power at 2.5 GHz and 1.5 GHz are 38.60 dBm with input power 24.17 dBm and 39.53 dBm with input power 24.20 dBm, respectively; the maximum measured gain at 2.5 GHz and 1.5 GHz are 18.72 dB and 21.69 dB, respectively; the maximum measured PAE at 2.5 GHz and 1.5 GHz are 56.17% with output power 38.60 dBm and 60.53% with output power 39.53 dBm, respectively.

2.2.7 New concurrent tri-band power amplifier (Wang *et al.*, 2012 b)

The proposed new tri-band PA has been published by me in (Wang *et al.*, 2012 b). The principle of tri-band matching network has been discussed in section 2.2.5 (b) already. To demonstrate the proposed tri-band matching network, in this section we designed and fabricated one tri-band class AB PA working at 1 GHz, 1.5 GHz, and 2.5 GHz. The substrate we used in this project is TLX-8 from Taconic with dielectric constant of 2.55 and thickness of 31mils. The transistor we used is CGH40010 from CREE Inc. ADS momentum simulation with Modelithics model has been employed for this design.

The parallel resonator groups designed by ADS as a frequency selection element to pass signal at 2.5 GHz, 1.5 GHz, and 1 GHz separately while blocking the signal generated at the remaining two operation frequency bands are shown in Fig. 123. Capacitor and inductor models from Modelithics are employed. For example, in Fig. 123 (a), ATC 600S capacitor model with capacitance 4.7 pF and CLC 0603HP inductor model with 3.9 nH are used to make the resonator whose resonant frequency is 1 GHz; ATC 600S capacitor model with capacitance 2 pF and CLC 0603HP inductor model with 4.3 nH are used to make the resonator whose resonant frequency is 1.5 GHz. Connecting these two resonator together, signal at 1 GHz and 1.5 GHz is blocked effectively while signal at 2.5 GHz can pass through this frequency selection element. With the same principle, the design schematic diagrams of the frequency selection elements to pass the signal at 1.5 GHz and 1 GHz are shown in Fig. 123 (b) and Fig. 123 (c), respectively. The simulated results of these frequency selection elements are shown in Fig. 124.

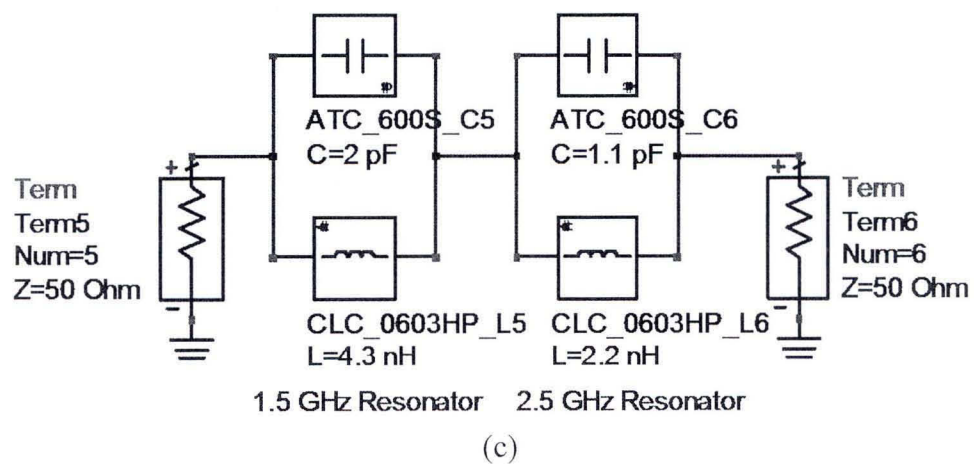
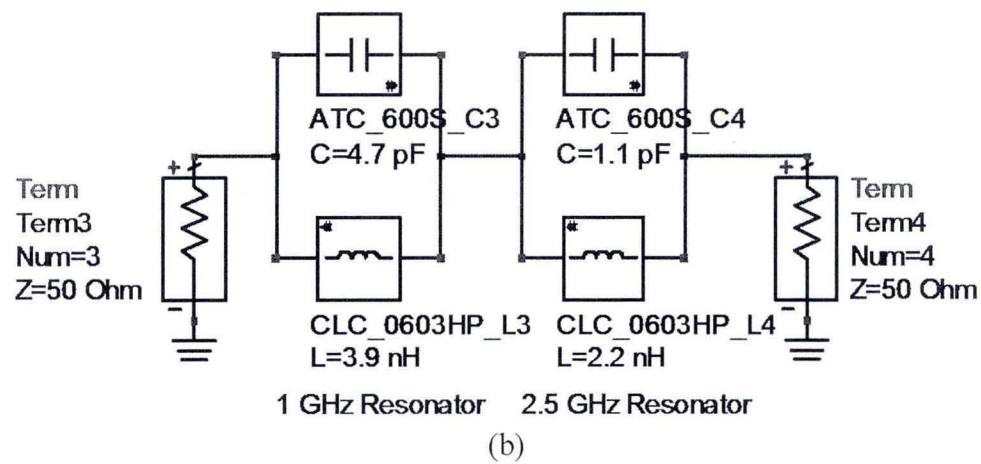
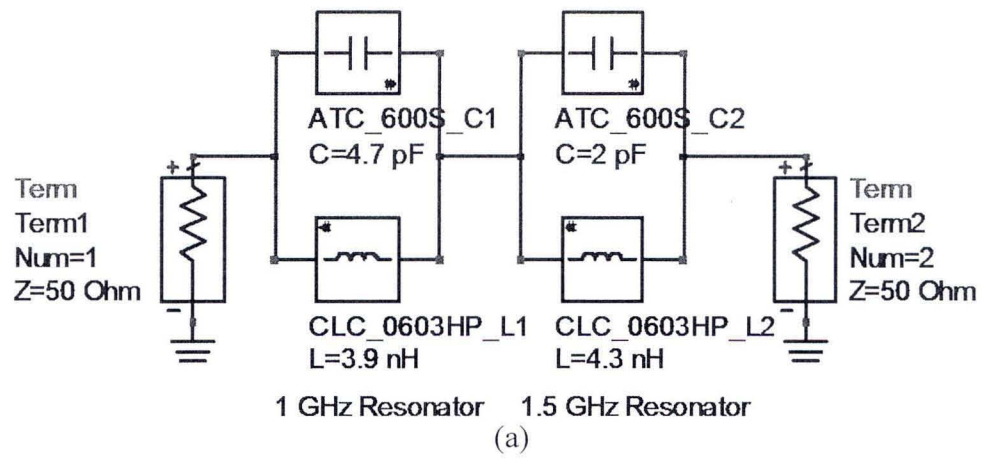


Figure 123: Resonator groups designed to pass the signal at (a): 2.5 GHz, (b): 1.5 GHz, and (c): 1 GHz

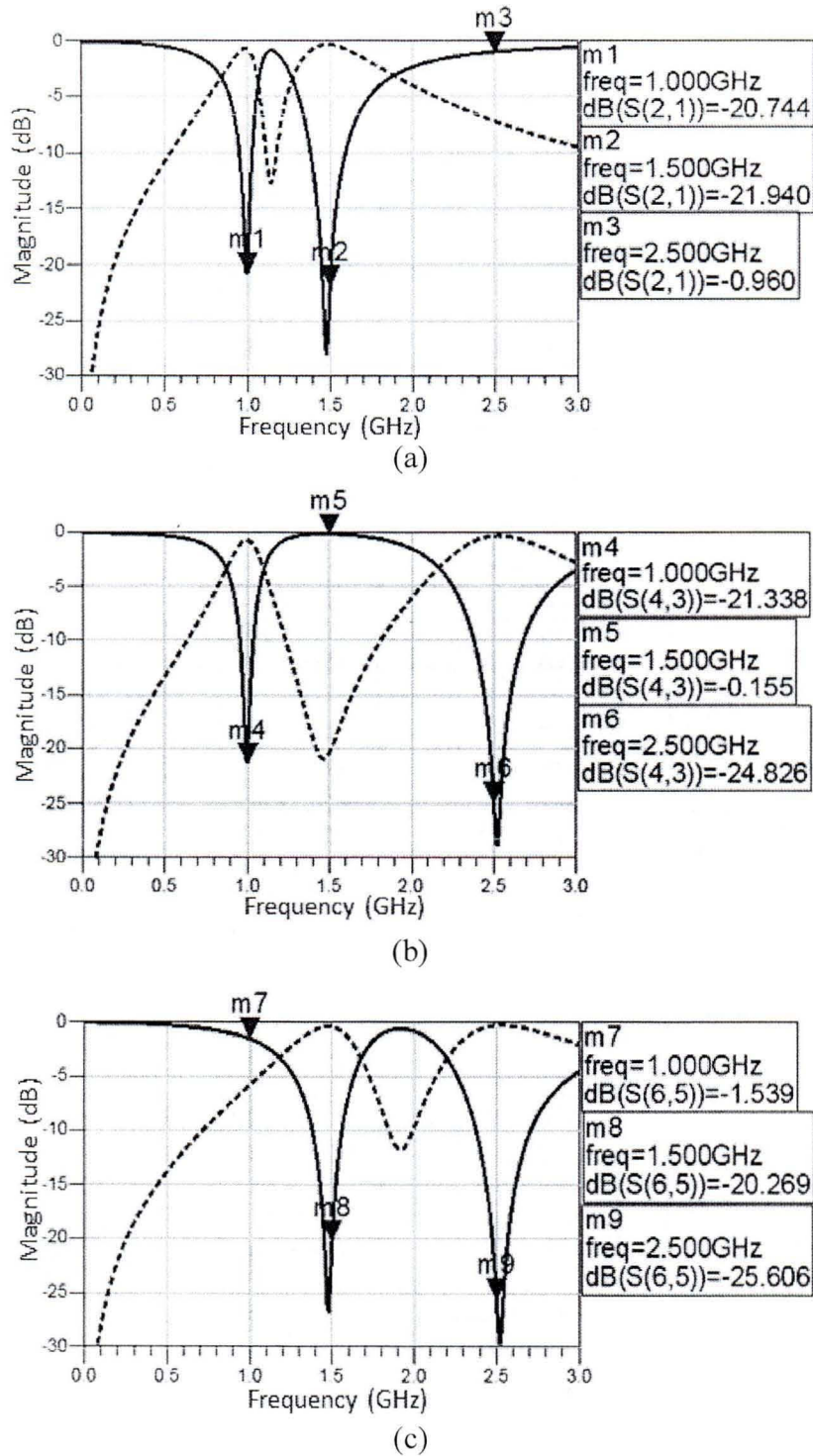


Figure 124: ADS simulated results of the resonator groups designed to pass the signal at

(a): 2.5 GHz, (b): 1.5 GHz, and (c): 1 GHz

The desired load impedance point for 1 GHz is $37.8 + j19.8 \text{ Ohm}$ as shown in Fig. 125 where Z_0 is 50 Ohm. The simplest L-type matching network structure designed for 1 GHz is shown in Fig. 126. The ideal electrical length of the series transmission line is 72.84° . According to the simplest L-type matching network, the ADS design schematic diagram of the matching network for 1 GHz using substrate TLX-8 is shown in Fig. 127.

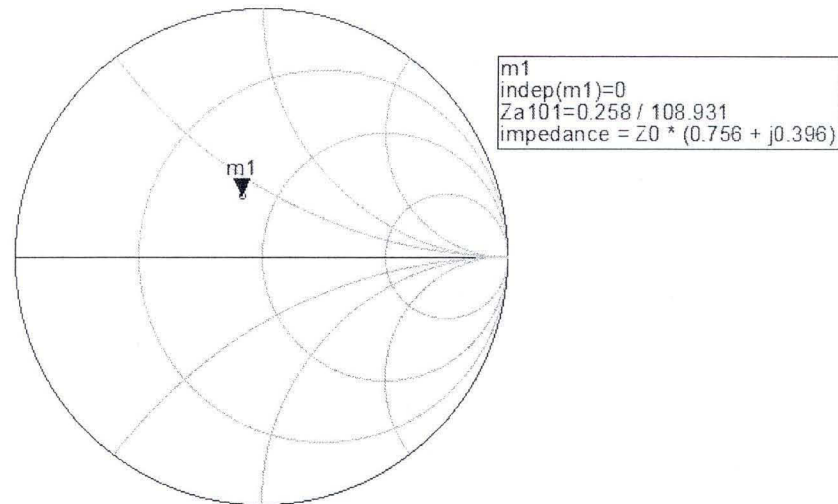


Figure 125: The desired load impedance point of CGH40010 for 1 GHz

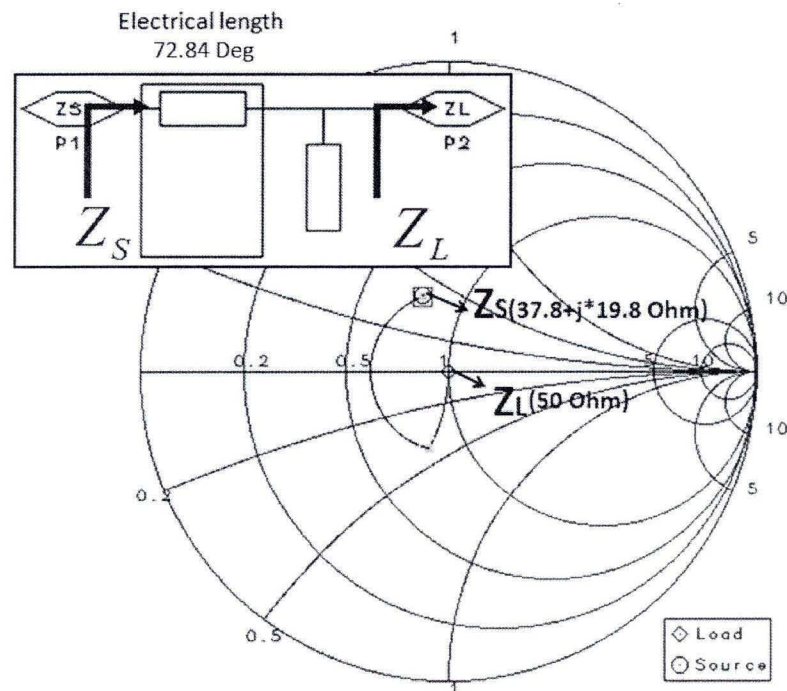


Figure 126: The simplest L-type matching network for 1 GHz

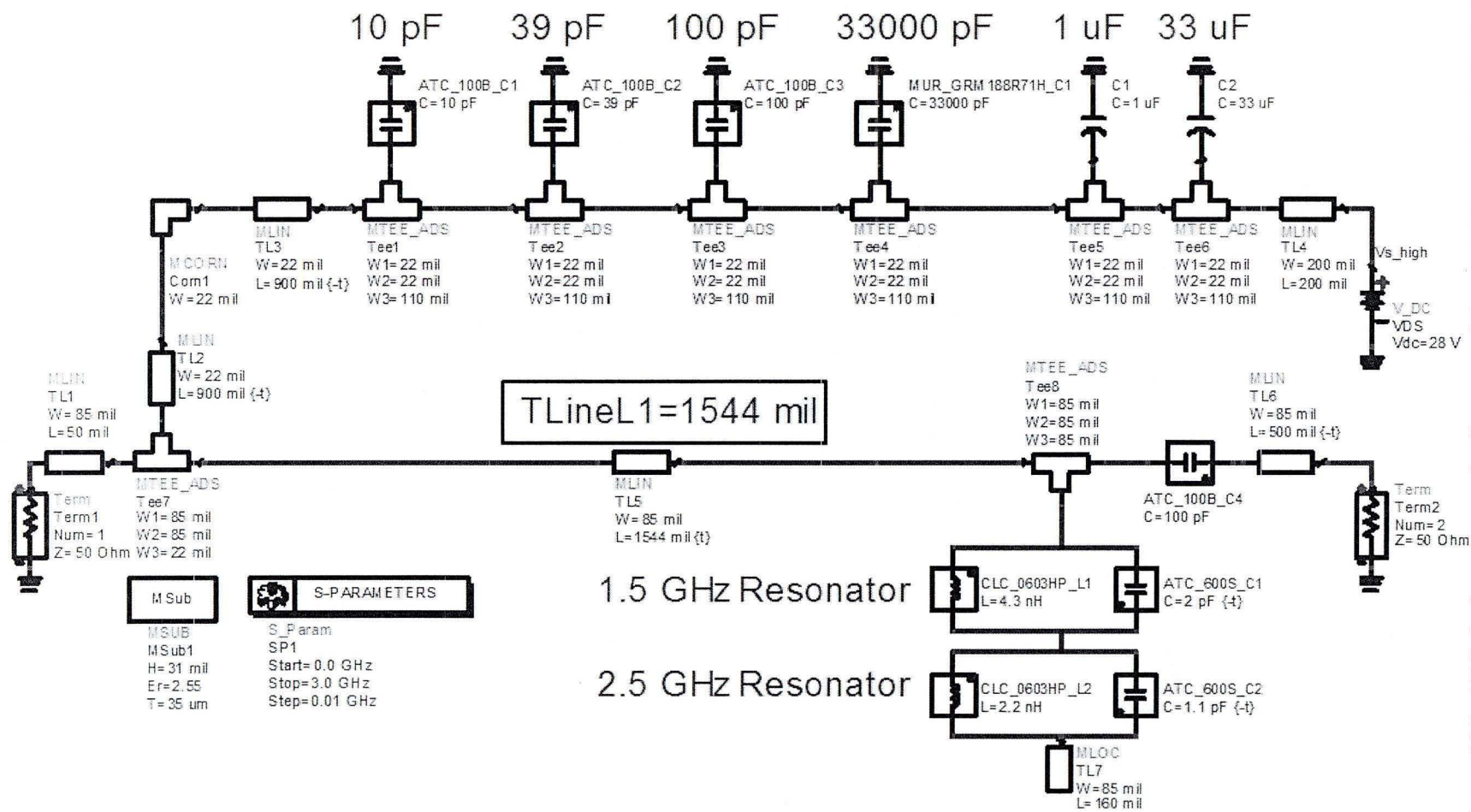


Figure 127: ADS design schematic diagram of the matching network for 1 GHz

The simulated result of the simplest L-type matching network design schematic diagram in Fig. 127 is shown in Fig. 128 where Z_0 is 50 Ohm.

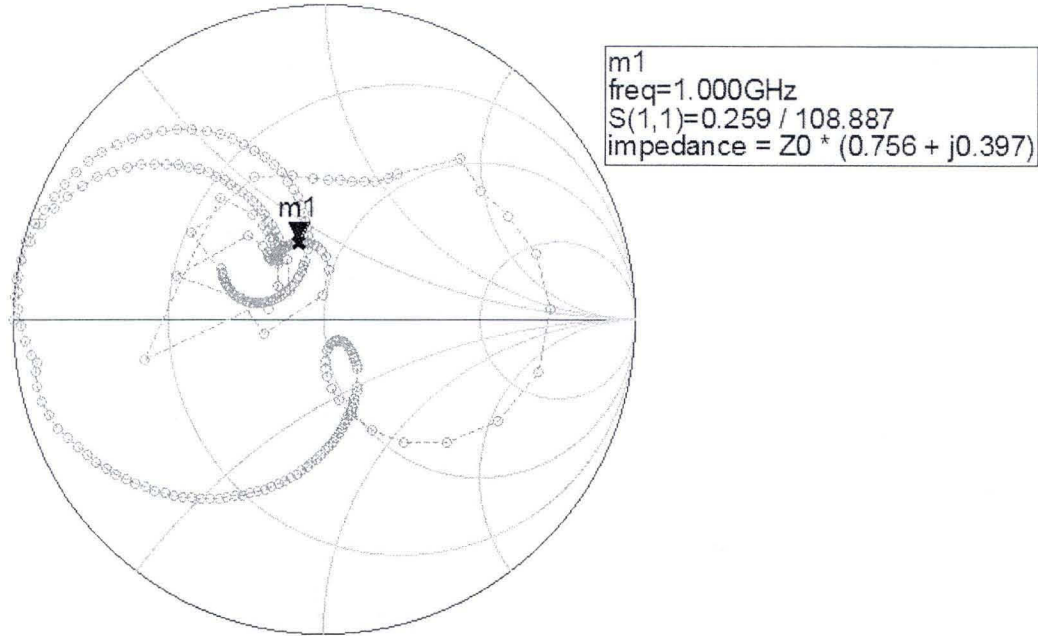


Figure 128: Simulated result of the 1 GHz matching network shown in Fig. 127 with frequency step 0.01 GHz

As shown in Fig. 127, the physical length of the series microstrip line $TLineL1$ is 1544 mil for 1 GHz load matching network. With the same electrical length, lower frequency is corresponding to larger size. In this project, we choose load impedance $37.8+j19.8$ Ohm for 1 GHz, $25.2+j19.5$ Ohm for 1.5 GHz, and $13.8+j14$ Ohm for 2.5 GHz. Using the tri-band matching network principle discussed in section 2.2.5 (b), the ADS design schematic diagram of the tri-band matching network for 1 GHz, 1.5 GHz, and 2.5 GHz is shown in Fig. 129. The simulated result of the proposed tri-band load matching network in Fig. 129 is shown in Fig. 130. As we noticed, in Fig. 129, the length of $TLineL2$ is 850 mil only for 1 GHz. The total tri-band matching network size is decided by the L-type matching network size designed for the lowest operation frequency. To reduce the size of the tri-band load matching network what means to reduce the length of $TLineL2$, the advanced ADS momentum design schematic diagram is shown in Fig. 131.

S_Param
SP1
Start=0.0 GHz
Stop=3.0 GHz
Step=0.01 GHz

MSub

MSUB
MSub1
H=31 mμ
Er=2.55
T=35 μm

MIN
TL1
W=85mm
L=50mm

Term
Term1
Num=

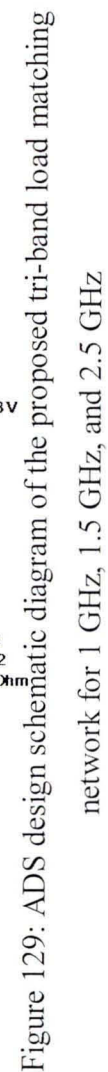


Figure 129: ADS design schematic diagram of the proposed tri-band load matching network for 1 GHz, 1.5 GHz, and 2.5 GHz

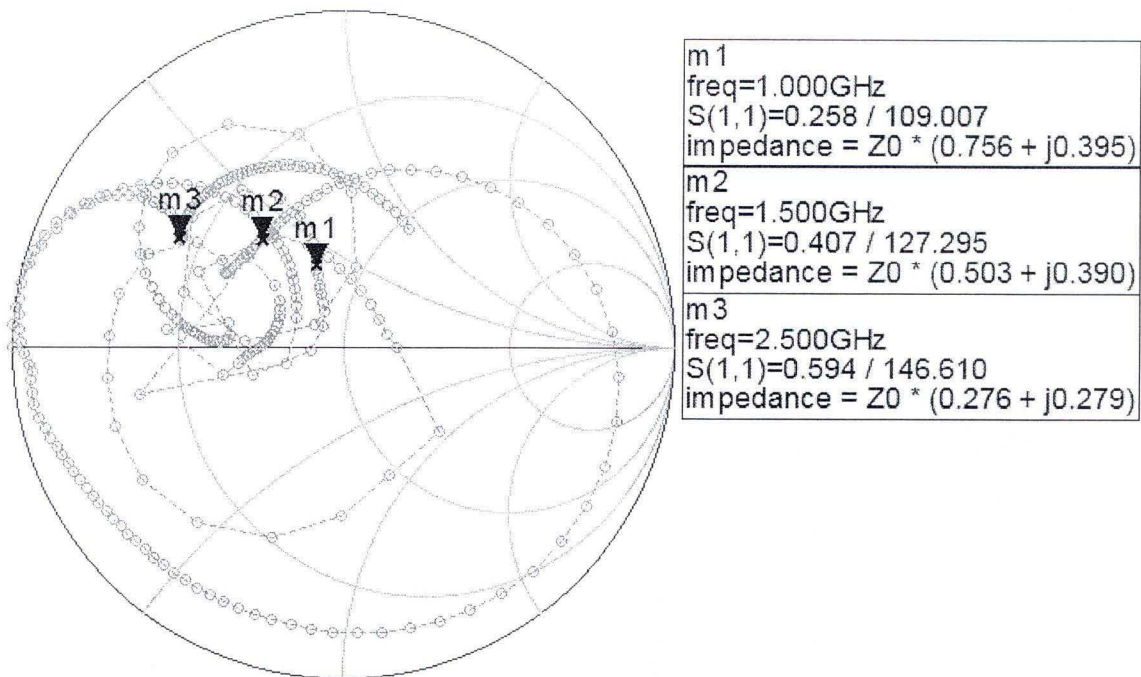


Figure 130: Simulated result of the proposed tri-band load matching network shown in Fig. 129, frequency step: 0.01 GHz

Fig. 131 shows the ADS momentum design schematic diagram of the proposed advanced tri-band load matching network. As shown in Fig. 125, the desired impedance point for 1 GHz is $37.8 + j19.8$ Ohm. We can use the bias circuit as the matching network for 1 GHz as shown in Fig. 131. After the bias circuit, we designed the load matching network for 1.5 GHz and 2.5 GHz using the frequency selection elements to pass the signal at 1.5 GHz and 2.5 GHz separately. With the advanced tri-band matching network structure, we just need two frequency selection elements instead of three, and the total size of the tri-band matching network is determined by 1.5 GHz, compared with the structure shown in Fig. 129, the size is smaller, the total length of the proposed tri-band output matching network is reduced by more than 800 mil. At 1 GHz, the equivalent matching network circuit of the proposed advanced tri-band matching network circuit is shown in Fig. 132. The simulated result of the proposed advanced tri-band matching network is shown in Fig. 133.

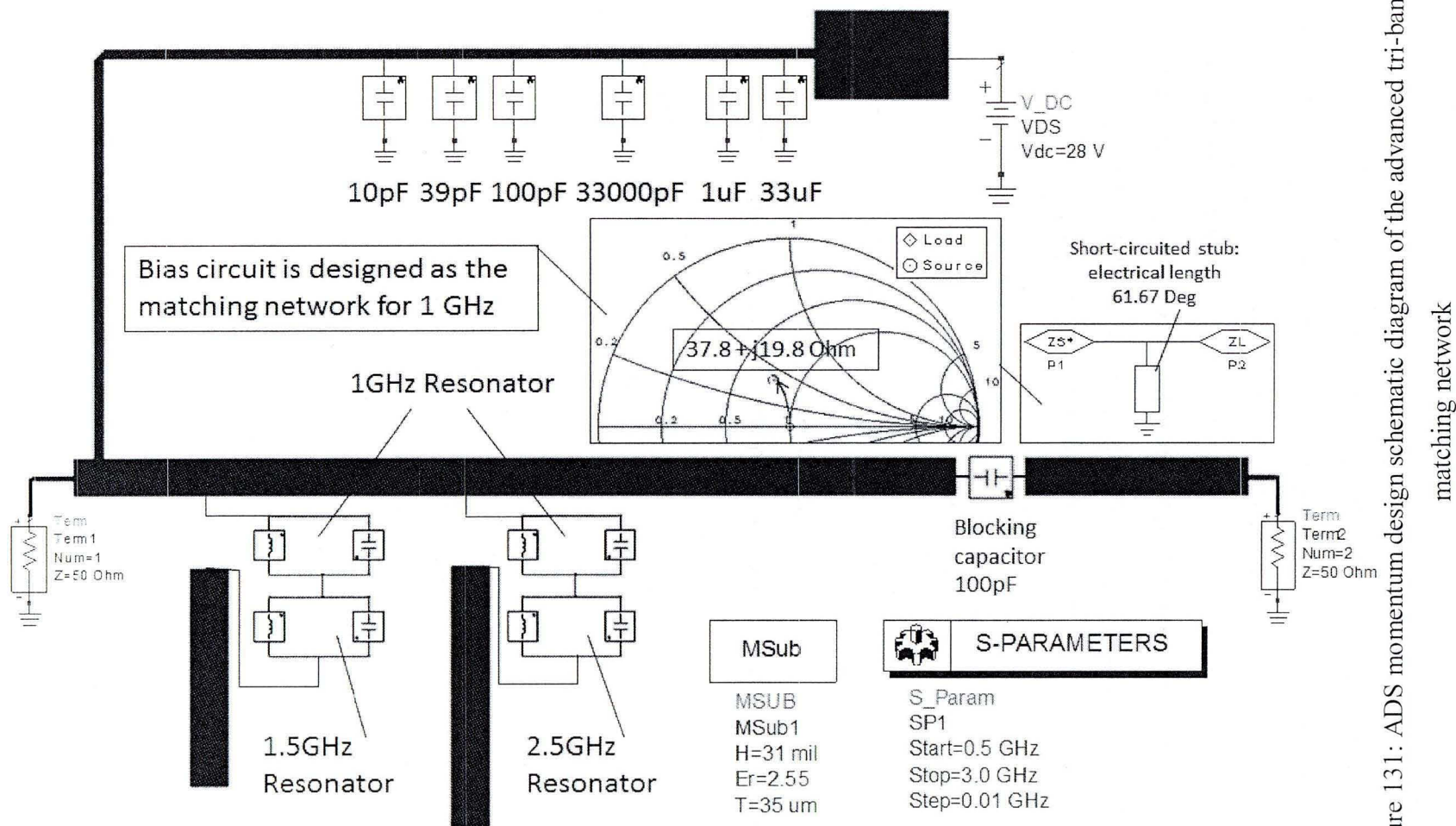


Figure 131: ADS momentum design schematic diagram of the advanced tri-band load matching network

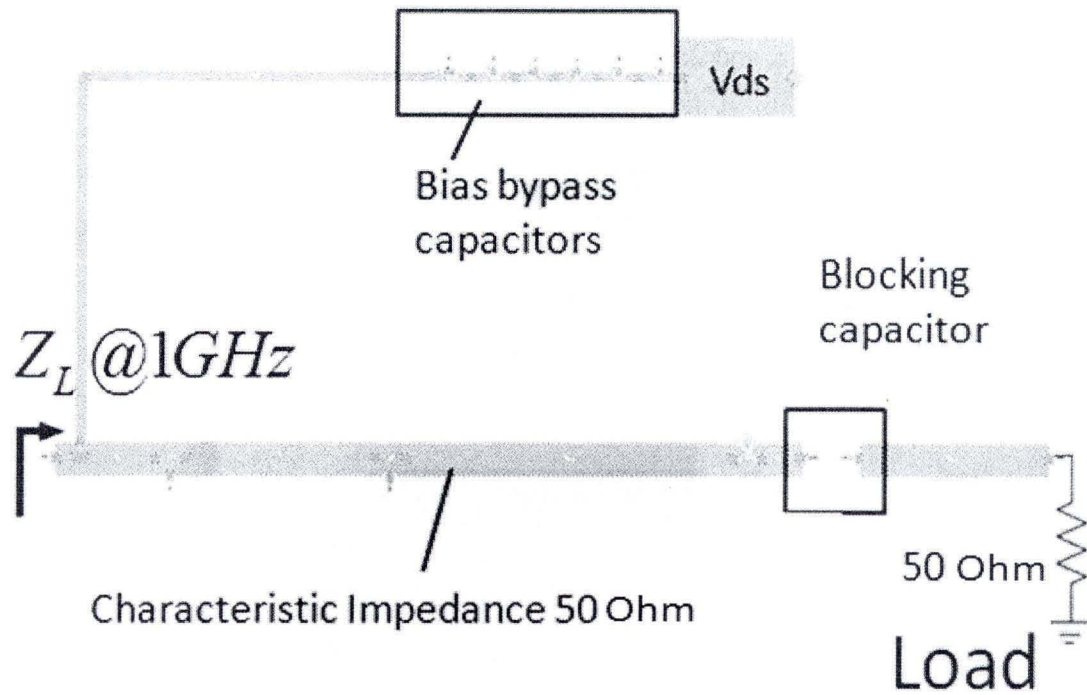


Figure 132: Equivalent matching circuit of the proposed advanced tri-band load matching network shown in Fig. 131 at 1 GHz

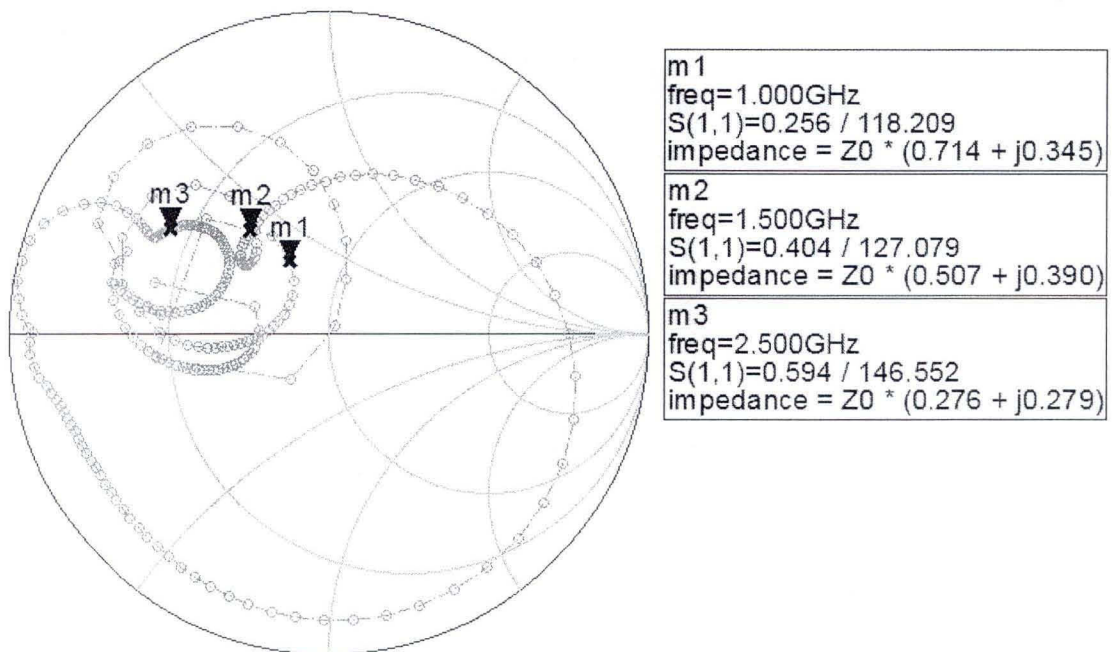


Figure 133: Simulated result of the proposed advanced tri-band load matching network

The ADS momentum design schematic diagram of the tri-band source matching network for 1 GHz, 1.5 GHz, and 2.5 GHz is shown in Fig. 134. The simulated result of the tri-band source matching network is shown in Fig. 135.

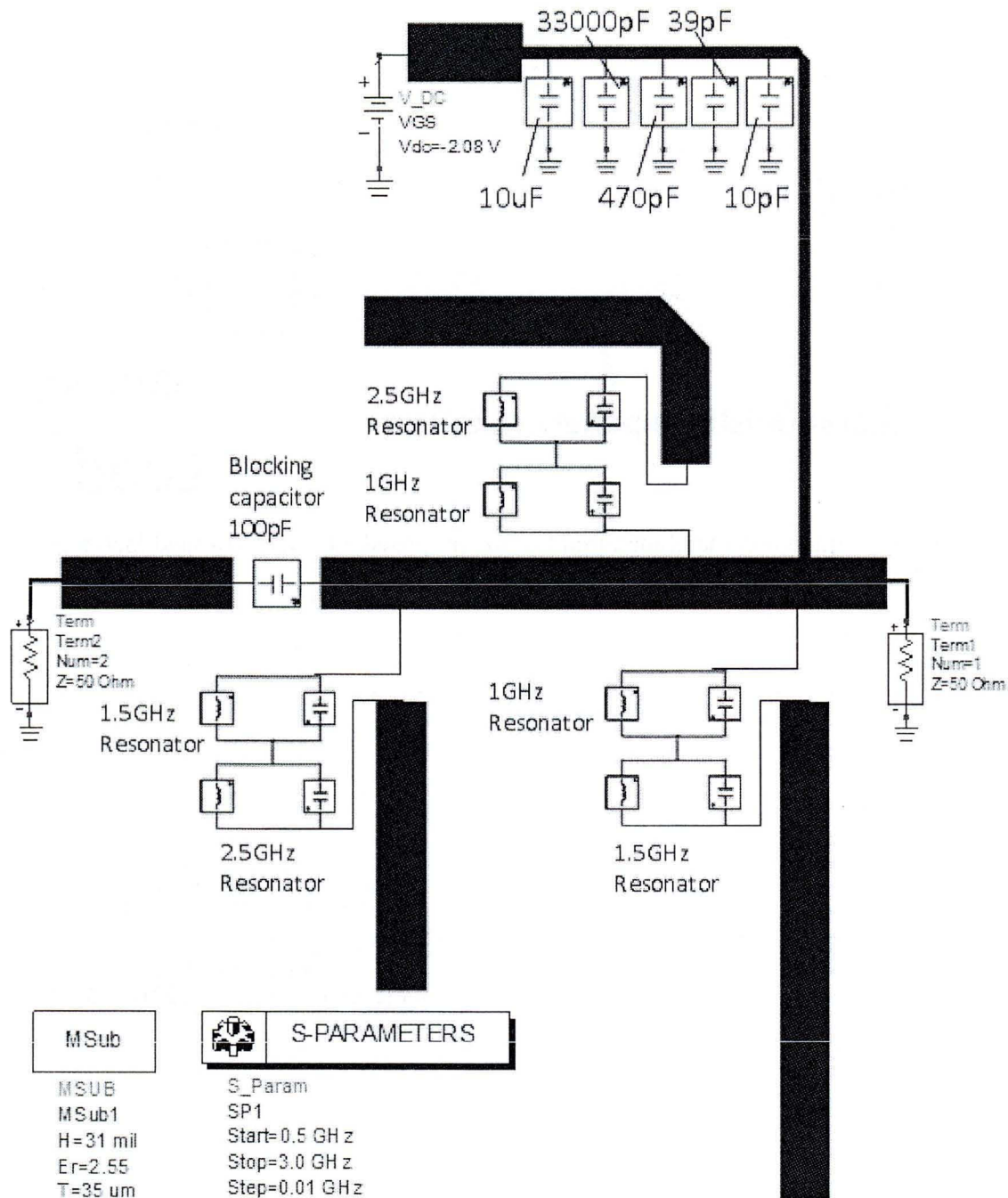


Figure 134: ADS momentum design schematic diagram of the proposed tri-band source matching network

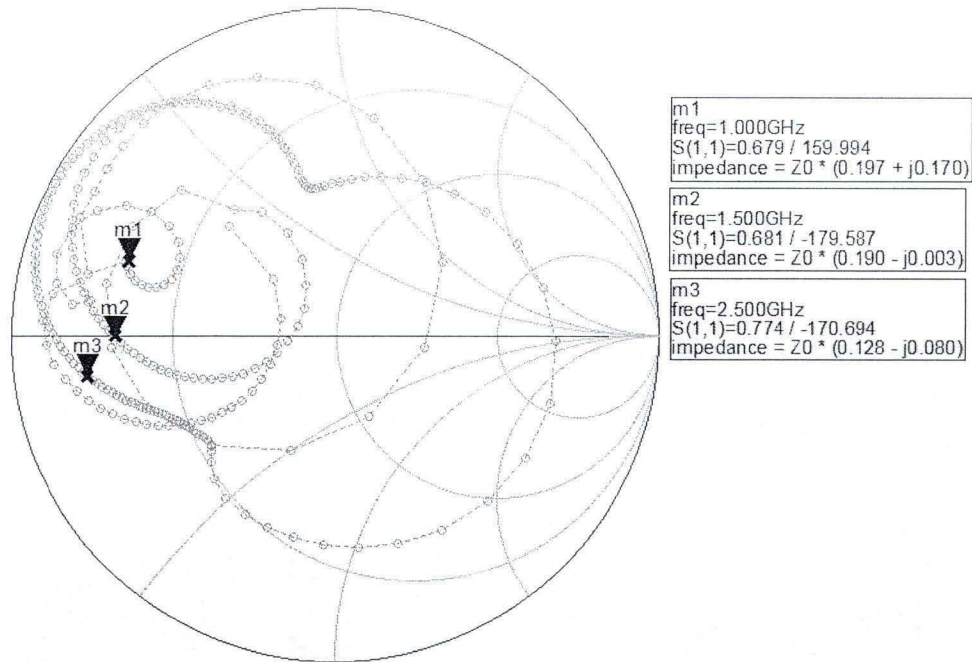


Figure 135: Simulated result of the proposed tri-band source matching network

The total layout of the proposed tri-band GaN HEMT class AB PA is shown in Fig.

136.

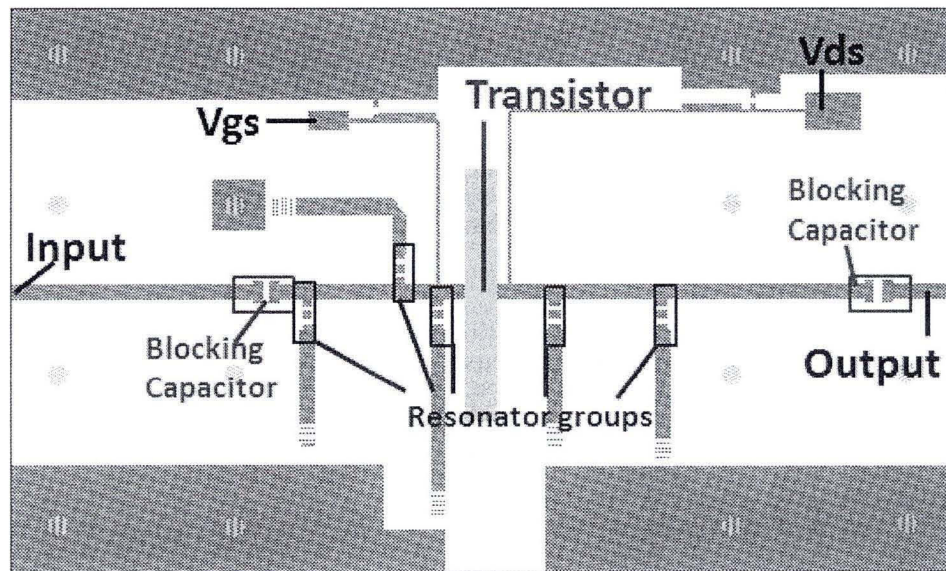


Figure 136: The layout of the proposed tri-band power amplifier

The fabricated proposed concurrent tri-band PA by using resonator groups in both input and output matching networks is shown in Fig. 137. We set bias point as class-AB operation, the $V_{gs} = -3V$, and $V_{ds} = 28V$.

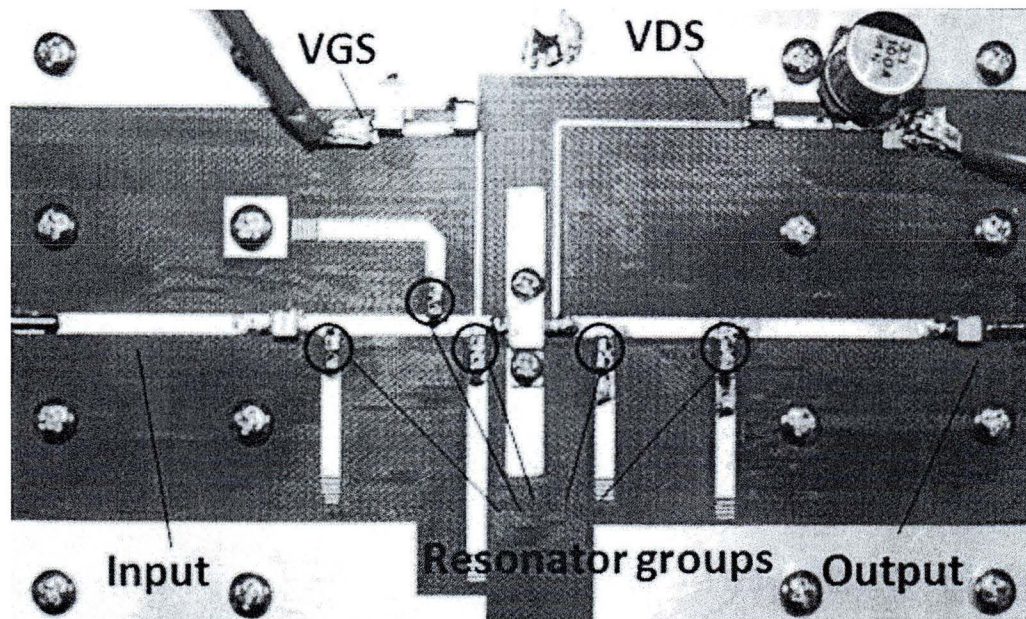


Figure 137: The fabricated proposed concurrent tri-band power amplifier

For verifying the resonator performance, the resonators constructed by capacitor and inductor are directly measured by the Vector Network Analyzer (VNA). Fig. 138 shows the measured results of the designed three resonators with the chosen capacitor and inductor. As measured results show, at 1GHz, 1.5 GHz, and 2.5GHz, insertion loss is better than 20 dB, signal can be suppressed well at each targeted suppressing frequency by the corresponding resonator.

For testing this tri-band amplifier, Anritsu signal generator MG3700A, Agilent signal analyzer N9020A, 40 dB ZHL-4240W pre-amplifier from Mini-Circuits, and 20 dB attenuator added after the tested tri-band PA are used. The test setup is the same as mentioned in section 2.2.6 (a) in Fig. 105.

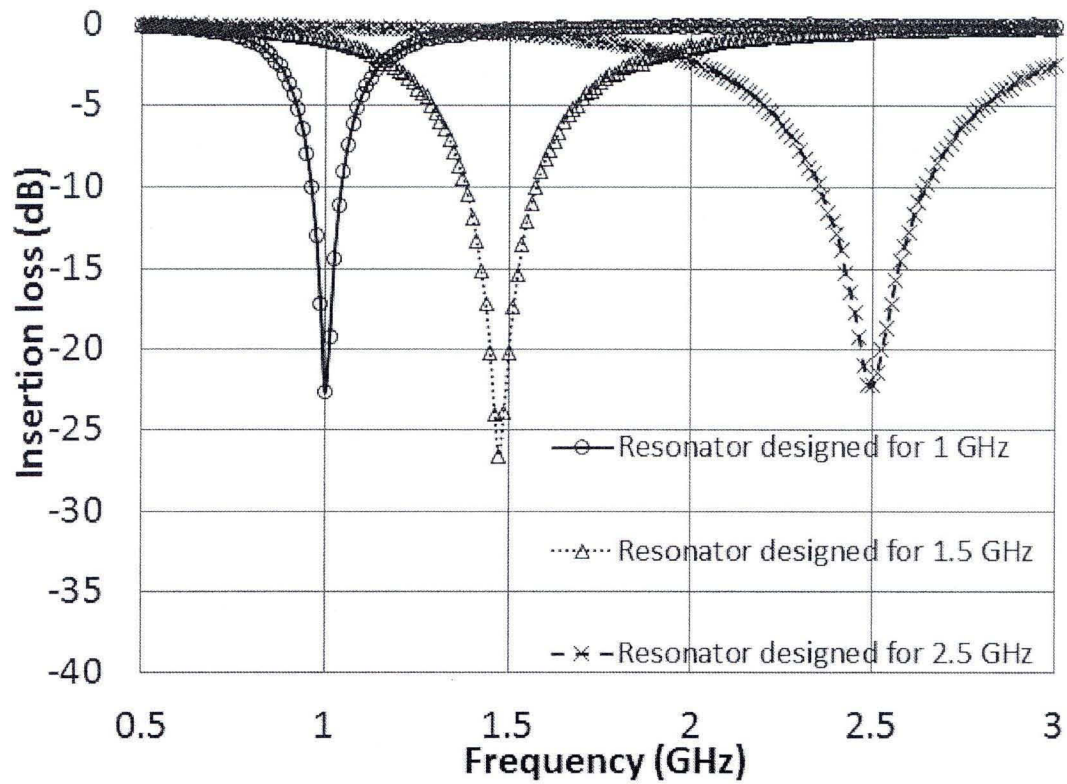


Figure 138: Measured results of the resonators designed for 1 GHz, 1.5 GHz, and 2.5 GHz

Fig. 139, Fig. 140, and Fig. 141 show the measured results of AM-AM, gain, and PAE of the proposed tri-band PA at 1 GHz, 1.5 GHz, and 2.5 GHz, respectively. The maximum PAE is obtained 56.4%, 58.3%, and 43.4% with output power 39.8 dBm, 40.8 dBm, and 38.9 dBm at 1GHz, 1.5GHz, and 2.5 GHz, respectively. The maximum output power is 39.8 dBm, 40.8 dBm, and 39.2 dBm at 1 GHz, 1.5 GHz, 2.5 GHz, respectively. The measured results are shown in Table 7.

Table 7: Measured results of the proposed tri-band power amplifier

Frequency (GHz)	Maximum PAE (%)	Maximum output power (dBm)	Maximum gain (dB)
2.5 GHz	43.4	39.2	12.6
1.5 GHz	58.3	40.8	17.0
1 GHz	56.4	39.8	22.4

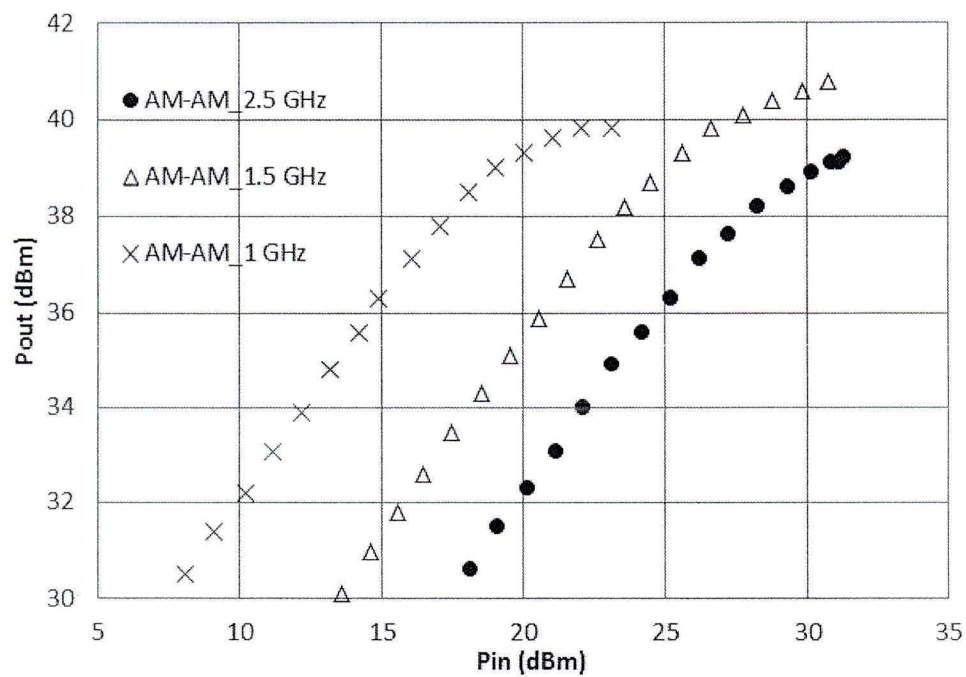


Figure 139: Measured results of AM-AM of the proposed tri-band power amplifier at 1 GHz, 1.5 GHz, and 2.5 GHz

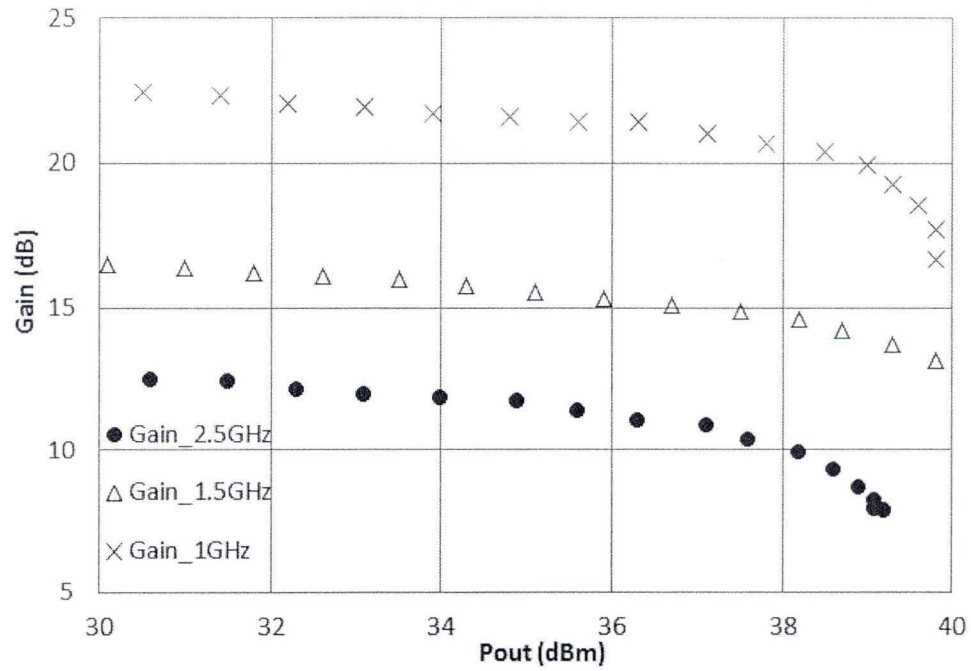


Figure 140: Measured results of gain of the proposed tri-band power amplifier at 1 GHz, 1.5 GHz, and 2.5 GHz

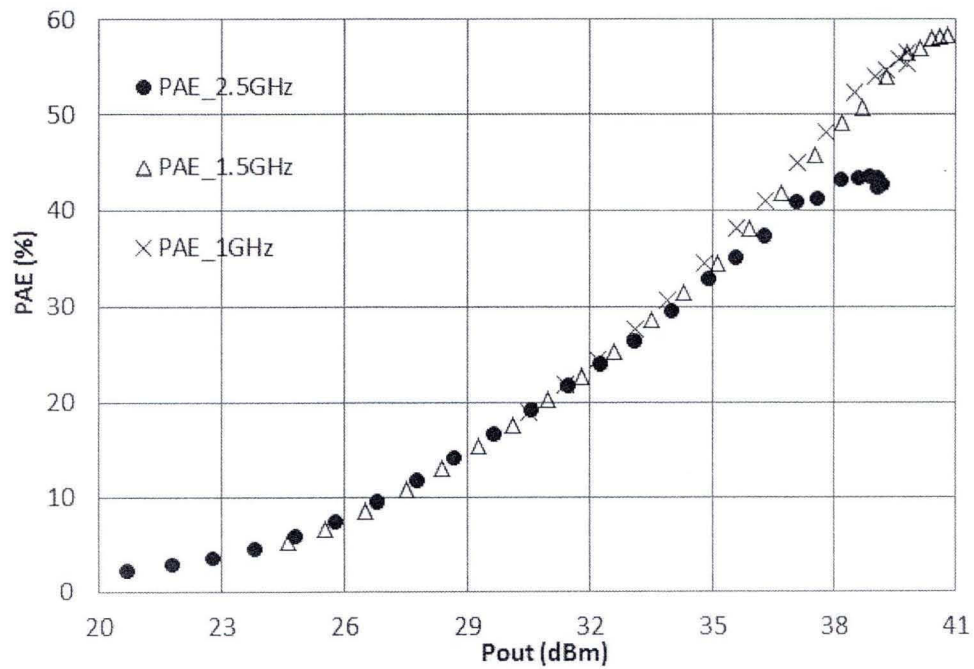


Figure 141: Measured results of PAE of the proposed tri-band power amplifier at 1 GHz, 1.5 GHz, and 2.5 GHz

2.2.8 Conclusion

In this chapter, the method of designing multiband PA using resonators in both input and output matching networks has been presented. In section 2.2.5, the principle of dual-band matching network and tri-band matching network using resonators in both input and output matching networks has been discussed in detail. For each operation frequency, the simplest L-type matching network has been employed.

To demonstrate the multiband matching network design method, I proposed two dual-band class AB PAs employing resonators in both input and output matching networks in section 2.2.6. By employing parallel resonators in input and output matching network, two dual-band class AB PAs with different types of resonators (capacitor with inductor and capacitor with microstrip line) are designed, fabricated, and tested. Measured results show the good performance of the two dual-band PAs.

In section 2.2.7, one concurrent tri-band GaN HEMT PA by employing resonator groups in both input and output matching networks as frequency selection elements is designed, fabricated and tested. Resonators are designed to block signal generated at each specified resonant frequency. By combining two resonators together, signal at the two corresponding frequencies is blocked while the signal at the remaining operation frequency can pass the resonator group. With the novel proposed structure, the source and load impedance are matched by the simplest L-type matching network structure at each operation frequency independently. The complexity of design procedure is reduced. In addition, we simplified the load matching network by using bias line to match the load impedance at 1 GHz to reduce the complexity of the proposed PA circuit. At three distinct operation frequencies 1 GHz, 1.5 GHz and 2.5 GHz, the PAE is 56.4%, 58.3%, and 43.4% and the maximum output power is 39.8 dBm, 40.8 dBm, and 39.9 dBm, respectively. This proposed dual-band and tri-band design method can be easily applied in multiband applications.

The contributions of this chapter are listed below:

1: In this chapter, two new dual-band PAs and one new tri-band PA has been presented. Comparing with the multiband PAs using switches, diplexers, or tunable electronic components, we do not need to toggle the switches between different circuits or adjust the tunable electronic components when the frequency changes. The proposed multiband design method can be applied in other multiband applications and other multiband circuits with more complex structures, such as multiband balanced PA and multiband Doherty PA.

2: The cost of the multiband PA is saved, especially the cost of transistor. As mentioned in this chapter, we just use one transistor with one multiband input and output matching networks to realize the proposed multiband PAs. In addition, in the proposed tri-band PA, by using the bias circuit as the matching network for the lowest operation frequency, two resonator groups are saved.

3: Comparing with the multiband structure using switches with parallel PAs or matching circuits, the size of the proposed multiband PA is reduced by using just one transistor, one input and one output matching networks.

4: The design procedure of the proposed multiband PA is simplified by using the simplest L-type matching network for multiband matching network design.

My original publications related to this chapter are listed below:

- [1] **Zhebin Wang** and Chan-Wang Park, "Concurrent Tri-Band GaN HEMT Power Amplifier Using Resonators in Both Input and Output Matching Networks," The 13th Annual IEEE Wireless and Microwave Technology (WAMI) Conference, pp. 1-4, Cocoa Beach, FL., U.S.A., 15-17 April 2012.
- [2] **Zhebin Wang** and Chan-Wang Park, "Dual-band GaN HEMT Power Amplifier Using Resonators in Matching Networks," The 12th Annual IEEE Wireless and Microwave Technology (WAMI) Conference, pp. 1-4, Clearwater, FL., U.S.A., 18-19 April 2011.

CHAPITRE 3

NOUVEL AMPLIFICATEUR DE PUISSANCE À LARGE BANDE EN UTILISANT LES STUBS RADIAUX MICRORUBANS POUR SUPPRIMER LES HARMONIQUES

3.1 RÉSUMÉ

Dans ce chapitre, un nouvel amplificateur de puissance (PA) à large bande est analysé, fabriqué et testé. MRS (microstrip radial stub) est utilisé à la fois dans les réseaux d'adaptation d'entrée et de sortie pour supprimer d'harmoniques de 2,14 GHz. L'angle du MRS et la longueur en dessous du MRS sont analysés pour la suppression d'harmoniques. La caractéristique large bande de suppression d'harmoniques du MRS est comparée à la ligne quarte d'onde normale de 50 Ohm. Les deuxième et troisième harmoniques de 2,14 GHz ont été respectivement supprimées à -38,37 dB et -29,53 dB. La bande passante de -15 dBc de suppression du MRS est plus large que 1,32 GHz. En utilisant les MRSs à la fois dans les réseaux d'adaptation d'entrée et de sortie, le PAE maximal mesuré est 80,52% avec 40.53 dBm d'une puissance de sortie à 2,14 GHz. Au moins 50% de PAE et 37 dBm de puissance de sortie sur une bande passante de 12%, de 2 GHz à 2,26 GHz, sont obtenus. Le gain maximal mesuré de l'amplificateur de puissance large bande proposé est 20,25 dB.

3.2 NOVEL WIDEBAND GAN HEMT POWER AMPLIFIER USING MICROSTRIP RADIAL STUB TO SUPPRESS HARMONICS (WANG *ET AL.*, 2012 C)

3.2.1 Abstract

In this chapter, a novel wideband GaN HEMT power amplifier (PA) using microstrip radial stub (MRS) in both input and output matching networks to suppress harmonic components of 2.14 GHz is analyzed, fabricated, and tested. The angle subtended by MRS and the bottom length of MRS are analyzed for harmonic suppressing purpose. The wideband harmonic suppressing characteristic of MRS is compared with normal 50 Ohm quarter-wave rectangular stub. The second and third harmonics of 2.14 GHz are suppressed by -38.37 dB and -29.53 dB, respectively. -15 dBc suppressing bandwidth over 1.32 GHz at both harmonic bands is obtained. By using the proposed MRS in both input and output matching network, the measured maximum power added efficiency (PAE) is 80.52% with 40.53 dBm output power at 2.14 GHz. At least 50% PAE and 37 dBm output power over a 12% bandwidth from 2 GHz to 2.26 GHz is achieved. The maximum measured gain is 20.25 dB.

3.2.2 Introduction

In 4th generation (4G) mobile telecommunications network systems, wideband performance of PA is required for greater data rates, such as LTE (Long Term Evolution) Advanced up to 100 MHz (Wu *et al.*, 2010; Wright *et al.*, 2009). Efficiency is also the particularly important parameter of the PA which generates high output power. High value of efficiency is related to low electricity consumption and low heat, hence the size and mass of the electrical systems, the performance required of the thermal control systems can be reduced (Maral *et al.*, 2002: 470). In the past, bi-harmonic or poly-harmonic modes are applied in waveform engineering to obtain high PAE, such as class F or inverse class F PA

where harmonic control circuit is needed (Wang *et al.*, 2011 e). To design a class F or inverse class F PA, generally normal rectangular quarter-wave stub is used to suppress the harmonic. The microstrip radial stub (MRS) which has intrinsic wide stopband characteristic in shunt has been studied and developed in previous works, such as ultra-wide stopband low-pass filter (Ma *et al.*, 2011). To enlarge the bandwidth of PA we use MRS in harmonic suppressing circuits. To the best of the authors' knowledge, this is the first time MRS is used to suppress harmonic components for switch-mode PA to increase the bandwidth.

3.2.3 Problem, objective, and methodology

As mentioned in introduction, in 4G mobile telecommunications network systems, the new communication standards, such as WiMAX, LTE, and LTE Advanced with wide bandwidth operation are applied to satisfy high data rate requirement. Components and devices with wide bandwidth performance are highly required. For PA, waveform engineering technology is widely used for achieving high PAE. Bi-harmonic or poly-harmonic modes are applied in waveform engineering, such as class F PA and inverse class F PA where harmonic control circuit is needed. However, the bandwidth of the 2nd harmonic and 3rd harmonic is 2 and 3 times larger than the bandwidth of the fundamental frequency, respectively. Take LTE Advanced at 2.14 GHz as an example, its fundamental frequency bandwidth is up to 100 MHz, the bandwidth of its 2nd harmonic and 3rd harmonic is up to 200 MHz and 300 MHz, respectively. To design a class F or inverse class F PA, generally normal rectangular quarter-wave stub is used to suppress the harmonic. But it has narrowband characteristic (Wu *et al.*, 2010), so it is difficult to design a wideband high PAE PA with classical method. To realize wideband high PAE PA, the main issue is to design wideband harmonic suppressing circuit to satisfy harmonic suppressing requirement in wide bandwidth.

Our objective is to design a wideband switch-mode PA with high PAE performance for LTE Advanced application with 100 MHz bandwidth. To do that at least 200 MHz and 300 MHz bandwidth for the 2nd and 3rd harmonic, respectively, should be suppressed better more than -20 dB in class F or inverse class F PA. In this chapter, with the wideband suppression characteristic of the MRS stub, I will use MRS stub in both input and output matching networks to suppress harmonic components to design a novel wideband GaN HEMT PA for LTE Advanced application. The harmonic suppression impact of the angle subtended by MRS and the bottom length of MRS will be analyzed in this chapter. The wideband harmonic suppressing characteristic of MRS will be compared with normal 50 Ohm quarter-wave rectangular stub also. By using the proposed MRS in both input and output matching network of the proposed PA, the wideband high PAE PA with wideband harmonic suppression bandwidth is achieved.

3.2.4 New analysis method of microstrip radial stub

In this section, a new wideband analysis method using MRS instead of conventional rectangular stub to suppress harmonic is presented. To achieve wideband harmonic suppressing performance, MRS is employed instead of rectangular quarter-wave stub. Fig. 142 shows the topology of the conventional MRS, where θ is the angle subtended by MRS, W is the bottom length of MRS, and L is the length of MRS. To investigate the characteristic of MRS, we sweep the value of θ and W separately while adjusting L to suppress harmonic components. For example, at 4.28 GHz, we sweep θ from 50° to 150° with a 20° step while adjudging the value of L to make the lowest insertion loss at 4.28 GHz. The same idea is applied to sweep W from 47 mil to 97 mil with a 10 mil step. The ADS schematic diagrams of MRSs with different values of θ and W to suppress the signal generated at the same frequency are shown in Fig. 143 and Fig. 145, respectively. The simulated results of the angle and bottom length sweep simulations are shown in Fig. 144 and Fig. 146, respectively.

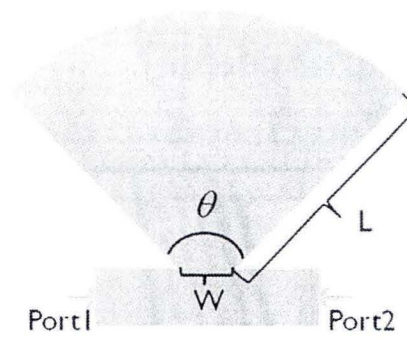


Figure 142: Microstrip radial stub (MRS), θ : the angle subtended by MRS, W : the bottom length of MRS, L : the length of MRS

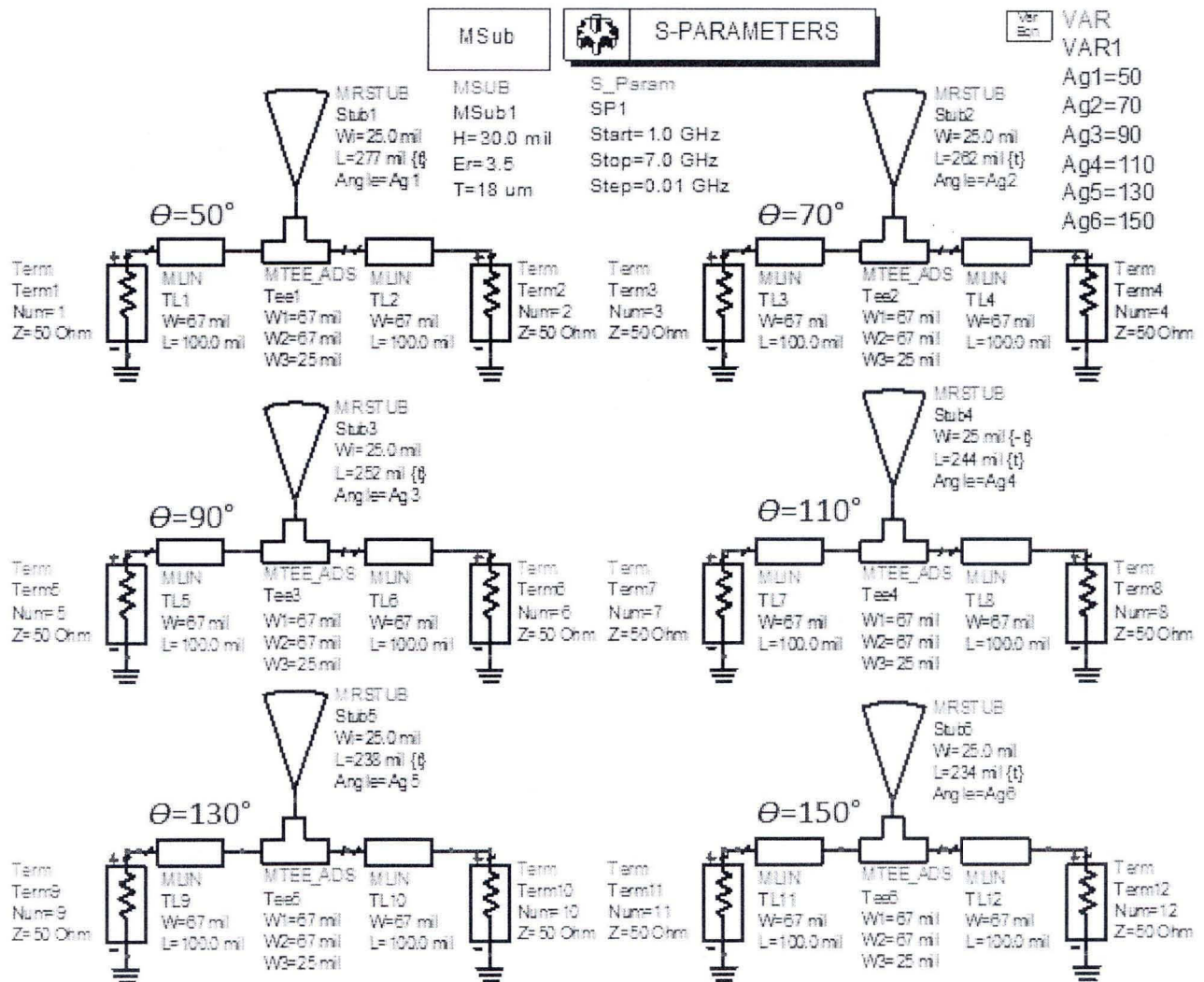


Figure 143: MRSs with sweeping θ from 50° to 150°

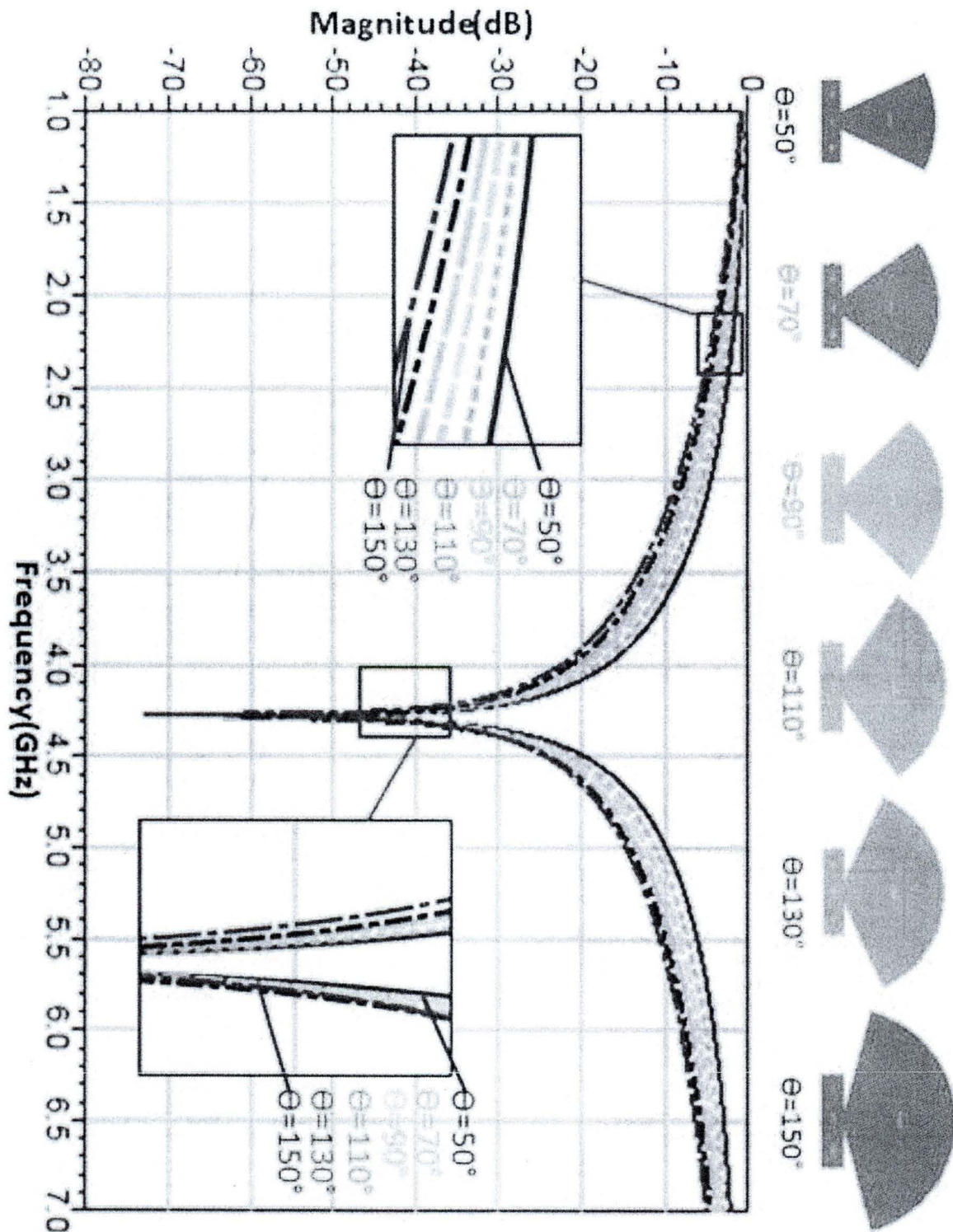


Figure 144: Simulated results of MRSs with sweeping θ from 50° to 150°

According to Fig. 144, when the value of θ is increased, the harmonic suppressing bandwidth (HSB) is increased, but the insertion loss at 2.14 GHz is increased. By considering both the insertion loss of 2.14 GHz and 4.28 GHz, there's a trade-off to choose the value of θ for MRS.

Fig. 145 below shows the MRSs with different values of W to suppress signal at 4.28 GHz, the simulated results of these MRSs are shown in Fig. 146.

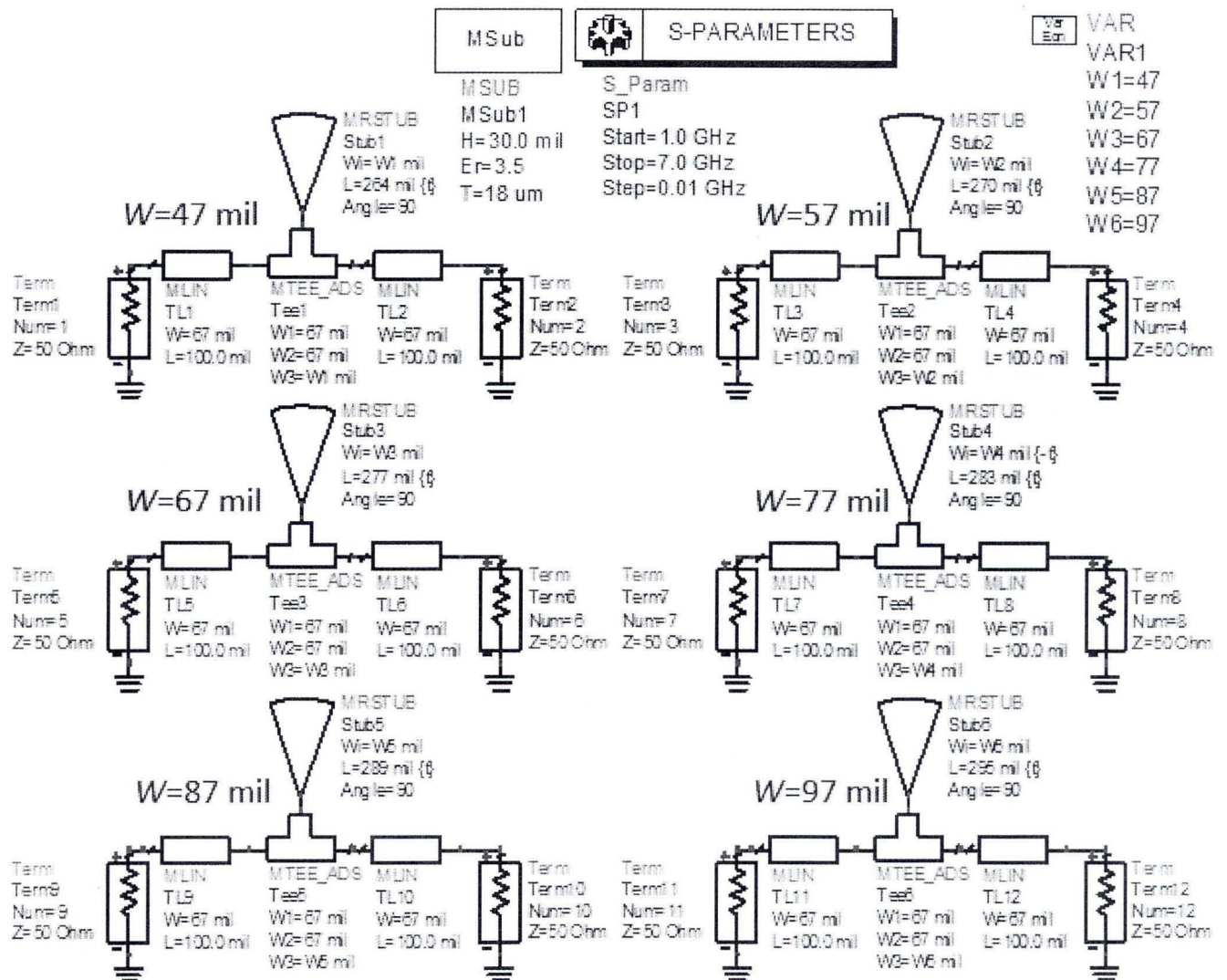


Figure 145: MRSs with sweeping W from 47 mil to 97 mil

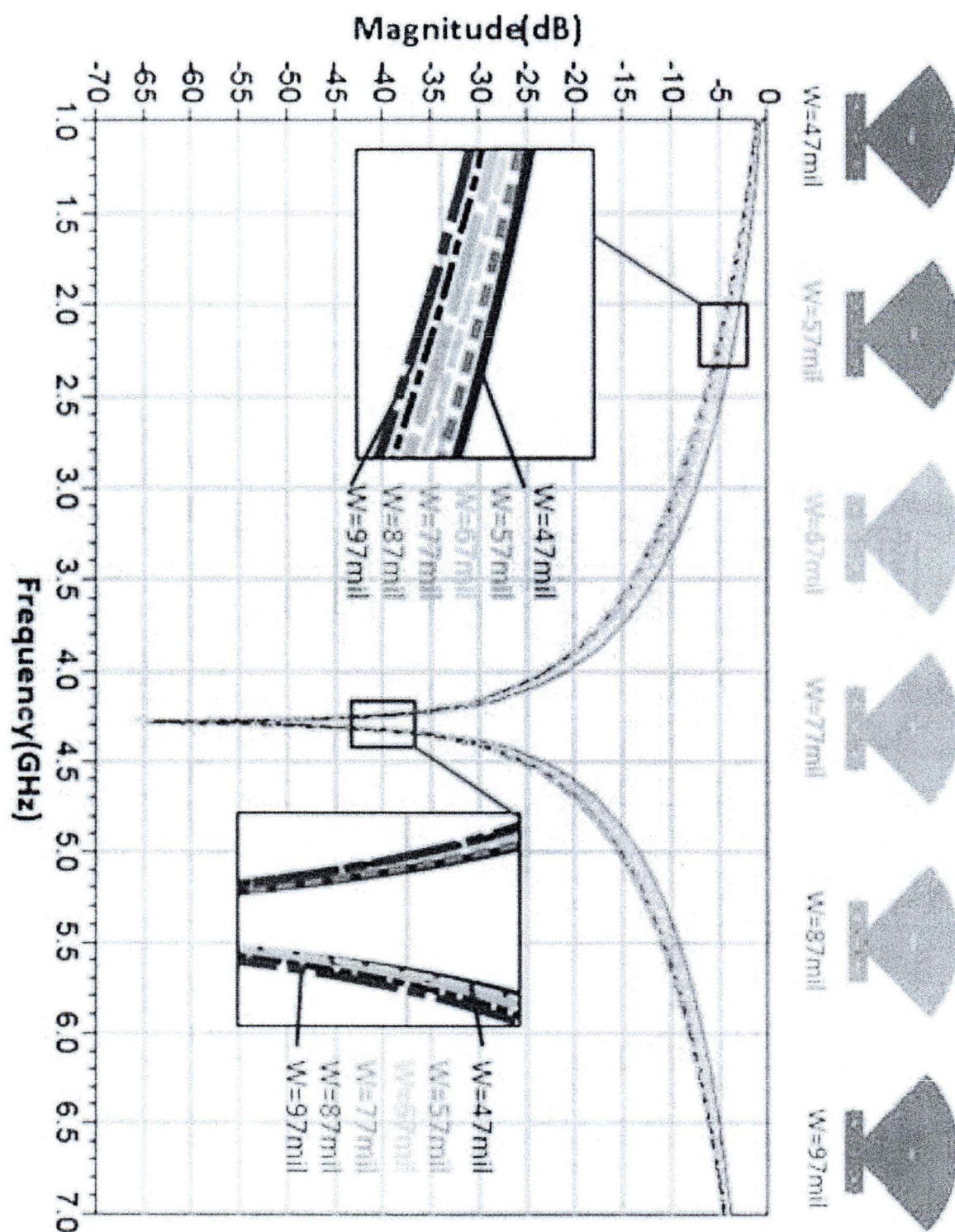


Figure 146: Simulated results of MRSs with sweeping W from 47 mil to 97 mil

According to Fig. 146, when we increase W , the HSB is increased while insertion loss at the fundamental frequency is increased. By considering both HSB and insertion loss at 2.14 GHz, we make a trade-off by choosing $\Theta = 90^\circ$, $W = 67$ mil, $L = 289$ mil for 4.28 GHz and $\Theta = 90^\circ$, $W = 67$ mil, $L = 199$ mil for 6.42 GHz.

Fig. 147 shows the ADS momentum design schematic diagrams of the MRSs and normal rectangular quarter-wave stubs designed to suppress signal at 2.14 GHz, 4.28 GHz and 6.42 GHz. Fig. 148 shows the simulated comparison of S_{21} of MRS and normal rectangular quarter-wave stub. -15 dBc harmonic suppressing bandwidth of MRS is at least 2.2 times larger than that of normal rectangular quarter-wave stub for suppressing the 2nd and 3rd harmonics.

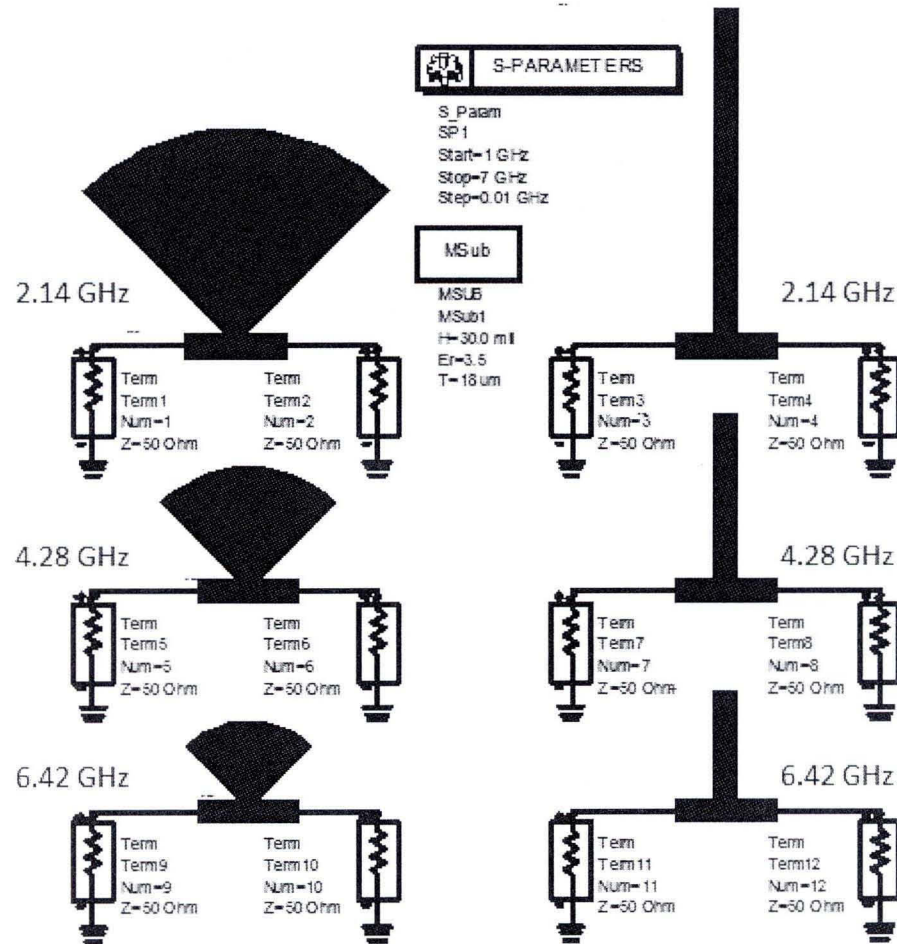


Figure 147: ADS momentum design schematic diagrams of the MRSs and normal rectangular quarter-wave stubs for 2.14 GHz, 4.28 GHz, and 6.42 GHz

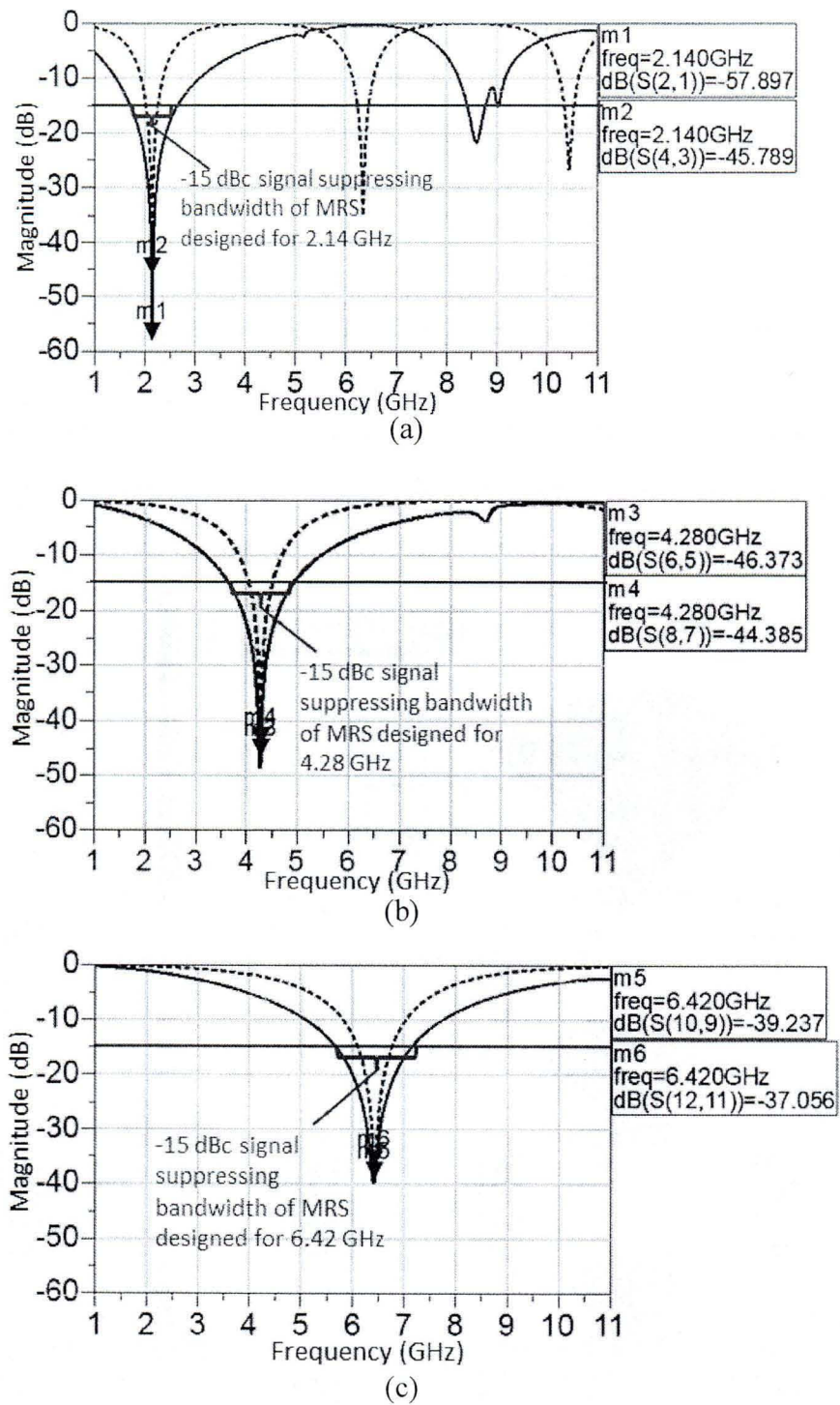


Figure 148: Simulated comparisons of the MRSs (solid line) and normal rectangular quarter-wave stubs (dot) designed for (a): 2.14 GHz, (b): 4.28 GHz, and (c): 6.42 GHz

3.2.5 Design of the proposed new wideband PA

The new wideband PA presented in this section has been published by me in (Wang *et al.*, 2012 c). The proposed PA circuit is designed by using MRS in both input and output matching networks to suppress the 2nd and 3rd harmonics of 2.14 GHz. We use GaN CGH40010 transistor from Cree Inc.

The input and output impedance points are shown in Fig. 149, for input matching network, the impedance of fundamental frequency, 2nd and 3rd harmonics are $5.30 - j2.05$ Ohm, $0.35 + j62$ Ohm, and $56.70 - j495.35$ Ohm, respectively. For output matching network, the impedance of fundamental frequency, 2nd and 3rd harmonics are $15.45 + j22.90$ Ohm, $0.10 + j18.20$ Ohm, and $1.30 + j86.30$ Ohm, respectively. With load pull simulation result in ADS as shown in Fig. 150, the PAE can reach to 86.05% while the output power is 40.24 dBm.

The topology of load matching network design is shown in Fig. 151 (a). We use quarter wavelength transmission line at 2.14 GHz in bias circuit. MRS is also designed at 2.14 GHz as a part of the bias circuit. There are three stages in the proposed output matching network. By changing *TL1* in *Stage1*, the reflection coefficient phase angle of the third harmonic can be tuned to the desired value and we can match the second harmonic impedance point by changing the length of *TL2* in *Stage2*. Finally, the fundamental impedance matching is achieved by *Stage3*. Blocking capacitor is implanted after the bias circuit. Using the same design procedure of the output matching network, the topology of the source matching network with MRS is designed as shown in Fig. 151 (b).

The ADS momentum simulation schematic diagrams of the output and input matching networks using MRS to suppress harmonic components are shown in Fig. 152 and Fig. 153, respectively.

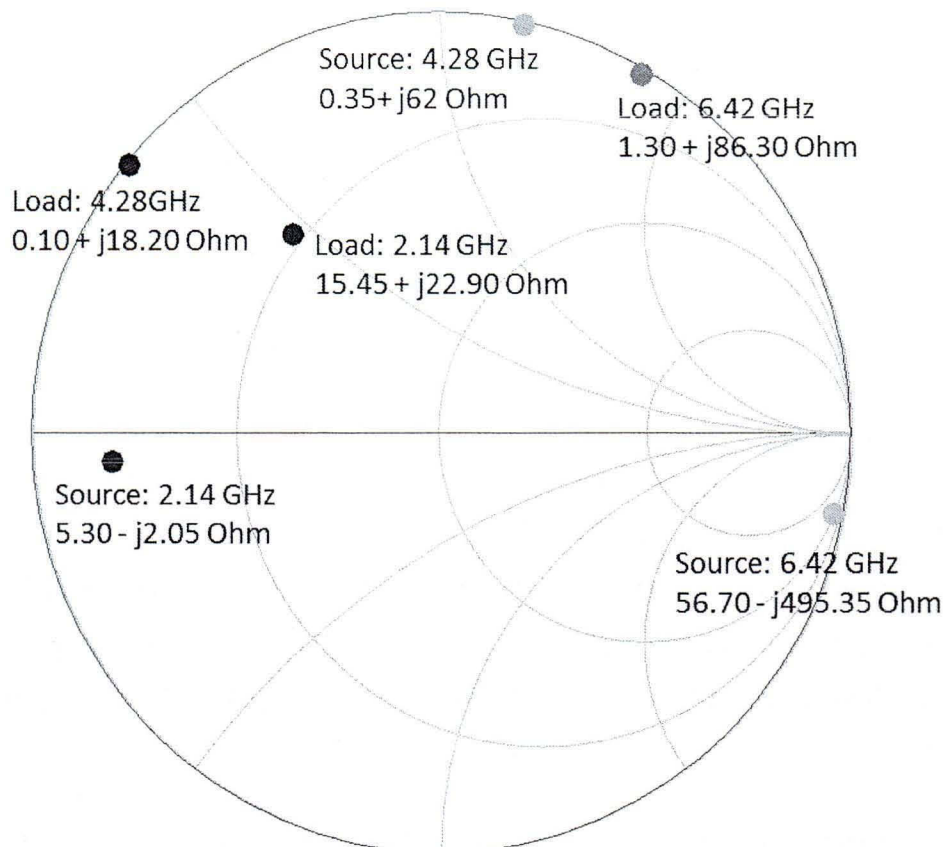


Figure 149: Desired input and output impedance points of CGH40010

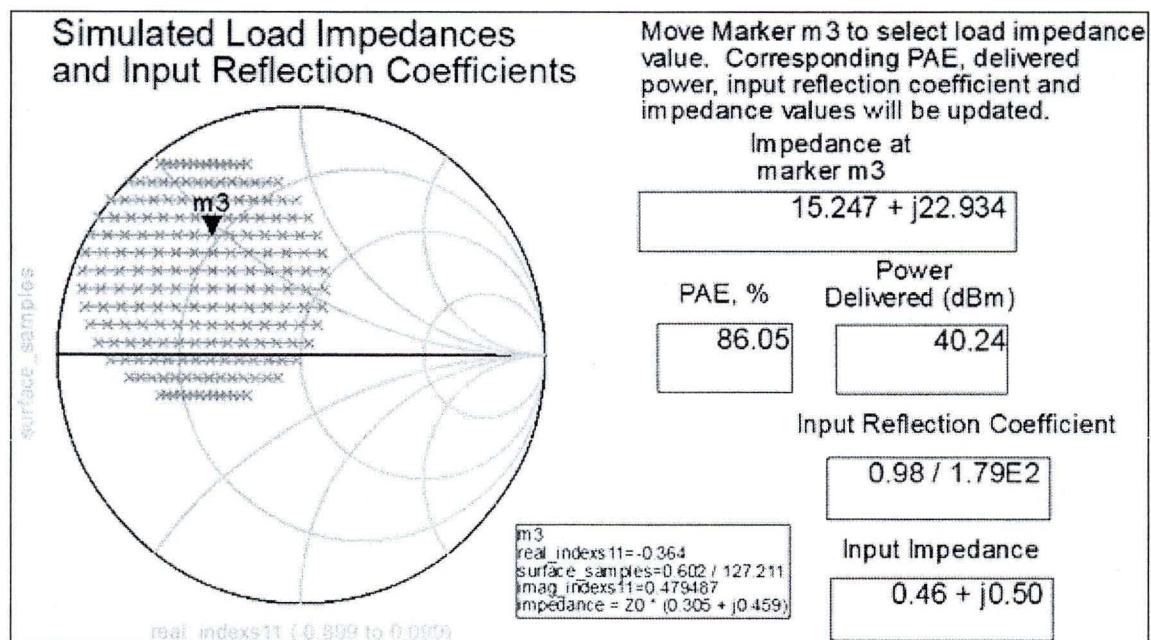


Figure 150: Simulated result of load pull simulation at 2.14 GHz

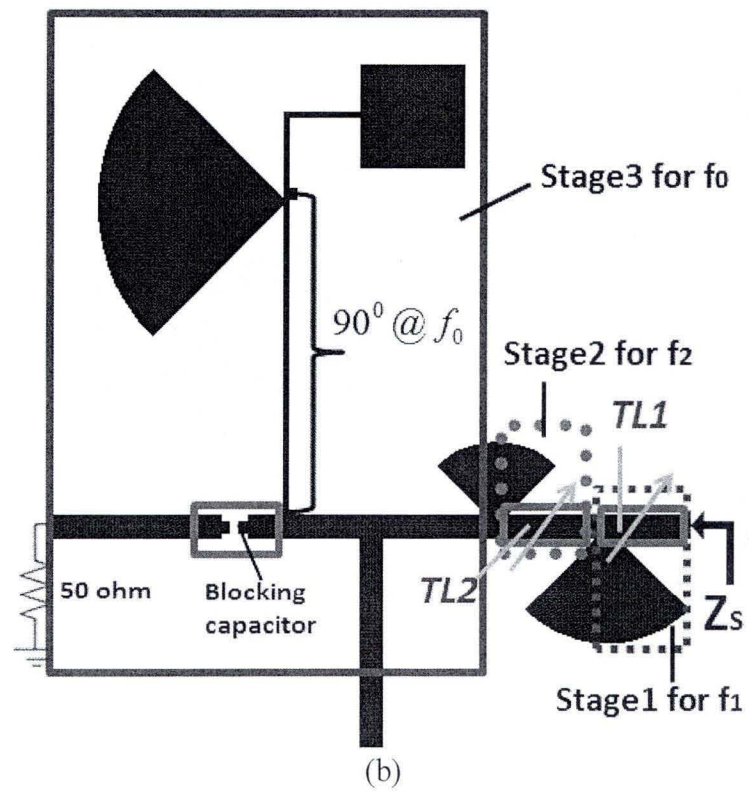
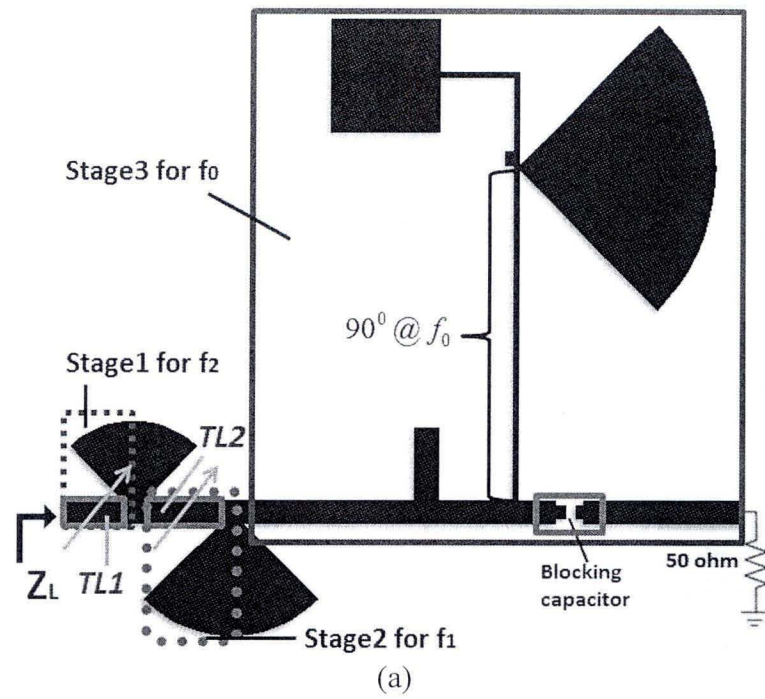


Figure 151: Topologies of the proposed MRS matching network, (a): output and (b): input

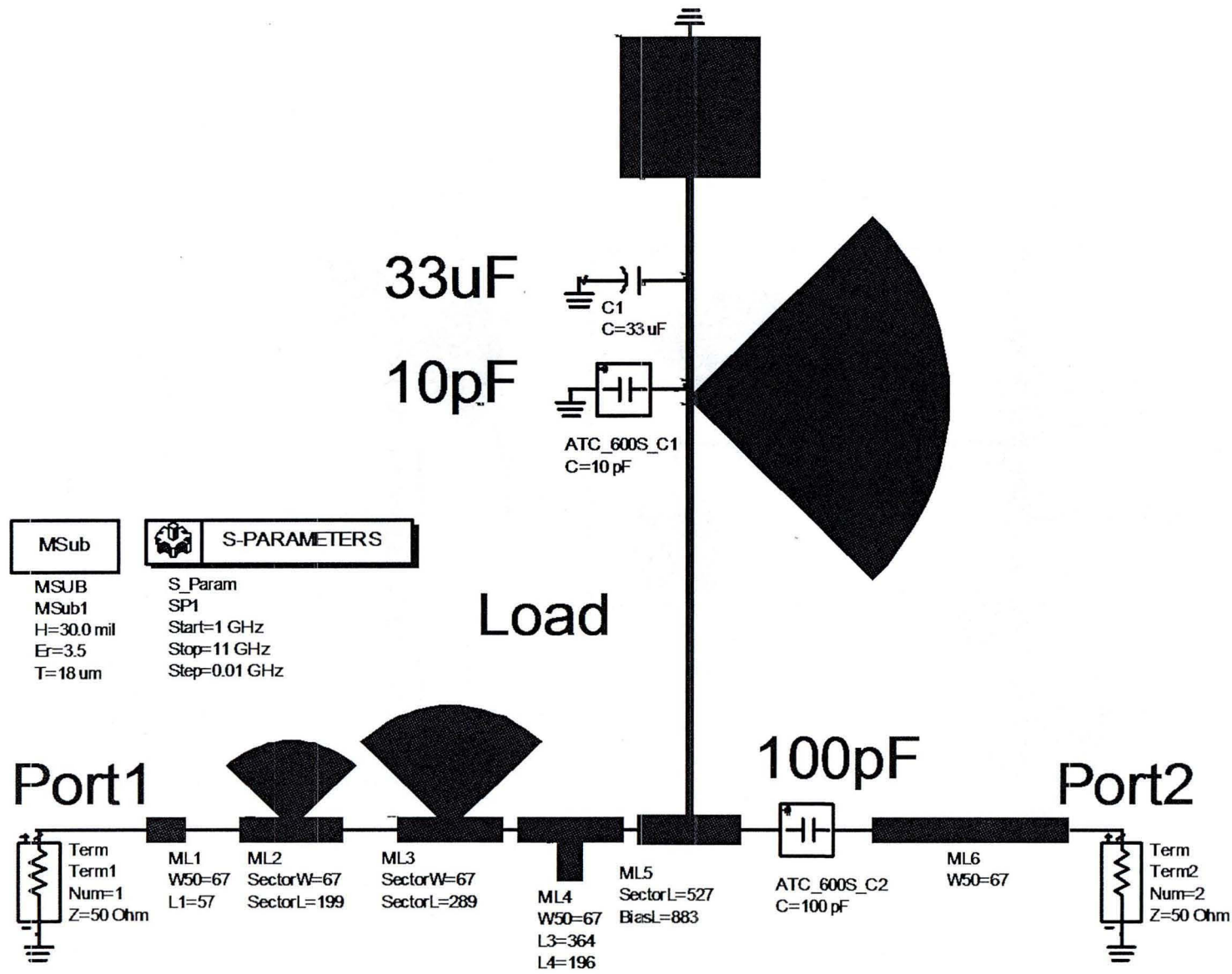


Figure 152: Momentum simulation circuit of the proposed MRS output matching network

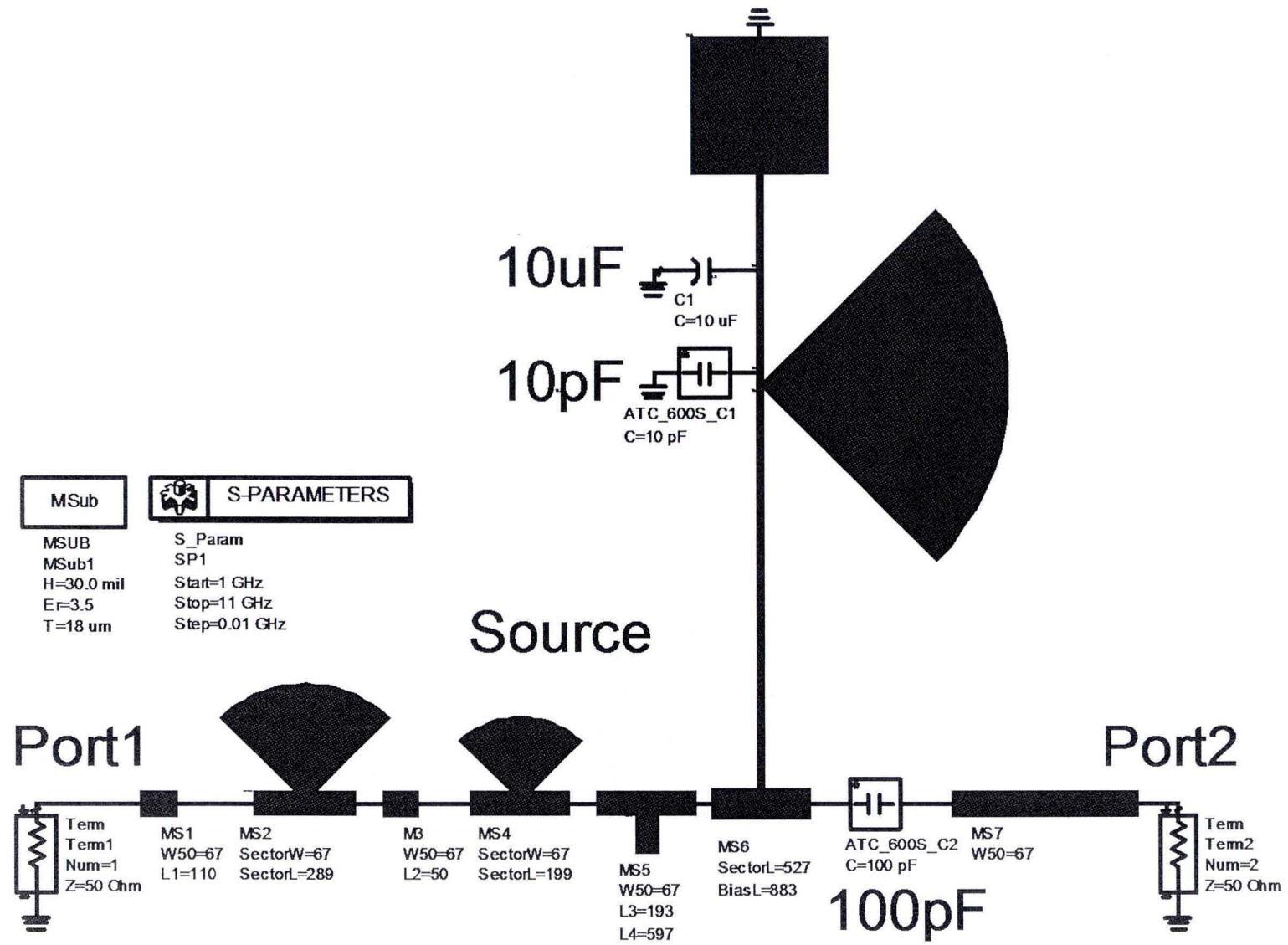


Figure 153: Momentum simulation circuit of the proposed MRS input matching network

By setting the reference impedance as 50 Ohm, the simulated result of the proposed output matching network is shown in Fig. 154. The simulation step is 0.01 GHz. The simulated impedance points of the fundamental frequency from 2.09 GHz to 2.19 GHz with 100 MHz bandwidth, the 2nd harmonic from 4.18 GHz to 4.38 GHz with 200 MHz bandwidth, and the 3rd harmonic from 6.27 GHz to 6.57 GHz with 300 MHz bandwidth are shown in Fig. 154.

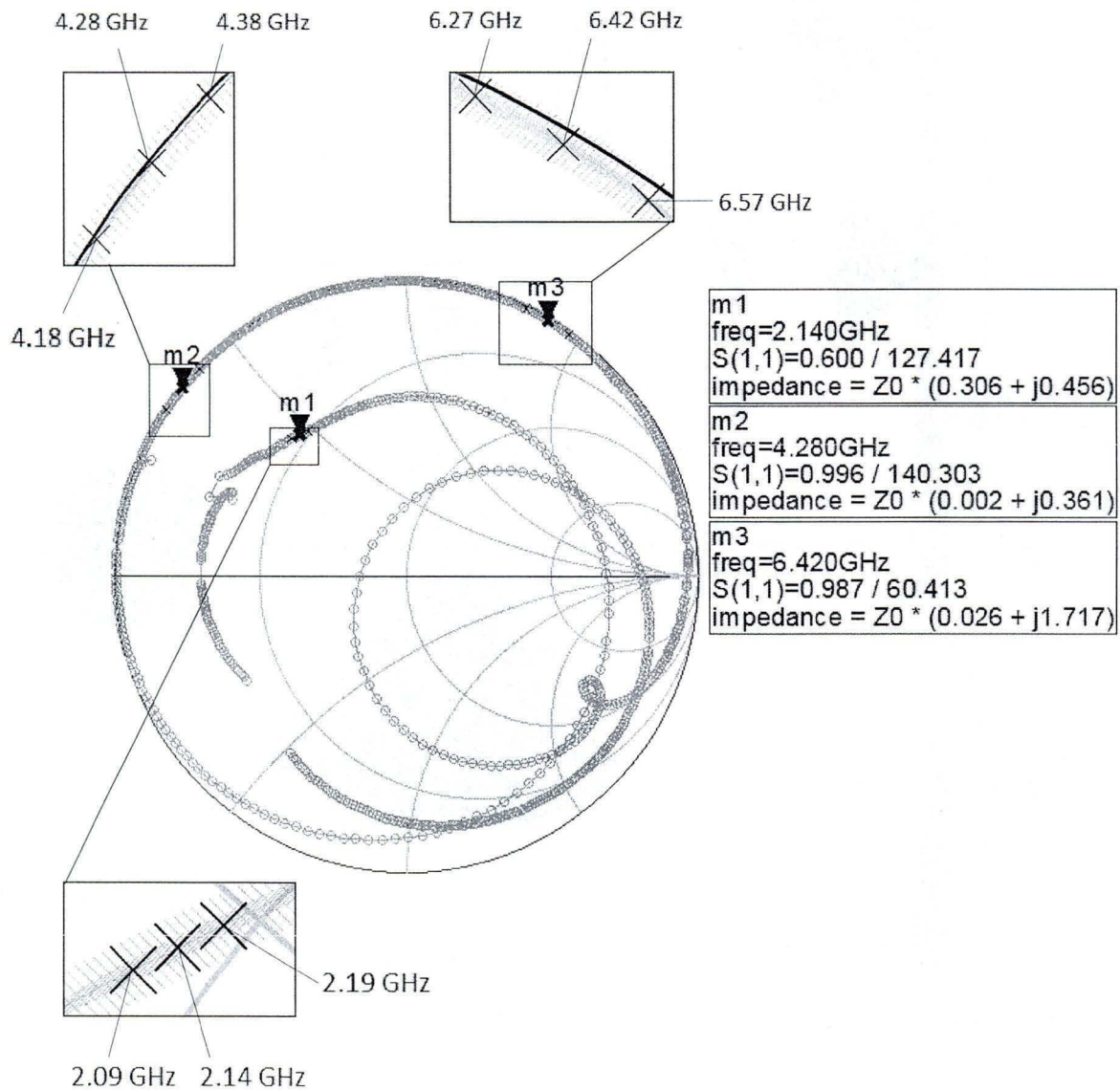


Figure 154: The simulated result of the proposed MRS output matching network

The simulated impedance result of the proposed input matching network is shown in Fig. 155. From Fig. 154 and Fig. 155, we see the 100 MHz bandwidth region of the fundamental frequency, the 200 MHz bandwidth region of the 2nd harmonic, and the 300 MHz bandwidth region of the 3rd harmonic with 0.01 GHz step. The distribution of the impedance points for the fundamental frequency, 2nd harmonic, and 3rd harmonic is concentrated in a relative small region in Smith chart. Wideband performance of the proposed output and input matching network is achieved.

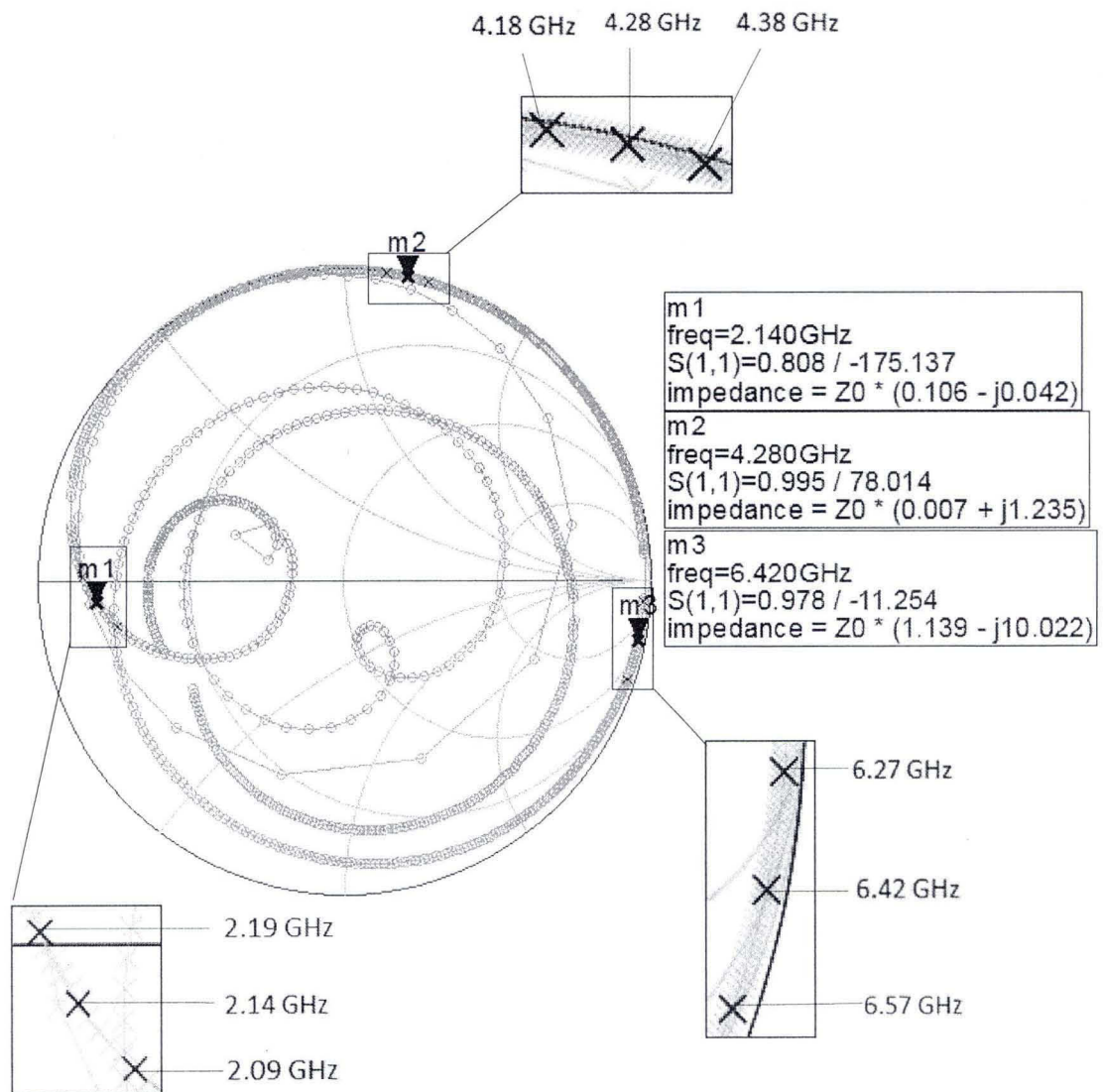


Figure 155: The simulated result of the proposed MRS input matching network

Set the reference impedance as $15.45 + j22.90$ Ohm for the proposed output matching network and the reference impedance as $5.30 - j2.05$ Ohm for the proposed input matching network. The simulated results of the proposed output and input matching network are shown in Fig. 156 (a) and (b), respectively.

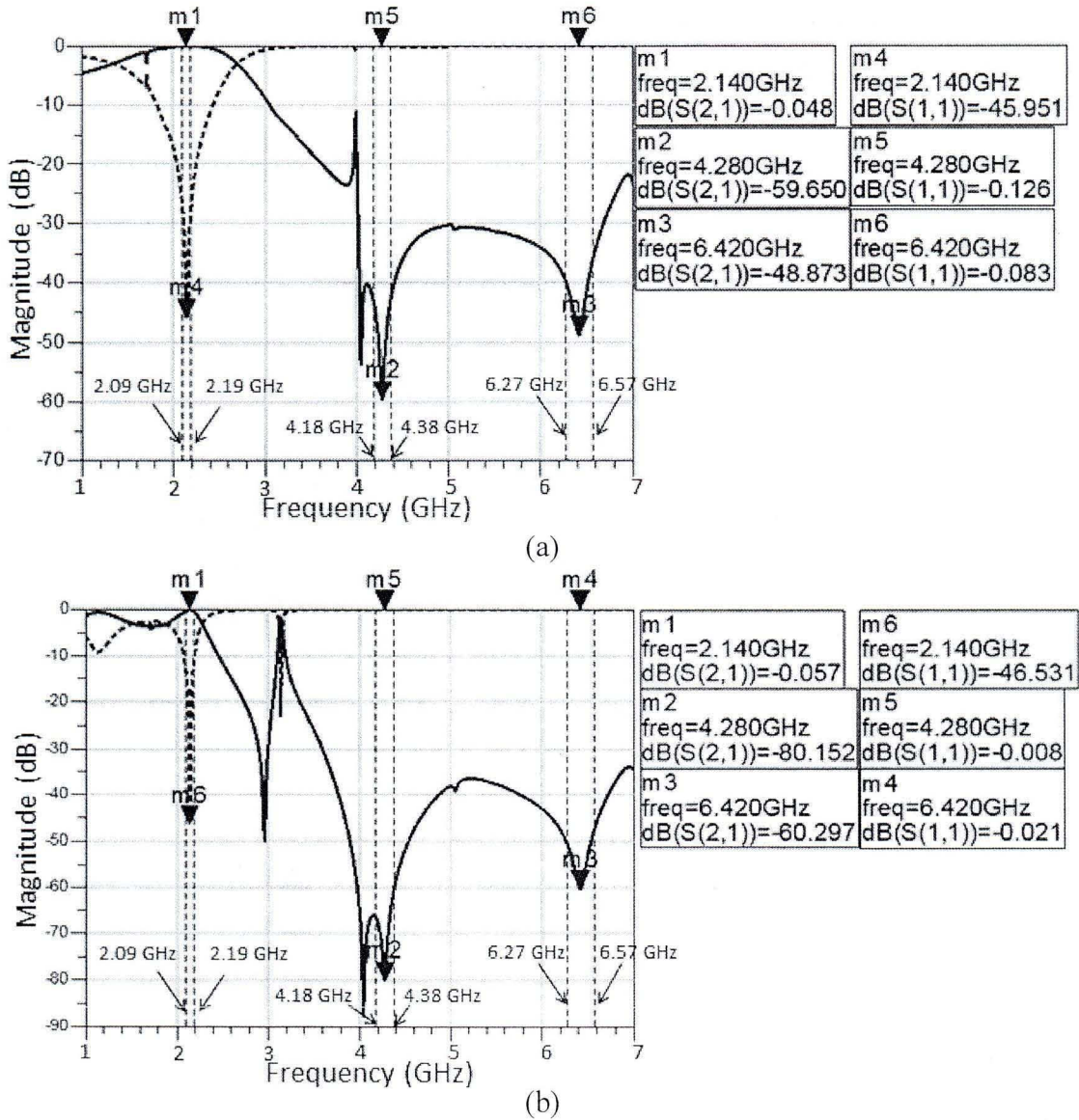


Figure 156: Simulated results of the proposed matching networks with MRSs, (a): output, (b): input, solid line: insertion loss, and dot line: return loss

For the proposed output matching network, with the simulated results shown in Fig. 156 (a), in the 100 MHz bandwidth region of the fundamental frequency, the maximum insertion loss is 0.07 dB; the 2nd harmonic is rejected by at least 42.10 dB in its 200 MHz bandwidth region; the 3rd harmonic is rejected by at least 35.81 dB in its 300 MHz bandwidth region. According to Fig. 156 (b), for the proposed input matching network, in the 100 MHz bandwidth region of the fundamental frequency, the maximum insertion loss is 0.44 dB; the 2nd harmonic is rejected by at least 60.34 dB in its 200 MHz bandwidth region; the 3rd harmonic is rejected by at least 47.49 dB in its 300 MHz bandwidth region. The proposed output and input matching networks match the load and source of the transistor CGH40010 to 50 Ohm load well, respectively. The proposed MRS suppresses the 2nd and 3rd harmonics effectively.

The whole layout of the proposed PA using MRS to suppress the 2nd and 3rd harmonics is shown in Fig. 157. For both input and output matching networks, we use MRS to suppress up to the 3rd harmonic. In the bias circuit, we use MRS on the shunt stub to suppress the fundamental frequency to provide ground condition at 2.14 GHz.

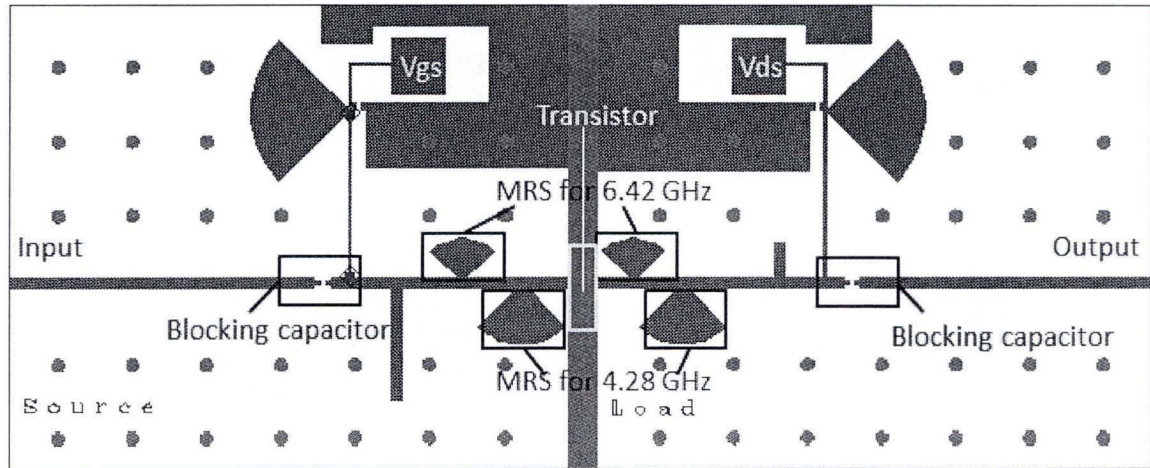


Figure 157: Layout of the proposed PA using MRS to suppress harmonic components

3.2.6 Fabrication and measurement

To demonstrate the new proposed wideband method, three MRSs and normal quarter-wave rectangular stubs are fabricated for the fundamental frequency (2.14 GHz), 2nd and 3rd harmonics as shown in Fig. 158. The measured results of the fabricated MRSs and normal quarter-wave rectangular stubs are compared in Fig. 159 to Fig. 161. Insertion loss of the 2nd and 3rd harmonics is better than 38.37 dB and 29.53 dB, respectively. In the 200 MHz bandwidth of MRS with center frequency 4.28 GHz, insertion loss is better than 28 dB. For the 3rd harmonic, in its 300 MHz bandwidth of MRS, insertion loss is better than 26 dB.

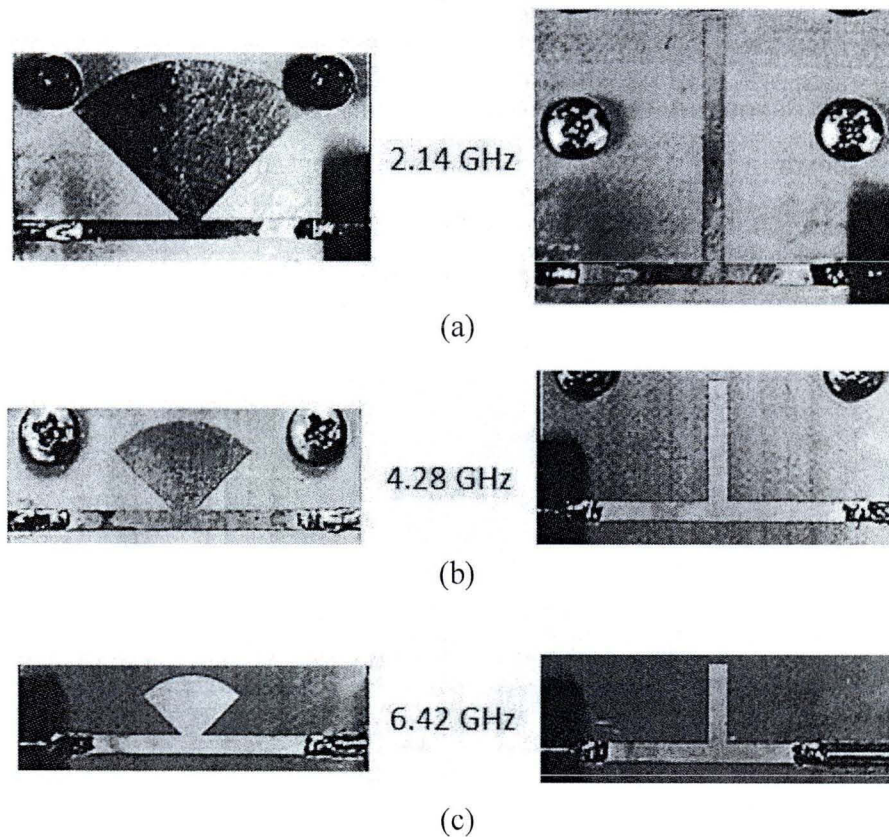


Figure 158: Fabricated MRSs and normal quarter-wave rectangular stubs, (a): 2.14 GHz, (b): 4.28 GHz, and (c): 6.42 GHz

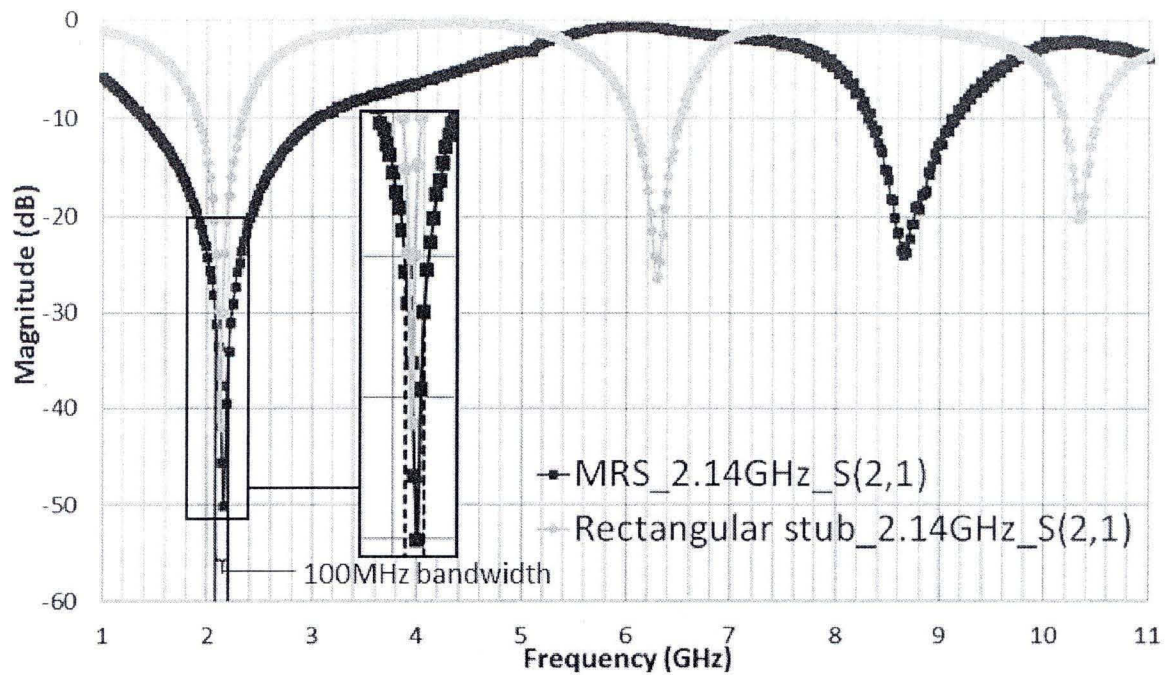


Figure 159: Measured results of the fabricated MRS and normal quarter-wave rectangular stub for 2.14 GHz

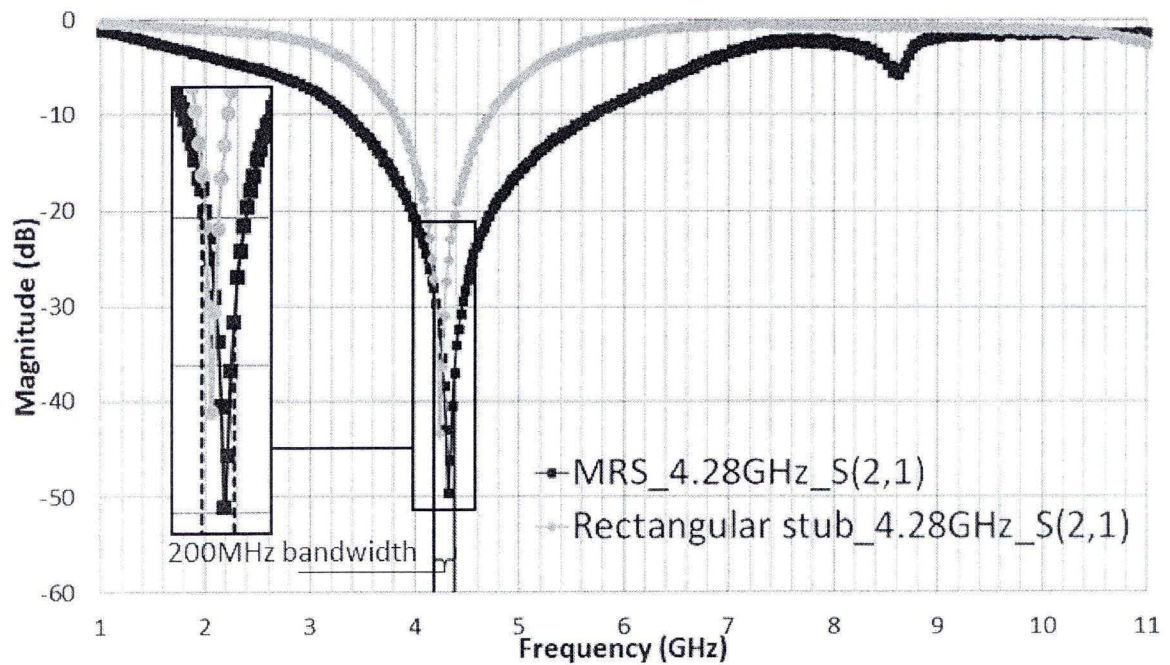


Figure 160: Measured results of the fabricated MRS and normal quarter-wave rectangular stub for 4.28 GHz

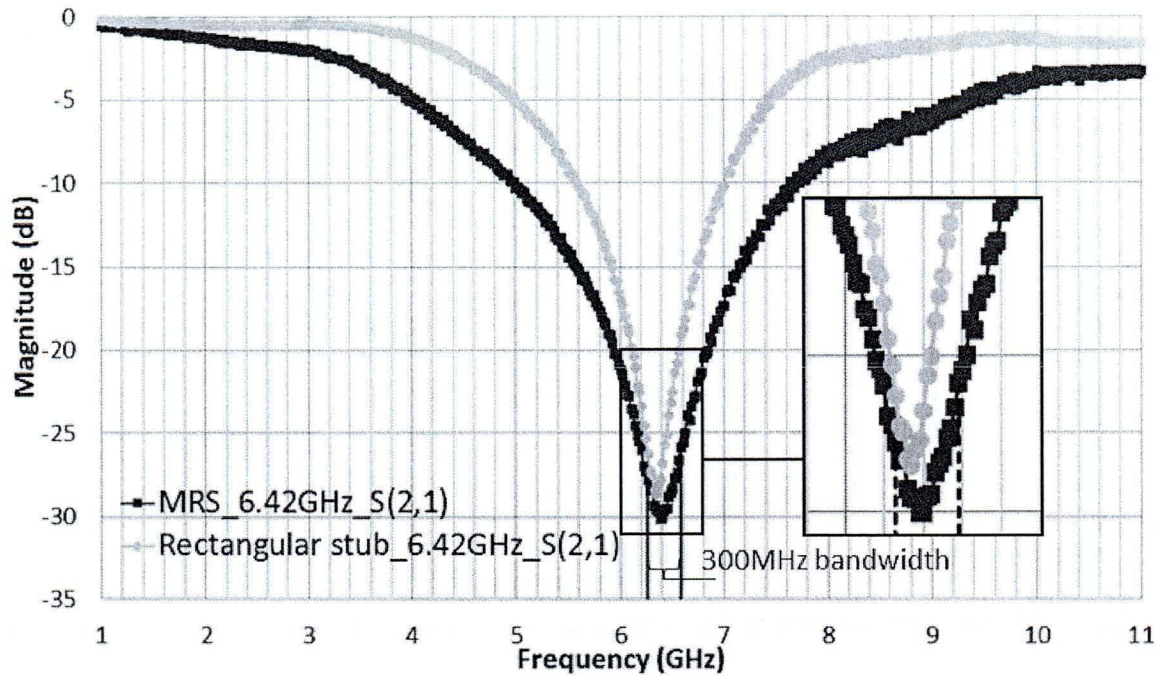


Figure 161: Measured results of the fabricated MRS and normal quarter-wave rectangular stub for 6.42 GHz

The fabricated wideband MRS harmonic suppressing PA is shown in Fig. 162. For the measurement, we set $V_{GS} = -2.24$ V and $V_{DS} = 28$ V. Continuous Wave (CW) excitation was employed. Measured AM-AM result and PAE and gain versus output power results are shown in Fig. 163 and Fig. 164, respectively. The maximum PAE we get is 80.52% with 40.53 dBm output power at 2.14 GHz. The maximum gain is 20.25 dB.

Fig. 165 shows the measured PAE and output power versus frequency results with input power 24.7 dBm. From 2 GHz to 2.26 GHz, at least 50% PAE and 37 dBm output power are achieved. Within the 100 MHz bandwidth centered at 2.12 GHz, the PAE is at least 73.6% and the output power is more than 40 dBm.

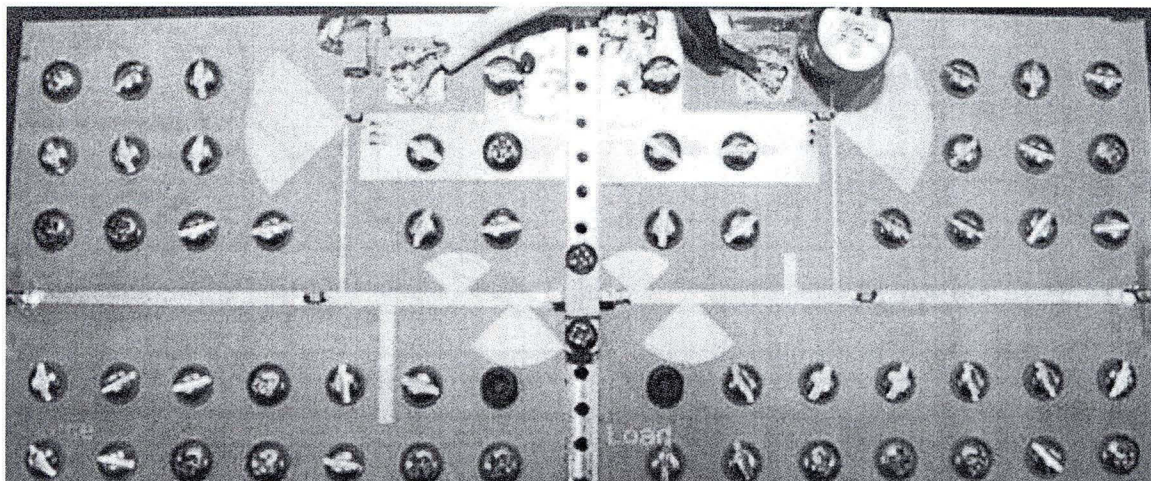


Figure 162: The fabricated proposed PA with MRS

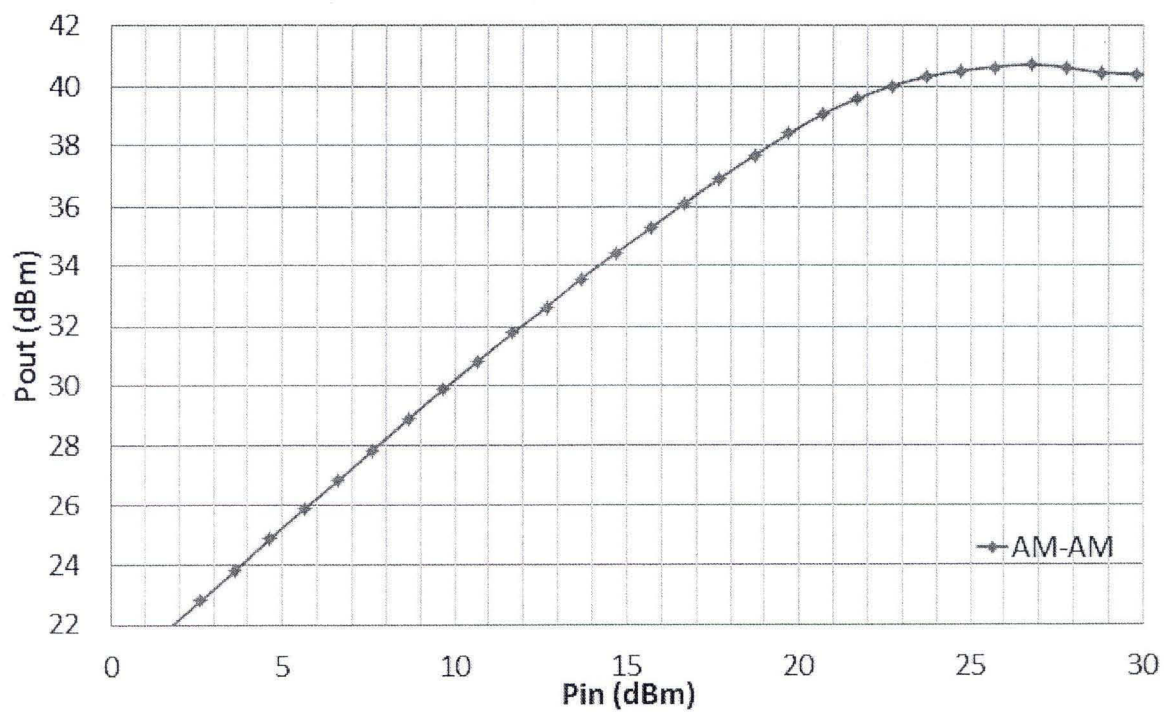


Figure 163: Measured AM-AM of the proposed PA with MRS

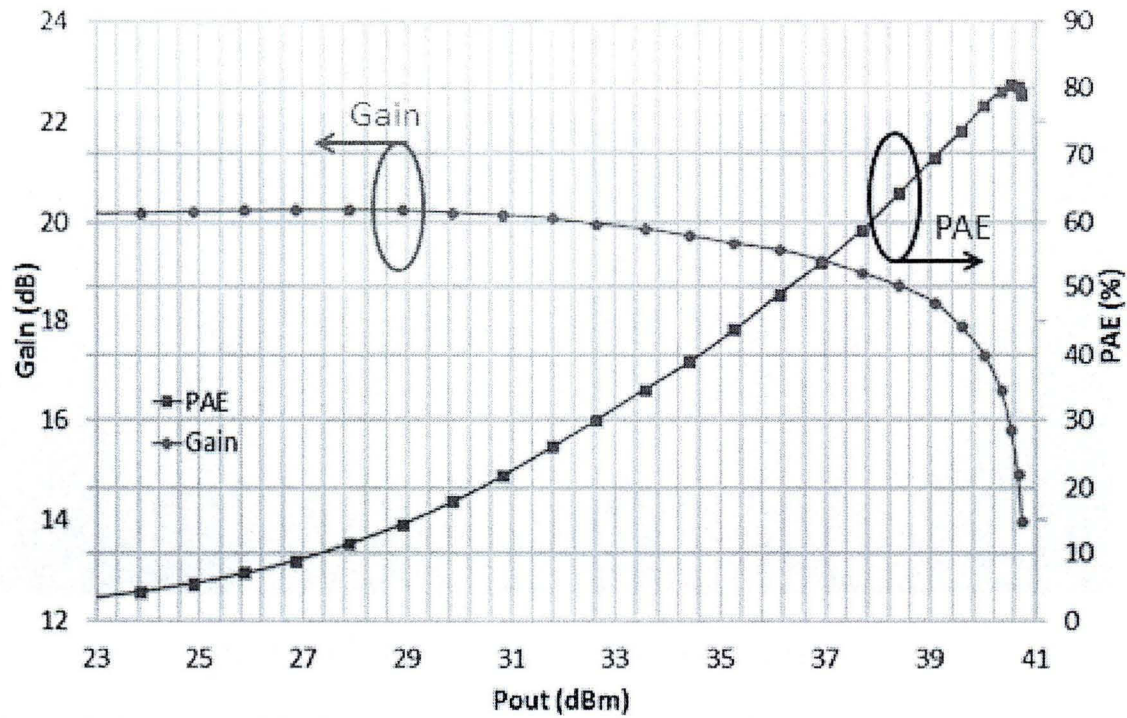


Figure 164: Measured PAE and gain versus output power of the proposed PA with MRS

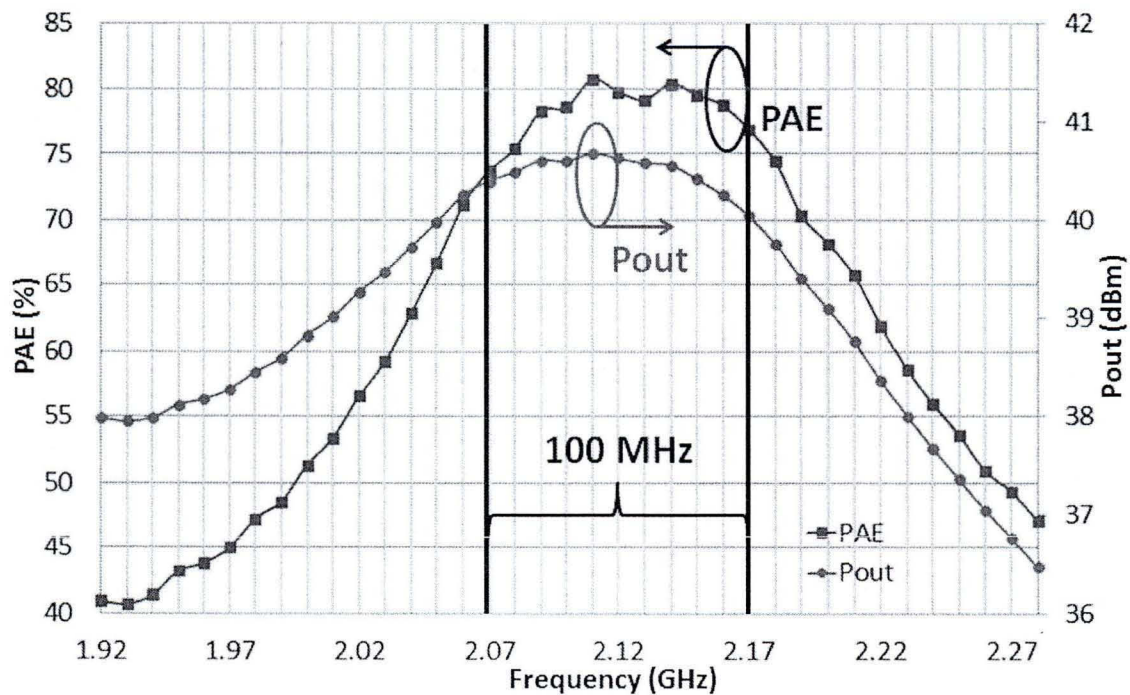


Figure 165: Measured PAE and output power obtained from 1.92 GHz to 2.27 GHz of the proposed PA with MRS

3.2.7 Conclusion

A novel type wideband GaN HEMT PA using MRS to suppress harmonic components is presented in this chapter. With the wideband harmonic suppressing characteristic of MRS, the 2nd and 3rd harmonics of 2.14 GHz are suppressed by -38.37 dB and -29.53 dB, respectively. Compared to normal rectangular quarter-wave stub, measured result shows that -15 dBc harmonic suppressing bandwidth of MRS is at least 1.9 times larger for both the 2nd and 3rd harmonics. A wideband MRS harmonic suppressing PA was designed and fabricated based on single frequency harmonic load pull results. Measured results show that the maximum PAE is 80.52% with 40.53 dBm output power at 2.14 GHz and the maximum gain is 20.25 dB. At least 50% PAE and 37 dBm output power over a 12% bandwidth from 2 GHz to 2.26 GHz is achieved. The design method of the proposed wideband PA can be applied for LTE Advanced application.

The contributions of this chapter are listed below:

1: To satisfy the wide bandwidth requirement in 4G mobile telecommunications network systems, one new wideband PA using MRS as harmonic suppression circuit in both input and output matching networks is demonstrated, designed, fabricated, and tested. This new type of wideband PA can be used for wideband applications.

2: A new method to analyze MRS stub for the purpose of harmonic suppression is demonstrated. The band suppression characteristic of the MRS stub and the conventional rectangular stub is compared. By changing the parameters (w and θ) of MRSs, the band suppression characteristic of MRS is revealed also. The bandwidth of harmonic suppression is enlarged by applying MRS stub in matching networks.

My original publication related to this chapter is listed below:

- [1] **Zhebin Wang** and Chan-Wang Park, "Novel Wideband GaN HEMT Power Amplifier Using Microstrip Radial Stub to Suppress Harmonics," IEEE MTT-S International Microwave Symposium Digest, pp. 1-3, Montréal, Canada, 17-22 June 2012.

CONCLUSION GÉNÉRALE

Dans les systèmes modernes de communication sans fil, il y a plusieurs types de standards de communication, comme WCDMA, WLANS, GSM, WiMAX, et LTE. L'interopérabilité et la coexistence entre les standards deviennent les problèmes principaux. Des composants ou dispositifs multibandes performants sont nécessaires pour satisfaire les diverses applications multibandes. Dans ce mémoire, les méthodes de conception multibandes sont explorées et démontrées dans le chapitre 1 et le chapitre 2 pour concevoir le diviseur de Wilkinson, la jonction *rat-race*, et l'amplificateur de puissance. En outre, pour les systèmes 4G à large bande passante, l'augmentation du débit de données et de la vitesse de communication mobile est nécessaire, par exemple, la bande passante de LTE *Advanced* va jusqu'à 100 MHz. La méthode de conception de l'amplificateur de puissance large bande à haut PAE est également discutée et présentée dans le chapitre 3.

Dans le chapitre 1, un diviseur de Wilkinson bibande, un diviseur de Wilkinson tribande, et une jonction *rat-race* tribande sont analysés, conçus, fabriqués et testés pour démontrer la méthode de conception multibande proposée. Le diviseur de Wilkinson conventionnel et la jonction *rat-race* conventionnelle se composent des lignes de transmission quarts d'onde. Pour réaliser le diviseur de Wilkinson multibande et la jonction *rat-race* multibande, nous devons concevoir une ligne de transmission quart d'onde multibande. En utilisant la matrice ABCD, le principe de ligne de transmission quart d'onde en forme de Pi avec des résonateurs est révélé. Nous avons appliqué la méthode proposée de la ligne de transmission quart d'onde multibande au diviseur de Wilkinson bibande, au diviseur de Wilkinson tribande, et à la jonction *rat-race* tribande. Avec l'aide de CAD (*Computer Aided Design*), les modèles de condensateurs, d'inductances, et de résonateurs parallèles sont comparés et analysés. Un diviseur de Wilkinson bibande, un diviseur de Wilkinson tribande, et une jonction *rat-race* tribande sont conçus et simulés. Pour maintenir la compacité de l'ensemble des circuits multibandes,

nous partageons les deux stubs avec résonateurs adjacents et mettons tous les stubs avec résonateurs dans les circuits multibandes. Enfin, les circuits multibandes proposés sont fabriqués et testés. Les résultats mesurés sont en bon accord avec les résultats de simulation.

Dans le chapitre 2, deux amplificateurs de puissance bibandes et un amplificateur de puissance tribande sont présentés. Le transistor que nous utilisons est GaN HEMT CGH40010 de CREE. L'amplificateur de puissance bibande est réalisé en mettant le résonateur LC parallèle entre la ligne microruban série et le stub circuit ouvert pour laisser passer ou bloquer le signal. La méthode de conception proposée du réseau d'adaptation bibande est appliquée à la fois aux réseaux d'adaptation d'entrée et de sortie. Deux amplificateurs de puissance bibandes sont présentés. On utilise le résonateur composé d'une capacité en parallèle avec une inductance pour l'un des deux amplificateurs et on utilise le résonateur composé d'une capacité en parallèle avec une ligne microruban étroite pour l'autre. L'avantage et le désavantage de ces deux types de résonateur sont présentés au chapitre 2 en détail. Les résultats mesurés montrent la bonne performance des deux amplificateurs de puissance bibandes. Pour l'amplificateur de puissance tribande, on utilise le groupe de résonateur composé de deux résonateurs LC parallèles comme un élément pour sélectionner la fréquence. En insérant le groupe de résonateurs entre la ligne microruban série et le stub circuit ouvert, le réseau d'adaptation tribande proposé est réalisé. Comme dans l'amplificateur de puissance bibande, nous appliquons la méthode proposée de conception de réseau d'adaptation tribande à la fois dans les réseaux d'adaptation d'entrée et de sortie. Un amplificateur de puissance tribande est ainsi réalisé. Le réseau d'adaptation de sortie de l'amplificateur de puissance tribande proposé est amélioré en utilisant le circuit de polarisation tel que le réseau d'adaptation pour la fréquence la plus basse, ainsi la longueur totale de l'amplificateur de puissance tribande proposée est réduite et deux groupes de résonateurs sont économisés. Les résultats mesurés montrent les bonnes performances de l'amplificateur de puissance tribande proposé. Par rapport à l'amplificateur de puissance multibande à l'aide des commutateurs ou des éléments électroniques ajustables, l'amplificateur de puissance multibande proposé peut

réaliser simultanément des performances multibandes. La taille de l'ensemble du circuit multibande est réduite, car en n'utilisant pas les amplificateurs de puissance parallèles ou réseaux d'adaptation parallèles, le coût de l'amplificateur de puissance multibande est réduit, en particulier le coût du transistor.

Dans le chapitre 3, un amplificateur de puissance large bande à haut PAE est présenté. Dans les systèmes 4G, la large bande passante est requise. Pour améliorer le PAE, normalement, nous utilisons un stub quart d'onde pour supprimer d'harmoniques. Mais, les bandes passantes du deuxième harmonique et du troisième harmonique sont respectivement deux et trois fois plus grandes que la bande de la fréquence fondamentale. Le MRS en parallèle avec la performance de suppression large bande est analysé et appliqué. Nous avons appliqué le MRS à la fois dans les réseaux d'adaptation d'entrée et de sortie pour supprimer la deuxième et la troisième harmoniques. Par rapport au stub quart d'onde normal, le résultat mesuré montre que -15 dBc de suppression de bande passante des harmoniques du MRS est au moins 1,9 fois plus grande. Les résultats mesurés montrent l'excellente performance de l'amplificateur de puissance à large bande en utilisant le MRS. Le PAE maximal est 80,52% avec 40,53 dBm de puissance de sortie à 2,14 GHz et le gain maximal est 20,25 dB. Au moins 50% de PAE et 37 dBm de puissance de sortie sur une bande passante de 12%, de 2 GHz à 2,26 GHz sont obtenus.

À l'avenir, la méthode de conception multibande du diviseur de Wilkinson, de la jonction *rat-race*, et de l'amplificateur de puissance proposée peut être facilement appliquée dans différentes applications multibandes. Par exemple dans les circuits multibandes avec une structure plus complexe, comme l'amplificateur équilibré et l'amplificateur de puissance Doherty. La méthode de conception proposée à large bande de l'amplificateur de puissance à haut PAE peut être largement utilisée pour les systèmes 4G.

RÉFÉRENCES BIBLIOGRAPHIQUES

- ADAR, A., J. DEMOURA, H. BALSHEM, et J. LOTT. 1998. « A high efficiency single chain GaAs MESFET MMIC dual band power amplifier for GSM/DCS handsets ». Dans *Gallium Arsenide Integrated Circuit Symposium*. (Atlanta, GA, USA, 1-4 novembre 1998), pp. 69-72.
- AFLAKI, Pouya, Renato NEGRA, et Fadhel M. GHANNOUCHI. 2010. « Dual-band rat-race balun structure using transmission-lines and lumped component resonators ». Dans *IEEE MTT-S International Microwave Symposium Digest*. (Anaheim, CA, USA, 23-28 mai 2010), pp. 1572-1575.
- ALKANHAL, Majeed A. S.. 2008. « Reduced-size dual band Wilkinson power dividers ». Dans *International Conference on Computer and Communication Engineering*. (Kuala Lumpur, Malaysia, 13-15 mai 2008), pp. 1294-1298.
- BAHL, Inder. 2003. *Lumped Elements for RF and Microwave Circuits*. Norwood, MA, USA. 488 p.
- BESSER, Les, et Rowan GILMORE. 2003. *Practical RF Circuit Design for Modern Wireless Systems: Passive Circuit and Systems*, Volume I. Norwood, MA, USA. 539 p.
- CHENG, Kwok-Keung M., et Fai-Leung WONG. 2007. « A new Wilkinson power divider design for dual band application ». *IEEE Microwave and Wireless Components Letters*, volume 17, numéro 9, (septembre), pp. 664-666.
- CHI, Pei-Ling, Cheng-Jung LEE, et Tatsuo ITOH. 2008. « A compact dual-band metamaterial-based rat-race coupler for a MIMO system application ». Dans *IEEE MTT-S International Microwave Symposium Digest*. (Atlanta, GA, USA, 15-20 juin 2008), pp. 667-670.
- CHIN, Kuo-Sheng, Ken-Min LIN, Yen-Hsiu WEI, Tzu-Hao TSENG, et Yu-Jie YANG. 2010. « Compact dual-band branch-line and rat-race couplers with stepped-impedance-stub lines ». *IEEE Transactions on Microwave Theory and Techniques*, volume 58, numéro 5, (mai), pp. 1213-1221.
- CHIOU, Yi-Chyun, Jen-Tsai KUO, et Chi-Hung CHAN. 2009. « New miniaturized dual-band rat-race coupler with microwave C-sections ». Dans *IEEE MTT-S*

- International Microwave Symposium Digest*. (Boston, MA, USA, 7-12 juin 2009), pp. 701-704.
- CHONGCHEAWCHAMNAN, Mitchai, Sumongkol PATISANG, Monai KRAIRIKSH, et Ian D. ROBERTSON. 2006. « Tri-band Wilkinson power divider using a three-section transmission-line transformer ». *IEEE Microwave and Wireless Components Letters*, volume 16, numéro 8, (août), pp. 452-454.
- CHOU, I-Tung, Chia-Mei PENG, et I-Fong CHEN. 2010. « A dual-band Wilkinson power divider with microstrip slow-wave structures ». Dans *Asia Pacific International Symposium on Electromagnetic Compatibility*. (Beijing, China, 12-16 avril 2010), pp. 723-726.
- CRIPPS, Steve C. 2006. *RF Power Amplifier for Wireless Communications*, 2^e édition. Norwood, MA, USA. 456 p.
- DONG, Yuandan, et Tatsuo ITOH. 2010. « Application of composite right/left-handed half-mode substrate integrated waveguide to the design of a dual-band rat-race coupler ». Dans *IEEE MTT-S International Microwave Symposium Digest*. (Anaheim, CA, USA, 23-28 mai 2010), pp. 712-715.
- DRASKOVIC, D., et D. BUDIMIR. 2009. « Varactor tuned dual-band Wilkinson power divider ». Dans *IEEE Antennas and Propagation Society International Symposium*. (Charleston, SC, USA, 1-5 juin 2009), pp. 1-4.
- EDWARDS, Terry. 1992. *Foundations for Microstrip Circuit Design*, 2^e édition. Chichester, West Sussex, England. 414 p.
- EO, YunSeong, et KwangDu LEE. 2004. « A 2.4GHz/5.2GHz CMOS power amplifier for dual-band applications ». Dans *IEEE MTT-S International Microwave Symposium Digest*. (Fort Worth, TX, USA, 5-12 juin 2004), volume 3, pp. 1539-1542.
- GARDIOL, Fred. 1994. *Microstrip Circuits*. New York, NY, USA: Kai Chang. 300 p.
- GONZALEZ, Guillermo. 1997. *Microwave Transistor Amplifiers Analysis and Design*, 2^e édition. Upper Saddle River, NJ, USA: Eric Svendsen. 506 p.
- HSU, Ching-Luh, Chin-Wei CHANG, et Jen-Tsai KUO. 2007. « Design of dual-band microstrip rat-race coupler with circuit miniaturization ». Dans *IEEE MTT-S International Microwave Symposium*. (Honolulu, HI, USA, 3-8 juin 2007), pp. 177-180.

- JEONG, Jinseong, Donald F. KIMBALL, Myoungbo KWAK, Chin HSIA, Paul DRAXLER, et Peter M. ASBECK. 2009. « Modeling and design of RF amplifiers for envelope tracking WCDMA base-station applications ». *IEEE Transactions on Microwave Theory and Techniques*, volume 57, numéro 9, (septembre), pp. 2148-2159.
- JOU, Christina F., Kuo-Hua CHENG, Chia-Min LIN, et Jia-Liang CHEN. 2003. « Dual band CMOS power amplifier for WLAN applications ». Dans *IEEE 46th Midwest Symposium on Circuits and Systems*. (Cairo, Al Qahirah, Egypt, 27-30 décembre 2003), vol. 3, pp. 1227-1230.
- KANG, Daehyun, Dongsu KIM, Jinsung CHOI, et Bumman KIM. 2010. « LTE power amplifier for envelope tracking polar transmitters ». Dans *European Microwave Conference (EuMC)*. (Paris, France, 28-30 septembre 2010), pp. 628-631.
- KANG, Daehyun, Dongsu KIM, Yunsung CHO, Jooseung KIM, Byungjoon PARK, Chenxi ZHAO, et Bumman KIM. 2011. « 1.6-2.1 GHz broadband Doherty power amplifiers for LTE handset applications ». Dans *IEEE MTT-S International Microwave Symposium Digest*. (Baltimore, MD, USA, 5-10 juin 2011), pp. 1-4.
- KIM, Dongsu, Jinsung CHOI, Daehyun KANG, et Bumman KIM. 2010. « High efficiency and wideband envelope tracking power amplifier with sweet spot tracking ». Dans *IEEE Radio Frequency Integrated Circuits Symposium*. (Anaheim, CA, USA, 23-25 avril 2010), pp. 255-258.
- KONG, C. P., et Kwok-Keung M. CHENG. 2006. « Dual-band rat-race coupler with bandwidth enhancement ». Dans *IEEE MTT-S International Microwave Symposium Digest*. (San Francisco, CA, USA, 11-16 juin 2006), pp. 1559-1562.
- KUNIHIO, Kazuaki, Shingo YAMANOUCHI, Takashi MIYAZAKI, Yuuichi AOKI, Kazuhiro IKUINA, Takashi OHTSUKA, et Hikaru HIDA. 2004. « A diplexer-matching dual-band power amplifier LTCC module for IEEE 802.11a/b/g wireless LANs ». Dans *IEEE Radio Frequency Integrated Circuits Symposium*. (Fort Worth, TX, USA, 6-8 juin 2004), pp. 303-306.
- LEE, Jin-Gul, Choon-Sik CHO, Jae W. LEE, et Sang-Ki EUN. 2008. « A Novel Dual-Band Wilkinson Power Divider Using Branch-line ». Dans *Asia Pacific Microwave Conference*. (Hong Kong, China, 16-20 décembre 2008), pp. 1-4.
- LEE, Yong-Sub, Mun-Woo LEE, Sang-Ho KAM, et Yoon-Ha JEONG. 2009. « A wideband multi-branch analog predistorter with memory-effect compensation for multi-carrier WCDMA repeater systems ». Dans *IEEE MTT-S International*

- Microwave Symposium Digest*. (Boston, MA, USA, 7-12 juin 2009), pp. 1081-1084.
- LIN, I-Hsiang, Marc DEVINCENTIS, Christophe CALOZ, et Tatsuo ITOH. 2004. « Arbitrary dual-band components using composite right/left-handed transmission lines ». *IEEE Transactions on Microwave Theory and Techniques*, volume 52, numéro 4, (avril), pp. 1142-1149.
- MA, Kaixue, et Kiat Seng YEO. 2011. « New ultra-wide stopband low-pass filter using transformed radial stubs ». *IEEE Transactions on Microwave Theory and Techniques*, volume 59, numéro 3, (mars), pp. 604-611.
- MARAL, Gerard, et Michel BOUSQUET. 2002. *Satellite Communications Systems: Systems, Techniques and Technology*, 4^e édition. Chichester, West Sussex, England. 757 p.
- MOHRA, Ashraf S. S.. 2008. « Compact dual band Wilkinson power divider ». Dans *25th National Radio Science Conference*. (Tanta, Egypt, 18-20 mars 2008), pp. 1-7.
- NEGRA, Renato, Alexandre SADEVE, Souheil BENSMIDA, et Fadhel M. GHANNOUCHI. 2008. « Concurrent dual-band class-F load coupling network for applications at 1.7 and 2.14 GHz ». *IEEE Transactions on Circuits and Systems II, Express Briefs*, volume 55, numéro 3, (mars), pp. 259-263.
- PARK, Myun-Joo. 2009 a. « Two-section cascaded coupled line Wilkinson power divider for dual-band applications ». *IEEE Microwave and Wireless Components Letters*, volume 19, numéro 4, (avril), pp. 188-190.
- PARK, Myun-Joo. 2009 b. « Dual-band Wilkinson divider with coupled output port extensions ». *IEEE Transactions on Microwave Theory and Techniques*, volume 57, numéro 9, (septembre), pp. 2232-2237.
- PARK, Myun-Joo, et Byungje LEE. 2008. « A Dual-Band Wilkinson Power Divider ». *IEEE Microwave and Wireless Components Letters*, volume 18, numéro 2, (février), pp. 85-87.
- POZAR, David M. 2001. *Microwave and RF Design of Wireless Systems*. New York, NY, USA: Bill Zobrist. 366 p.
- POZAR, David M. 2005. *Microwave Engineering*, 3^e édition. Hoboken, NJ, USA: Bill Zobrist. 700 p.

- RYU, Jong-In, Jong-Won MOON, Dongsu KIM, et Jun Chul KIM. 2009. « Implementation of the front-end module with a power amplifier for dual-band wireless LAN ». Dans *The 39th European Microwave Conference*. (Nuova Fiera di Roma, Rome, Italy, 28 septembre 2009 - 2 octobre 2009), pp. 1357-1360.
- SISO, Gerard, Jordi BONACHE, et Ferran MARTIN. 2009. « Dual-band rat race hybrid coupler implemented through artificial lines based on complementary split ring resonators ». Dans *IEEE MTT-S International Microwave Symposium Digest*. (Boston, MA, USA, 7-12 juin 2009), pp. 625-628.
- SRISATHIT, Sarayut, Sarayut VIRUNPHUN, Kamorn BANDUDEJ, Mitchai CHONGCHEAWCHAMNAN, et Apisak WORAPISHET. 2003. « A dual-band 3-dB three-port power divider based on a two-section transmission line transformer ». Dans *IEEE MTT-S International Microwave Symposium Digest*. (Philadelphia, PA, USA, 8-13 juin 2003), pp. 35-38.
- STEINBEISER, Craig, Thomas LANDON, et Charles SUCKLING. 2007. « 250W HVHBT Doherty with 57% WCDMA efficiency linearized to -55dBc for 2c11 6.5dB PAR ». Dans *IEEE Compound Semiconductor Integrated Circuit Symposium*. (Portland, OR, USA, 14-17 octobre 2007), pp. 1-4.
- UJIE, Ryuichi, Hisayasu SATO, et Noboru ISHIHARA. 2007. « A dual band RFCMOS amplifier using inductive reactance switching ». Dans *2007 Topical Meeting on Silicon Monolithic Integrated Circuits in RF Systems*. (Long Beach, CA, USA, 10-12 janvier 2007), pp. 131-134.
- WANG, Zhebin, Shengjie Gao, et Chan-Wang PARK. 2010. « A simple method for tunable load impedance matching network of power amplifier ». Dans *IEEE International Conference on Microwave and Millimeter Wave Technology*. (Chengdu, Sichuan, China, 8-11 mai 2010), pp. 484-487.
- WANG, Zhebin, Jae Sik JANG, et Chan-Wang PARK. 2011 a. « Compact dual-band Wilkinson power divider using lumped component resonators and open-circuited stubs ». Dans *The 12th Annual IEEE Wireless and Microwave Technology (WAMI) Conference*. (Clearwater, FL, USA, 18-19 avril 2011), pp. 1-4.
- WANG, Zhebin, Jae Sik JANG, et Chan-Wang PARK. 2011 b. « Tri-band Wilkinson power divider using resonators ». Dans *IEEE Radio and Wireless Symposium*. (Phoenix, AZ, USA, 16-19 janvier 2011), pp. 287-290.
- WANG, Zhebin, Jae Sik JANG, et Chan-Wang PARK. 2011 c. « Tri-band rat-race coupler using resonators ». Dans *International Conference on Microwave*

- Technology & Computational Electromagnetics*. (Beijing, China, 22-25 mai 2011), pp. 186-189.
- WANG, Zhebin, et Chan-Wang PARK. 2011 d. « Dual-band GaN HEMT power amplifier using resonators in matching networks ». Dans *The 12th Annual IEEE Wireless and Microwave Technology (WAMI) Conference*. (Clearwater, FL, USA, 18-19 avril 2011), pp. 1-4.
- WANG, Zhebin, Shengjie GAO, Fathi NASRI, et Chan-Wang PARK. 2011 e. « GaN power amplifier with harmonic controlled by dual band-notched UWB band-pass filter ». Dans *European Microwave Integrated Circuits Conference (EuMIC)*. (Manchester, UK, 9-14 octobre 2011), pp. 240-243.
- WANG, Zhebin, et Chan-Wang PARK. 2012 a. « Multiband Pi-shaped structure with resonators for tri-band Wilkinson power divider and tri-band rat-race coupler ». Dans *IEEE MTT-S International Microwave Symposium Digest*. (Montréal, QC, Canada, 17-22 juin 2012), pp. 1-3.
- WANG, Zhebin, et Chan-Wang PARK. 2012 b. « Concurrent tri-band GaN HEMT power amplifier using resonators in both input and output matching networks ». Dans *The 13th Annual IEEE Wireless and Microwave Technology (WAMI) Conference*. (Cocoa Beach, FL, USA, 15-17 avril 2012), pp. 1-4.
- WANG, Zhebin, et Chan-Wang PARK. 2012 c. « Novel wideband GaN HEMT power amplifier using microstrip radial stub to suppress harmonics ». Dans *IEEE MTT-S International Microwave Symposium Digest*. (Montréal, QC, Canada, 17-22 juin 2012), pp. 1-3.
- WILKINSON, Ernest J.. 1960. « An N-way hybrid power divider ». *IRE Transactions on Microwave Theory and Techniques*, volume 8, numéro 1, (janvier), pp. 116-118.
- WRIGHT, Peter, Jonathan LEES, Johannes BENEDIKT, Paul J. TASKER, et Steve C. CRIPPS. 2009. « A methodology for realizing high efficiency class-J in a linear and broadband PA ». *IEEE Transactions on Microwave Theory and Techniques*, volume 57, numéro 12, (décembre), pp. 3196-3204.
- WU, Cho-Yu, Yi-Chyun CHIOU, et Jen-Tsai KUO. 2009 a. « Dual-band rat-race coupler with arbitrary power divisions using microwave C-sections ». Dans *Asia Pacific Microwave Conference*. (Singapore, 7-10 décembre 2009), pp. 2108-2111.

- WU, Yongle, Yuanan LIU, Yaxing ZHANG, Jinchun GAO, et Hui ZHOU. 2009 b. « A dual band unequal Wilkinson power divider without reactive components ». *IEEE Transactions on Microwave Theory and Techniques*, volume 57, numéro 1, (janvier), pp. 216-222.
- WU, David Yu-Ting, Farouk MKADEM, et Slim BOUMAIZA. 2010. « Design of a broadband and highly efficient 45W GaN power amplifier via simplified real frequency technique ». Dans *IEEE MTT-S International Microwave Symposium Digest*. (Anaheim, CA, USA, 23-28 mai 2010), pp. 1090-1093.
- YAMAMOTO, K., T. ASADA, S. SUZUKI, T. MIURA, A. INOUE, S. MIYAKUNI, J. OTSUJI, R. HATTORI, Y. MIYAZAKI, et T. SHIMURA. 2002. « A GSM/EDGE dual-mode, 900/1800/1900-MHz triple-band HBT MMIC power amplifier module ». Dans *Radio Frequency Integrated Circuits Symposium*. (Seattle, WA, USA, 2-4 juin 2002), pp. 245-248.

